Event shape dependent pion femtoscopy of proton-proton collisions at 7 TeV center-of-mass energy

Simatović, Goran

Doctoral thesis / Disertacija

2015

Degree Grantor / Ustanova koja je dodijelila akademski / stručni stupanj: **University of Zagreb, Faculty of Science / Sveučilište u Zagrebu, Prirodoslovno-matematički fakultet**

Permanent link / Trajna poveznica: https://urn.nsk.hr/urn:nbn:hr:217:411364

Rights / Prava: In copyright/Zaštićeno autorskim pravom.

Download date / Datum preuzimanja: **2025-04-02**

UNIVERSITY OF ZAGREB

FACULTY OF SCIENCE

DEPARTMENT OF PHYSICS

Goran Simatović

EVENT SHAPE DEPENDENT PION FEMTOSCOPY OF PROTON-PROTON COLLISIONS AT 7 TeV CENTER-OF-MASS ENERGY

Thesis presented in partial fulfillment of the requirements

for the degree of

Doctor of Natural Sciences in the Field of Physics

Zagreb, 2015

SVEUČILIŠTE U ZAGREBU

PRIRODOSLOVNO-MATEMATIČKI FAKULTET

FIZIČKI ODSJEK

Goran Simatović

PIONSKA FEMTOSKOPIJA SUDARA PROTONA I PROTONA NA ENERGIJI 7 TEV U CENTRU MASE U OVISNOSTI O OBLIKU SUDARA

Doktorska teza predana je kao djelomično ispunjenje uvjeta
za stjecanje stupnja
Doktora Prirodnih Znanosti u Području Fizike

Zagreb, 2015

DOCUMENTATION CARD

Event shape dependent pion femtoscopy of proton-proton collisions at 7 TeV center-of-mass energy

Goran Simatović

Faculty of Science, Zagreb

We present a measurement of event shape dependent two-particle momentum space correlations for identical pions in pp collisions at $\sqrt{s} = 7$ TeV obtained by the ALICE detector. Homogeneity radii are extracted and studied as a function of pair $k_{\mathrm{T}} = \left| p_{\mathrm{T}}^1 + p_{\mathrm{T}}^2 \right|/2$ in a wide range of event multiplicities for spherical and jet-like events. Spherical or jet-free events show a large reduction in (non-femtoscopic) background contributions to two-particle correlations which expands the k_{T} range of the analysis and allows for a bias-free data driven femtoscopic analysis. For jet-like events the non-femtoscopic contributions are measured to be several times larger than the observed Bose-Einstein signal. By comparing ALICE measurements to PYTHIA and PHOJET generated data, a background signal removal method is developed and in-jet HBT radii are obtained. For both spherical and jet-like events, the extracted 1D homogeneity radii show a diminished k_{T} dependence, differing to previously observed behavior in minimum bias events. After constraining the λ parameter, spherical event radii continue to have no k_{T} dependence, which suggests a lack of radial flow, while jet-like event radii develop a clear k_{T} and multiplicity dependence similar to the one observed in published sphericity integrated results.

(143 pages, 57 references)

Supervisor: prof.dr.sc. Mirko Planinić

Committee:

1. prof.dr.sc. Vuko Brigljević

2. doc.dr.sc. Davor Horvatić

3. dr.sc. Krešo Kadija

Thesis accepted in 2015

TEMELJNA DOKUMENTACIJSKA KARTICA

Pionska femtoskopija sudara protona i protona na energiji 7 TeV u centru mase u ovisnosti o obliku događaja

Goran Simatović

Prirodoslovno-matematički fakultet, Zagreb

Prikazana su mjerenja dvočestičnih korelacija impulsa za identične pione u protonskim sudarima na energiji od 7 TeV u centru mase sa ALICE detektorom. Određena je ovisnost radijusa homogenosti o srednjem transverzalnom valnom vektoru para $k_\mathrm{T} = \left| p_\mathrm{T}^1 + p_\mathrm{T}^2 \right| /2$ za širok spektar multipliciteta sudara visoke i niske sferičnosti. Sferični sudari pokazuju smanjenje nefemtoskopskih doprinosa dvočestičnim korelacijama što dopušta analizu podataka, znatno šireg dosega u k_T, bez potrebe za dodatnim pretpostavkama. Za sudare sa mlazovima, nefemtoskopski doprinosi sadržavaju signal višestruko veći od oni induciranih Bose-Einsteinovim korelacijama. Usporedbom mjerenja ALICE detektora te PYTHIA i PHOJET generatora razvijena je metoda uklanjanja pozadinskih signala te su izmjereni HBT radijusi unutar mlazova. Korištene su Gausova i eksponencijalna funkcija prilagodbe te su prokomentirane razlike. Izmjereni 1D radijusi homogenosti za obje ekstremne vrijednost sferičnosti pokazuju nisku ovisnost o k_T. Nakon ograničavanja λ parametra, sferični događaji i dalje ne pokazuju k_T ovisnost, što sugerira manjak radijalnog toka čestica, dok događaji sa mlazovima pokazuju jasnu ovisnost o k_T i multiplicitetu, vrlo slično već objavljenim rezultatima.

ključne riječi: ALICE, femtoskopija, HBT, transverzalna sferičnost, kvark gluonska plazma, hidrodinamička kolektivnost, hadronizacijska duljina, protonski sudari sa $\sqrt{s} = 7$ TeV

(143 stranice, 57 referenci)

Mentor: prof.dr.sc. Mirko Planinić

Ocjenjivači:

1. izv. prof. dr. sc. Vuko Brigljević

2. doc.dr.sc. Davor Horvatić

3. dr.sc. Krešo Kadija

Rad prihvaćen 2015.

Acknowledgements

Table of contents

List of figures

Chapter 1

Introduction

Measuring particle correlations in high energy collision experiments is a proven precision tool for investigating spatio-temporal scales of the created emission source. By measuring the radial evolution of the created fireball, one is able to extract important information on the state of the produced partonic matter. Apart from being important in this respect, a detailed understanding of the femtoscopic aspects of proton-proton collisions is also necessary for a natural extrapolation to heavy-ion research. With the start of the 7 TeV center-of-mass energy regime at the Large Hadron Collider (LHC), proton-proton collision multiplicities are becoming comparable to the ones measured in peripheral heavy-ion collisions at the Relativistic Heavy Ion Collider (RHIC) and LHC [1], thus increasing the need for a detailed inspection of nucleon-nucleon collisions. For this analysis we use charged pions, the most numerous of all created mesons ($\approx 60\%$), which allow for a rich statistical analysis with the ability to go beyond minimum bias events and explore various event categories in detail.

The aim of this research is to explore identical particle correlations, charged pion in particular, cutting for specific event shapes of special interest. By characterizing events by their topology, using transverse sphericity [2, 3] as the main global event shape variable, one is able to differentiate between jet-like events and a variety of soft producing events with the idea that the two mentioned categories of events differ in interaction hardness and, as such, carry characteristic information in their own respect on the perturbative and non-perturbative aspects of the created QCD matter.

From previous studies[4] it is known that background contributions to two-particle interferometry (HBT) coming from jets or jet-like structures create a significant signal in the high pair k_T region. Due to a small signal-to-background ratio, these correlations are effectively stopping any attempt of analysis in this higher k_T domain ($k_T > 0.6$ GeV/c). Such background were also observed in other collision systems[5] and were shown to be significantly suppressed using the three-pion cumulant approach[6]. It is still an open question of what is the best way to take into account all background contributions and extrapolate correct homogeneity radii with their proper

interpretations. In this thesis we propose a novel method using event event shape classification. It is based on the fact that with a proper event shape cut it is possible to remove a large portion of the jet background, thus extensively expanding the k_T range of the HBT analyses, and extract homogeneity radii which are non-biased and assumption free with respect to possible background functions and event generators respectively. Also, by cutting on different event shape variables, it is possible to investigate a spectrum of QCD systems with different hardness and observe the jet+underlying event correlation function structure. This approach could also offer some hints at in-medium energy loss.

Considering jet-like events, an attempt is made to identify most of the background correlations by comparison to event generator data. By comparing measured ALICE data to PYTHIA and PHOJET event generator results for both identical and non-identical pion pairs, it is possible to produce a corrected correlation function and extract for the first time the in-jet Bose-Einstein correlations and offer a possible interpretation. Several options for an effective background removal method are suggested and compared within the analysis.The possibility of non-Gaussian correlation functions is explored and fit results for several realistic options of data motivated fit function generalizations are offered.

In this thesis we explore in detail the effects of event shape selection on two-pion interferometry analysis for proton-proton collision at $\sqrt{s} = 7$ TeV. The second and third chapter offer a short overview of quantum field theory and quark-gluon plasma research. The fourth chapter describes the experimental setup of the detector and its detector subsystems. The fifth chapter explains in short what femtoscopy is, its connection to the Hanbury-Brown and Twiss effect (HBT) and its experimental application. In the sixth chapter event shape characterization and the transverse sphericity observable are defined. There we make the connection to femtoscopic research and its possible application. The seventh chapter is a detailed description of the analysis method with all the event, track and quality cuts used. The eight and ninth chapter show correlation functions (CFs) obtained using measured ALICE data and Monte Carlo generated data respectively. In the tenth chapter a comparison between measured and simulated data is made for both same charge and opposite charge pion pairs. The eleventh chapter contains all the systematic checks made to ensure that the physics message is stable within a reasonable variation of analysis cuts and data sets. The twelfth chapter contains approved ALICE preliminary plots and various internal consistency checks. In the thirteenth chapter we consider λ and α variables in the fitting procedure and their effects on the final result. In the final chapter an overview of the results with suggestions for further investigations is given with a clear aim at physical interpretation and generalization of the results. The appendix contains a derivation of a method for comparing Gaussian and exponential fit results.

Chapter 2

Quantum Field Theory

Field theories are a two century old success story. Intuitively introduced by Michael Faraday in the 19th century, field theory is an firmly established constituent of the physical sciences. Its first detailed mathematical application was obtained by James Clerk Maxwell in the form of four differential equations which unified electricity and magnetism. By allowing the derivation of the properties of light from equations concerning the electric and magnetic fields field theory suggested a possible wide application of such concepts in science.

In the 20th century, Einstein recognized that gravity can also be attributed to the behavior of a field. This field not only described the gravitational force but also the metric of space-time. It agreed with all known measurements and provided insight into many new gravitational effects. This theory, now known as the general theory of relativity (GTR), is the best known theory for describing space-time and its interaction with matter and energy. Successes like these lead to a wide investigation of the properties of fields and their application in science.

Quantum field theory (QFT) was created as a natural response to the need to successfully marry two of the most profound theories of the 20th century. First put forth by Planck and later extended by many others into its standard form which we know today, quantum theory, or the "theory of the small", was joined with Einsteins' special relativity, or "theory of the fast", with the hope of developing a theory which will encompass all known aspects of the natural world. Both the world of the large and the slow were considered to be fairly understood at the time so if a theory was proposed with the capabilities to tie down both extremes of size and relative speed then this grand scheme would become the crowning achievement of the 20th century physics.

From it's start quantum field theory was a success. As before, it all started with electromagnetism where the need to treat electrons and the electromagnetic field (photons) on the same footing, as elementary particles, gave rise to a common formalism of creation and annihilation operators, frequently called "the second quantization". It was a paradigm shift in the whole field which quickly lead to the creation of the fermion pair creation and annihilation picture of quantum

electrodynamics (QED). Consequently, a prediction was made, and shortly after a discovery announced, of the existence of antimatter. Championed by Richard Feynman, a formalism to perturbatively calculate scattering probabilities, dubbed Feynman diagrams, soon proved to agree in great detail with many known experimental results. Because of its great success, to this day QED remains the best scientific theory with regards to its predicting power, making QFT a firmly established approach in physics.

Following the example of QED, other known fundamental forces are today described by the QFT formalism. The weak and strong nuclear force, one primarily known for delegating nuclear decay and the other for holding the hadrons together, are now understood by using quantum field theory. They are experimentally confirmed to be non-abelian local gauge theories with SU(2) and SU(3) symmetries respectively. Since they hold a SU(n) symmetry they belong to the Young-Mills category of theories. In 1979, the weak force was united with QED making the electro-weak theory which correctly predicted the existence of $W^\pm$ and Z gauge bosons and was consequently awarded the Nobel prize.

Quantum chromodynamics (QCD), the biggest of challenges due to its non-perturbative characteristic, is the main topic of this study. Historically know as the strong nuclear force, it tries to explain all the complexity and observed interactions between partons. In QCD the elementary fermionic species are called quarks and they are brought together to create hadrons by exchanging bosonic fields called gluons. Quarks come in six different types called flavors while gluons are all of the same kind but can have 8 different charges. This wealth of variety creates a complicated situation for research in QCD, but the overall formalism has been confirmed on many different levels and is still an abundant source of new research.

2.1   Lagrangian formalism

A standard way of calculating the behavior of fields in QFT is through the use of the least action principle. One starts with a general definition

$$S(q) = \int_{t_1}^{t_2} L\big(q(t), \dot{q}(t)\big) dt,$$

where q are called *"generalized coordinates"*, $S(q)$ is the action and L is the Lagrangian. A fundamental result of classical physics, every smooth solution to this variational problem satisfies the Euler-Lagrange equation (ELE). The ELE is a second order differential equation used to produce equations of motion for the described system.

$$\frac{\partial L}{\partial q_i} - \frac{d}{dt}\frac{\partial L}{\partial \dot{q}_i} = 0$$

Classically the Lagrangian is the difference of the systems kinetic and potential energy $L(q_i, \dot{q}_i) = T - V$. Observing that the Lagrangian does not explicitly depend on time t, and using the Noether theorem, the solutions to the Euler-Lagrange equation also preserve the energy of the system

$$E(t) = p(t)\dot{q}(t) - L\big(q(t), \dot{q}(t)\big), \qquad \frac{dE(t)}{dt} = 0$$

which is, of course, a physical requirement of any solution wanting to describe the natural world. In QFT the Lagrangian formalism is expanded to make room for the idea that position and its derivative are no longer the main dynamic variables. In QFT, quantum fields (Φ, Ψ, $\bar{\Psi}$, ..) and their derivatives naturally take over the role of q.

$$S[\phi_i] = \int \mathscr{L}\big(\phi_i(x)\big)^4 x$$

where $\mathscr{L}$ is the Lagrangian density defined with $L = \int \mathscr{L} d^{n-1} x$. Following an obvious prescription, the Euler-Lagrange equation for QFT is of the form

$$\frac{\partial \mathscr{L}}{\partial \phi_i} - \frac{\partial}{\partial q^\mu} \frac{\partial \mathscr{L}}{\partial \phi_i / \partial q^\mu} = 0$$

where ϕ_i stands for any field in the system and μ goes over all four space-time dimensions. Modern Lagrangians try to describe, free or interacting, massive or massless, quantum fields of different spin and charge. For example:

The Klein-Gordon Lagrangian - $\mathscr{L} = \frac{1}{2}\left(\partial^\mu \phi \partial_\mu \phi - m^2 \phi^2\right)$

 massive scalar field used to describe particles like pions $(\pi^\pm, \pi^0)$ or the Higgs field

The free Maxwell Lagrangian - $\mathscr{L} = \frac{1}{2} F^{\mu\nu} F_{\mu\nu}$

 massless vector fields like the classical electric and the magnetic fields

The Dirac Lagrangian - $\mathscr{L} = \bar{\Psi}\left(i\gamma^\mu p_\mu + m\right)\Psi$

 massive spin 1/2 fields such as electrons or quarks

QED Lagrangian - $\mathscr{L} = \bar{\Psi}\left(i\gamma^\mu (\partial + ieA)_\mu + m\right)\Psi - \frac{1}{4} F^{\mu\nu} F_{\mu\nu}$

 an interacting Lagrangian density consisting of both the Maxwell and Dirac fields.

In Feynmans picture of quantum mechanics, an equivalent but cognitively different approach, path integrals play the leading role. Here the motion of a field Ψ is best described with quantum propagators

$$\mathscr{P}(x_1, t_1; x_0, t_0) = \int e^{iS[q]/\hbar} \mathscr{D}q.$$

By using the operator $\mathscr{P}$ it is possible to calculate the dynamics of the function Ψ

$$\Psi(x_1, t_1) = \int_{-\infty}^{\infty} \mathscr{P}(x_1, t_1; x_0, t_0) \Psi(x_0, t_0) dt$$

for all positions x_1 and all times $t_1 > t_0$. Here again it is obvious that the central role for all predictions is played by the Lagrangian density. With this said, obviously, the Lagrangian formalism is an indispensable tool in QFT.

In modern research, the emphasis is put on discovering extensions to the known Lagrangian forms or possible approximation which would lead to greater insight into the considered system. There are many forms of Lagrangian densities used for the description of natural processes. Effective Lagrangian densities and renormalization procedures are just a few topics which are too wast to be mentioned in this work but are necessary for the overall understanding of the underlying physics in this analysis and, of course, in many others. It is sufficient to say that the Lagrangian formalism is extensively explored and is an unavoidable stepping stone in modern particle physics research.

2.2 The Standard Model

The Standard Model (SM) is a common title for the quantum field theory of quarks, leptons and force mitigating gauge bosons that best describes the known experimental data. Coined by the Nobel prize winner Steven Weinberg, the name Standard Model stands for the quantum field theory of three known fundamental forces; electrodynamics, the strong and weak nuclear force. These forces (without gravity) are united in a common QFT formalism. Because of this, SM is regarded as the best mathematical framework for describing all observed particle interactions. All known fermionic fields are massive and they constitute all the known matter in
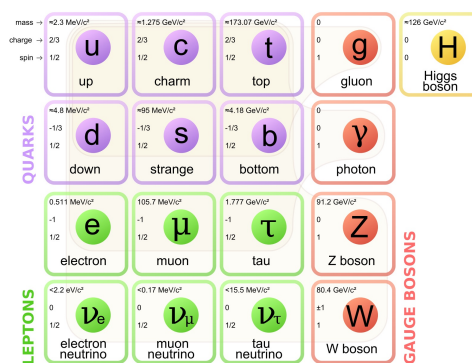
Fig. 2.1 List of the Standard Model particles, source and license[57].

the Universe. Interactions between these fields are mitigated by bosonic fields corresponding to different fundamental charges. The bosonic fields form the myriad of particle interaction

and define the dynamics of all quantum fields. As of 2012, the Higgs field, the only known fundamental scalar field, is among the Standard Model particles[7, 8].

Still a work-in-progress, the Standard Model is natural starting point for further progress in the field and a highly potent consistency check with the known experimental data. Following this, many extension to the Standard Model have been proposed. For example, a need to explain dark matter fuels various further investigations in the possible additions to the particle spectrum. On the other hand, driven by aesthetics, a possible fermion-boson symmetry called supersymmetry offers to double the number of fundamental particles by attributing a supersymmetric partner to each member of the Standard Model. With regards to gravity, many approaches attempt to expand the SM particle zoo using non-commutative geometries, space-time quantization or varying particle topology. A good candidate has still to arise, followed, most certainly, by an outbreak of new research.

2.3   Quantum Cromodynamics

Quantum Chromodynamics (QCD) is a quantum field theory of quarks and gluons. As was mentioned before, in QCD hadrons are considered to be a captured state of massive spin 1/2 particles called quarks, which are interacting via an exchange of massless spin 1 gauge bosons called gluons. There are six known kinds of quarks called flavors, the *up*, *down*, *strange*, *charm*, *top* and *bottom* quark, or for short u, d, s, c, t and b. As in every reasonable field theory each field has its conjugate field, meaning that, for every quark their is an antiquark $(u, d, s, c, t, b) \rightarrow (\bar{u}, \bar{d}, \bar{s}, \bar{c}, \bar{t}, \bar{b})$. These fields can combine into quark or antiquark triplets making the known baryon specter $(p, n, \Delta, \Lambda, \Sigma, \Xi, \Omega)$. They can also combine into quark-antiquark pairs to produce all the known mesons $(\pi, \eta, b, \rho, \omega, \phi, \Upsilon, \Theta, ..)$. In both cases the interactions is governed by the same gluonic exchange. The QCD charge is called color and there are three charge types popularly called *red*, *green* and *blue*, or r, g, b for short. At first glance, QCD is similar to QED but because of its Yang-Mills characteristic there arise some significant differences which are important to mention.

2.3.1   Short theoretical overview

The standard form of the QCD Lagrangian density, without a gauge fixing and ghost parts, is

$$\mathscr{L}_{QCD} = -\frac{1}{4} F^a_{\mu\nu} F^{\mu\nu}_a + \sum_{flavours} i \bar{\Psi}_A \gamma^\mu \left(\partial_\mu - ig \frac{\Lambda_a}{2} A^a_\mu - m \right) \Psi_B,$$

where the non-Abelian gluon field strength tensor is

$$F^a_{\mu\nu} = \partial_\mu A^a_\nu - \partial_\nu A^a_\mu + g f_{abc} A^b_\mu A^c_\nu$$

7

and f_{abc} are the SU(3) group structure constants. The color current vector of the quarks is standardly defined as

$$j_a^\mu = g\bar{\Psi}\gamma^\mu \frac{\Lambda_a}{2}\Psi.$$

Here the metric is given by $g_{\mu\nu} = diag(1,-1,-1,-1)$, we set $\hbar = c = 1$ and the indexes a,b,c run over the eight color degrees of freedom of the gluon field. The right most term of the gluon field strength tensor induces non-Abelian differences to QED. Because of this, there exist three and four gluon vertexes in QCD which comparing to QED induce significant difference in the overall behavior. Most striking of these differences is called "asymptotic freedom" and will be mentioned in later chapters. The gamma matrices satisfy an anticommutation relationship,

$$\{\gamma^\mu, \gamma^\nu\} = 2g^{\mu\nu}.$$

SU(3) generators t^a can be used to define f_{abc}. They are hermitian, traceless and define the Lie algebra of SU(3) by the commutation relations

$$[t^a, t^b] = if^{abc}t^c.$$

Here the usual representation is via Gell-Mann matrices $t^a = \frac{1}{2}\lambda^a$

$$\lambda_1 = \begin{pmatrix} 0 & 1 & 0 \\ 1 & 0 & 0 \\ 0 & 0 & 0 \end{pmatrix}, \quad \lambda_2 = \begin{pmatrix} 0 & -i & 0 \\ i & 0 & 0 \\ 0 & 0 & 0 \end{pmatrix} \quad \lambda_3 = \begin{pmatrix} 1 & 0 & 0 \\ 0 & -1 & 0 \\ 0 & 0 & 0 \end{pmatrix} \quad \lambda_4 = \begin{pmatrix} 0 & 0 & 1 \\ 0 & 0 & 0 \\ 1 & 0 & 0 \end{pmatrix}$$

$$\lambda_5 = \begin{pmatrix} 0 & 0 & -i \\ 0 & 0 & 0 \\ i & 0 & 0 \end{pmatrix}, \quad \lambda_6 = \begin{pmatrix} 0 & 0 & 0 \\ 0 & 0 & 1 \\ 0 & 1 & 0 \end{pmatrix} \quad \lambda_7 = \begin{pmatrix} 0 & 0 & 0 \\ 0 & 0 & -i \\ 0 & i & 0 \end{pmatrix} \quad \lambda_8 = \frac{1}{\sqrt{3}}\begin{pmatrix} 1 & 0 & 0 \\ 0 & 1 & 0 \\ 0 & 0 & -2 \end{pmatrix}.$$

The SU(n) groups have $n^2 - 1$ generators whose eigen values can be used to classify particle spectra. As was previously mentioned, QCD, being an SU(3) theory, contains 8 different quark charges. To be able to perform perturbative QCD calculations it is needed to fix the gauge of the theory. To do this a gauge fixing term is introduced into the Lagrangian density followed by a ghost field term. This step is needed for a meaningful definition of the gluon propagator.

$$\mathcal{L}_{gauge} = -\frac{1}{2\lambda}(\partial^\mu A_\mu^a)^2$$

This choice of gauge fixes the class of covariant gauges with gauge parameter λ. In non-Abelian theories a covariant fixing term is always followed by a ghost Lagrangian density term.

$$\mathcal{L}_{ghost} = \partial^\mu \eta^{a\dagger}(D_{ab}^\mu \eta^b)$$

Here the η^a is a complex scalar field with Fermi statistics. First introduced by Faddeev and Popov[9], ghost fields are used to cancel unphysical degrees of freedom which would manifest in the gluon propagator.

2.3.2 Symmetries

While considering QCD physics it is sometimes useful to separate quarks in subgroups. We recognize light quarks (u,d,s) and heavy quarks (c,b). The t quark is usually not considered at all here since it is expected to decay via the weak interaction much too soon for any reasonable chromodynamic interaction.

Quark	*u*	*d*	*s*	*c*	*b*	*t*
$Mass(MeV/c^2)$	$1.7 - 3.1$	$4.1 - 5.7$	100^{+30}_{-20}	1290^{+50}_{-110}	4190^{+180}_{-60}	172900 ± 1100

A quark is considered heavy if its Compton wavelength is much smaller that the hadron state radius (about 1 fm, because $m_q \gg 200$ MeV). At extreme temperatures quarks can be considered massless and a chiral symmetric field theory is applicable. In this case for the lightest two quarks, u and d, we have a chiral SU(2) group, a symmetry which considers separately left- and right-handed particles. In nature QCD does not have this symmetry due to a difference in quark mass. With the cooling of QCD matter, the ultrarelativistic massless limit is not realistic and the masses of quarks start to play a role breaking the symmetry as a consequence. Spontaneously broken chiral SU(2) group leaves $SU(2)_v \otimes U(1)_v$ symmetry of isospin and baryonic number conservation. It is known that if an exact symmetry of the Lagrangian is broken, a number of Goldstone bosons, equal to the number of broken symmetry generators, will be contained in the theory. The pion triplet $(\pi^\pm, \pi^0)$ is a product of such a symmetry breaking. Since the u and d quark masses are much smaller than the standard energies used in high energy experiments their masses can essentially be considered as perturbations to the chiraly symmetric theory. Such an approach gives results which are consistent with experimental data. Adding the strange quark $(m_s \approx 100$ MeV/$c^2)$ would give a chiral SU(3) theory. This group would break, in the same manner as before, into $SU(3)_v$ creating eight pseudoscalar Goldstone bosons historically known as the flavour SU(3) octet $(\pi^\pm, \pi^0, K^\pm, K^0, \bar{K}^0, \eta)$. Since these are the lightest known mesons the perturbative chiral theory would still be applicable and reasonable results should be obtained. For heavy quarks a different approach is used. Due to their large mass they can be considered to be a static source of color charge. The idea is similar to atomic physics where the characteristics of the spectrum are basically insensitive to the mass of the nucleus. With these considerations an effective Lagrangian could be constructed depending on the physical situation under considerations. The mass would drive the correction amplitude usually of the $1/m_q$ order.

2.3.3 Asymptotic freedom and the running coupling constant

In order to calculate a physical observable within the QCD framework, a common practice is to introduce a perturbation series in the coupling $\alpha_s = q^2/4\pi$. In order to control ultraviolet divergences a renormalization procedure is performed and a second mass scale μ is introduced. This scale represents the point at which the divergences are removed. A consequence of this is the necessity of an additional degree of freedom μ to the calculated observable. For a dimensionless observable $R(Q)$ such a dependence can be mathematically expressed as

$$\mu^2 \frac{d}{d\mu^2} R(Q^2/\mu^2, \alpha_s) \equiv \left[\mu^2 \frac{d}{d\mu^2} + \mu^2 \frac{d\alpha_s}{d\mu^2} \frac{d}{d\alpha_s} \right] R = 0$$

Simplifying the notation

$$\beta(\alpha_s) = \mu^2 \frac{d\alpha_s}{d\mu^2}, \quad t = ln\left(\frac{Q^2}{\mu^2}\right)$$

produces a first order differential equation

$$\left[-\frac{\partial}{\partial t} + \beta \frac{\partial}{\partial \alpha_s} \right] R(e^t, \alpha_s) = 0.$$

This equation is solved by defining a new running coupling constant $\alpha_s(Q^2)$ by

$$\alpha_s(\mu^2) \equiv \alpha_s, \quad t = \int_{\alpha_s}^{\alpha_s(Q^2)} \frac{dx}{\beta(x)}.$$

By differentiating this result a new expression, called the renormalization group equation, is obtained

$$Q^2 \frac{\partial \alpha_s}{\partial Q^2} = \beta(\alpha_s)$$

In QCD the β function can be written in a perturbative expansion in the following manner

$$\beta(\alpha_s) = -b\alpha_s^2(1 + b'\alpha_s + b''\alpha_s^2 + O(\alpha_s^3))$$

where (b, b', b'') are constants of the theory and carry information on the number of light flavours. In comparison to QED which has the expression

$$\beta(\alpha_{QED}) = \frac{1}{3\pi}\alpha^2 + O(\alpha^3)$$

the QCD β function has the opposite sign. This has a significant consequence most easily observed by solving for α_s

$$\alpha_s(Q^2) = \frac{\alpha_s(\mu^2)}{1 + \alpha_s(\mu^2)bt}.$$

As $t = ln(Q^2/\mu^2)$ gets larger, meaning that the interaction energy or the temperature of the system increases, the coupling constan gets smaller. This characteristic is called asymptotic freedom and stands for the observation that for very large Q^2 the characteristic strength of the QCD force goes to zero and particles become free. This result is standardly used to construct a picture of hadrons melting in heavy ion collisions.

2.3.4 Lattice QCD

Lattice QCD is a general term for computer based finite element calculations of QCD problems. Due to its non-perturbative nature QCD lacks analytic solutions in the low energy regime. One way of tackling this problem is to introduce a momentum cut-off which would effectively regularize the theory and allow meaningful calculations. In lattice QCD space-time is divided into a finite element 4 dimensional grid and a point-by-point calculation is performed. The grid, with its discrete elements induces a momentum cut-ff at the order of 1/a, where a is the lattice spacing. This approach has many advantages and allows a more pragmatic way of solving QCD based problems. To restore the continuous QCD limit the spacings should go to zero $a \to 0$ and the grid should be made infinitely large. By manipulating these two variables of the system it is possible to control the level of precision of the final result. Due to its rich structure it is an
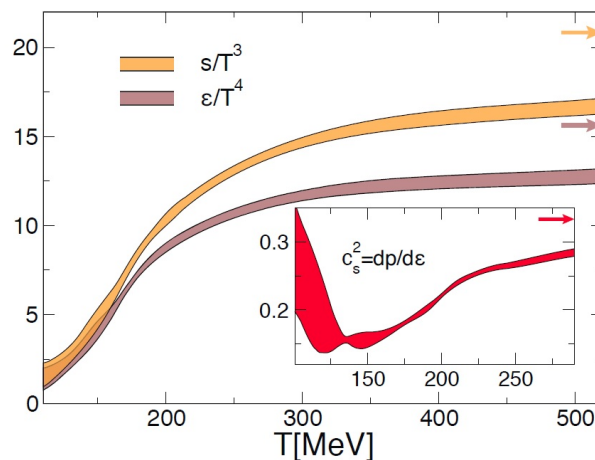
Fig. 2.2 LQCD calculation of entropy s and energy density ε. Picture taken from [17].

indispensable tool in the study of finite temperature and density QCD. The exploration of lattice QCD has hinted at the possible existence of many novel phenomena in relativistic heavy ion collisions such as Quark-Gluon Plasma (QGP), the Color Glass Condensate (CGC), Disoriented Chiral Condensate (DCC) or the Chiral Magnetic Effect (CME). These calculations are done on large computing farms and are considered to be the most precise calculations of non-perturbative QCD.

2.4   String theory

String theory is a novel theory of elementary particles, very similar to QFT but with a significant difference. It rests on the hypothesis that the basic constituents of matter and radiation are not pointlike particles but one dimensional objects, called strings.

String-like theories were first introduced in the 1960s as a way of explaining pion-pion interactions and an experimentally observation that the spin J and mass M_J satisfy the relation $J \propto M_J^2$ called Regge trajectories[10]. The main idea was that specific particles corresponded to different oscillation modes of the fundamental string. Since the fundamental string spectrum contained a massless spin-two particle further considerations into the strong nuclear force were substituted by QCD and another application for string theory was found. The initially undesired spin-two particle made string theory a prime candidate for a quantum theory of gravity since the mode was recognized to be the hypothesized graviton, the quantum of gravity. This meant that general realtivity arose naturally from within the string theory framework, which is not the case for QFT with point like particles. This prompted extensive research in string theory, discovering many general characteristics of QFT along the way. Several string theories emerged and were successfully united into one, dubbed M-theory, during the 1990s "superstring revolution".

A general characteristic of any potentially realistic string theory is a requirement of supersymmetry, a symmetry which makes a one-to-one connection between bosons and fermions. It is a crucial stipulation of string theory that the Natural world contains local supersymmetry. Another prerequisite for a mathematically consistent string theory is the existence of extra dimensions. Superstring theories require minimally ten-dimensional space-time to be consistent. To explain this clear disagreement with experimental evidence, string theorists borrowed an idea of dimensional compactification first proposed by Kaluza and Klein in the 1920s. It suggested that extra dimensions were curled up into compact spaces of very small extent, making their existence very hard to (dis)prove experimentally. Additional dimensions also naturally changed the spectrum of oscillations, adding more issues to be solved. The extra six (or more) dimensions were required to have specific symmetries in order to explain the observed particle spectra. First objects that showed to be good candidates for a compactified six-dimensional space were the Calabi-Yau manifolds, as they removed some unneeded symmetries which simpler manifolds, such as S^n, had. Research in this field of string theory still continues.

To this day supersymmetry has not been discovered. Extensive searches for supersymmetric partners to the Standard Model particles were performed by the ATLAS and CMS experiments at CERN and no candidates were found. This of course does not disprove string theory but, at least, shows that at the current energies the LHC experiments are not sensitive to the string degrees of freedom. One of the ways of explaining this is by hypothesizing that the length of the

fundamental string is at the Planck scale.

$$l_P = \left(\frac{\hbar G_N}{c^3}\right)^{1/2} = 1.6 \times 10^{-33} cm, \qquad m_P = \left(\frac{\hbar c}{G}\right)^{1/2} = 1.2 \times GeV/c^2.$$

By recognizing that a one dimensional generalization of the fundamental shape of particles is further applicable, a natural extension to higher dimensions was obvious. A string was imagined to be just a special case of a more general p-brane. The name was chosen to recognize the next higher dimensional object, the membrane, and the free number of dimensions p. In M-theory, p-branes play a crucial role being a candidate for a higher-dimensional slice of the space-time on which our four-dimensional space-time is connected to. Obviously, string theory allows for a immense range of possibilities making it capable of encapsulating basically any theory.

2.4.1 World-volume action and the string Lagrangian

In the same manner as point particles draw out a worldline in space-time a string sweeps out a world sheet. For a general p-brane the action extremized contains a (p+1)-dimensional volume. In the case of a string with p=1 the volume of the worldsheet is two-dimensional and the Polyakov action is classically equivalent to the Nambu-Goto action.

$$S_{NG} = -\frac{T}{2} \int \sqrt{-h} h^{\alpha\beta} \eta_{\mu\nu} \partial_\alpha X^\mu \partial_\beta X^\nu d\sigma d\tau$$

where $T = 1/2\pi l_s^2$ with l_S being the fundamental string length, $h^{\alpha\beta}(\sigma, \tau)$ is the auxiliary world-sheet metric and $h = \det(h_{\alpha\beta})$. The functions $X^\mu(\sigma, \tau)$ describe the space-time world-sheet of the considered string. The parameter σ parameterizes the string at specific world-sheet time τ. If the string is closed, one needs to impose additional symmetry to $X^\mu(\sigma, \tau)$. In this case a periodicity in the spatial parameter σ must be introduced $X^\mu(\sigma, \tau) = X^\mu(\sigma + \pi, \tau)$. It is worth to mention that all string theories contain closed string, and the graviton is just a massless mode in the closed-string spectrum.

For open strings, boundary conditions need to be specified at string endpoints, $\sigma = 0$ and $\sigma = \pi$. Standard Dirichlet and Neumann boundary condition can be attributed to each end of the string. The Dirichlet condition then specifies a space-time hypersurface on which the string endpoint is attached to. These objects, called D-branes, should have some physical meaning which makes them subject to immense inquiry in string theory. In the case of Neumann condition, the endpoints can be at any point of space-time and hence these signify the free endpoints condition. It is worth mentioning that in the path integral approach, while correctly taking into account gauge fixing and local symmetries, issues arise while performing a Feynman path integral. A conformal anomaly was proven to be avoidable only if the space-time is D=26 dimensional.

This requirement of absence of negative norm states constraints the spacetime dimension of the superstring theories to be $D = 10$.

2.4.2 S, T and U dualities

As noted before, string theory is abundant in symmetries. S, T and U dualities are a useful manifestation of the overall symmetry of the theory. They allow various simplifications of calculations and fast understanding of systems via dual system analogies.

- S-duality recognizes the equivalence between theories with coupling g_S and theories with coupling $1/g_S$. This is important because it allows a non-perturbative theory $g_S \gg 1$ to be investigated using the perturbative dual theory where $g_S \ll 1$.

- T-duality makes a connection between various cases of extra dimensions, making them physically equivalent. Simplest example would be the equivalence of a circle of radius R with a circle of radius l_P^2/R. This connection allows a quick analogy between large and small compactified space-times in a similar way how S-duality does for perturbative and non-perturbative theories.

- U-duality connects both S- and T-dualities of a system making a bridge between geometry and coupling constants. It is dependent on the background space and is abundantly used in M-theory.

A good example of the sheer usefulness of such dualities is the existence of the AdS/CFT correspondence.

2.4.3 AdS/CFT

Anti-de Sitter space and conformal field theory correspondence, AdS/CFT for short, stands for a conjecture which claims exact equivalence between conformally invariant quantum field theory and M-theory on a D=5 dimensional anti-de Sitter space[11–13]. It stems from a more general set of ideas that claim that gauge field theories in four dimensions should be dual to gravity theories in curved space with one extra dimension. Anti-de Sitter space is a maximally symmetric space-time with a negative curvature. An example of the correspondence, without going into details, would be the connection between SU(N) Yang-Mills theory with N=4 supersymmetry in four dimensions and a type IIB superstring theory in a ten-dimensional space-time consisting of a product between a five-dimensional sphere S^5 and a five-dimensional anti-de Sitter space. The duality is usefull when one considers a high temperature limit of QCD, when QCD becomes conformal. AdS/CFT then allows a calculation of high temperature QCD processes using the string formalism. There are many other hypothesized extensions to the duality which would allow access to non-perturbative aspects of QCD again using string theory.

Chapter 3

Quark-gluon Plasma

Quark-gluon plasma (QGP) is a hypothetical state of matter where quarks and gluons move freely due to high temperature. In this chapter we give a historic overview of investigation into parton deconfinement and the quark-gluon plasma. A description of the various experiments is offered and the main results are explained.

3.1   General overview

With the discovery of asymptotic freedom it was realized that partonic matter should, at high enough density and pressure, "melt" from colorless hadrons into a new deconfined phase called quark-gluon plasma. It is now thought that the Universe passed through such a phase, 10^{-12}s after the Big Bang, lasting for 10 microseconds. As the Universe expanded, quark-gluon plasma hadronized, mesons and baryons were produced and partons got confined. Historically the
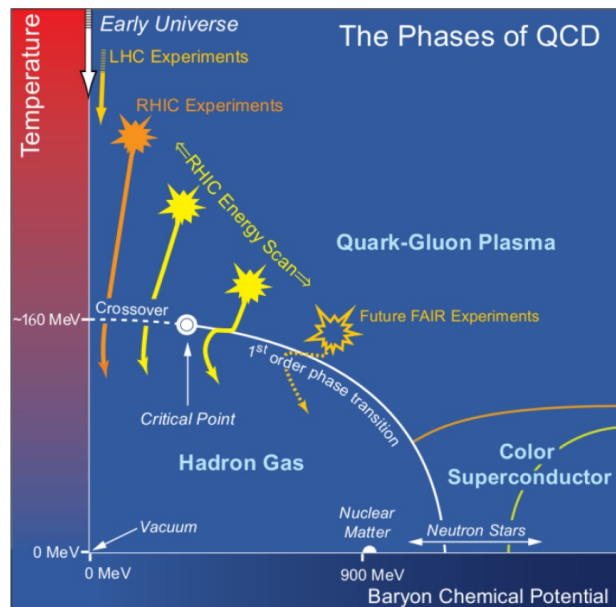
Fig. 3.1 The QCD matter phase diagram. Picture taken from [42].

transition from free quarks to hadrons was theorized to be a first order phase transition and various calculations placed the critical temperature just above the mass of the π-meson[14, 15]. With advances in computing technology numerical QCD calculations on a space-time lattice (LQCD) offered much more sophisticated calculations and showed that, in fact, the transition is a smooth crossover[16, 17]. With the acceptance of QGP, a list of experimentally observable phenomena and prerequisites was made pertaining to the deconfined phase.

Experimentally, conditions needed to obtain deconfinement are only realistically achieved by using particle accelerators which collide particles above the GeV scale. The following section will give a short overview of the experimental search for QGP.

3.2   Heavy Ion Collisions

Since the early 1980s, heavy ion collisions have allowed scientists to experimentally probe matter at high densities and temperatures. Tools, both theoretical and experimental, needed to be constructed in order to allow a meaningful scientific investigation. Observables like temperature and pressure were an obvious choice but they belong to the realm of thermodynamics and as such necessitate a large number of particles interacting with a rate much larger than the lifetime of the system. Collisions of electrons or protons produce much lower multiplicities than needed to allow investigations into the existence of quark-gluon plasma. On the other hand, it is known that collisions of nuclei at high enough energies produce a fireball of interacting quarks and gluons above the temperature which is needed for deconfinement. In comparison to the Big Bang fireball, or rather fire world, which had a lifetime of 10^{-5}s, heavy-ion collisions create a system with a significantly shorter lifetime. Within 10^{-21}s all the hadronization is done and no signs of QGP are left. For 30 years collisions of atomic nuclei have been studied with the
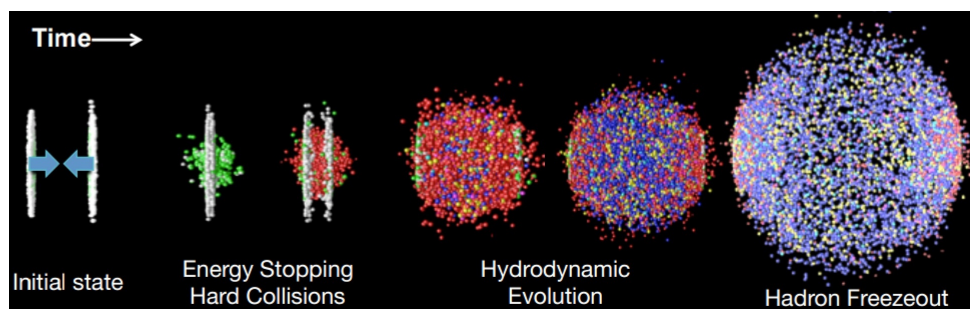
Fig. 3.2 Schematic of a heavy-ion collision. Picture taken from [22].

experimental programs starting in parallel at the Super Proton Synchrotron (SPS) at CERN, and at the Alternating Gradient Synchrotron at Brookhaven National Laboratory (BNL) in Upton, New York. Both experiments started their research with light nuclei, only switching to heavier nuclei in the early 1990s. The energy regime run by the CERN accelerator allowed a confirmation

of the creation of a new state of matter [23, 24]. Soon the next generation of accelerators started to work. At BNL the Relativistic Heavy Ion Collider (RHIC) went into operation, together with four experiments, called BRAHMS, PHENIX, PHOBOS and STAR. The energy regime at RHIC guaranteed a significant step forward achieving $\sqrt{s_{NN}} = 200$ GeV or 40 TeV center-of-mass energy. As was expected, all four experiments confirmed the creation of a new state of matter [25–28]. The findings also showed that the hot QCD matter produced experimentally did not act as a weakly interacting gas but exhibited a robust collective flow phenomena resembling a low viscosity near-perfect relativistic liquid [29]. Today, both RHIC and LHC accelerators provide their experiments with heavy-ion collision in order to further our understanding of the created hot QCD matter.

In the next section we present some of the signature phenomena which are expected to follow the creation of QGP.

3.3 Signatures of QGP

If a state of deconfined partons is achieved experimentally, a change in many physical observables is expected. While the list of such observables is long, we present some of the first observed and most striking in character.

3.3.1 Jet quenching

Jet quenching is a phenomenon that is considered to be fully dependent on a deconfined parton assumption. In particle collisions hard parton interactions frequently lead to back-to-back jet production. If the jet production point is located somewhere on the edge of the created system there is a possibility that one of the jet has a significantly longer propagation length through the QCD matter. Theoretical considerations predict that due to interaction with the hot QCD material, the hard scattered parton should shed energy via a form of QCD bremsstrahlung. This characteristic leads to the conclusion that if parton deconfinement is achieved a longer propagating jet should be observed as having a suppressed energy and p_{T} with regards to its counterpart. The ALICE collaboration has observed strong jet suppression[18]. In Fig. 3.3 we show the nuclear modification factor R_{CP}, which is a ratio of central and peripheral collisions, as a function of multiplicity. The measurement shows that as the multiplicity raises the quenching effect gets stronger. This observation is in complete agreement with the expectations of a hot QCD medium produced.
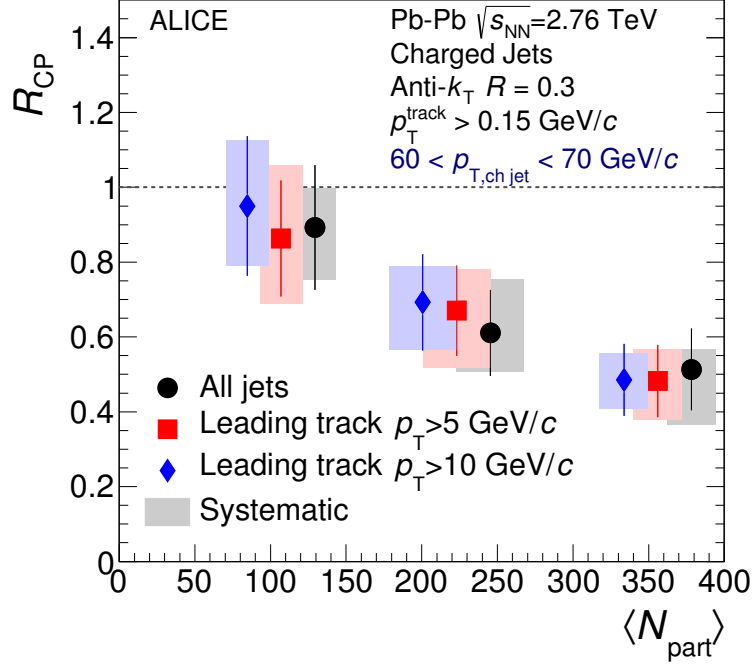
Fig. 3.3 Nuclear modification factor R_{CP} as function of the average number of participants for biased and unbiased jets, R=0.3. Source [18]

3.3.2 Quarkonium suppression

Quarkonia are mesons made from same flavour quarks. We distinguish $c\bar{c}$ and $b\bar{b}$, called J/Ψ and Υ respectively. In a hot QCD medium, partons are influenced by the abundant QCD fields
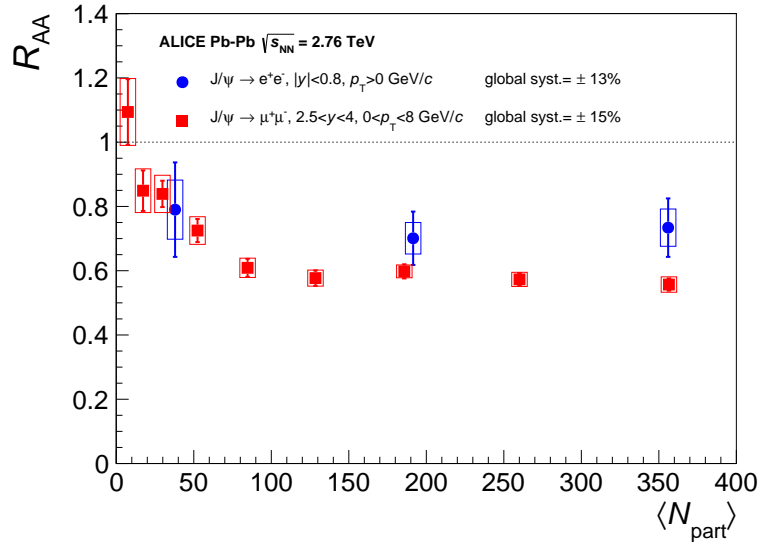
Fig. 3.4 Centrality dependence of the nuclear modification factor, R_{AA} of inclusive J/Ψ production in Pb-Pb collisions at $\sqrt{s_{NN}} = 2.76$ GeV, measured at mid-rapidity and at forward-rapidity by the ALICE collaboration. Source [19]

which produce a screening effect similar to the one observed in electromagnetism for ionized plasma. As a consequence, quarkonia which have to transverse a large hot QCD medium have a significantly enhanced probability of pair disassociation effectively breaking the meson bond. Figure 3.4 shows a centrality dependence of the nuclear modification factor, R_{AA} of inclusive J/Ψ production. It shows a clear suppression in production, again, in full agreement with QGP expectation.

3.3.3 Strangeness enhancement

Strangeness enhancement is a prediction for QGP where due to an excess in particles and temperature a surplus of strange hadrons is produced. The surplus is measured by comparing heavy-ion collision with pp collision results where QGP is not expected. The ALICE experiment

ALI-PREL-43104
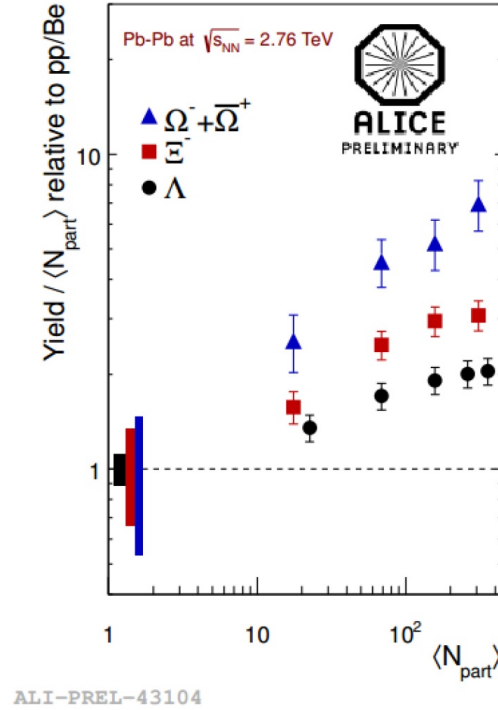
Fig. 3.5 Strange hadron yields in Pb-Pb collsions relative to pp collisions measure by the ALICE collaboration [20].

sees a clear enhancement for all strange particles which increases with event multiplicity. It is also worth noting that in Fig. 3.5 the enhancement is also connected to the strangeness content of the measured particles.

3.3.4 Flow

Signatures of hydrodynamic flow of particles is consistent with the existence of QGP but should not be considered as proof. A particularly useful observable is the anisotropic flow. It measures

the anisotropy of the detected momentum distribution as a function of the azimuthal angle. In non-central heavy-ion collisions, the overlap between the colliding nuclei has an almond shape, which creates a pressure gradients, between the hot center the edge of the system, that varies with the azimuthal angle Φ. This leads to anisotropies in the momentum distribution of the emitted particles which are then presented as the v_n flow coefficients

$$dN/d\Phi \approx 1 + \sum_{n=1}^{\infty} 2v_n \, cos[n(\Phi - \Psi_n)]$$

where Φ is the azimuthal angle, n is the order of the flow harmonic, Ψ_n is the nth-order reaction plane. Current results show that eliptic flow (v_2) using multi-particle cumulants ($\{2\}, \{4\}, \{6\}$)
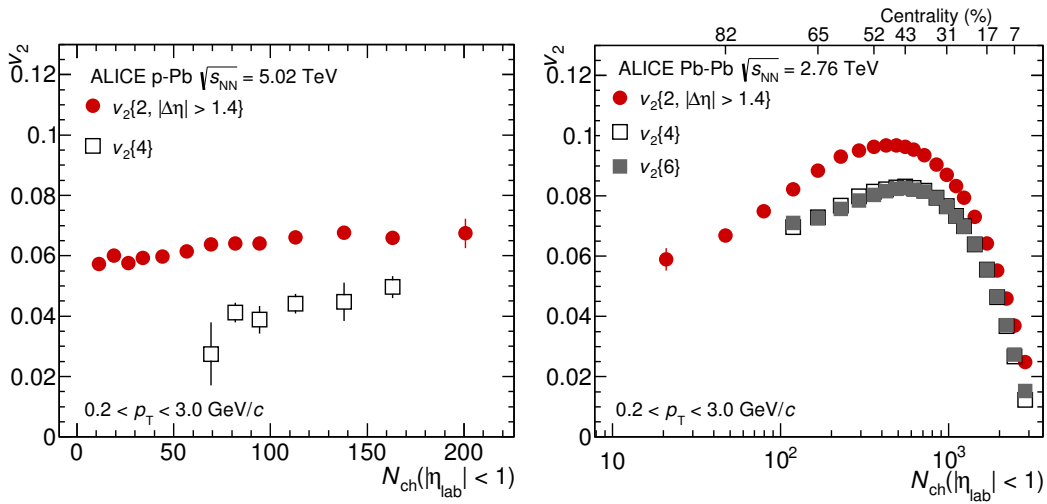
Fig. 3.6 Measurements of $v_2\{2\}$, $v_2\{4\}$, and $v_2\{6\}$ in p-Pb (left panel) and Pb-Pb (right panel) collisions. The measurements of $v_2\{2\}$ are obtained with a $|\Delta\eta| > 1.4$ gap. [21]

is the leading contributor in the flow harmonic spectrum. It contains information on the general elliptic shape of the overlap region and the hydrodynamic response of the created QCD medium. Higher harmonics have also shown a wealth of information. It is now accepted that initial fluctuation induce higher order harmonics which develop relative to their own symmetry plane. All these results suggest possible deconfinement and are used as an additional argument for the creation of QGP.

Chapter 4

Experimental set-up

4.1   Large Hadron Collider - LHC

The Large Hadron Collider[30] is a 27 km long circular particle accelerator. Built by the European Organization for Nuclear Research (CERN), beneath the Franco-Swiss border near Geneva, in the same tunnel which was previously used by the Large Electron-Positron (LEP) accelerator, it is the worlds largest and most powerful particle accelerator. The LHC is a product of a vast collaboration of more than 10000 scientists from over 100 nations, several hundred institutes and laboratories. Its general aim is to explore in detail physics at the TeV scale. The project was approved in 1994 and construction began in 2000. Research at the LHC is divided between four large experiments called ATLAS[31], ALICE[32], CMS[33] and LHCb[34]. ATLAS and CMS are both general purpose detectors and their main research interests lie in the exploration of the Higgs sector, search for supersymmetry and other possible signs of new physics at the new energy scale. The LHCb experiment is a forward facing detector specializing in b-physics and the accompanied CP violation present in b-hadron interactions. ALICE is a detector built with the intention of exploring heavy ion collisions. Since this thesis was done using data collected by the ALICE experiment, the full experimental setup will be described in the following sections.

Because of various practical reasons, the LHC accelerator is accompanied by a series of smaller accelerators. These accelerators were used in previous experiments, each newly built being connected to the previous set of accelerators, creating a sequence of " gear shifts" gradually ramping up the particle beam up to TeV energies. First, electrons are stripped from their nuclei making them positively charged and easily controlled by electric fields. The nuclei are then inserted into the first accelerating system called LINAC2 which is a linear accelerator capable of providing bunches of 50-MeV protons. After the first acceleration the beam is fed into the Proton Synchrotron Booster (PSB) which ramps up the energy to 1.4 GeV and injects the beam into the Proton Synchrotron (PS). There the beam is further accelerated to 26 GeV and sent to the Super Proton Synchrotron (SPS). The SPS is the final step before insertion into the LHC ring
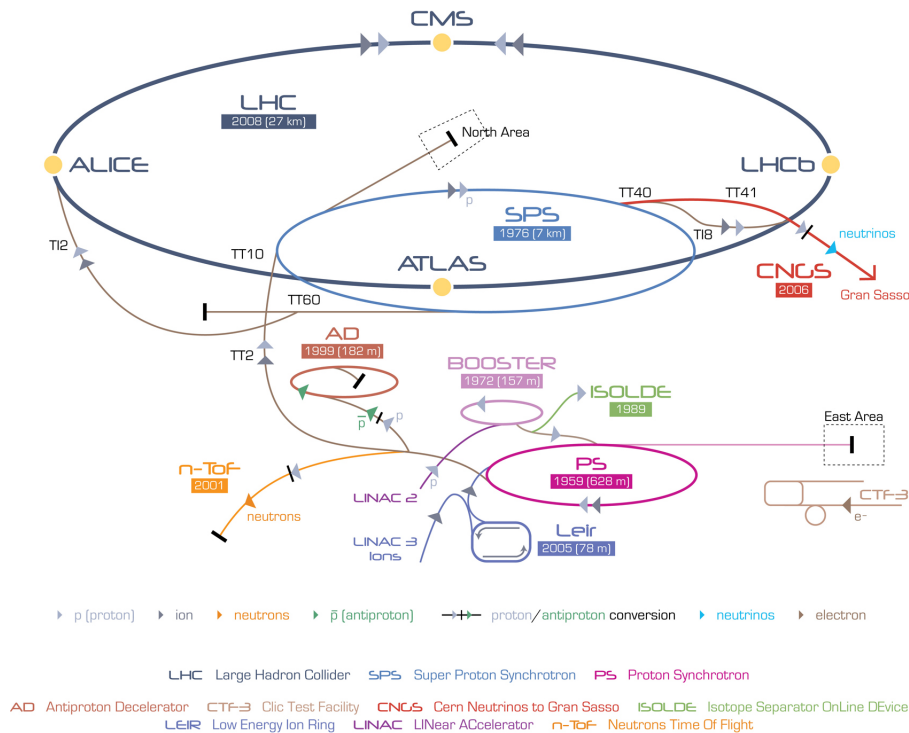
Fig. 4.1 Schematic of the Large Hadron Collider complex at CERN.

providing protons with 450 GeV of energy. When injected into the main LHC ring, bunches are accumulated and accelerated to a maximal energy of 7 TeV per proton or 14 TeV center-of-mass energy. While in operation the LHC superconducting magnets, over 1600 in total, operate at a temperature of 1.9 K and produce magnetic fields of up to 8 T. To keep the whole system at its nominal temperature 96 tonnes of superfluid helium 4 is needed. At full LHC energy two particle beams circulate at 99.9999991% of the speed of light for several hours and are collided at four interaction points. The beams last for several hours and complete about 11000 revolutions per second with bunches colliding every 75 ns, the design luminosity of the LHC being $10^{43}cm^{-2}s^{-1}$.

The LHC accelerator was also designed to accelerate heavy ions to much greater energies than the ones produced at the Relativistic Heavy Ion Collider (RHIC) at Brookhaven National Laboratory in Upton, New York. Acceleration of heavy ions follows a similar path as does proton acceleration. First, ionized lead atoms are fed into LINAC3, an accelerator designed to provide lead ion beams for both LHC and various fixed-target experiments at CERN. Since it was built with the sole purpose of providing accelerated ion beams, it is planed for production of other ion beams, including argon and xenon. After the initial stage of ion acceleration, the beam is sent to the Low-Energy Ion Ring (LEIR). The accepted beams contain long pulses of ions. It takes 2.5s for the LINAC3 to create 4 short and dense bunches which are more suitable for injection to the LHC. After that the bunches are sent to the PS and SPS for further acceleration similar to how proton beams are processed.

In March 2010 first successful proton-proton collisions at $\sqrt{s} = 7$ TeV were produced. The run lasted until November when it was changed to Pb-Pb collisions at $\sqrt{s_{NN}} = 2.76$ TeV. These collisions confirmed the finding of the RHIC experiments and produced the hottest temperature ever attained in an experiment. To analysis all of the produced data CERN had to develop a worldwide network of more that 170 computing centers across 36 countries. At current rate, the LHC experiments produce 25 petabytes per year which is about 1% of the whole World communication. To keep with the advancements in experimental setup and data intake CERN is still building computing centers which now in total contain more than 350000 processor cores. Among many important discoveries produced at the LHC one stands out as the most awaited. On 4th of July 2012, both ATLAS and CMS collaborations announced the discovery of a new particle with a mass between 125 and 127 GeV/c^2 [7, 8]. A few moths later it was confirmed that the new particle had all the characteristics expected for the Higgs boson. The discovery proved a 40 year old theory predicted and derived in three papers written by Robert Brout and François Englert[35], Peter Higgs[36] and Gerald Guralnik, Richard Hagen and Tom Kibble[37]. On 10th of December 2013, Peter Higgs and François Englert were awarded the Nobel Prize in Physics for their work.

4.2 A Large Ion Collider Experiment - ALICE

ALICE is an experiment optimized for the study of heavy-ion collisions at a center-of-mass energy of 5 TeV per nucleon. Its aim is to study the behavior of nuclear matter at high densities and temperatures, with the idea of investigating QGP and chiral symmetry restoration. The ALICE experiment was proposed in the early 1990s as a dedicated heavy-ion experiment at the new LHC accelerator facility. In 1995 the collaborations technical proposal [38] was submitted demonstrating a possibility of building a high efficiency PID detector with the capability of enduring LHCs high luminosity and produced event multiplicities. The proposal was accepted by CERN in 1997.

ALICE consists of a central part, composed of detectors mainly devoted to the study of hadronic signals and dielectrons, and the forward muon spectrometer, devoted to the study of quarkonia. The design of the experiment heavily depended on the multiplicity prediction for PbPb collision at TeV energies. An assumption was made based on the highest predicted value, 8000 charged particles per unit of rapidity. With this multiplicity the granularity of the detectors and their optimal distance from the colliding beams were set. The central part, which covers 45 degrees ($|\eta| < 0.9$) over the full azimuth, lies in a large magnet with a weak solenoidal magnetic field. The inner most part consists of the Inner Tracking System (ITS), outside of which there are is the TPC barrel and a large area PID array of time-of-flight (TOF) counters. The next layer is the Transitional Radiation Detector (TRD) which is the experiments main electron PID device. In

Fig. 4.2 ALICE schematic layout[32]
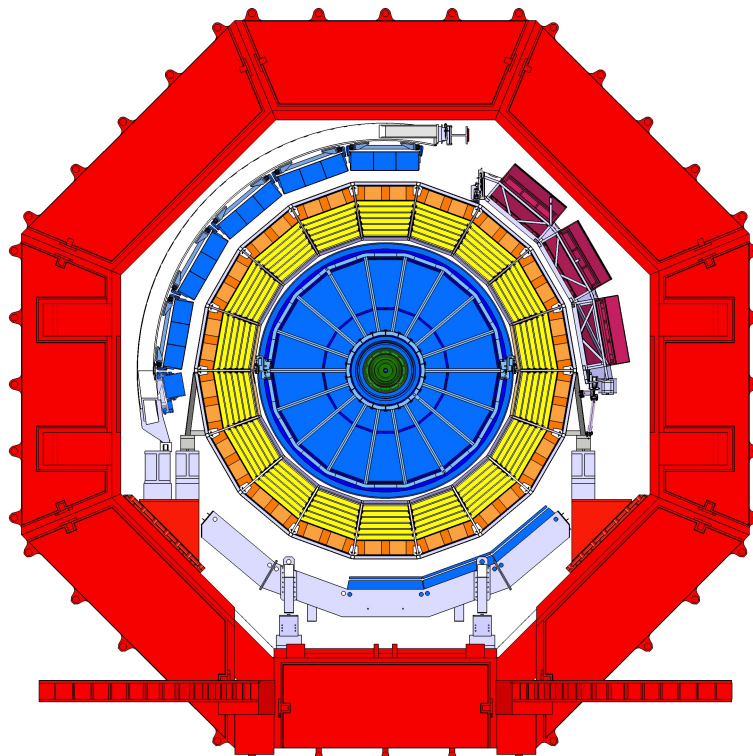
Fig. 4.3 Schematic of the ALICE cross section [32]

addition, there are two small-area single-arm detectors: an electromagnetic calorimeter (Photon Spectrometer, PHOS) and an array of RICH counters optimized for high-momentum inclusive particle identification (HMPID). For triggering and time referencing the ALICE detector uses multiple detectors (V0, T0, ZDC, FMD) which offer fast timing and wake-up calls for various central barrel detector systems.

4.2.1 Inner Tracking System - ITS

The ITS[39] consists of six cylindrical layers of silicon detectors. The number and position of the layers is optimized for efficient track finding and impact parameter resolution. It is primarily used for low-momentum particle identification and the determination of primary and secondary interaction vertexes. It works in tandem with the TPC giving ALICE a good track momentum and angle measurement. Because of the large multiplicities achieved in PbPb collisions a high granularity and a good two-track separation was a key requirement by the ALICE collaboration. This required that the four innermost layers ($r \leq 24$ cm) had to be truly two-dimensional devices. To accomplish this task the silicon pixel and silicon drift detectors were chosen. The final two layers, the outer pair, are equipped with double-sided silicon microstrip detectors due to a rather low track density below 1 cm^{-2}. Each of the three levels in the ITS were designed taking
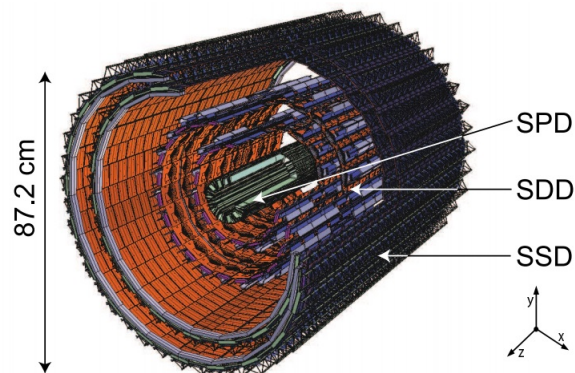
Fig. 4.4 Schematic of the ALICE Inner Tracking System [50].

into account the needed acceptance, dE/dx measurement, material budget, spatial precision and granularity, radiation level and the readout rate. Since the whole system is silicon based the ITS is used as a triggering detector. It is accompanied by other similarly fast detectors as the T0 or V0 in the triggering scheme.

The ITS physics is of a general sort. It was designed to aid in the momentum resolution of the TPC and as such is in charge of measuring the lowest momenta. By studying low momenta one is able to investigate large scale collective effects. For the study of resonances and the influence of dense media on particle mass, a quality momentum resolution is also needed. The ITS aids in measuring the strangeness and charm production which is of great interest in physics.

The excellent performance of the ITS also helps in finding the secondary vertices close to the interaction point thus allowing detection of the D meson by identifying the full decay topology.

4.2.2 Time Projection Chamber - TPC

The Time Projection Chamber[40] is the main detector device in the ALICE experiment. It was designed to successfully track up to 20000 charged particles per collision in full azimuthal coverage and an pseudorapidity interval of $|\eta| < 0.9$. Since the ALICE experiment specializes
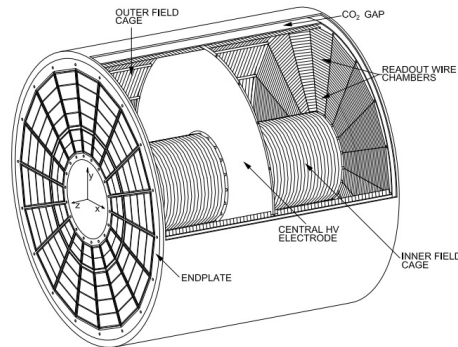
Fig. 4.5 Schematic of the TPC field cage [51].

in low momentum particle identification and tracking, the TPC requirements were set on a high resolution measurement of charged particle dE/dx and p_T in a sufficiently large acceptance in pseudorapidity. The TPC design is cylindrical in shape with a volume close to 90 m^3 and is operated in a 0.5 T solenoidal magnetic field parallel to its axis. The drift gas uses 90% Ne, 10% CO_2 mixture, as is was used in the NA49 experiment. The TPC field cage provides a highly uniform electrostatic field in a cylindrical high-purity gas volume transporting charged particles over lengths of up to 2.5 meters towards the readout end-plates. The ALICE TPC readout chambers are conventional multiwire proportional chambers with cathode pad readout, a common design over numerous other TPC detectors.

4.2.3 Time-Of-Flight detector - TOF

The TOF detector[41] was introduced to the ALICE experiment with the purpose of providing the best charged particle identification in the intermediate momentum range. Its range is above that of the ITS/TPC duo and has an overlap with HMPID on the lower end of the momentum spectrum. It has a cylindrical shape, covering polar angles between 45 degrees and 135 degrees over the full azimuth and consists of 18 sectors in Φ, each of which is divided into 5 modules along the beam direction. General characteristics of TOF are its large acceptance, high efficiency and an excellent time resolution. Its high granularity and rate allow functioning in the demanding ALICE environment. The motivation for including TOF into the ALICE experiment is to aid in PID and tracking for higher momenta. The TPC dE/dx measurement is also correlated to
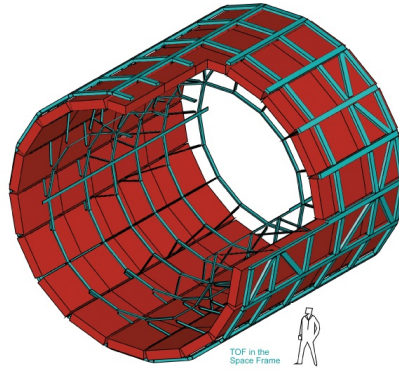
Fig. 4.6 A sketch of the ALICE TOF detector, source [52].

the TOF mass measurement which introduces another constraint for the PID algorithm. Prior to construction it was known from simulations that a clear distinction between pions, kaons and proton mass was possible up to 3 GeV/*c* clearly extending the PID reach for the mentioned particles.

4.2.4   Transitional Radiation Detector - TRD

The TRD is the main electron detector in the ALICE experiment. It is placed radially after the ITS, TPC and TOF detectors and its main purpose is to aid in distinguishing pions from electron. With an enhanced electron PID the TRD detector allows the study of light and heavy vector meson production, semi-leptonic decays of hadrons and jets with high E_T requiring several high p_T tracks in one single TRD module. In general, particle detection in the TRD is simple. A
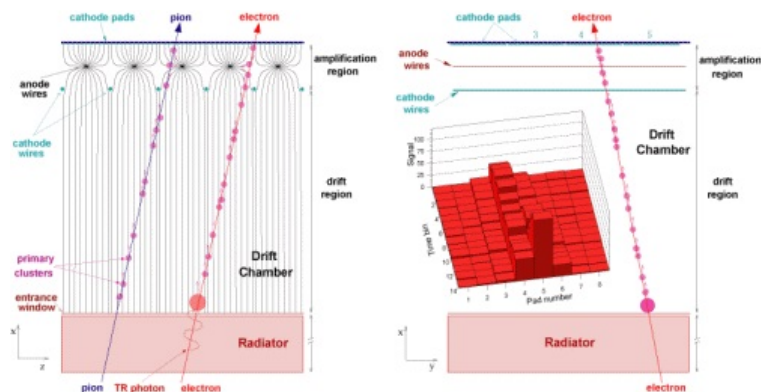
Fig. 4.7 Principle of operation demonstrated on a TRD module cross-section.

charged particle passing through the radiator generates transitional radiation which then enters the conversion and drift zones where the readout pickups the signal and sends it to the front readout electronics. The TRD is a relatively fast detector which at standard running is capable of full event tracking within 6.5 μs. The reason why particles create explicitly transitional
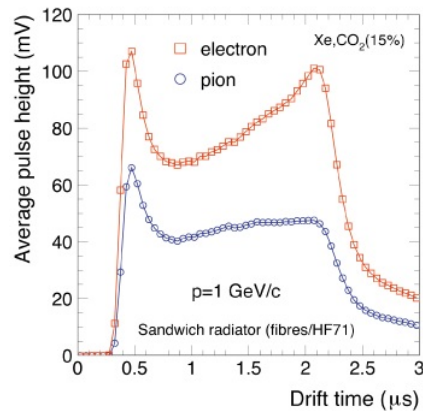
Fig. 4.8 Drift time distribution of the average pulse height summed over adjacent pads for pions and electrons.

radiation is because the radiator is made of a foam which to a particle seems as an endless series of material and vacuum transitions. For each transition between mediums there is a probability that additional radiation will be created. The difference between observed signals in the TRD coming from electrons and pions significantly adds to the PID capabilities of the ALICE experiment. TRD detector is made of 18 supermodules each consisting of five stacks with six-layers. Individual modules consist of a radiator and a drift chamber operated with Xe/CO_2 mixture (85%/15%). The drift field of 700 V/cm induces a drift velocity of 1.5 cm/ηs and a multi-wire proportional counter amplifies the secondary electrons with a gas gain of around 5000. The radiator was optimized to provide the best compromise between transition radiation yield, radiation thickness and mechanical stability.

4.2.5   High Momentum Particle Identification Detector - HMPID

The ALICE HMPID uses proximity focusing Ring Imaging Cherenkov (RICH) counters mounted in an independent support cradle. It was designed to extend PID of protons and kaons up to 5 GeV/c and 3 GeV/c respectively. Data collected by the HMPID is relevant to the pre-equilibrium state of the produced fireball.

4.2.6   PHOton Spectrometer - PHOS

The PHOS detector is a leadtungstate crystal based electromagnetic calorimeter. It is used for measuring direct single photons and di-photons for initial phase studies and jet-quenching for deconfinement studies.

4.2.7 Electromagnetic Calorimeter - EMCal

The EMCal is a lead scintillator calorimeter. It has a pseudorapidity range of $|\eta| < 0.7$ and a 110 degree acceptance in azimuth. The EMCal is primarily used for high energy jet physics and enhancing particle identification for high momentum photons and electrons.

4.2.8 Muon Chamber - MCH

The ALICE forward muon spectrometer will study the complete spectrum of heavy quarkonia by measuring their decay in to a muon pair. With high temperatures obtained with PbPb collisions the production of quarkonia is expected to be suppressed due to color screening so a leptonic probe is useful for this kind of study. The MCH is truly a forward detector with the acceptance of $2.5 \leq \eta \leq 4$. The invariant mass resolution is around 70 MeV for the J/Ψ and about 100 MeV for the Υ, so that it is possible to measure all five resonances.

4.2.9 T0 detector

The T0 detector is used for *Level 0* triggering. It is made from a pair of arrays of photomultiplier tubes equipped with Cherenkov radiators. The arrays are placed on both sides of the beam line, at $4.6 < \eta < 4.9$ and $-3.27 < \eta < 2.97$. The T0 detectors provide a wake-up signal for the TRD and a collision time reference for the TOF.

4.2.10 V0 detector

The V0 detector (also called *VZERO*) is a pair of scintillator counter arrays, called VZERO-A and VZERO-C, placed at both sides of the beam pipe. The arrays have asymmetric placement with the VZERO-A being placed at $z = 3.4$ m with $2.8 < \eta < 5.1$ and the VZERO-C at $z = -0.9$ m and $-3.7 < \eta < -1.7$. Its primary use is as an online *Level 0* centrality trigger.

4.2.11 Zero-Degree Calorimeter - ZDC

The ZDC is a three segment calorimeter primarily used for measuring the centrality of heavy-ion collisions. It is placed on both sides of the ALICE detector, 116 m away from the center of the TPC. Its primary task is to measure the number of spectator nucleons at close to zero degrees of the beam, which also allows it to be used for triggering.

4.2.12 Forward Multiplicity Detector - FMD

The FMD consists of 51200 silicon strip channels, which are distributed in 5 ring counters. It has an acceptance of $-3.4 < \eta < -1.7$ and $1.7 < \eta < 5.03$ in pseudorapidity, and it is used for providing precise charged particle multiplicity information.

4.2.13   ALICE COsmic Ray Detector - ACORDE

ACORDE consists of an array of plastic scintillator modules, which are placed on the top sides of the central ALICE magnet. It is used as a *Level 0* cosmic ray trigger.

Chapter 5

Femtoscopy

Historically, two-particle correlations were first used in astronomy by Robert Hanbury-Brown and Richard Twiss[45, 46]. They measured the angular size of stars by studying the intensity of photons on a pair of Earth-based detectors. The measurement was successful and the approach coined a name *" Henbury-Brown Twiss effect"* (HBT).

In contemporary high energy collision experiments a similar approach to the one used by Hanbury-Brown and Twiss is used. Its name is femtoscopy and it has been in use for about 40 years[47]. In femtoscopy identical particles are paired up, event by event, and a distribution of their relative momentum is used to measure the particles emission source radius. In this chapter we give a short overview of the underlying theory and the current state of the field.

5.1   Short theoretical introduction

Consider a discrete set of emission points i. To calculate the probability $P(\mathbf{p})$ of observing an emission of one particle with momentum $\mathbf{p}$ one needs to sum over all possible emission contributions i. The form of the final summation depends on the (in)coherence of the emission source. If the source is coherent one needs to sum over amplitudes or to sum over probabilities if the source is incoherent.

$$P_C(\mathbf{p}) = \left| \sum_i F_i \, \Psi(r_i) \right|^2, \qquad P_I(\mathbf{p}) = \sum_i |F_i \, \Psi(r_i)|^2 \tag{5.1}$$

where $\Psi(r_i)$ is the wave function of the emitted particle, $F_i(\mathbf{r}) = F_i \delta(\mathbf{r} - \mathbf{r}_i)$ is the emission probability amplitude and expressions $P_C(\mathbf{p})$ and $P_I(\mathbf{p})$ stand for coherent and incoherent single probabilities respectively. In the continuum case the expressions are:

$$P_C(\mathbf{p}) = \left| \int F(\mathbf{r}) \, \Psi(\mathbf{r}) d^3 r \right|^2, \qquad P_I(\mathbf{p}) = \int |F(\mathbf{r})|^2 \, d^3 r \tag{5.2}$$

The probability of observing an emission of two particles with momenta $\mathbf{p}_1$ and $\mathbf{p}_2$ the expressions are derived similarly

$$P_C(\mathbf{p}_1, \mathbf{p}_2) = \left| \int f(\mathbf{r}_1) f(\mathbf{r}_2) \, \Psi_{1,2} \, d^3 r_1 d^3 r_2 \right|^2, \quad P_I(\mathbf{p}_1, \mathbf{p}_2) = \int |\Psi_{1,2}|^2 \, f(\mathbf{r}_1) f(\mathbf{r}_2) \, d^3 r_1 d^3 r_2 \tag{5.3}$$

where $f = |F|^2$. If we assume that we are dealing with identical particles, then, depending on their spin, the wave function needs to be symmetrized or antisymmetrized, in the usual manner.

$$\Psi_{1,2} = \frac{1}{\sqrt{2}} \left(e^{i(\mathbf{p}_1 \mathbf{r}_1 + \mathbf{p}_2 \mathbf{r}_2)} \pm e^{i(\mathbf{p}_1 \mathbf{r}_2 + \mathbf{p}_1 \mathbf{r}_1)} \right) \tag{5.4}$$

plus being for bosons and minus for fermions. If we define $\widetilde{f}$ as the Fourier transform of f then the probabilities take the shape of

$$P_C(\mathbf{p}_1, \mathbf{p}_2) = \widetilde{f}_1 \widetilde{f}_2, \qquad P_I(\mathbf{p}_1, \mathbf{p}_2) = \left| \widetilde{f_I}(0) \right|^2 \pm \left| \widetilde{f_I}(\mathbf{p}_1 - \mathbf{p}_2) \right|^2 \tag{5.5}$$

It is possible to express one probability using the other. For the discrete emission source if follows that

$$P_C(\mathbf{p}_1, \mathbf{p}_2) = P_I(\mathbf{p}_1, \mathbf{p}_2) + \sum_{i,j \neq k,l} \frac{1}{2} \Psi_{1,2}(\mathbf{r}_i, \mathbf{r}_j) \Psi_{1,2}^*(\mathbf{r}_k, \mathbf{r}_l) F_i F_j F_k^* F_l^* \tag{5.6}$$

If we introduce a normalized second-order correlation function

$$C_2(\mathbf{p}_1, \mathbf{p}_2) = \frac{P_2(\mathbf{p}_1, \mathbf{p}_2)}{P_1(\mathbf{p}_1) P_2(\mathbf{p}_2)} \tag{5.7}$$

one gets a simple expression for the incoherent boson correlation function

$$C_2(\mathbf{p}_1, \mathbf{p}_2) = 1 + \left| \widetilde{f}(\mathbf{q}) \right|^2. \tag{5.8}$$

This form is very general and has to be amended with the introduction of experimental facts. The point would be to consecutively introduce more information and in this way extract a more meaningful form of the correlation function.

5.1.1 Resonances, coherence, resolution and the λ factor

In order to extract valuable information on the emission source a detailed understanding of the experimental situation must first be obtained. Resonances, secondary particle production through parent particle decay, have a twofold effect on the correlation function. First, the interference between primary produced particles and secondaries coming from short-lived resonances creates a narrow peak at small relative momenta q. Such an effect is not expected from long-lived decay products, which can be hard to measure experimentally thus effectively lowering the intercept

of $C_2(0)$. Both of these effects have to be taken into account if the measurement is used to give a statement on the source coherence. From 5.8 it is expected that the height of the correlation function be $C_2(0) = 2$, which doesn't take into account the possibility of a coherent fraction of particles which would lower the $C_2(0)$ value. Also, limited statistics or not measuring some of the degrees of freedom would also induce a decrease in the measured correlation function.

Experiments have shown that it is very difficult to measure $C_2(0) = 2$. This lead to the introduction of the λ parameter,

$$C_2(\mathbf{k}_1, \mathbf{k}_2) = 1 + \lambda \left| \widetilde{f}(\mathbf{q}) \right|^2, \tag{5.9}$$

which was first imagined as a possible way of describing partially coherent sources. In this picture, a fully coherent source would give $\lambda = 0$ while a chaotic source have $\lambda = 1$. Today it is understood that various effects influence the λ parameter and not only coherence. Still, the λ parameter is sometimes called the *coherence* or *chaoticity* parameter because of its initial interpretation and reason for introduction.

5.2 Bowler-Sinyukov expression

Modern femtoscopy analysis disentangle particle correlations in 3 dimensions. The coordinate system, which is standardly chosen for this 3D analysis, is the longitudinally co-moving system (LCMS) where the pair longitudinal momentum vanishes. The systems coordinates are called *out*, *side* and *long*. The *out* direction is parallel to the pair transverse momentum $k_T = 1/2 \left| p_1^T + p_2^T \right|$. The *long* direction is parallel to the particle beam and *side* is normal to both *out* and *long*. Investigating particle correlations in these three directions offers a way to extract information on geometric size of the emmiter and also on the emission process and time.
Assuming that the dependence on the longitudinal component of $\mathbf{k} = 1/2 (\mathbf{k}_1 + \mathbf{k}_2)$ is negligible and that the emission source has a Gaussian shape it is possible to show that:

$$C_2(\mathbf{q}) = 1 + \lambda \, exp \left(-R_{out}^{G}{}^2 q_{out}^2 - R_{side}^{G}{}^2 q_{side}^2 - R_{long}^{G}{}^2 q_{long}^2 \right) \tag{5.10}$$

The Gaussian shape assumption was firstly motivated by reasons like the Central Limit theorem, which would force the shape into a Gaussian through many averaging, and by a relatively good agreement with measured data. Later, the ALICE experiment proved that a Lorenzian and exponential shapes in some cases describe data better.

Since in this analysis we will investigate two-pion correlations additional contributions pertaining to Coulomb and Strong force interactions must be considered. For describing a pair of

opposite sign pions, the following wave function is used:

$$\Psi^{(+)}_{-\mathbf{k}^*}(\mathbf{r}^*, \mathbf{k}^*) = \sqrt{\frac{A_C(\eta)}{2}} \left[e^{-i\mathbf{k}^*\mathbf{r}^*} F(-i\eta, 1, i\zeta^+) + f_C(\mathbf{k}^*) \frac{\widetilde{G}(\rho, \eta)}{\mathbf{r}^*} \right]. \tag{5.11}$$

where A_C is the Gamow factor, F is a confluent hypergeometric function, $\eta = 1/(k^* a_c)$, $\zeta = k^* r^* (1 + \cos\theta^*)$, f_C is the strong scattering amplitude modified by the Coulomb interaction and $\widetilde{G}$ is a combination of a regular and singular s-wave Coulomb functions. Here it is assumed that the two particles are produced at the same time in a heavy-ion collision and interact via the Strong and Coulomb interaction, also called final-state interaction (FSI). After their final interaction they propagate to the detectors as plane waves. When symmetrized the wave function becomes:

$$\Psi^{(+)}_{-\mathbf{k}^*}(\mathbf{r}^*, \mathbf{k}^*) = \sqrt{\frac{A_C(\eta)}{2}} \left[e^{-i\mathbf{k}^*\mathbf{r}^*} F(-i\eta, 1, i\zeta^+) + e^{i\mathbf{k}^*\mathbf{r}^*} F(-i\eta, 1, i\zeta^-) \right]. \tag{5.12}$$

This expression can be simplified by assuming that the Coulomb contribution can be factorized out. After applying the Bowler-Sinykov fitting procedure[48, 49] the following form of the correlation function is obtained:

$$C_2(\mathbf{q}) = (1 - \lambda) + \lambda K_C \left[1 + exp\left(-R^G_{out}{}^2 q^2_{out} - R^G_{side}{}^2 q^2_{side} - R^G_{long}{}^2 q^2_{long} \right) \right] \tag{5.13}$$

where the K_C function pertains to the factorized Coulomb interaction part. Equation 5.13 again reproduces the Gaussian shape. In this analysis we will use this functional for fitting but in a 1D form with a free exponent:

$$C_2(Q_{inv}) = (1 - \lambda) + \lambda K_C \left[1 + exp\left(-R^\alpha_{inv} Q^\alpha_{inv} \right) \right] \tag{5.14}$$

In Eq. 5.14 the α parameter is used to experimentally verify the Gaussian assumption on the shape of the emission region.

5.3 Contemporary experimental results

Current femtoscopic research has started to branch into numerous directions. Initially research was conducted using only pions because of their dominance in the produced meson spectrum but due to availability of large data sets kaons, protons and lambdas have started to be investigated as well. The LHC program has delivered data on three different collision systems:

1. proton-proton (*pp*) collisions at $\sqrt{s} = 0.9$ and 7 TeV

2. proton-lead (*pPb*) collisions at $\sqrt{s_{NN}} = 5.02$ TeV

3. lead-lead (*PbPb*) collisions at $\sqrt{s_{NN}} = 2.76$ TeV
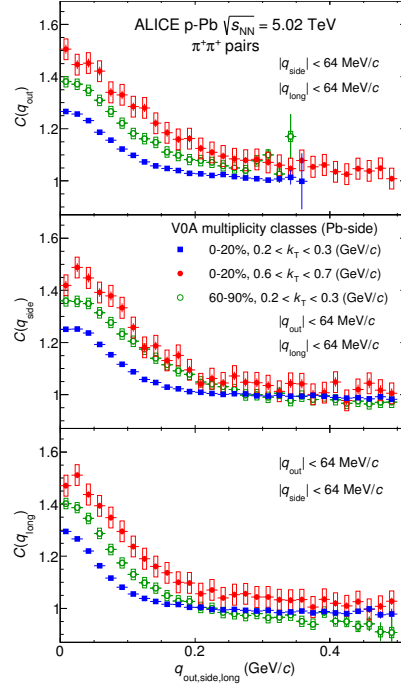
Fig. 5.1 Projections of the three-dimensional $\pi^+\pi^+$ correlation functions for three multiplicity and kT ranges along the out (top), side (middle), and long (bottom) direction.[44]

New methods for extracting homogeneity radii have also been explored. Particularly, methods using cumulants and correlations between more than two identical particles. Comparisons
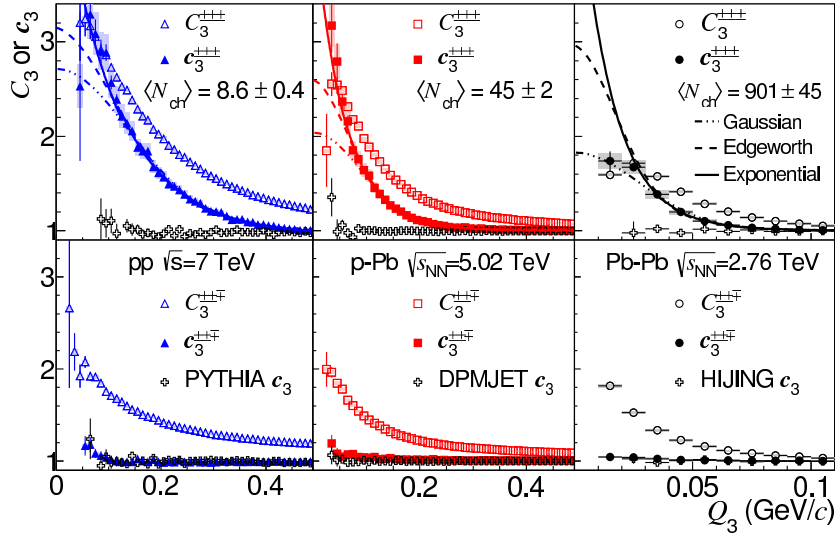
Fig. 5.2 Three-pion correlation functions C_3 for $0.16 < k_T < 0.3$ GeV/c in *pp* , *pPb* and *PbPb* collision data compared to PYTHIA, DPMJET and HIJING generator-level calculations. Top panels are for same-charge triplets, while bottom panels are for mixed-charge triplets. [53]

between different collision systems has also given insight into the details of Comparison of

femtoscopic characteristics between different systems allow a detailed understanding of the created matter. A linear dependence has been observed between measured homogeneity radii
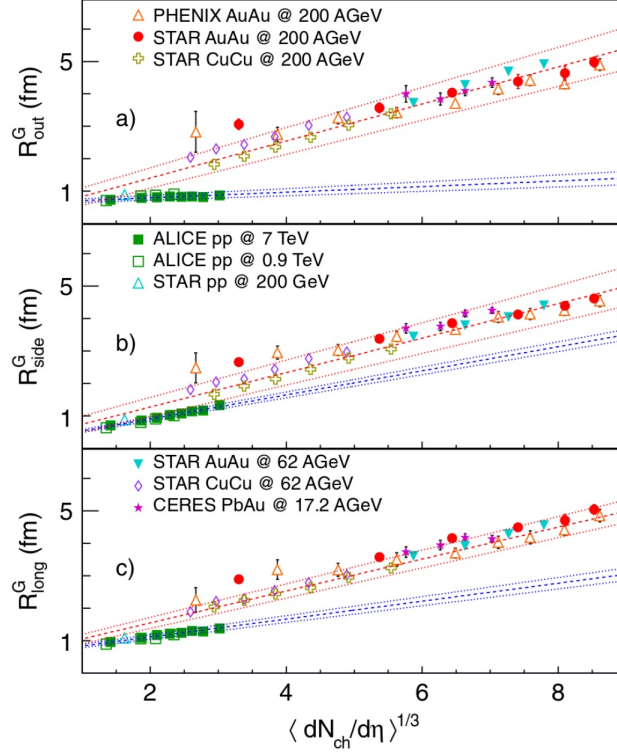
Fig. 5.3 Measurement of homogeneity radii as a function of $\langle dN_{ch}/d\eta \rangle^{1/3}$ for LHC, RHIC and SPS results. Source [43]

in heavy-ion collision and $\langle dN_{ch}/d\eta \rangle^{1/3}$. In *pPb* collisions the measured radii show a falling trend with k_T, similar to heavy-ion and high multiplicity *pp* collisions. The three-pion cumulent method compared three collision systems produced by LHC. Due to an enhanced QS signal and the removal of two-particle background this method is useful in extracting more detailed information on the emission source. A deviation from the standardly assumed Gaussian shape of the correlation function has been observed and quantified using the Edgeworth functional form. In this thesis we explore these deviations in more detail and consider other fit functions.

5.4 Measuring two-particle correlations

Correlations are observed using the $C(Q_{inv})$ correlation function, where $Q_{inv} = |\mathbf{q}| = |\mathbf{p}_1 - \mathbf{p}_2|$ is the relative pair 3-momentum. The two-particle correlation function is experimentally defined as a ratio

$$C(Q_{inv}) = \frac{A(Q_{inv})}{B(Q_{inv})}, \tag{5.15}$$

where $A(Q_{inv})$ and $B(Q_{inv})$ are two distinct measured two-particle Q_{inv} distributions. $A(Q_{inv})$ is the standard event-by-event two-particle Q_{inv} distribution where as $B(Q_{inv})$ is also a two-particle

Q_{inv} distribution, created in the same manner, but for mixed event pion pairs. With such a definition the $B(Q_{inv})$ distribution keeps all the information on single particle momentum spectra, but is void of any multi-particle correlations which exist in $A(Q_{inv})$. In the mixing procedure of this analysis we chose to mix events of similar z-vertex, multiplicity and sphericity in packs of 10. We also vary this number as a systematic check.

By dividing $A(Q_{inv})$ and $B(Q_{inv})$, and relying on the separability of Bose-Einstein correlations from the kinematic part (of particle production), one is able to isolate quantum statistical effects from the background and extract information about the emission source. There are some additional contributions to the $C(Q_{inv})$ correlations which are kept in the final results, such as the Coulomb contribution at very low Q_{inv} or the contributions from the energy and momentum conservation laws which play a role at very high Q_{inv}. They are all well understood and taken into account in the final fitting procedures.

Chapter 6

Event shape and transverse sphericity

The possibility of using event topology for effective event characterization by hardness lies on the fact that the dominating QCD production mechanism changes depending on the total invariant mass $Q^2 = \sum_i (p^\mu p_\mu)_i$ of the initial parton collision. Soft interaction processes are characterized by a non-perturbative QCD low mass meson production with no preferred direction and thus no particle collimation. Jets, the product of hard scattering, are within the perturbative-QCD regime and collimate most of the produced particles. This basic distinction of event topologies offers a computationally easy way of distinguishing hard and soft processes.

For high multiplicity events a large energy to mass process needs to occur. This can either be a single high energy hard scattering which produces jets or a multi-parton interaction where many lower energy scatterings occur and a net high energy process produces many low mass mesons. These scenarios will produce very different spreads of particles in the $\eta - \phi$ plane and an event shape observable should be sensitive to them.

In this analysis we choose transverse sphericity (S_T) as our event observable of choice and analyze different implications of its use in a pion femtoscopy analysis.

6.1   Transverse sphericity

Transverse sphericity is a scalar event shape observable which characterizes the spread of particles in the $\phi - \eta$ plane in a simple way. It concerns all primary charged particles in the event and is therefore named a "directly" global event shape variable. S_T is used to differentiate between jet-like and isotropic event topologies, separating them on opposite sides of the sphericity spectrum. Events which show particle bunching are identified as jet-like with low sphericity while the events with an event spread in the $\phi - \eta$ plane are identified as spherical with a higher sphericity.

In order to avoid bias from the boost along the beam axis we restrict ourselves to the transverse momentum space and calculate sphericity in terms of transverse momentum matrix eigenvalues:

$$S_{XY} = \frac{1}{\sum_i p_T^i} \sum_i \frac{1}{p_T^i} \begin{pmatrix} (p_x^i)^2 & p_x^i \cdot p_y^i \\ p_x^i \cdot p_y^i & (p_y^i)^2 \end{pmatrix}, \tag{6.1}$$

with the eigen values being λ_1 and λ_2. The transverse sphericity is then defined as

$$S_T = \frac{2 \cdot \min(\lambda_1, \lambda_2)}{\lambda_1 + \lambda_2}. \tag{6.2}$$
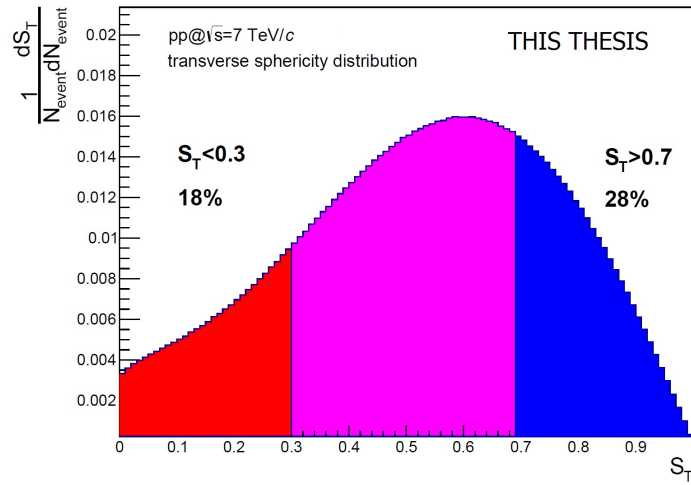
Fig. 6.1 Transverse sphericity distribution for proton-proton collisions at $\sqrt{s} = 7$ TeV.

With this construction $S_T \in [0, 1]$, with $S_T \approx 0$ being a highly non-spherical or "pencil-like" event topology containing a jet-like structure and $S_T \approx 1$ being a completely spherical and isotropic event. This characterization of events offers a possibility to carefully choose sphericity bins and investigate a variety of event topologies. Events with such a topology that they are characterized as "mid-spherical" ($0.4 < S_T < 0.6$) generally contain events which are hard to identify as jet-like since they either do not contain jets but seem somewhat collimated or contain jets which are masked by an underlying event particle spread. Also there is a possibility that an event containing no jets happens to have a somewhat jet-like structure. Such events will also be interpreted as mid-spherical. For this analysis we calculate transverse sphericity in the same manner explain in equation 6.1 using all tracks within $|\eta| < 0.8$ and $p_T > 0.5$.

New Pythia tunes incorporate the observed transverse sphericity spectrum and exhibit a noticeable improvement in describing the data. For the needs of this femtoscopic analysis a differential examination in S_T is performed and the effects of MC generator bias is included in the systematical uncertainties.
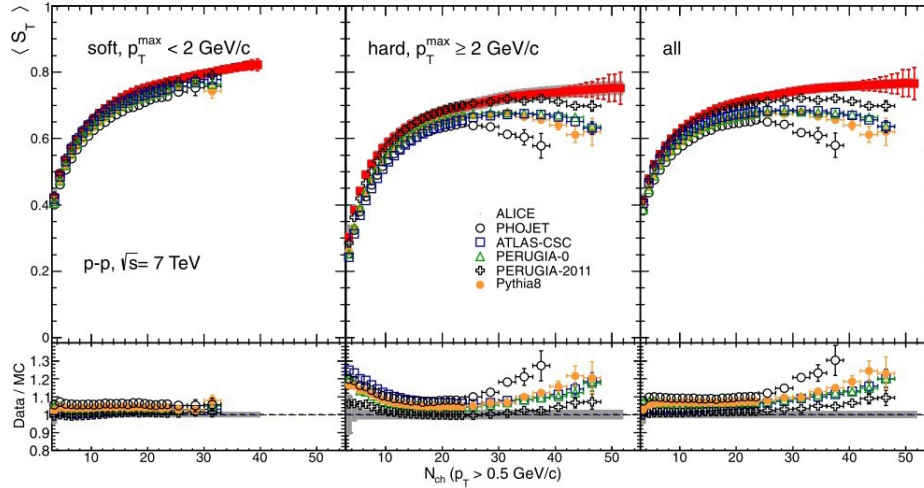
Fig. 6.2 Mean transverse sphericity as a function of charged particle multiplicity. The ALICE data are compared with five models: PHOJET, PYTHIA6 (tunes: ATLAS-CSC, PERUGIA-0 and PERUGIA-2011) and PYTHIA8. [2]

6.1.1 Spherical events $(S_{\mathbf{T}} > 0.7)$

Spherical events are a subset of all minimum bias events that show no obvious jet structure or particle collimation. These events do not contain hard production dominance or possible quenched jet signatures. In such isotropic events most of the energy is spent on a thermal-like
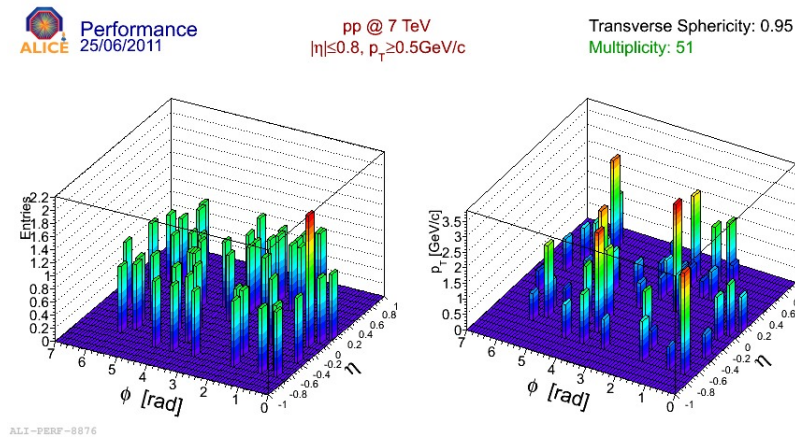
Fig. 6.3 High transverse sphericity event with its characteristic "hedgehog" structure.

production of light mesons so that the p_{T} spectra are shifted toward lower values in comparison to the minimum bias p_{T} spectrum. Also, in the $\phi - \eta$ plane there are no localized structures of particles or larger p_{T} towers because the p_{T} spectrum does not contain a power-law tail at higher momenta which will be shown in the following sections.

Higher multiplicity spherical events should be understood as mainly being the kind of event where particle production is dominated by low energy QCD field hadronizations and not hard

particle scattering where a more Feynman diagram-like approach can be used.

By definition, there is an inherent multiplicity dependence in the transverse sphericity observable. In practice this means that high multiplicity events will tend to be more spherical with $S_\mathrm{T} \approx 1$ and low multiplicity events will be more jet-like with $S_\mathrm{T} \approx 0$. This characteristic is well observed in the data. We stress that this should not be understood as a direct functional dependence or a mapping between transverse sphericity and multiplicity, or that every high multiplicity event is spherical and every low multiplicity event is jet-like, as this analysis will demonstrate.

6.1.2 Low sphericity jet-like events ($S_\mathbf{T} < 0.3$)

Jet-like events are such events which exhibit explicit particle collimation coming from jets, mini-jets or quenched jets. They are pencil-like in structure and exhibit in-jet production characteristics.
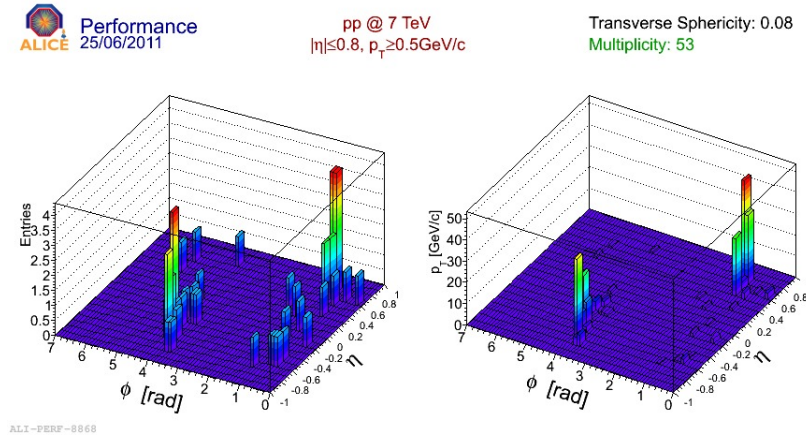
Fig. 6.4 High multiplicity and low transverse sphericity event with a "pencil" structure.

With jet collimation comes multiparticle momentum space correlation. Constituents of each jet have similar directions and momenta, a characteristic which is not of quantum statistical origin, but of jet hadronization in nature. This excess in particle correlations increases the apparent measured two-particle correlations in the traditional femtoscopic analysis and is treated as background in need of parametrization and/or removal. In this analysis we show that a S_T cut is a valid background removal method.

Figure 6.4 demonstrates that in comparison to spherical events, the p_T towers in the $\eta - \phi$ plane for low sphericity jet-like events are substantially larger and that a high multiplicity event with a distinct pencil-like structure is correctly identified as jet-like using the transverse sphericity observable.

Comparison of p_T spectra for spherical and jet-like events

The differences between spherical and jet-like event p_T spectra demonstrate a correct understanding of spherical events as being more "thermal-like". By choosing events with high sphericity one is able to remove the power law tail from the p_T spectrum which is still present in the jet-like events.
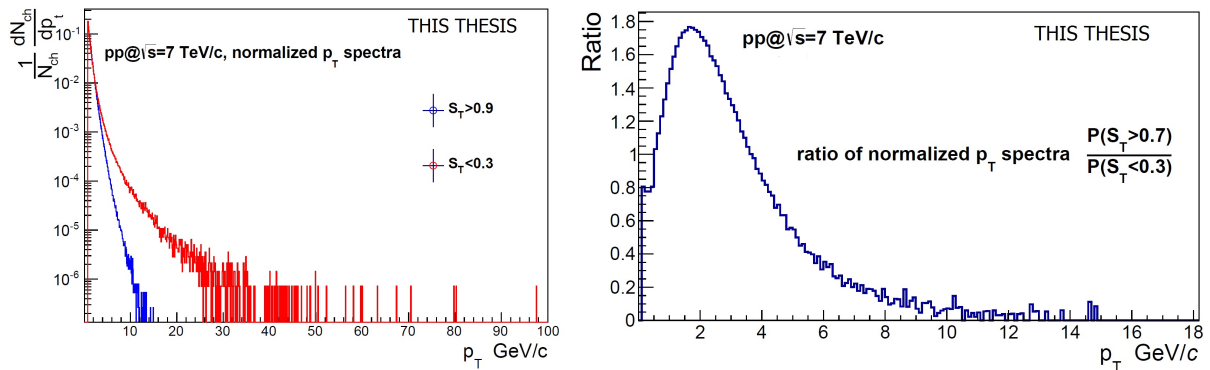
Fig. 6.5 A comparison of p_T distributions for spherical and jet-like proton-proton collisions.

Since in Figure 6.5 the ratio of the spectra is never asymptotic to unity, the spectra differ in behaviour for all values of p_T and as such demonstrate a significant difference in the physical conditions of the two event classes. QCD systems characterized by such p_T spectra differ in particle production mechanisms and this should show in multi-particle correlation analysis.

Two particle correlation analysis are especially affected by jet-like background contributions because of their inability to suppress such signals through combinatorics or a simple track cut without seriously suppressing event statistics or the effective range of the analysis. A three-particle analysis is thus a natural alternative for a background-suppressed femtoscopic analysis[53].

Chapter 7

Analysis method

7.1 Data analysis and cuts

7.1.1 Data sets

In 2010 the LHC produced *pp* collisions at $\sqrt{s} = 7$ TeV. Approximately 5×10^8 minimum-bias events were collected by the ALICE detector. The minimum-bias trigger required at least one hit in the SPD or the VZERO detectors in coincidence with two beam bunches crossing in the ALICE interaction region. The main subdetectors used for this analysis were the ITS, TPC, TOF and the ZDC. Vertexing was performed using matching tracks of the ITS na TPC. The dE/dx measurement was collected from the TPC and TOF detectors and compared to the pion expectation. The selection criteria is optimized to obtain a high-purity sample while maximizing efficiency. An offline event selection is applied to reject beam-halo and beam-gas induced background. For two-particle track effects, merging and splitting, cuts are applied to minimize their effect. It is known that they become negligible for $Q_{inv} > 80$ MeV/c.

We analyzed Analysis Object Data (AOD) files but for various checks and possible systematic effects we used Event Summary Data (ESD) for comparison.

7.1.2 Event selection

Here we mention event selection cuts and the publicly available AliRoot code which was used:

- Events with the number of tracks within the pseudorapidity range of $|\eta| < 0.8$ less than 3 have been rejected

- Events with the reconstructed primary vertex further than 8 cm form the center of the TPC were rejected

- standard methods were used for rejecting pile-up events

- in SPD we set the number of contributors to 3.

Charged-particle multiplicity (in AOD) was estimated within the pseudorapidity range of $|\eta| <$ 0.8. Initially we chose events from two categories, multiplicity and sphericity:

- transverse sphericity: jet-like $S_T < 0.3$, spherical $S_T > 0.7$

- uncorrected multiplicities [3-25], [26-40], [41-55], [56-70]

- corrected multiplicities 9 ± 5, 32 ± 5, 48 ± 5, 63 ± 5

For mixed event track pair creation we mix 10 events of the same multiplicity and sphericity bin. The corrected multiplicity estimation was done in the same manner as in [53].

7.1.3   Track selection

In this analysis we used primarily AOD data for both measured ALICE data and PYTHIA reconstructed. For reference:

- https://twiki.cern.ch/twiki/bin/view/ALICE/AddTaskInfoAOD147

- https://twiki.cern.ch/twiki/bin/view/ALICE/AddTaskInfoAOD161.

The interferometry analysis was performed using a pseudorapidity acceptance of $|\eta| < 1.2$ and a transverse momenta cut of $0.13 < p_T < 4.0$ GeV/c. For event selection, the transverse sphericity calculation was performed using all charged tracks with $|\eta| < 0.8$ and $p_T > 0.5$ GeV/c. The procedure for electron rejection uses the energy loss measured by the TPC to remove electrons from conversions and the π^0-Dalitz decays. We use the standard 3 σ cut:

$$N\sigma_{TPC_e} < 3 \quad , \quad N\sigma_{TPC_\pi} > 3 \quad , \quad N\sigma_{TPC_K} > 3 \quad , \quad N\sigma_{TPC_p} > 3.$$

Here we take care that each detector contributes in the range where it is most sensitive in particle identification. This procedure has a final $0.13 < p_T < 4.0$ GeV/c integrated pion purity of 98% in the relevant p_T range of this analysis.

7.1.4   Cuts for sphericity, femtoscopic quality and particle identification

Anti-gamma cut

We use cuts to remove electron-positron made by gamma conversion. The cut checks for tracks with opposite sign charges which have a small $\Delta\theta$ angle difference and calculates their invariant mass. All pairs which have their invariant mass close to 0 are removed.

Femtoscopy quality cuts

Femtoscopic quality cuts remove contributions coming from track splitting and merging effects. Here a single particle track is mistakenly identified as two tracks (splitting) or two particle tracks are identified as one (merging) or not identified at all.

To ensure these contributions are removed several requirements are enforced. To significantly decrease splitting each track is required to be simultaneously reconstructed in the TPC and the ITS. Next, each TPC cluster is flagged "shared" if it is used in the reconstruction of more than one track. Since split tracks share most of their clusters, we remove all pairs that share more than 5% of their TPC clusters. Finally a "share quality" check is performed to remove contributions from a single particle tracks which are split in two segments in the TPC. Two segments, split by the TPC central membrane and a TPC sector boundary, are usually correctly connected and identified as a single track. In case of mistakes, we count the number of times that both tracks have a non-shared cluster in the TPC pad row and remove all track pairs for which this number is less than the half of the total number of clusters.

Sphericity cuts

For the transverse sphericity calculations all particles with $p_\mathrm{T} > 0.5$ GeV/c and $|\eta| < 0.8$ were accepted. Spherical and jet-like events were selected from the full 2010 ALICE minimum bias set as those events which have $S_\mathrm{T} > 0.7$ and $S_\mathrm{T} < 0.3$ respectively.

Particle identification

We combine TPC and TOF information for pion identification:

- $N\sigma_{TPC} < 3$ without TOF signal for $p < 0.5$ GeV/c

- $N\sigma_{TPC} < 2$ without TOF signal for $p \in [0.5, 0.65]$ GeV/c

- tracks without TOF for $p > 0.65$ GeV/c were rejected

- $N\sigma_{TPC} < 3$ and $N\sigma_{TOF} < 3$ for tracks with TOF for $p < 0.65$ GeV/c

- $N\sigma_{TPC} < 5$ and $N\sigma_{TOF} < 3$ for $p \in [0.65, 1.5]$ GeV/c

- $N\sigma_{TPC} < 5$ and $N\sigma_{TOF} < 2$ for $p > 1.5$ GeV/c.

7.1.5   Quality assurance

Here we present some basic quality assurance plots for both spherical and jet-like events.
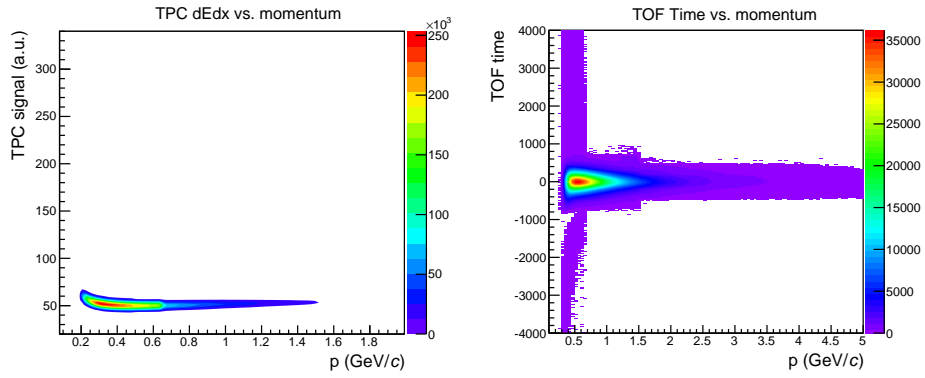
Fig. 7.1 TPC particle energy loss (left plot) and TOF time - expected time (right plot).
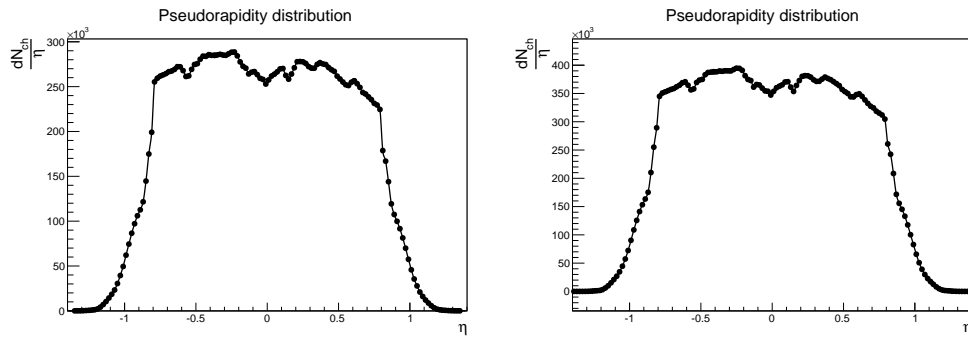
Fig. 7.2 η distribution for spherical (left) and jet-like (right) events.
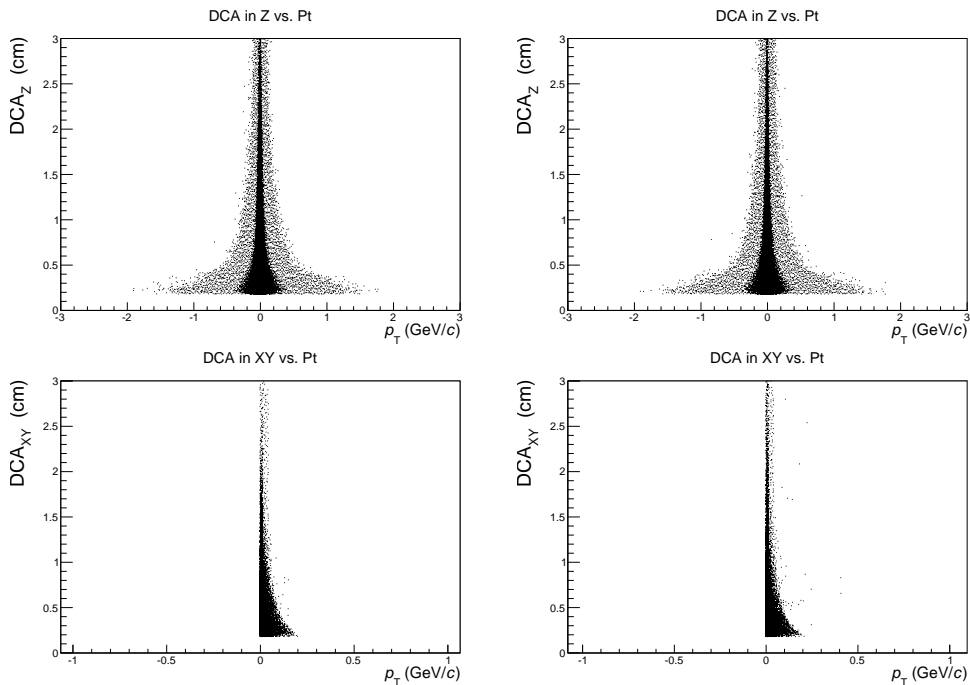
Fig. 7.3 Distribution of DCA (distance of closest approach) in the Z(top) XY(bottom) directions and transverse momenta for spherical (left) and jet-like (right) events.

7.1.6 Analysis framework

The analysis was done within the `AliRoot` framework, using the `AliFemto` package (release v5-05-27-AN). New event cut class was defined `AliFemtoSphericityEventCut.cxx` to accommodate for the event shape variables. The sphericity code followed the earlier mentioned definition of the S_T observable for sphericity calculation. No additional change in the ALICE Femtoscopy code was done. For the fitting procedure the `Minuit2` minimization package was used from within the `RooFit` framework and as a stand-alone package.

7.2 Jets and k_T

An important characteristic of measured homogeneity radii is their dependence on the pair kT parameter.

$$k_T = \frac{|\mathbf{k}_T^1 + \mathbf{k}_T^2|}{2} \tag{7.1}$$

In jet-like events high k_T particle pairs belong predominantly to the same jet structure, while this is generally not the case for low k_T. A high k_T particle pair belonging to a single jet will also have a small $\mathbf{q}$, while a low k_T opposite jet pair will have a larger $\mathbf{q}$. The understanding of k_T
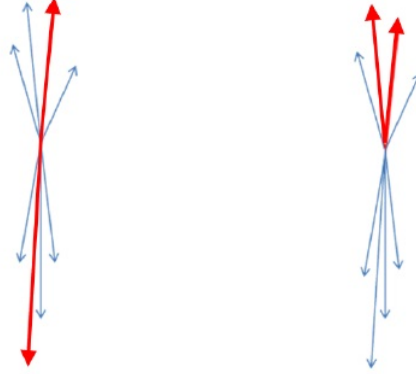
Fig. 7.4 Cartoon depiction of pair association via a k_T cut in jet-like events. Opposite jet particle pairs (left) with high Q_{inv} and low k_T and same jet particle pairs (right) with low Q_{inv} and high k_T.

and $\mathbf{q}$ dependence in jets is accessible by considering the energy and momentum conservation constraints to particle production. These conservation laws were also shown to be the source of non-femtoscopic correlations at high $\mathbf{q}$. The existence of jet induced, k_T dependent, contributions to $\mathbf{q}$ correlation is also easily confirmed by J_T considerations alone, as it consequently observed in ALICE data and Monte Carlo simulations. This observation suggests that it may be possible to correctly identify jet-induced non-femtoscopic correlations observed in minimum bias events and, when this background signal is understood, inspect quantum statistics contributions to correlations of same-jet particle pairs.

For femtoscopic analysis one needs to take into account only the quantum statistical correlations without kinematic or detector effect contributions. Due to separability of Bose-Einstein symmetrization and fragmentation function contributions to particle production and spread, the quantum statistical signal in two-particle momentum space correlations will have no information on jet association.

$$(\mathbf{p_1} - \mathbf{p_2}) \propto P(HBT) \cdot P(kinematics) \tag{7.2}$$

Since non-femtoscopic correlations are caused by same-jet collimation effects they tend to increase, and actually dominate, in the high k_T region. This connection between background non-femtoscopic correlations and pair k_T means that isotropic events are a natural choice for a data driven (background and model free) femtoscopic analysis, since they carry no jet structure.

Chapter 8

Q_{inv} correlation functions - ALICE data

A 1D femtoscopic analysis was performed in various multiplicity and k_T bins for minimum bias and two extreme values of S_T. The created two-pion correlation functions were normalized so that the lowest (and if possible low error) bin value outside of the relevant femtoscopic area was set to unity. Here we assume that there are no unknown large anticorrelation effects which would force the correlation function below unity, which is the theoretically set lower limit for identical bosons. Figure 8.1 demonstrates the general idea of this analysis. Spherical event contain far
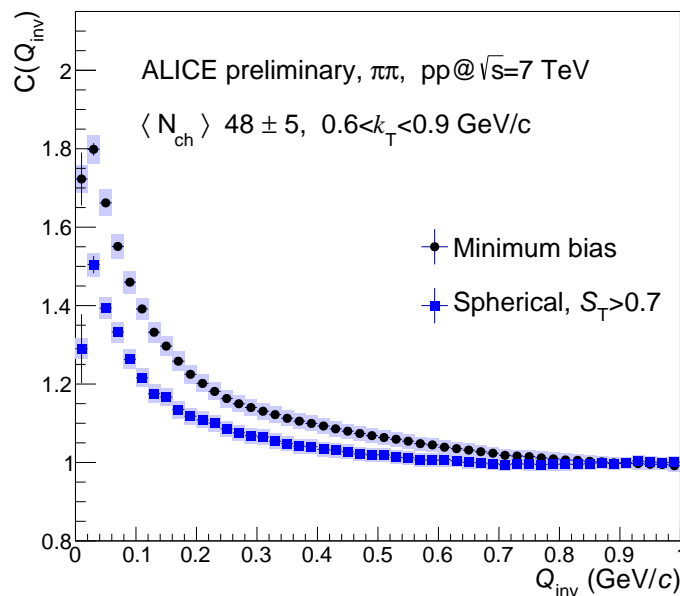
Fig. 8.1 Comparison of $C(Q_{inv})$ correlation functions for minimum bias and spherical events.

less non-femtoscopic correlations than minimum bias and are thus far better behaved at high k_T . In general, Monte Carlo event generators contain enough information to describe most of the background but with a sphericity cut one is able to reach larger pair k_T without introducing

unwanted assumptions or model bias. For jet-like events this model bias should not be a problem since any reasonable event generator correctly reproduces p_T, J_T and N_{ch} spectra so that the bulk of the non-femtoscopic contribution is also incorporated.

8.1 No sphericity cut

ALICE collaboration has published pion femtoscopy results in pp and PbPb collision systems[1]. Here we present a Q_{inv} correlation function measurement without an event shape cut. At low k_T the measured correlations contain almost no non-femtoscopic contributions coming from jets and should only show the Coulomb repulsion induced steep drop in correlations at very low Q_{inv}. With rising k_T the jet contribution start to contribute more and in the highest k_T bin
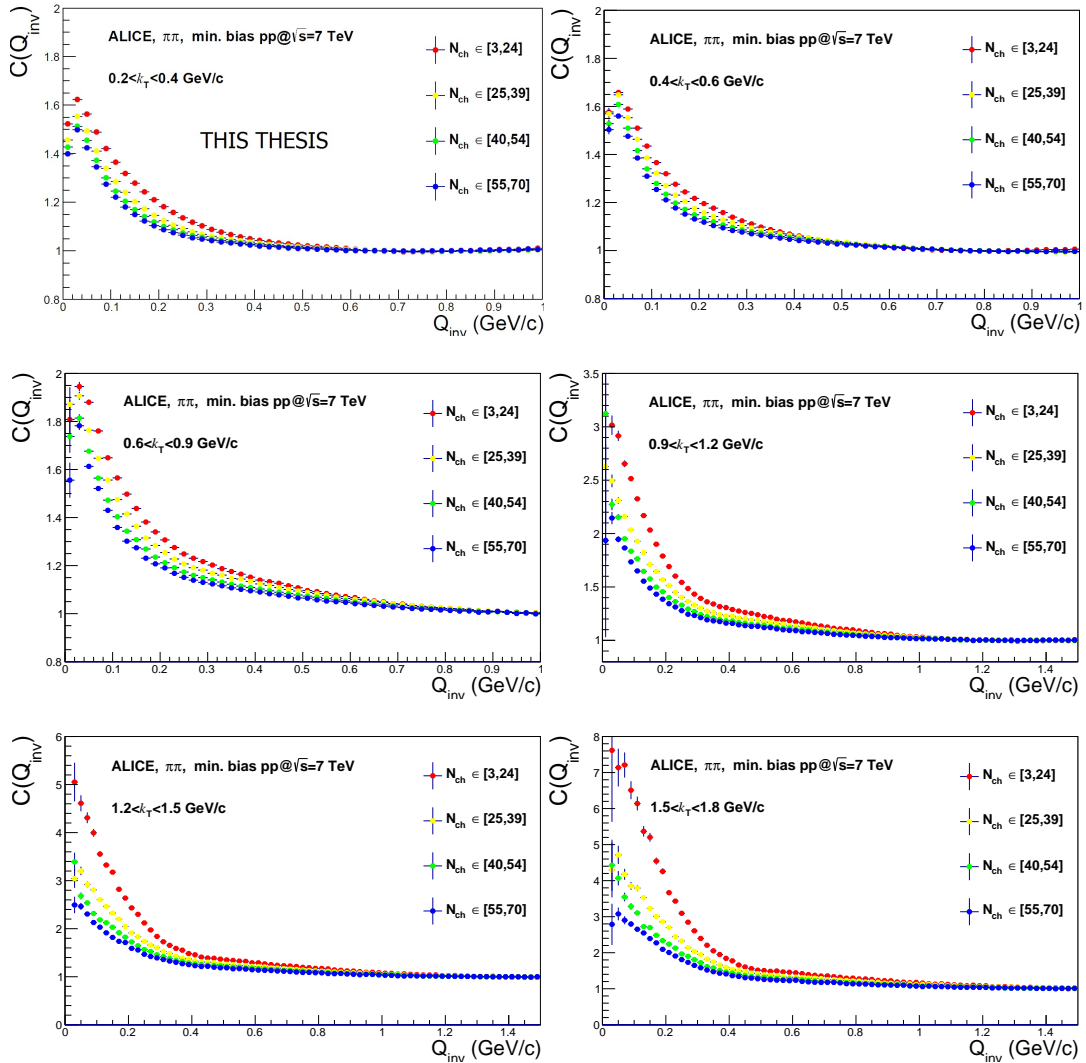
Fig. 8.2 Same-sign pion correlation functions $C(Q_{inv})$ for six k_T bins of measured ALICE pp collisions at $\sqrt{s} = 7$ TeV.

dominates the correlation. These contributions send the measured correlation function above

the theoretical limit signaling a clear limit to traditional analysis with minimum bias events. As observed, correlations are expected to decrease in amplitude and width for higher multiplicities, which is understood as an increase in homogeneity radii. The middle bin $0.6 < k_T < 0.9$ GeV/c is the effective reach of the traditional femtoscopy analysis. There the lowest multiplicity bin is close to the theoretical limit. In the next k_T bin all the correlation functions cross this limit and no homogeneity radii can be extracted without a good understanding of the background and a proper method of removing it. This is where event generator bias might contribute significantly.

8.2 Spherical events ($S_T > 0.7$)

For this analysis we choose the value of $S_T > 0.7$. As we will show in the following chapters, it is strong enough to remove most of the jet contributions and not severely limit data statistics. About 28% of the full minimum bias data set passes this requirement. In Fig. 8.3 low k_T bins show standard behavior with very little difference to the results obtained without a sphericity cut. Correlation functions for higher k_T bins show similar shape and size, but very large error bars due to statistical limitations. We also observe in the lowest multiplicity bin novel behaviour. This is a consequence of the sphericity cut. A simple explanation would be that a lower multiplicity event with high sphericity, for example containing 10 particles, will have an even spread of particles in ϕ which translates in a close to constant $\Delta\phi$ separation between all the particle tracks. In this respect, it is highly unlikely for a low multiplicity spherical event to obtain a track pair with very low Q_{inv} because for this the pair would need a very small separation in ϕ. In mixed event pairing of tracks this is not the situation since we mix 10 events and any $\Delta\phi$ between tracks is equally possible. This effect of low Q_{inv} suppression with S_T should be visible in simulations and diminished with the rise in multiplicity. In further chapters we show this is the case.

8.3 Jet-like events ($S_T < 0.3$)

In comparison to previous results, Fig. 8.4 shows that jet-like events have a larger correlation function amplitude and a wider correlation signal. This is due to non-femtoscopic correlations which, even for lower k_T's, are not negligible in comparison to the whole correlations signal. In later sections we discuss the shape, range and amplitude of the non-femtoscopic contributions and ways of extracting homogeneity radii in jet-like events. As expected, with higher k_T the non-femtoscopic signal rises and starts to dominate the correlation. This is due to the high k_T cut choosing mostly same-jet pion pairs which have an intrinsic collimation and thus small Q_{inv}. This trend is kept for all k_T bins where for the highest bin the measured correlation function even overshoots the theoretical upper limit five times. This is a clear sign that these correlation functions contain large non-femtoscopic contributions or that there is a serious misunderstanding of theory and/or experiment.
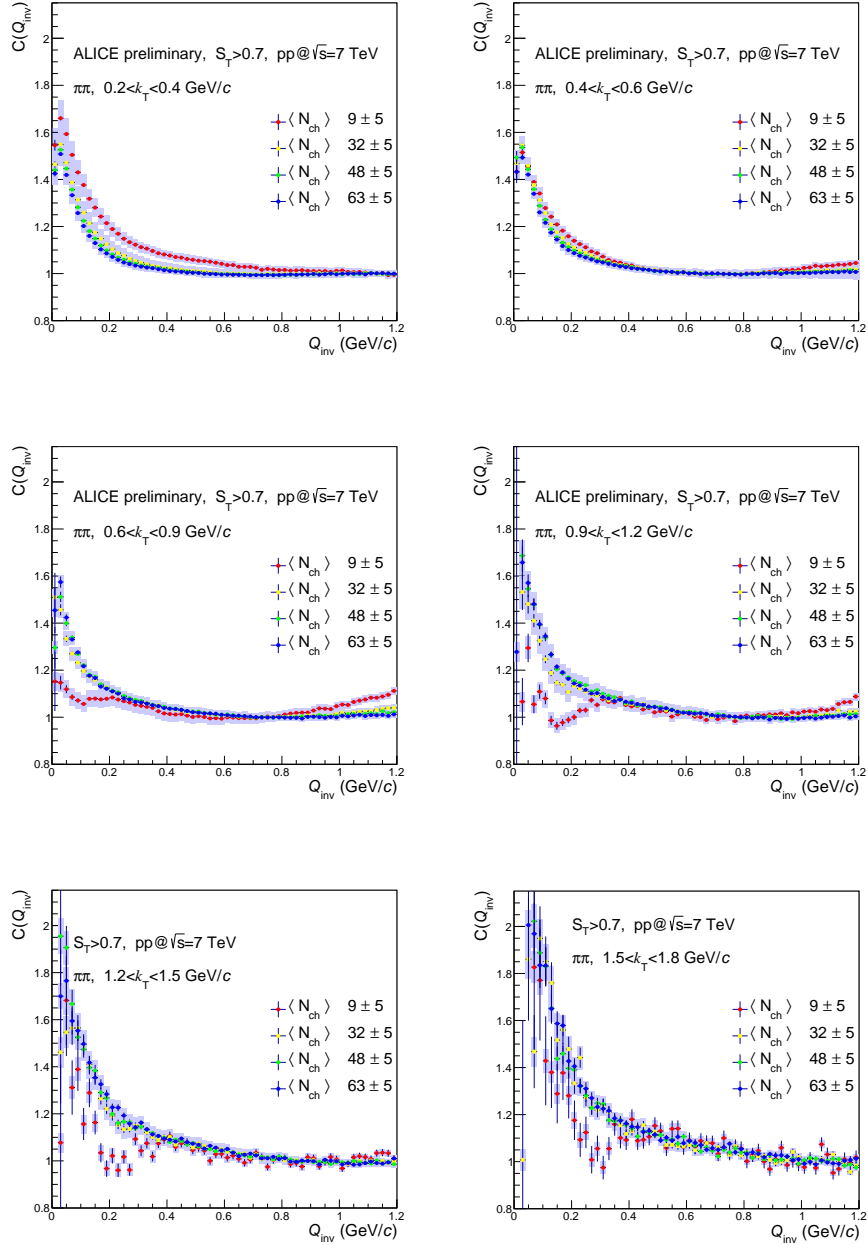
Fig. 8.3 Same-sign pion correlation functions $C(Q_{inv})$ for six k_T bins of ALICE measured spherical pp collisions at $\sqrt{s} = 7$ TeV.

Since the jet contributions constitute a large portion of the measured correlations, and in general have a different shape than Bose-Einstein contributions, it should be possible to see where quantum statistics and the non-femtoscopic background signal exchange dominance. In our plots this happens around $Q_{inv} \approx 0.4$ GeV/c. Correlation functions still resemble in shape the minimum bias results, but when fitted for homogeneity radii give lower values and very large chaoticity parameter λ.
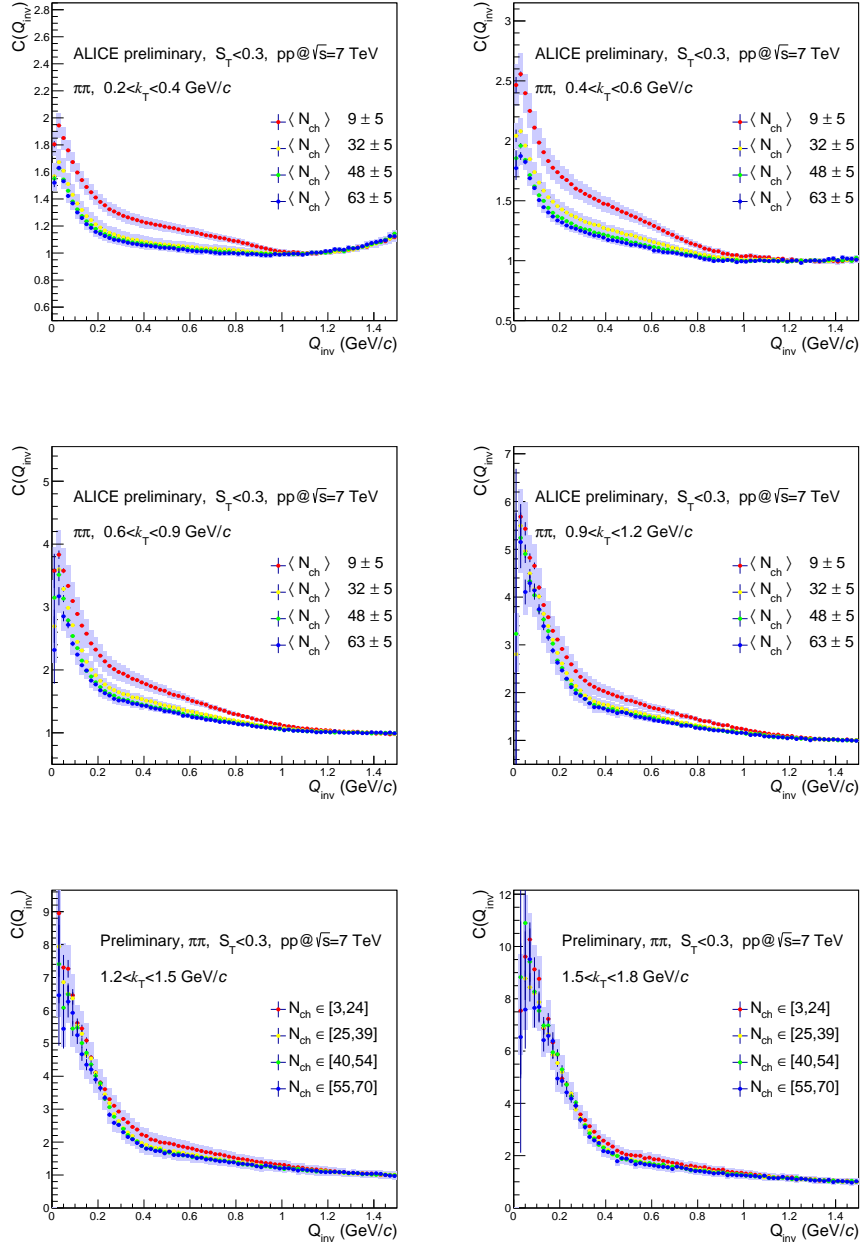
Fig. 8.4 Same-sign pion correlation functions $C(Q_{inv})$ for six k_T bins of ALICE measured jet-like *pp* collisions at $\sqrt{s} = 7$ TeV.

From a practical standpoint the background signal seems to be smooth, without oscillations, so the quantum statistics signal should be, in practice, extractable using a well chosen model motivated by Monte Carlo simulations. Here the introduced bias is also possible to control since every state-of-the-art event generator should have correct ϕ, N_{ch} and p distribution for jet constituents. In the next section we show the quality of Monte Carlo data and a possible way of removing the jet background in a more natural way.

Chapter 9

Monte Carlo event generator data

9.1 Kinematical contributions using PYTHIA Perugia0 event generator

Since in the present analysis the Monte Carlo data do not include a femtoscopic signal, it is to be expected that only non-femtoscopic correlations due to constrains in kinematics coming from laws of conservation, Coulomb interaction and jet collimation will be observed in these plots. Event generators differ in their approach and assumption. We wish to introduce no unnecessary assumptions into the analysis. A natural way to check the quality of simulations without Bose-Einstein contributions is to use opposite charge pion correlation. PYTHIA data should produce jet kinematics with a good agreement with measured data and jet-induced correlations are expected in both same-sign and opposite-sign pion pairs so PYTHIA should have them in both.

It was suggested that non-femtoscopic contributions could be estimated using the opposite sign pair analysis. To check, one could argue that in PYTHIA data, without HBT weights, the only difference between same sign and opposite sign analysis is the existence of meson resonances and Coulomb interaction. This will be shown not to be the case and that a difference in slope is also observed which could originate from charge conservation considerations.

9.1.1 Minimum bias events

Here we check for the kinematic contributions to two-particle correlations that should be accessible using the PYTHIA event generator. As already mentioned, the non-femtoscopic contributions to two-particle correlations should play no role at low pair k_T but should be evident in the high pair k_T region. In a published ALICE paper[4], these contributions were fitted with a Gaussian function. The extracted width of the Gaussian was used during the first fitting procedure to ensure that the contributions from non-femtoscopic sources were controlled and not understood

as legitimate Bose-Einstein signals. The amplitude of the Gaussian was left as a free parameter since there is no apparent connection between the amplitudes in non-femtoscopic contributions within PYTHIA and ALICE data.
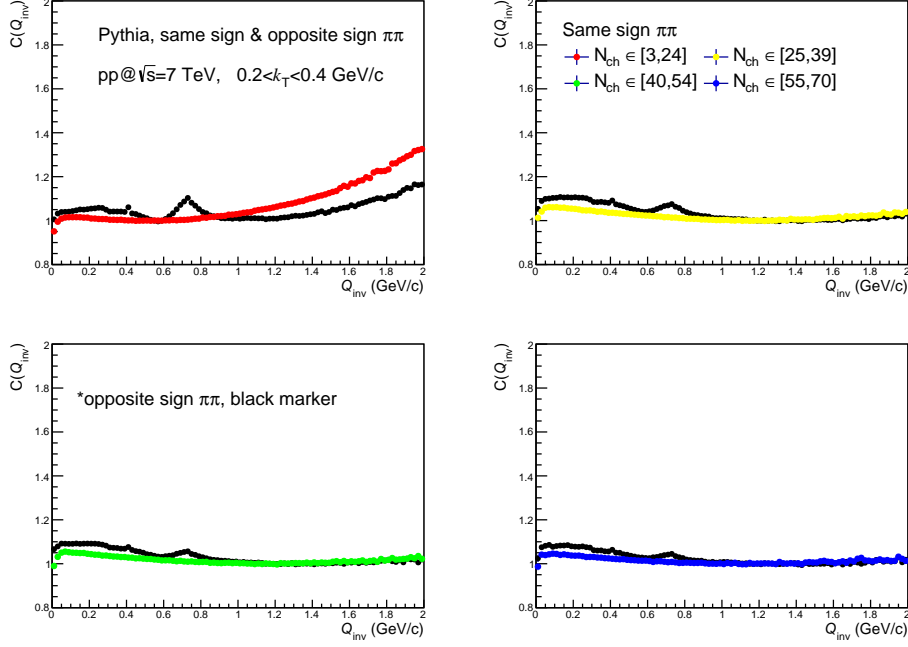
Fig. 9.1 Pion pair correlations for $0.2 < k_T(\text{GeV}/c) < 0.4$ in PYTHIA pp collisions at $\sqrt{s} = 7$ TeV.
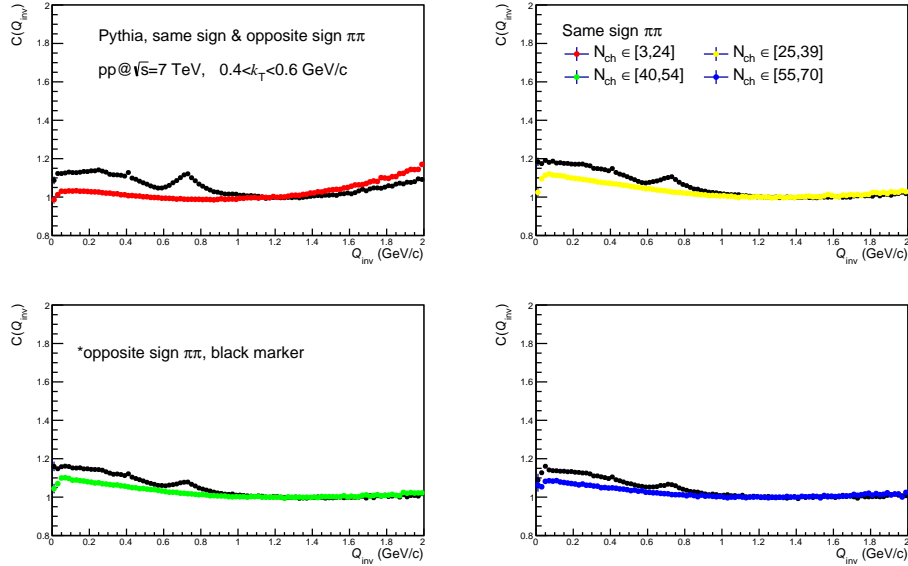
Fig. 9.2 Pion pair correlations for $0.4 < k_T(\text{GeV}/c) < 0.6$ in PYTHIA pp collisions at $\sqrt{s} = 7$ TeV.
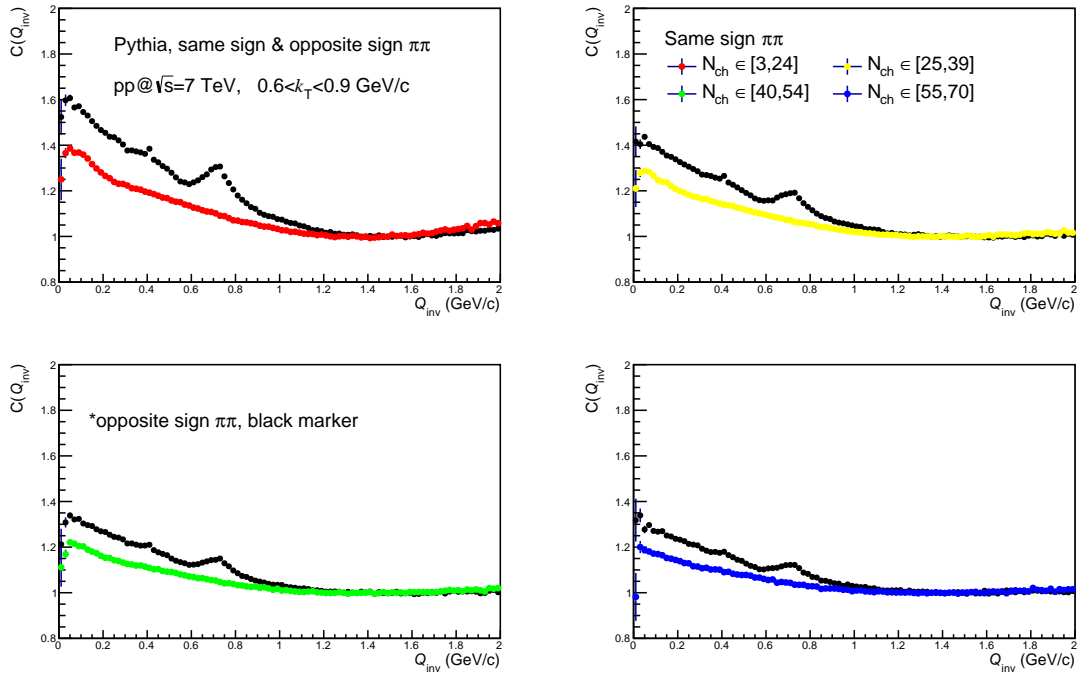
Fig. 9.3 Pion pair correlations for $0.6 < k_\mathrm{T}(\mathrm{GeV}/c) < 0.9$ in PYTHIA pp collisions at $\sqrt{s} = 7$ TeV.
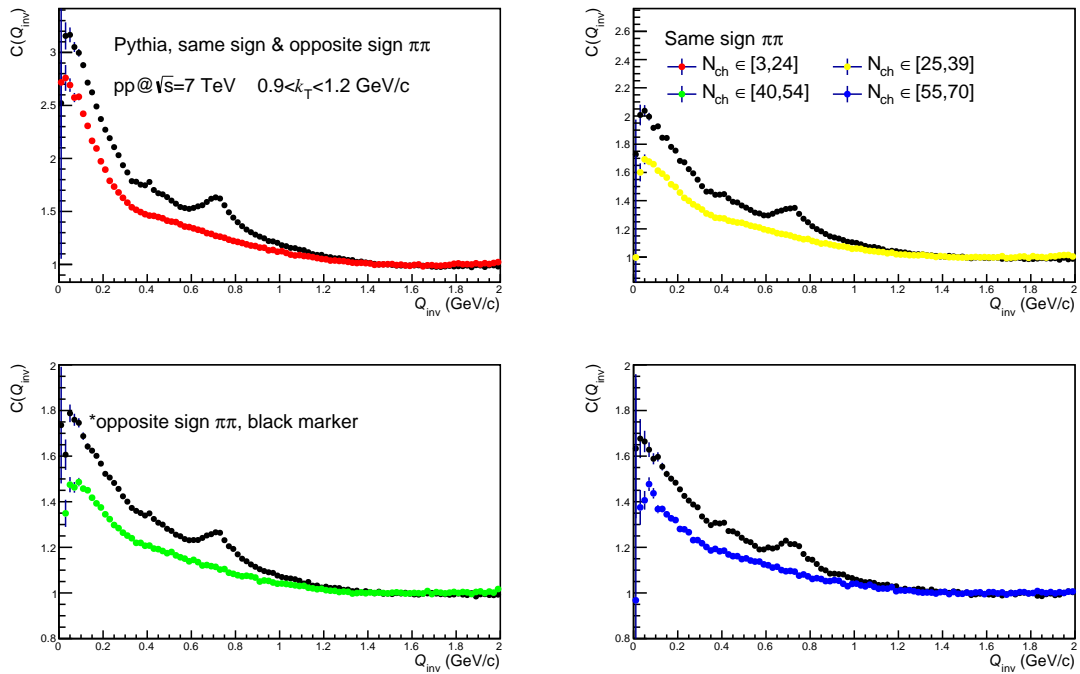
Fig. 9.4 Pion pair correlations for $0.9 < k_\mathrm{T}(\mathrm{GeV}/c) < 1.2$ in PYTHIA pp collisions at $\sqrt{s} = 7$ TeV.
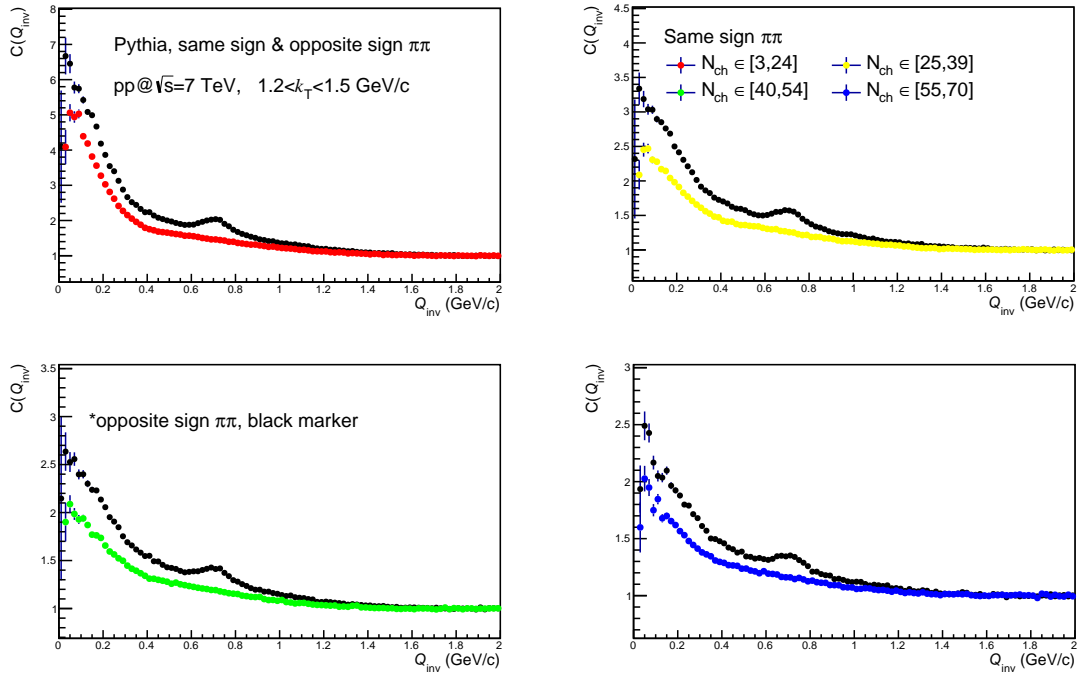
Fig. 9.5 Pion pair correlations for $1.2 < k_{\mathrm{T}}(\mathrm{GeV}/c) < 1.5$ in PYTHIA *pp* collisions at $\sqrt{s} = 7$ TeV.
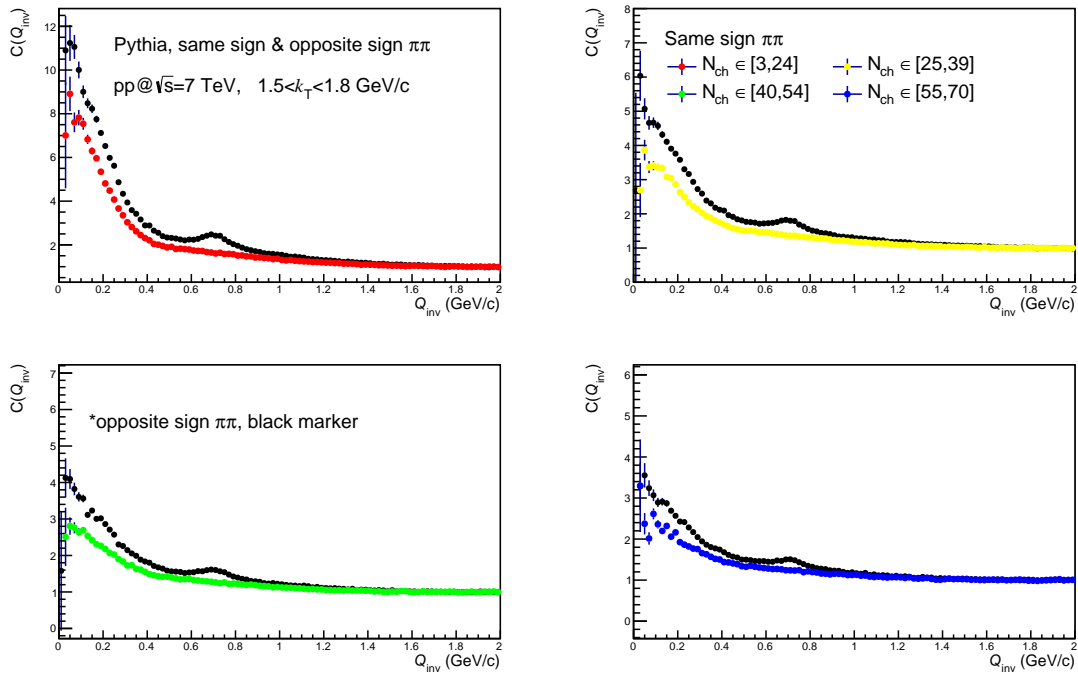
Fig. 9.6 Pion pair correlations for $1.5 < k_{\mathrm{T}}(\mathrm{GeV}/c) < 1.8$ in PYTHIA *pp* collisions at $\sqrt{s} = 7$ TeV.

9.1.2 Jet-like events ($S_T < 0.3$)

Jet-like events are expected to contain large jet collimation contributions to pair correlations in both same-sign and opposite-sign pion pairs.
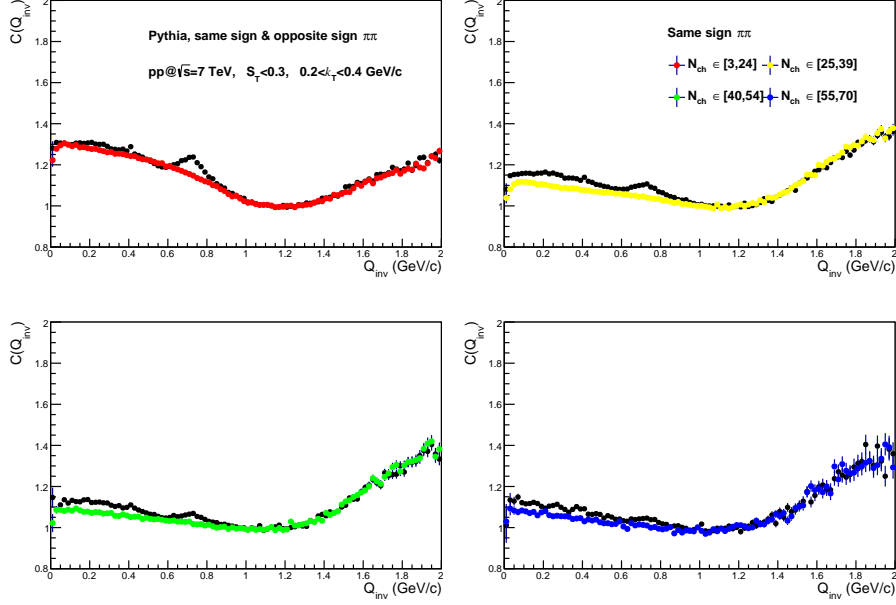
Fig. 9.7 Pion pair correlations in PYTHIA jet-like *pp* collisions at $\sqrt{s} = 7$ TeV for $0.2 < k_T(\text{GeV}/c) < 0.4$.
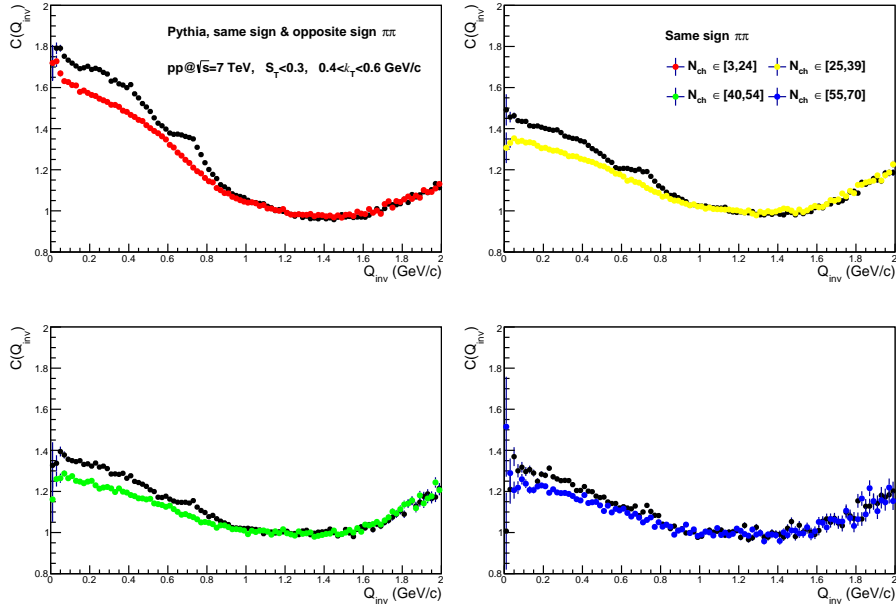
Fig. 9.8 Pion pair correlations in PYTHIA jet-like *pp* collisions at $\sqrt{s} = 7$ TeV for $0.4 < k_T(\text{GeV}/c) < 0.6$.
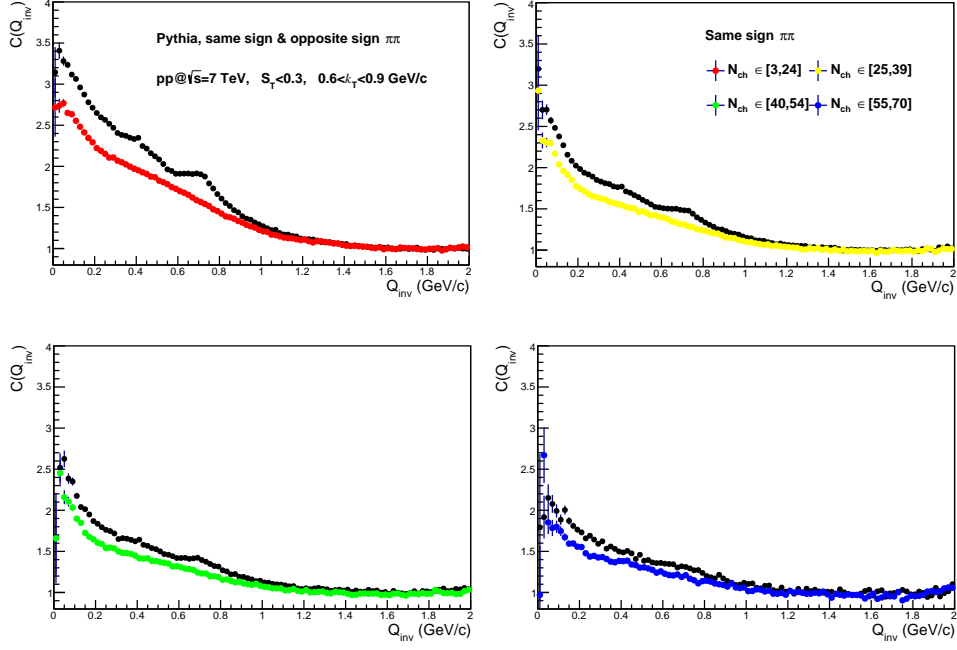
Fig. 9.9 Pion pair correlations in PYTHIA jet-like *pp* collisions at $\sqrt{s} = 7$ TeV for $0.6 < k_{\mathrm{T}}(\mathrm{GeV}/c) < 0.9$.
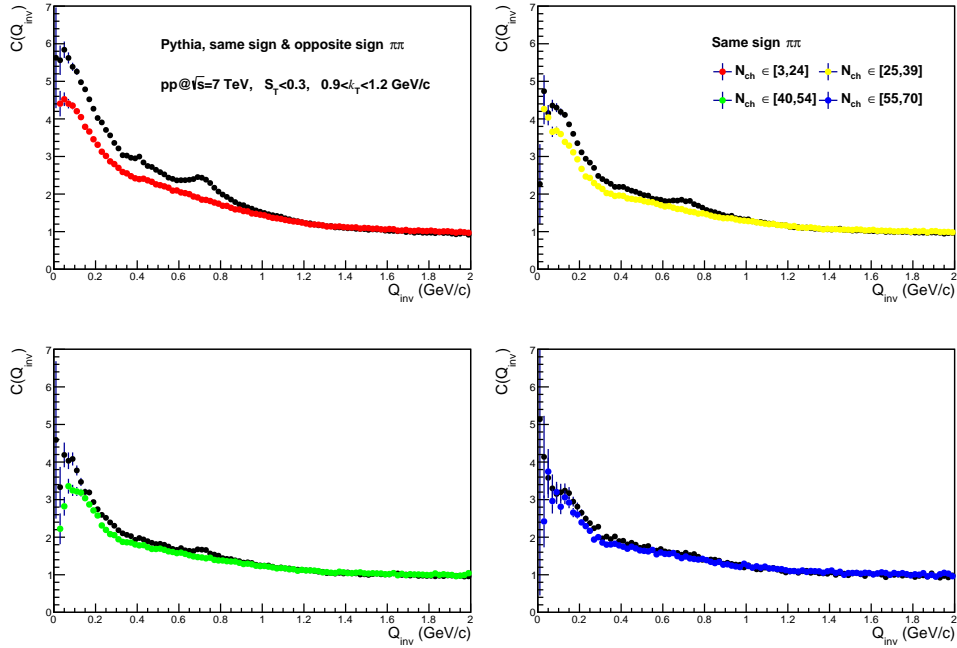
Fig. 9.10 Pion pair correlations in PYTHIA jet-like *pp* collisions at $\sqrt{s} = 7$ TeV for $0.9 < k_{\mathrm{T}}(\mathrm{GeV}/c) < 1.2$

With the rise of pair k_{T}, the jet correlations should rise because same jet pairs have large k_{T}-s and there is no physical constraint for an anticorrelation effect. As it can be seen, low k_{T} pairs have the smallest non-femtoscopic contributions and this is true for both same-sign and
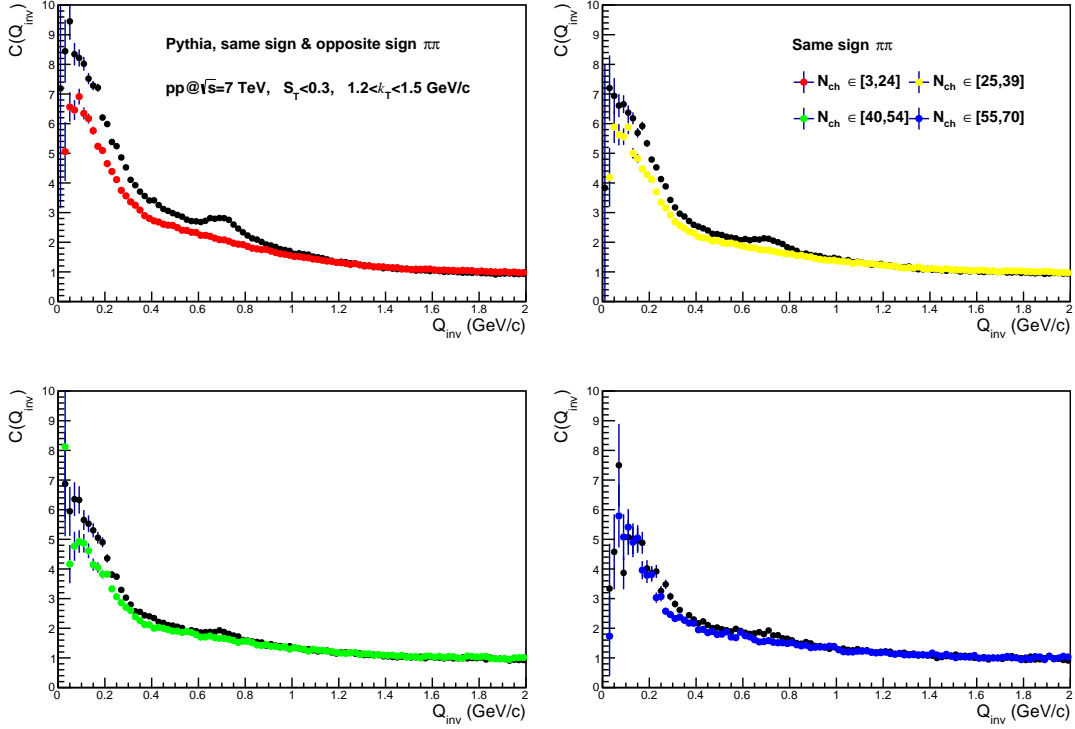
Fig. 9.11 Pion pair correlations in PYTHIA jet-like *pp* collisions at $\sqrt{s} = 7$ TeV for $1.2 < k_{\text{T}}(\text{GeV}/c) < 1.5$

opposite-sign pion pairs. The peaks in the opposite sign pairs are resonances coming from meson decays. If we assume that the pion pairs $\pi^+\pi^-$ are the only decay products then the mass of the decaying meson is calculable from

$$Q_{\text{peak}}^2 = M^2 - 4m_\pi^2. \tag{9.1}$$

where Q_{peak} is the peak position, m_π the pion mass and M the resonance mass. By inserting masses for mesons which are known to have large $\pi^+\pi^-$ branching ratios the peaks are recognized as the $K_{\text{S}} \to \pi^+\pi^-$ and the $\rho_0 \to \pi^+\pi^-$ resonances.

Particle	mass (MeV)	Q_{peak} (MeV)
K_{S}	497.61	411.94
ρ_0	775.49	723.50

There are other two-pion resonances which are harder to spot because of their low amplitude and a three particle resonance $\omega \to \pi^+\pi^-\pi^0$ which will contribute with a wide, low Q_{inv} peak. In all multiplicity bins the correlation trends are the same. This is to be expected if the source of correlations is a constraint which is required of both same-sign and opposite-sign pairs. The differences between same sign and opposite sign correlation functions also decrease with multiplicity, which is consistent with our understanding of the effect as charge conservation.
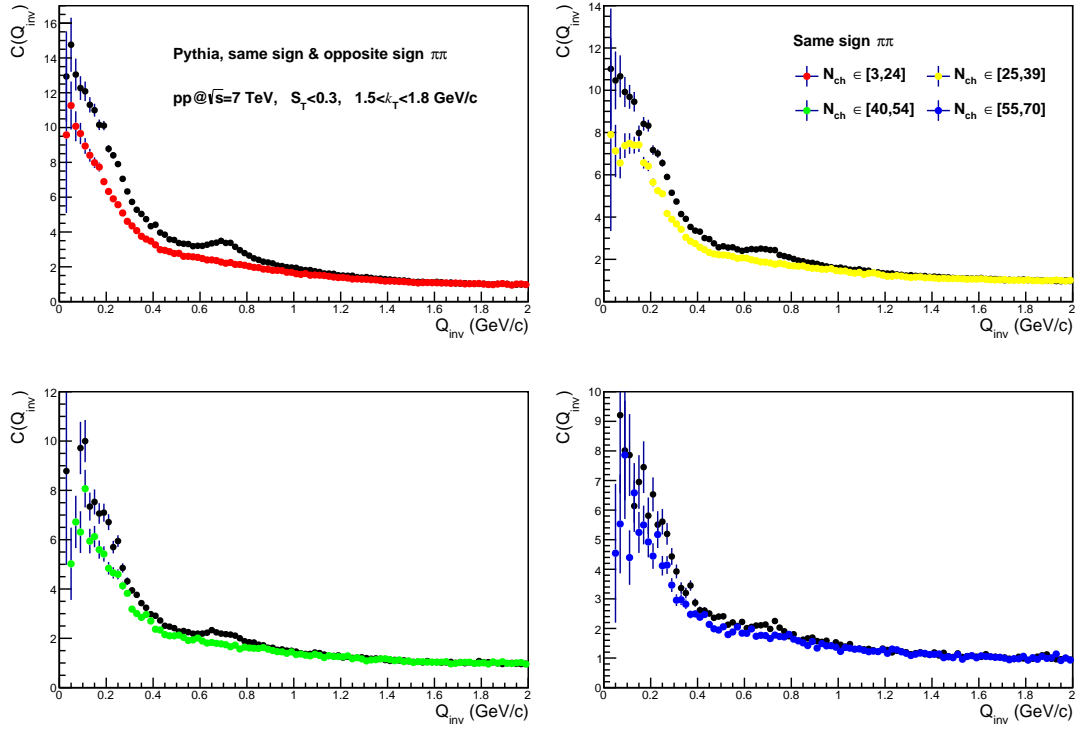
Fig. 9.12 Pion pair correlations in PYTHIA jet-like *pp* collisions at $\sqrt{s} = 7$ TeV for $1.5 < k_{\mathrm{T}}(\mathrm{GeV}/c) < 1.8$

Since the correlations rise with pair k_{T} and the only difference in the general shape and amplitude of pair correlations are contributions from resonances in the opposite-sign analysis, we conclude that measured non-femtoscopic contributions to correlations are dominated by jet collimation.

9.1.3 Spherical events ($S_T > 0.7$)

Spherical events are expected to contain much less non-femtoscopic contributions which are, as was shown, reserved for high k_T jet-like collimation. In spherical events a high pair k_T bin should still have some non-femtoscopic contributions but much less than in minimum bias events. Most of the background signal is removed with a sphericity cut but a drawback from this approach is that it reduces the available statistics. This is still not an issue, since the number of analysed pairs is proportional to the square of multiplicity, so that spherical events, which are usually of higher multiplicity, do not suffer a large reduction in statistics. Main differences are driven by
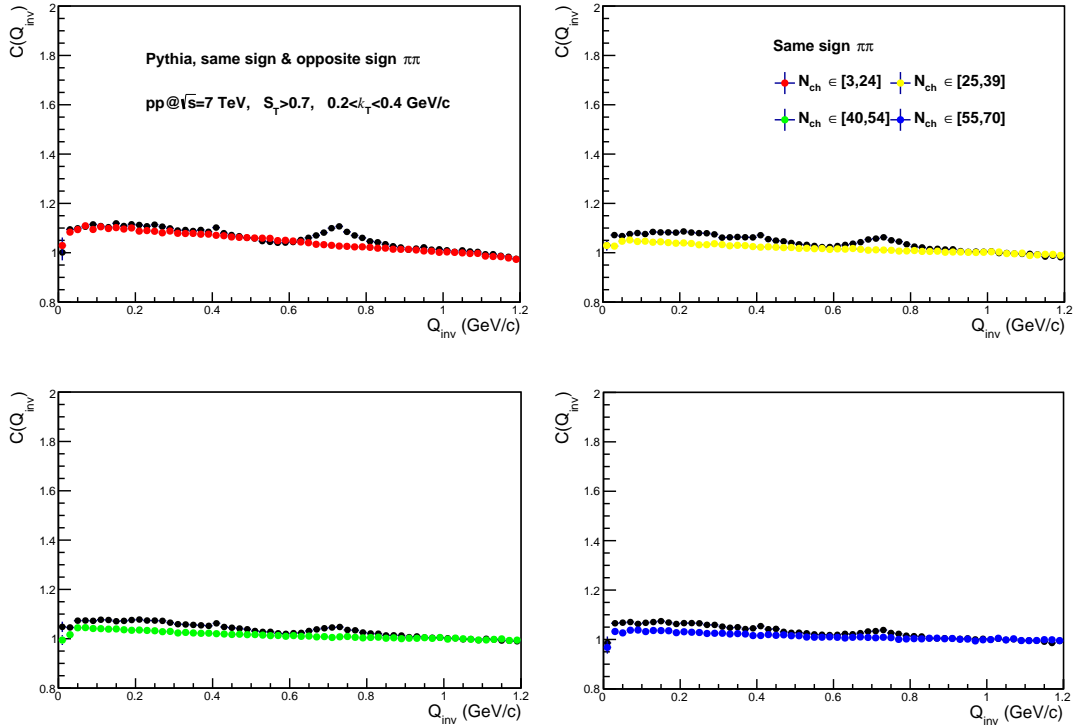
Fig. 9.13 Pion pair correlations in PYTHIA spherical *pp* events at $\sqrt{s} = 7$ TeV for $(0.2 < k_T(\text{GeV}/c) < 0.4)$.

resonances. There are some non-femtoscopic contributions but they are observed in the two highest pair k_T bins. For reference, the minimum bias event femtoscopic analysis only reached $k_T = 0.7$ GeV/c. This shows that with a sphericity cut it is possible to extend the k_T range by at least a factor of two depending on the available statistics.
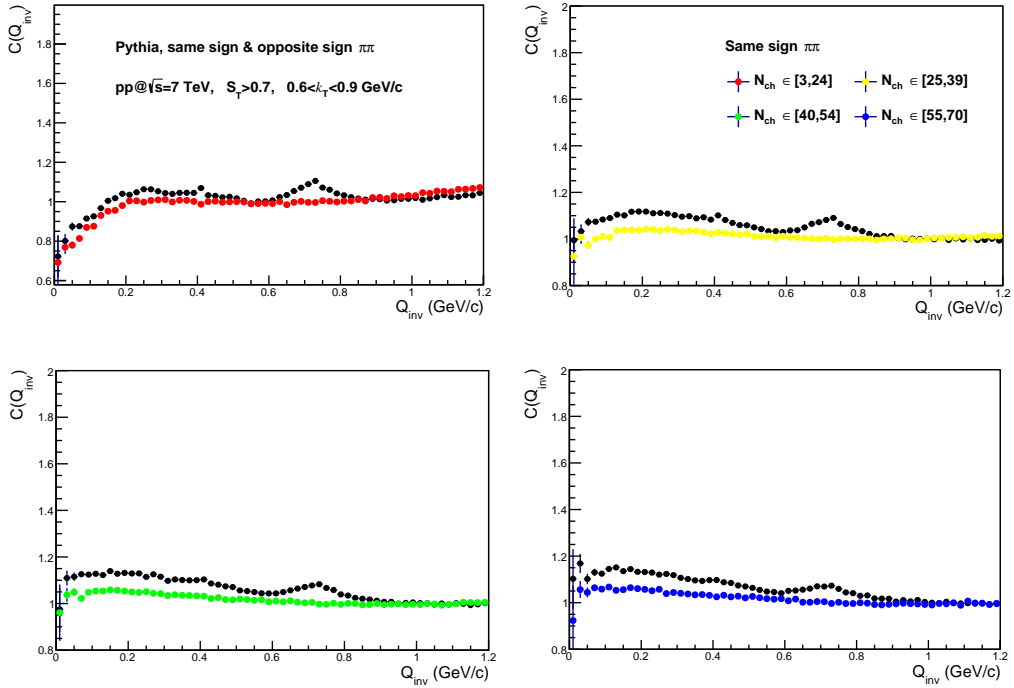
Fig. 9.14 Pion pair correlations in PYTHIA sperical *pp* events at $\sqrt{s} = 7$ TeV for $(0.4 < k_{\mathrm{T}}(\mathrm{GeV}/c) < 0.6)$.

Fig. 9.15 Pion pair correlations in PYTHIA spherical *pp* events at $\sqrt{s} = 7$ TeV for $(0.6 < k_{\mathrm{T}}(\mathrm{GeV}/c) < 0.9)$.
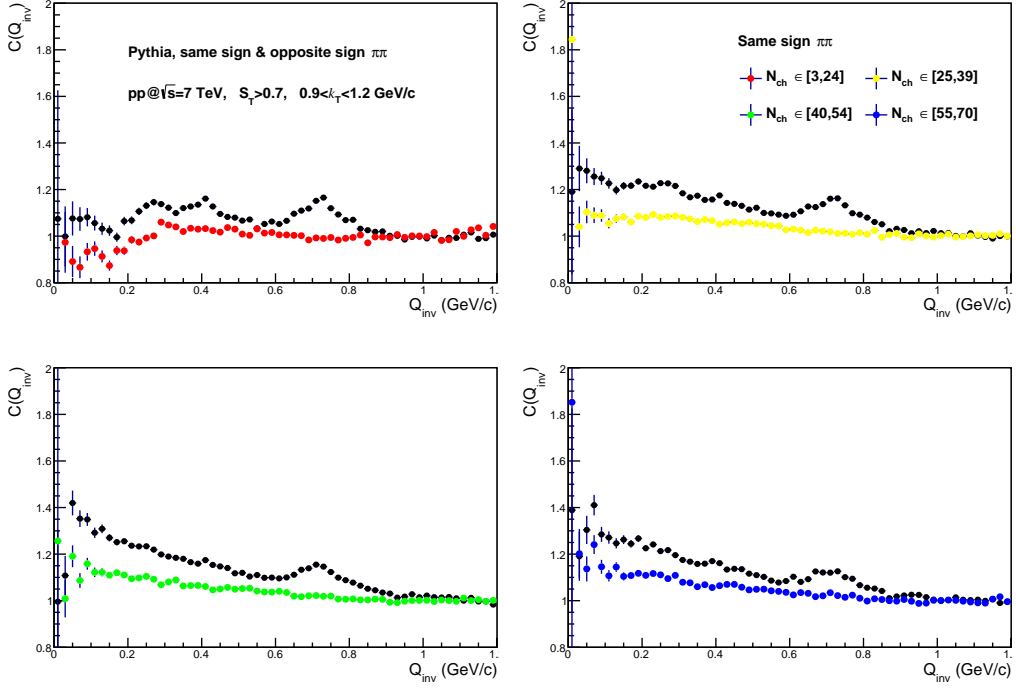
Fig. 9.16 Pion pair correlations in PYTHIA spherical *pp* events at $\sqrt{s} = 7$ TeV for $(0.9 < k_{\text{T}}(\text{GeV}/c) < 1.2)$.
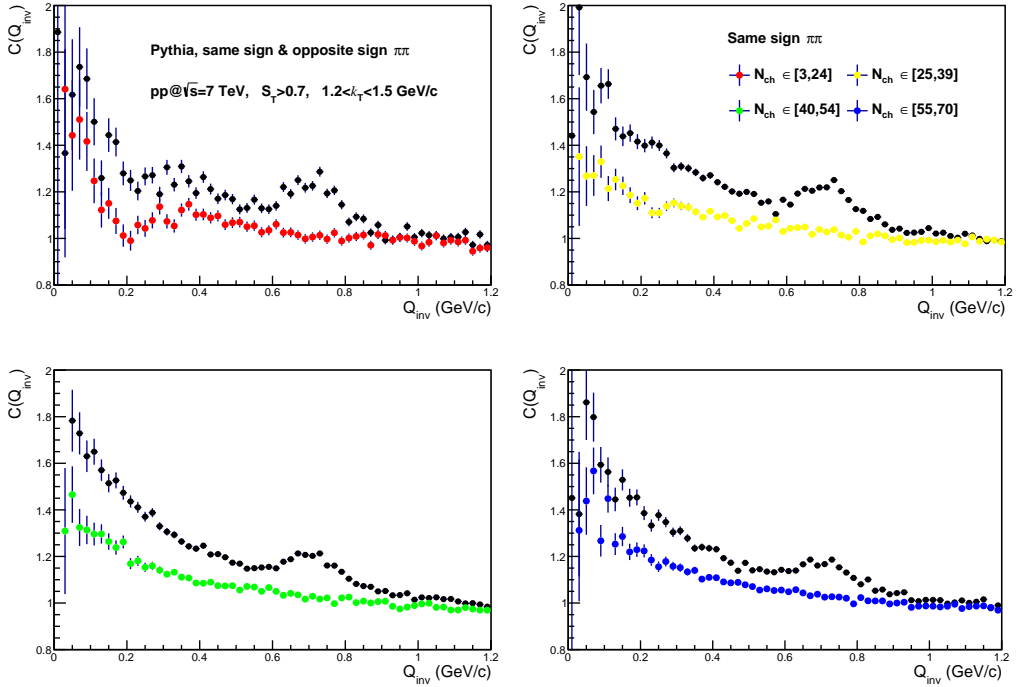
Fig. 9.17 Pion pair correlations in PYTHIA spherical *pp* events at $\sqrt{s} = 7$ TeV for $(1.2 < k_{\text{T}}(\text{GeV}/c) < 1.5)$.

Fig. 9.18 Pion pair correlations in PYTHIA spherical *pp* events at $\sqrt{s} = 7$ TeV for $(1.5 < k_{\mathrm{T}}(\mathrm{GeV}/c) < 1.8)$.

9.2   Comparison of PYTHIA-Perugia0 and PHOJET

In this section we compare two Monte Carlo event generators. The check is to assure that we really understand the source of non-femtoscopic background and are not just introducing model bias.

We expect good agreement between PYTHIA and PHOJET because the jet structure and particularly N_{ch}, p_T and ϕ distributions are well reproduced in both event generators. In spherical events, where there are no jets, the flat correlation around unity should also be reproduced in both event generators and only a deviation in the smallest Q_{inv} is expected because of statistical reasons.

In later chapters we use this comparison as an estimate of the systematic uncertainty on extracted homogeneity radii introduced by possible event generator bias.

Fig. 9.19 $C(Q_{inv})$ for PYTHIA and PHOJET spherical analysis for $(0.2 < k_T(\text{GeV}/c) < 0.4)$.
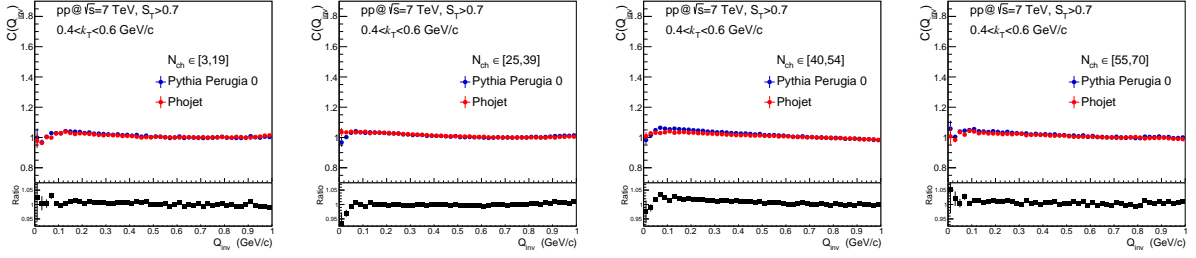
Fig. 9.20 $C(Q_{inv})$ for PYTHIA and PHOJET spherical analysis for $(0.4 < k_T(\text{GeV}/c) < 0.6)$.
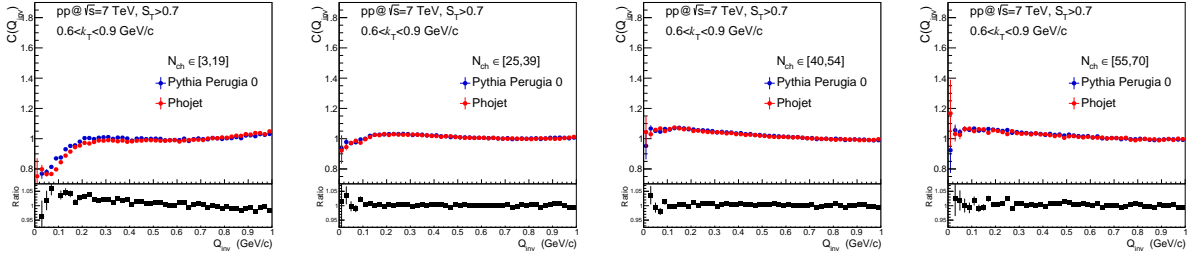
Fig. 9.21 $C(Q_{inv})$ for PYTHIA and PHOJET spherical analysis for $(0.6 < k_T(\text{GeV}/c) < 0.9)$.
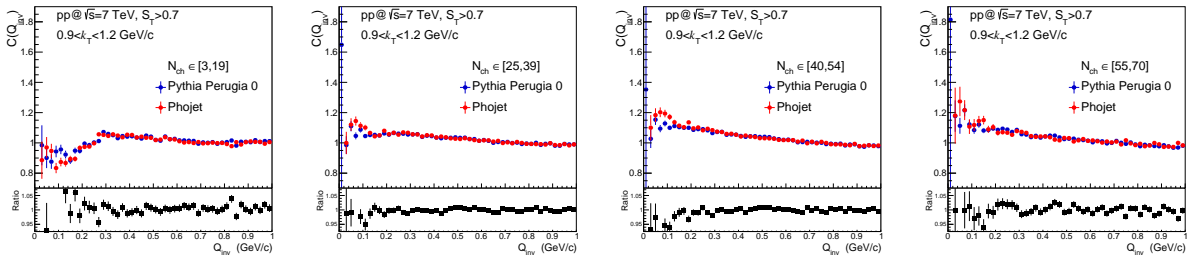
Fig. 9.22 $C(Q_{inv})$ for PYTHIA and PHOJET spherical analysis for $(0.9 < k_T(\text{GeV}/c) < 1.2)$.

Fig. 9.23 $C(Q_{inv})$ for PYTHIA and PHOJET jet-like event analysis for $(0.2 < k_T(\text{GeV}/c) < 0.4)$.
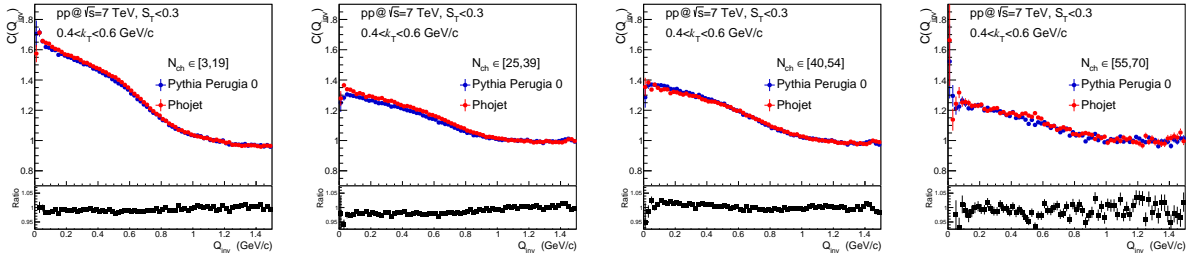
Fig. 9.24 $C(Q_{inv})$ for PYTHIA and PHOJET jet-like event analysis for $(0.4 < k_T(\text{GeV}/c) < 0.6)$.
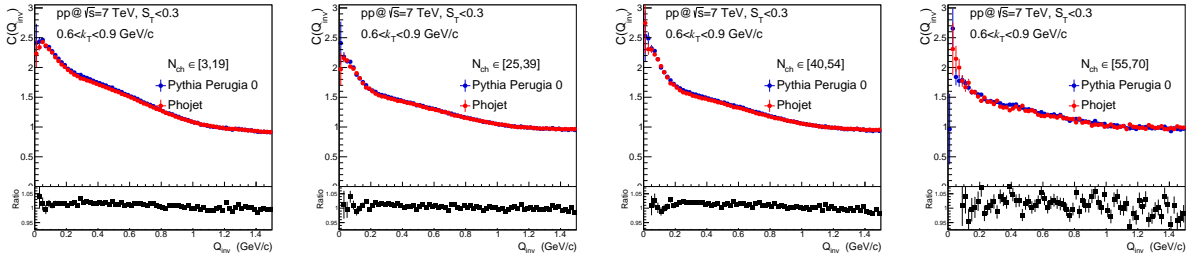
Fig. 9.25 $C(Q_{inv})$ for PYTHIA and PHOJET jet-like event analysis for $(0.6 < k_T(\text{GeV}/c) < 0.9)$.
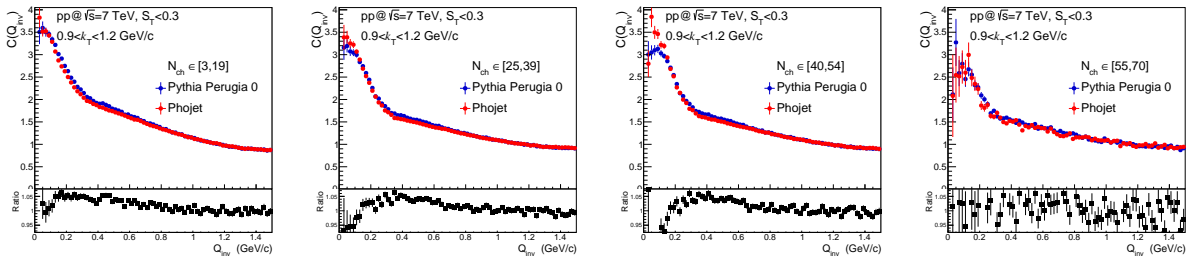
Fig. 9.26 $C(Q_{inv})$ for PYTHIA and PHOJET jet-like event analysis for $(0.9 < k_T(\text{GeV}/c) < 1.2)$.

Chapter 10

Comparison of ALICE data to PYTHIA

Here we present the comparison between correlation functions for jet-like events in measured data and in PYTHIA-Perugia0. These checks are made so as to prove that PYTHIA contains most, if not all, kinematic contributions to two-particle pion correlations in jet-like events, reproduces them accurately and that it can be used as a baseline for a background removal method.

10.1 Spherical events ($S_{\mathrm{T}} > 0.7$)
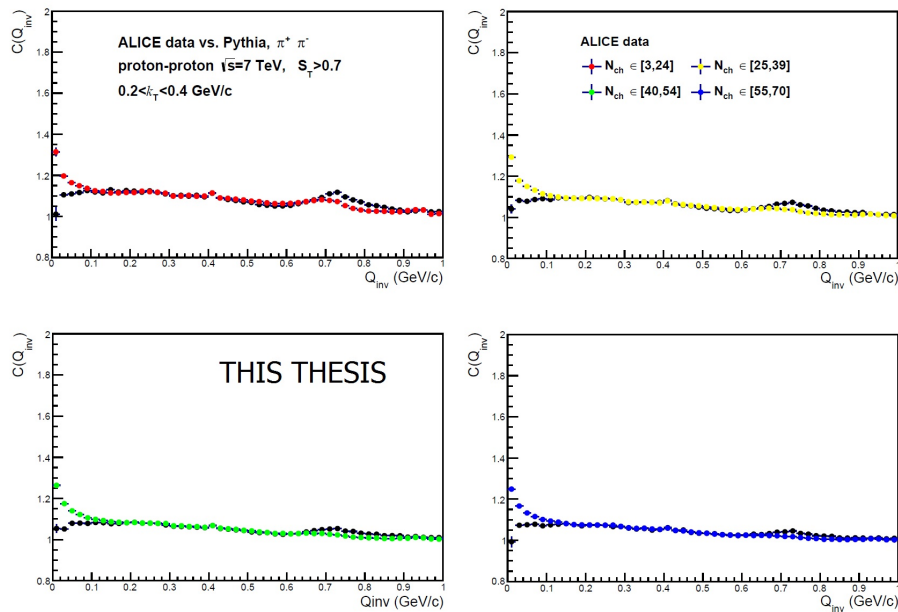
Fig. 10.1 Comparison of ALICE data and PYTHIA for opposite sign pion pair correlations for spherical pp events at $\sqrt{s} = 7$ TeV for $(0.2 < k_{\mathrm{T}}(\mathrm{GeV}/c) < 0.4)$.
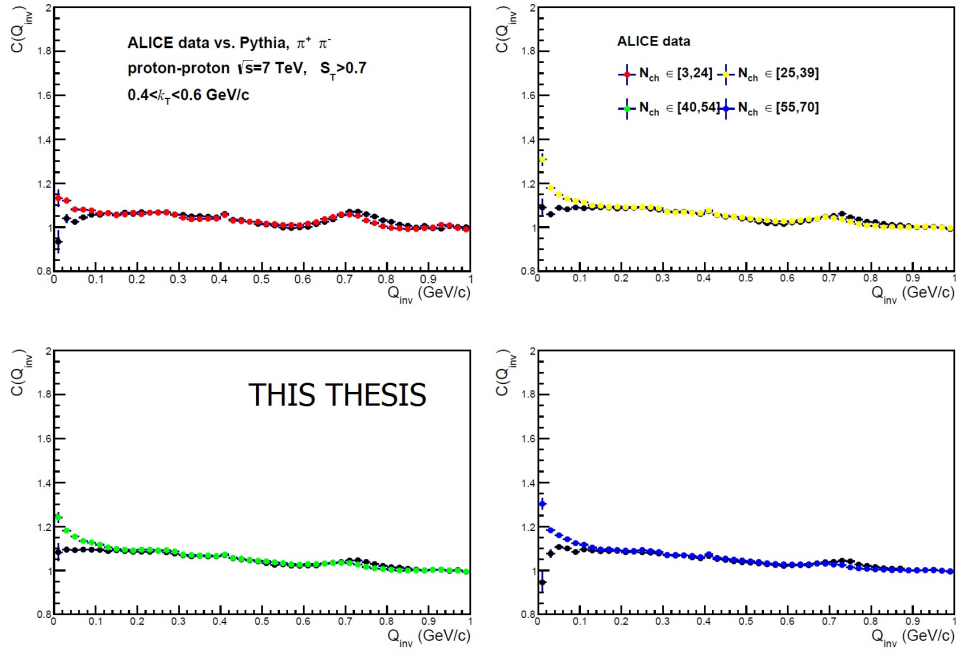
Fig. 10.2 Comparison of ALICE data and PYTHIA for opposite sign pion pair correlations for spherical *pp* events at $\sqrt{s} = 7$ TeV for $(0.4 < k_T(\text{GeV}/c) < 0.6)$.
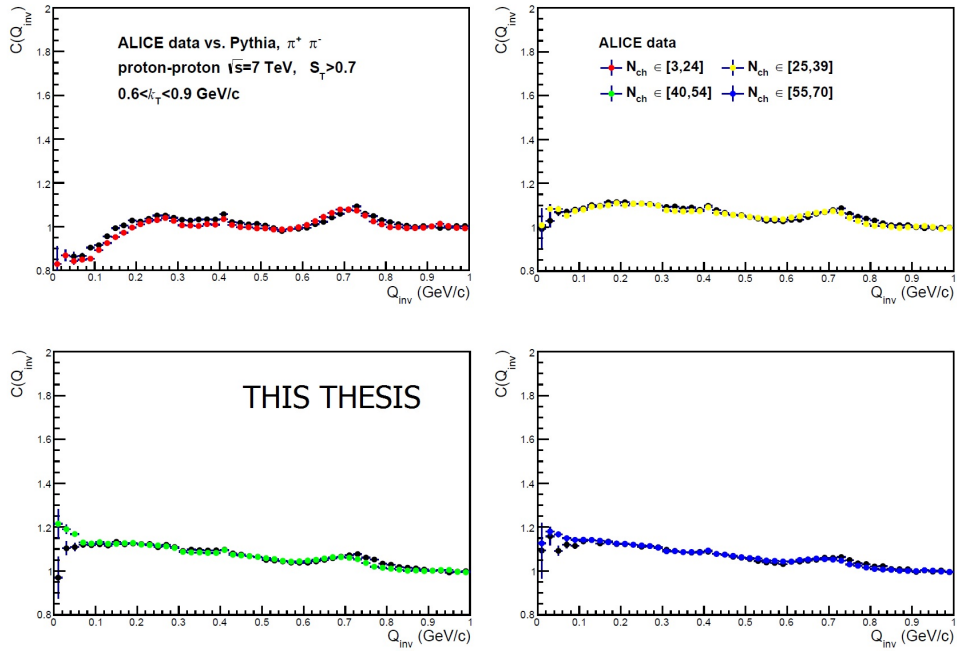
Fig. 10.3 Comparison of ALICE data and PYTHIA for opposite sign pion pair correlations for spherical *pp* events at $\sqrt{s} = 7$ TeV for $(0.6 < k_T(\text{GeV}/c) < 0.9)$.
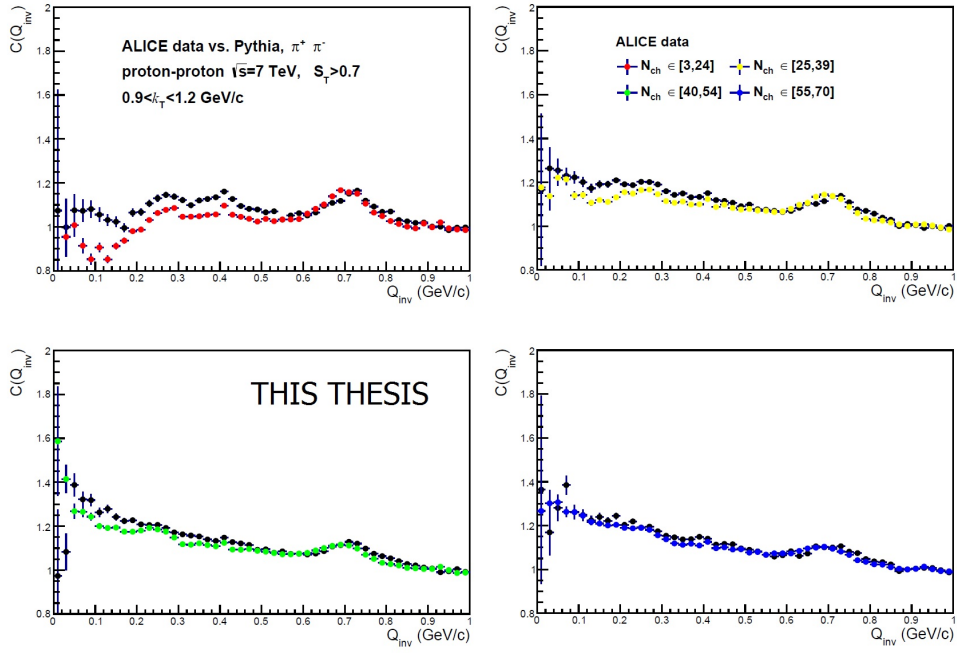
Fig. 10.4 Comparison of ALICE data and PYTHIA for opposite sign pion pair correlations for spherical *pp* events at $\sqrt{s} = 7$ TeV for $(0.9 < k_T(\text{GeV}/c) < 1.2)$.
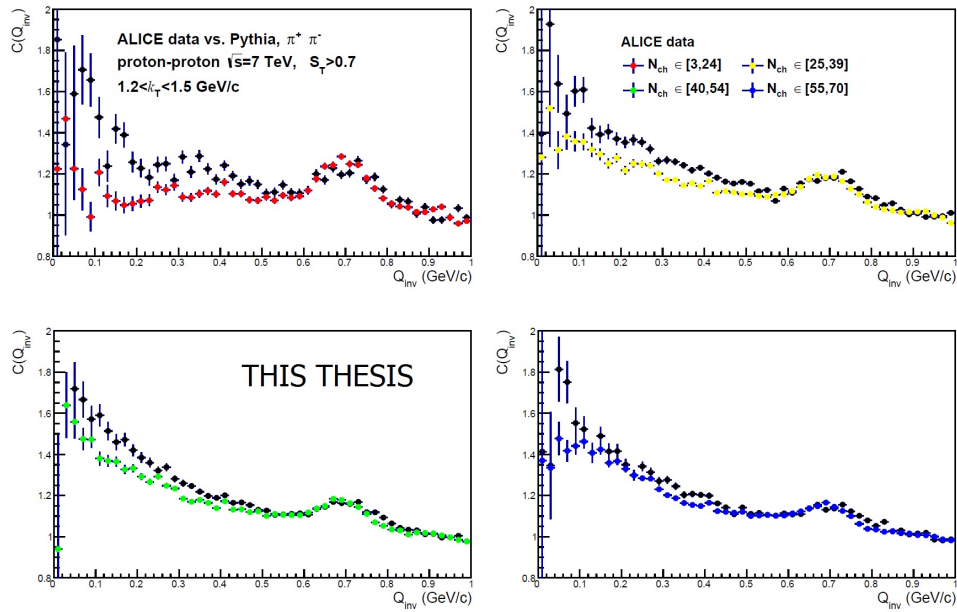
Fig. 10.5 Comparison of ALICE data and PYTHIA for opposite sign pion pair correlations for spherical *pp* events at $\sqrt{s} = 7$ TeV for $(1.2 < k_T(\text{GeV}/c) < 1.5)$.
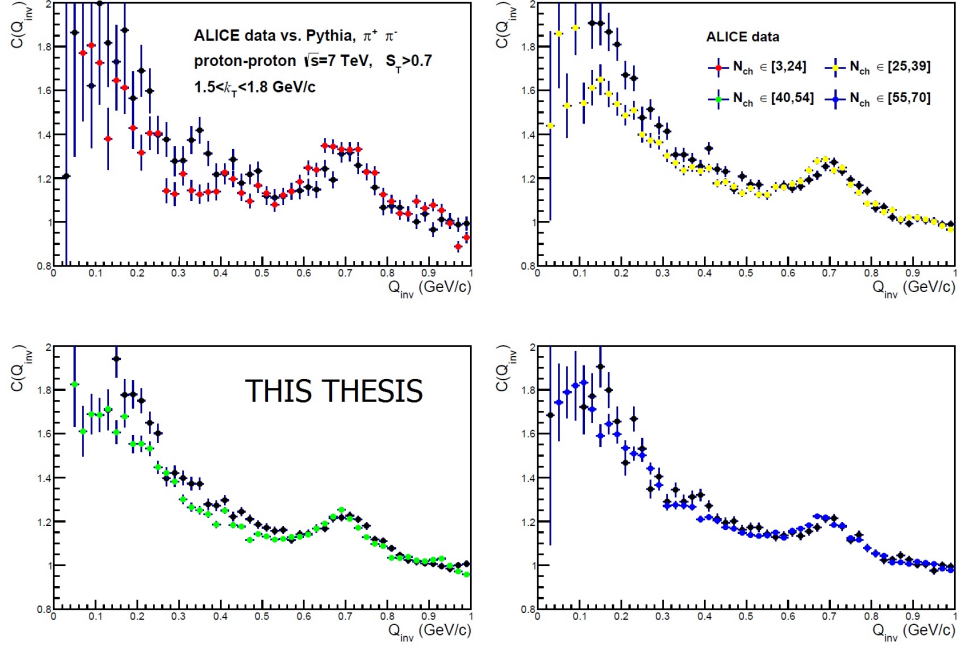
Fig. 10.6 Comparison of ALICE data and PYTHIA for opposite sign pion pair correlations for spherical *pp* events at $\sqrt{s} = 7$ TeV for $(1.5 < k_{\mathrm{T}}(\mathrm{GeV}/c) < 1.8)$.

As it was expected, the spherical events opposite sign pion correlations strongly agree between generator and experiment. This is because they carry only the basic particle information like the angular and momentum distributions which should be well described in any reasonable generator. For the lowest Q bins, measured data shows a rise due to Coulomb effects which are not present in the generator. Positions of resonances and their relative amplitudes also agree between generator and experiment reassuring us that the generator is reproducing all the relevant physics conditions needed for a successful usage as a background description. In the case of jet-like events, again generators should be well equipped to describe the physics needed in our analysis. The amplitudes will be higher for both resonance and k_{T} dependent correlations and the difference induced by Coulomb should be present.

10.2   Jet-like events ($S_T < 0.3$)

It is expected that low k_T pairs show the lowest non-femtoscopic contributions in PYTHIA. This is consistent with our observations from ALICE data and published papers. In earlier sections it was explained that in jet-like events low k_T pairs are mostly opposite jet pairs with high Q_{inv} and this should not create high background in the relevant HBT area ($Q_{inv} < 0.5$ GeV/c). Here we show that in higher k_T -s the apparent non-femtoscopic correlations are extremely high and well behaved. One could fit them with a polynomial and try to use in a fitting procedure but this approach is not without drawback. A "bad choice" of fit function could produce large deviations for fitted radii. Also, if a background function with a large number of parameters is chosen, there is an inherent risk of fitting a part of Bose-Einstein correlations into the background function.
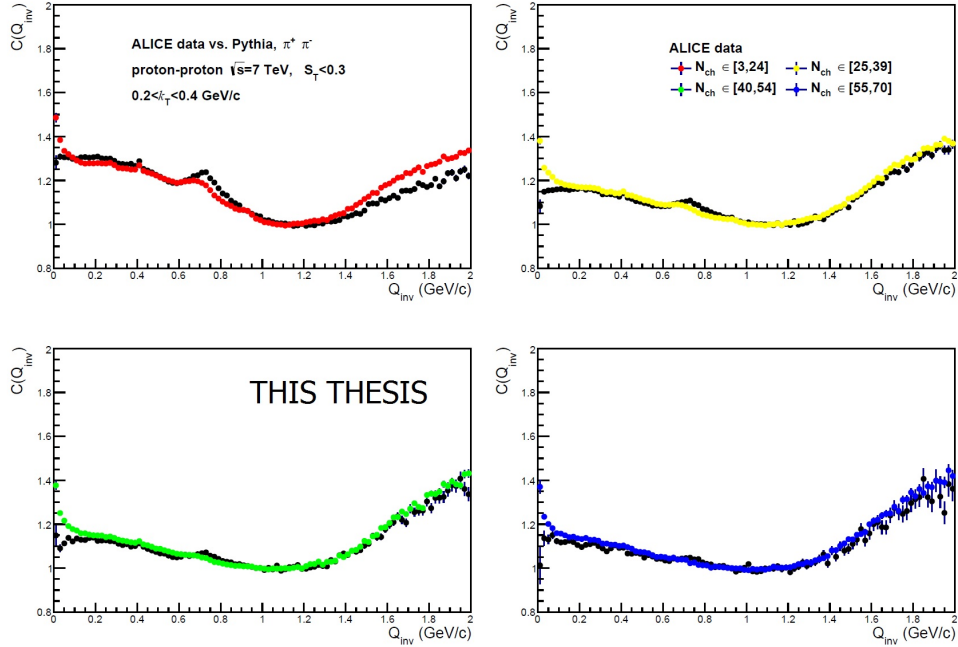
Fig. 10.7 Comparison of ALICE data and PYTHIA for opposite sign pion pair correlations for jet-like *pp* events at $\sqrt{s} = 7$ TeV for $(0.2 < k_T(\text{GeV}/c) < 0.4)$.
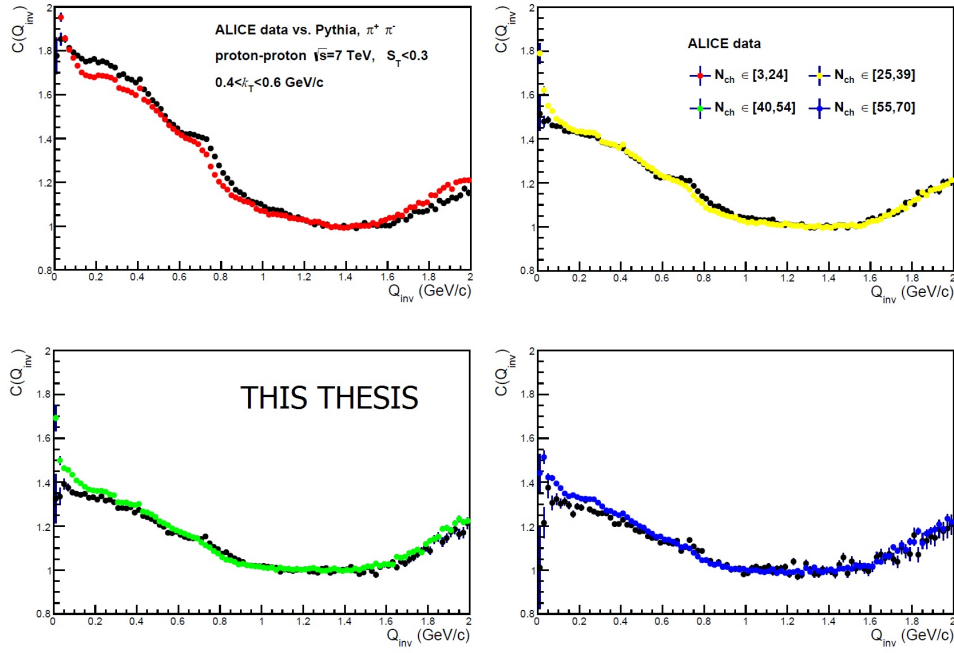
Fig. 10.8 Comparison of ALICE data and PYTHIA for opposite sign pion pair correlations for jet-like *pp* events at $\sqrt{s} = 7$ TeV for $(0.4 < k_T(\text{GeV}/c) < 0.6)$.
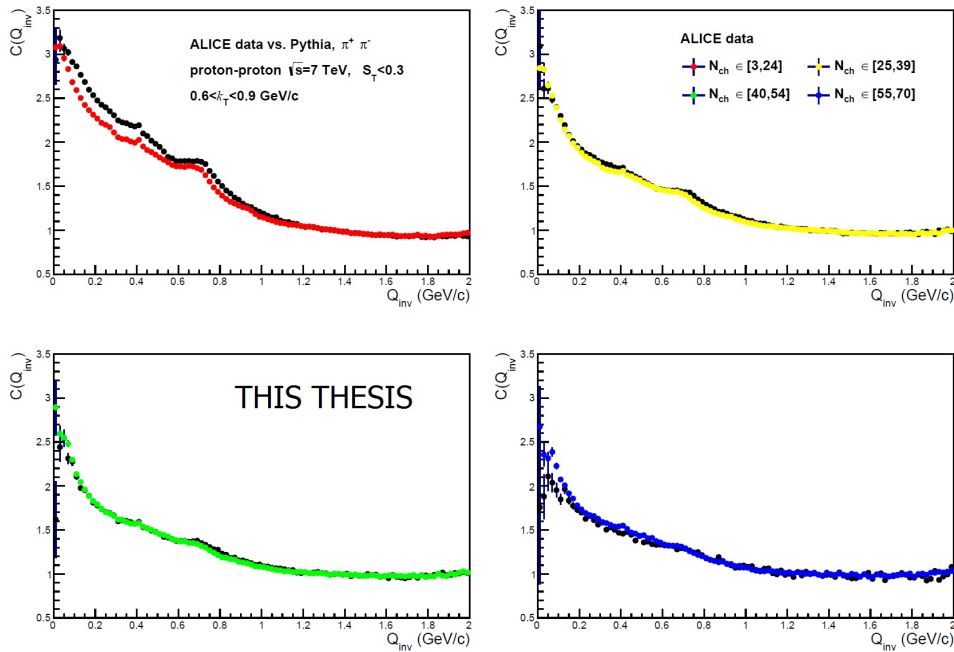
Fig. 10.9 Comparison of ALICE data and PYTHIA for opposite sign pion pair correlations for jet-like *pp* events at $\sqrt{s} = 7$ TeV for $(0.6 < k_T(\text{GeV}/c) < 0.9)$.
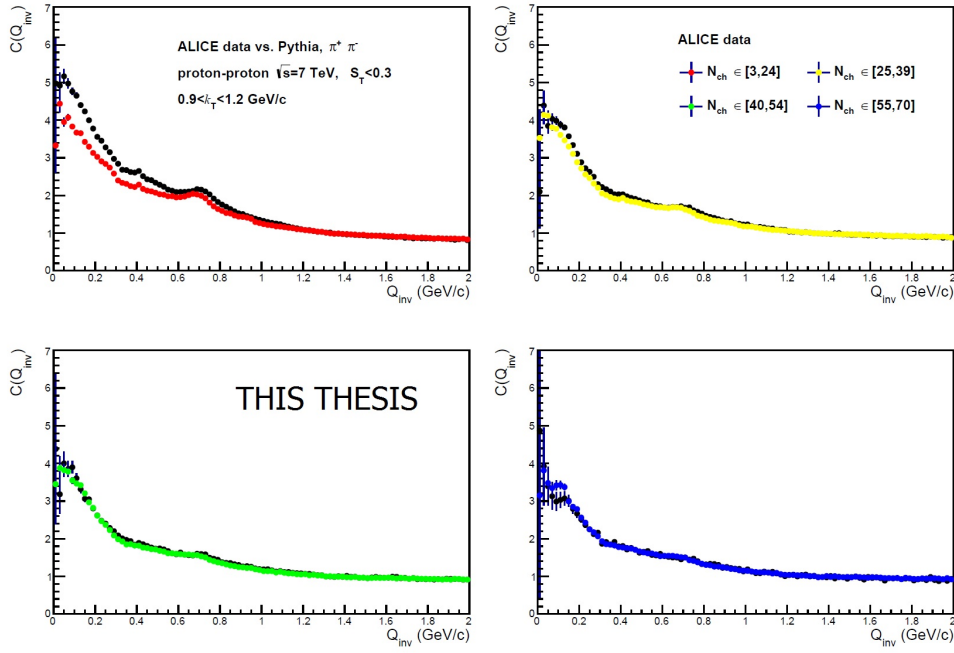
Fig. 10.10 Comparison of ALICE data and PYTHIA for opposite sign pion pair correlations for jet-like *pp* events at $\sqrt{s} = 7$ TeV for $(0.9 < k_{\text{T}}(\text{GeV}/c) < 1.2)$.
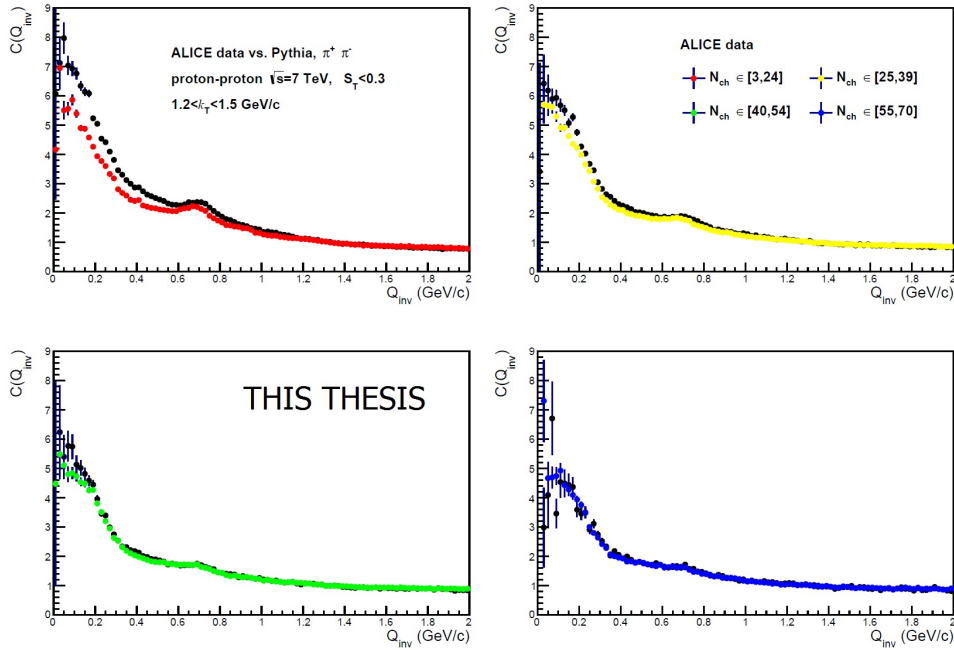
Fig. 10.11 Comparison of ALICE data and PYTHIA for opposite sign pion pair correlations for jet-like *pp* events at $\sqrt{s} = 7$ TeV for $(1.2 < k_{\text{T}}(\text{GeV}/c) < 1.5)$.
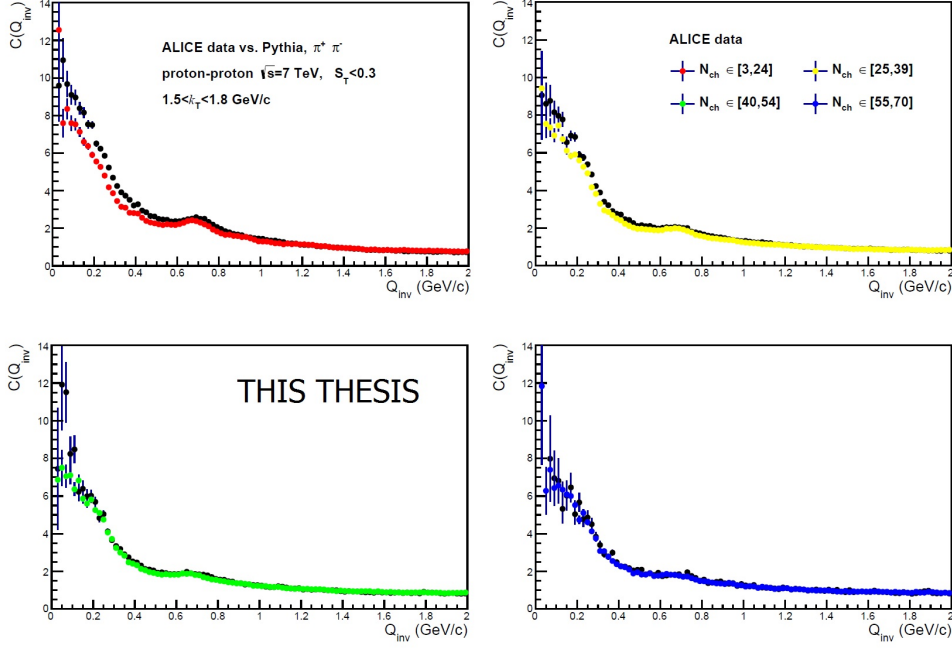
Fig. 10.12 Comparison of ALICE data and PYTHIA for opposite sign pion pair correlations for jet-like *pp* events at $\sqrt{s} = 7$ TeV for $(1.5 < k_{\mathrm{T}}(\text{GeV}/c) < 1.8)$.

10.3 Background suppression

There are various approaches used to control non-femtoscopic correlations. A good option is parametrization of the background signal with a known analytic function. This could be used, but with some difficulty, since there is no theoretical derivation of the background signal and one is forced to choose an appropriate "guessed" function. Event generator data suggests the background resembles a Gaussian and this is the approach which is most often used.

An alternative explored in this thesis is to directly divide measured ALICE and PYTHIA distributions. Both correlation functions can be created from probability distributions:

$$Q_{\text{data}}(\mathbf{q}) \;=\; Q_{\text{data}}(\mathbf{p}_1 - \mathbf{p}_2) = \frac{P_{\text{data}}(\mathbf{q})}{P(\mathbf{p}_1)P(\mathbf{p}_2)} \approx \frac{P(HBT) \cdot P(\text{kinematic}) \cdot P(O^2)}{P(\mathbf{p}_1)P(\mathbf{p}_2)} \qquad (10.1)$$

$$Q_{\text{sim.}}(\mathbf{q}) \;=\; Q_{\text{sim.}}(\mathbf{p}_1 - \mathbf{p}_2) = \frac{P_{\text{sim.}}(\mathbf{q})}{P(\mathbf{p}_1)P(\mathbf{p}_2)} \approx \frac{P(\text{kinematic}) \cdot P_{\text{sim.}}(O^2)}{P(\mathbf{p}_1)P(\mathbf{p}_2)}, \qquad (10.2)$$

where $P(\mathbf{p})$ is the one-particle momentum distribution, $P(\mathbf{p}_1 - \mathbf{p}_2)$ two-particle relative momentum distribution and $P(O^2)$ additional distributions from other possible physics effects. Here it was assumed that the simulated data were tuned to contain $P(\mathbf{p})$ spectra identical to measured data, but it was not assumed that the simulated data contains all other possible physics constrains and thus we differentiate between $P(O^2)$, which represents known or unknown true physics constrains and $P_{\text{sim.}}(O^2)$, which carries possible Monte Carlo biases. Both of these distributions,

$P(O^2)$ and $P_{\text{sim.}}(O^2)$, are taken to be close to unity and should play no role in this analysis.

$$\frac{Q_{\text{data}}(\mathbf{q})}{Q_{\text{sim.}}(\mathbf{q})} \equiv C_{\text{corr.}}(\mathbf{q}) \tag{10.3}$$

Ratio of $Q_{\text{data}}(\mathbf{q})$ and $Q_{\text{sim.}}(\mathbf{q})$ is a new Monte Carlo corrected correlation function which does not contain jet collimation (non-femtoscopic) correlations and is more susceptible to a fitting procedure without a background function. Such an approach was already tested by others in pion femtoscopy [54]. Benefits form this approach are numerous. First, all the amplitudes are well
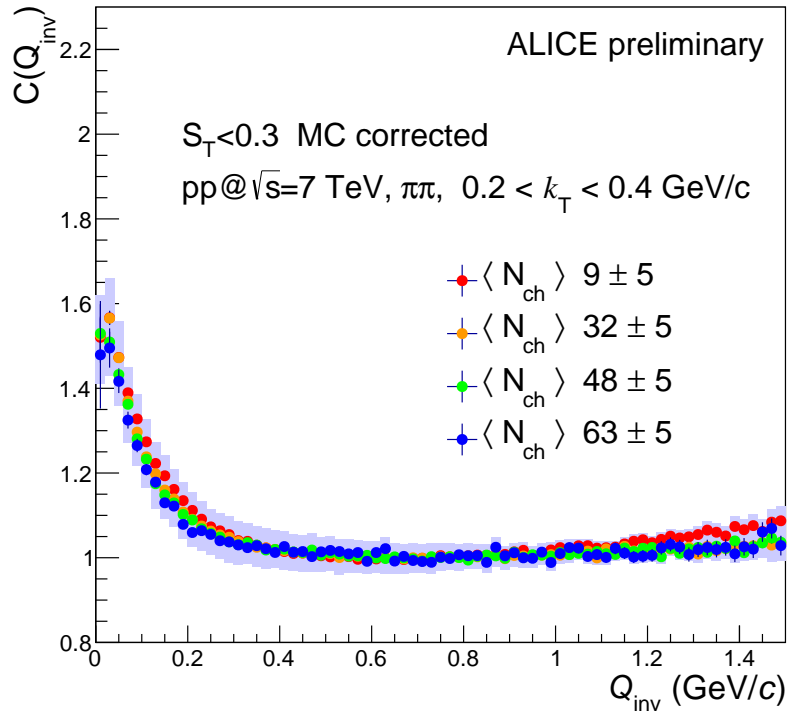
Fig. 10.13 Pythia corrected correlation function for identical pions in jet-like *pp* collisions at $\sqrt{s} = 7$ TeV for $(0.2 < k_{\text{T}}(\text{GeV}/c) < 0.4)$

behaved and take physicaly sound values. Following this, the background is in agreement with opposite sign correlations which means that there is no obvious assumption made on the part of the generators which is not consistent with experimental data. Thirdly, since generators do not contain Coulomb effects this part of correlation stays in the final function allowing standard fit functions to be used.
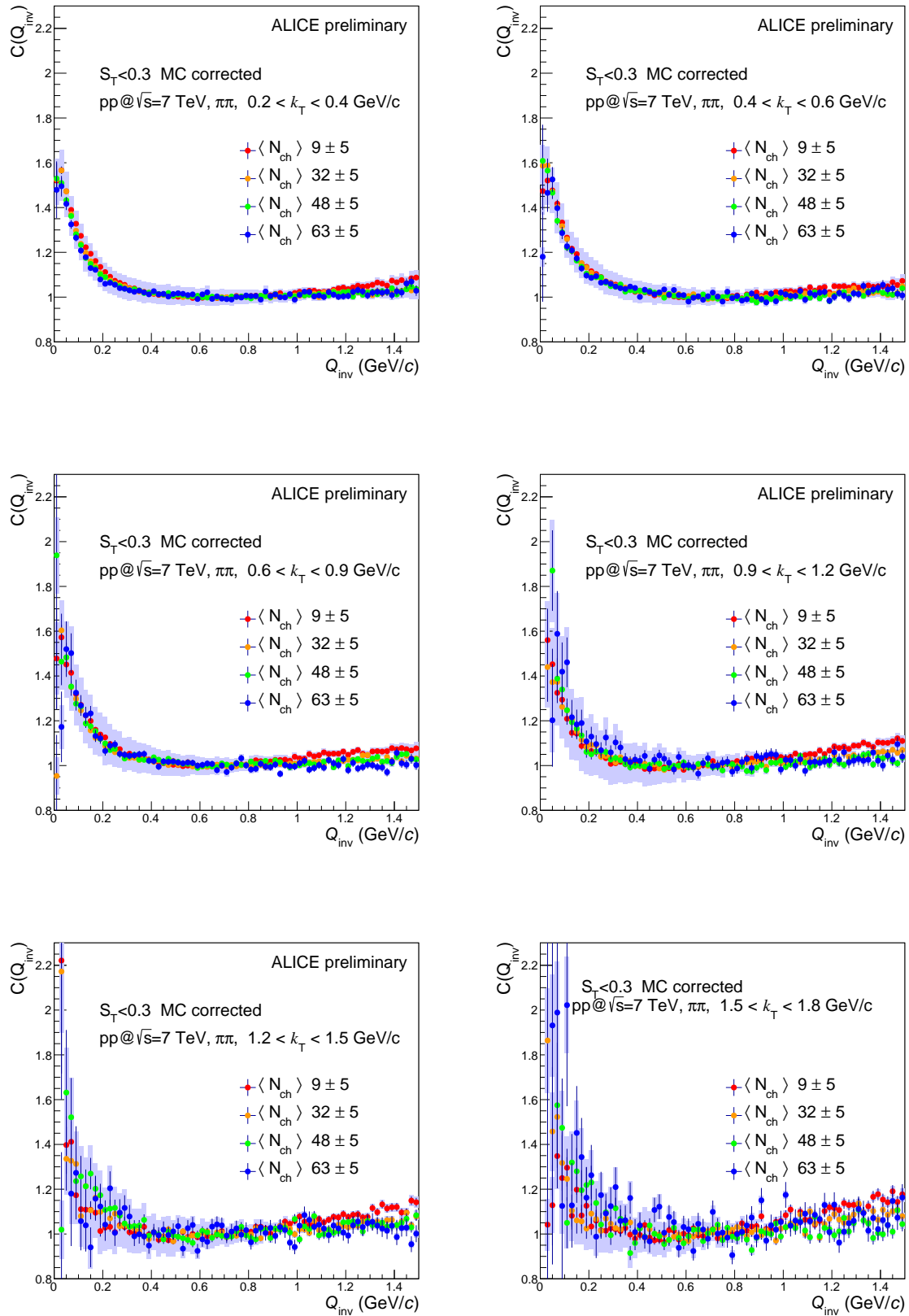
Fig. 10.14 Pythia corrected correlation functions for identical pions in jet-like *pp* collisions at $\sqrt{s} = 7$ TeV for various k_T bins.

Correlations at low k_T show almost no change due to flat Pythia correlation shown in the previous section. Corrected correlation functions are well described with the exponential function. Other fit functions have also been used, specifically the Gaussian which is a natural starting point, especially with low statistics. For higher k_T-s the signal-to-background ratio is greatly enhanced and the correlations resemble those measured in spherical events. At this point a fitting function has to be chosen. We chose a simple exponential function and fit the corrected correlations in the same manner as before

$$C_{HBT,jet}(Q_{inv}) = 1 + \lambda' \, exp(-Q_{inv}R_{HBT,jet}) \tag{10.4}$$

because the intercept amplitudes, which measure the chaoticity parameter, are within theoretical boundaries and there is no *a priori* reason to use any other fit function. In our case, the abundance of statistics is slightly decreased, but allows for a reasonable homogeneity radius fit. It is now a matter of interpretation what the extracted homogeneity radii will mean. If one is to take a simple picture of a jet hadronizing as the leading parton sheds energy while transversing a QCD vacuum, than for high k_T-s the extracted HBT radii might carry information on hadronization lengths. On the other hand, a low k_T where the pair is mostly not in the same jet, the extracted HBT radii should measure the length before hadronization. We will consider the interpretation of fit results in later chapters.

Chapter 11

Systematic effects

We test various sources of systematic effects to final fit results of the HBT radii. From previous analysis it is known that the full systematic effects to fitted radii can go, depending on the multiplicity and k_T bin, up to 20%.

Estimation of the systematical uncertainty does not have a prescribed procedure. It should contain contributions from all reasonable sources of uncertainty. Standardly checked sources of systematic uncertainty are the physical cuts used in the analysis. These checks follow from the natural inclination of the experimentalist to question the absolute precision of the measurement. This approach makes the overall physics statement stronger because it can be shown to be valid even with the additional assumption of error.

11.1 Sources of systematic uncertainty

In our analysis we recognize possible systematic uncertainty coming from event and track cuts, momentum resolution, particle identification, reconstruction procedure and overall detector quality.

11.1.1 $\pi^+\pi^+$ and $\pi^-\pi^-$ comparison

Differences in (+) and (-) analysis suggests there could be some minor effects that should be checked. Since we are using only big multiplicity bins we estimate the total contribution to systematic uncertainty to be less than 1%.

11.1.2 Track cut variation

We can use the ITS, TPC and TOF detectors for PID. If the ITS is excluded a small deviation is expected in the low Q_{inv} region (< 100 MeV) coming from track merging effects. We estimate the total influence to systematic uncertainty to be a few percent.

11.1.3   Sphericity cut variation

Sphericity cuts vary the data set which is observed. We chose to vary the sphericity cut by 0.05 on both sides and estimate a total contribution of about 2-3%.

11.1.4   Run periods

In this analysis we used LHC10c,d and e data sets. From previous studies minor contributions to systematics are expected, less than 1%.

11.1.5   Magnetic field orientation

During data taking, the ALICE detector has used both possible orientations of its magnetic field. We do not expect any contributions to systematic uncertainty. This is in agreement with data.

11.1.6   Variation of the number of mixed events

Since in this analysis we use big multiplicity bins, the total contribution to systematics originating from variation of the number of mixed events is expected to be negligible.

11.1.7   Momentum resolution

In our analysis we use a bin width of 20 MeV/c which insures us that contributions to systematic uncertainty coming from momentum resolution are negligible.

In the following pages we show full systematic checks. Compared distributions are plotted with their ratio. When estimating their contributions to extracted radii, we separately fit and compare to the baseline results. The final uncertainty is shown with symmetric error boxes.
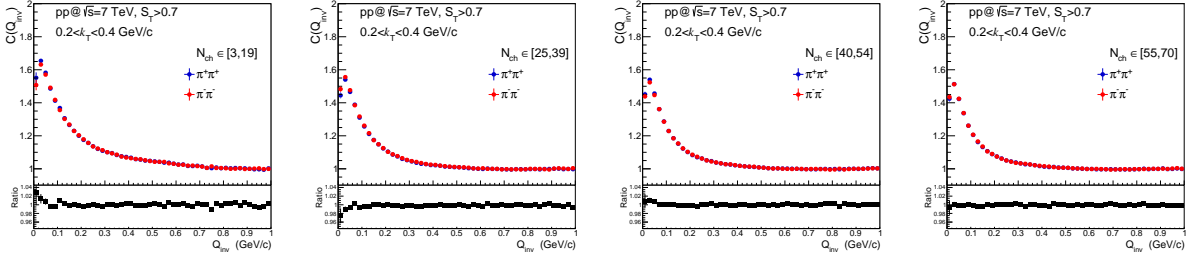
Fig. 11.1 $C(Q_{inv})$ for $\pi^+\pi^+$ and $\pi^-\pi^-$ in spherical analysis for $(0.2 < k_{\mathrm{T}}(\mathrm{GeV}/c) < 0.4)$.
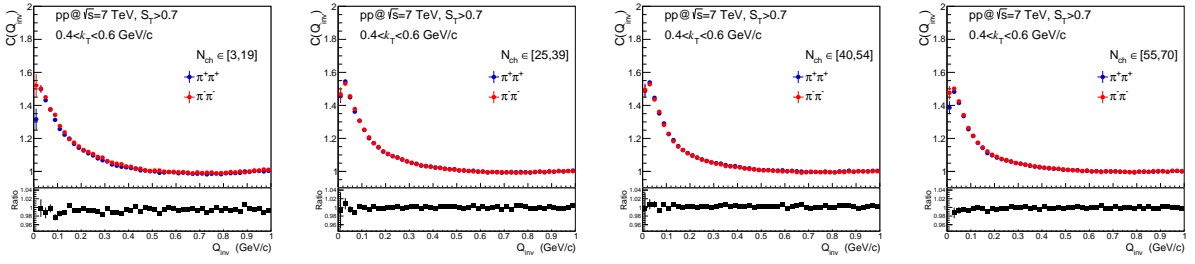
Fig. 11.2 $C(Q_{inv})$ for $\pi^+\pi^+$ and $\pi^-\pi^-$ in spherical analysis for $(0.4 < k_{\mathrm{T}}(\mathrm{GeV}/c) < 0.6)$.
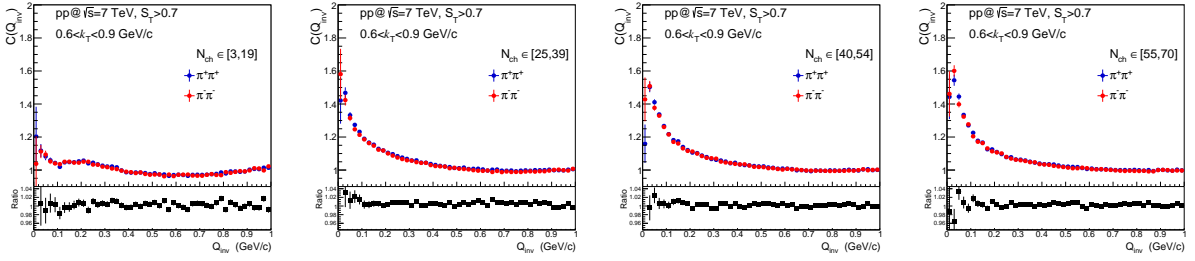
Fig. 11.3 $C(Q_{inv})$ for $\pi^+\pi^+$ and $\pi^-\pi^-$ in spherical analysis for $(0.6 < k_{\mathrm{T}}(\mathrm{GeV}/c) < 0.9)$.
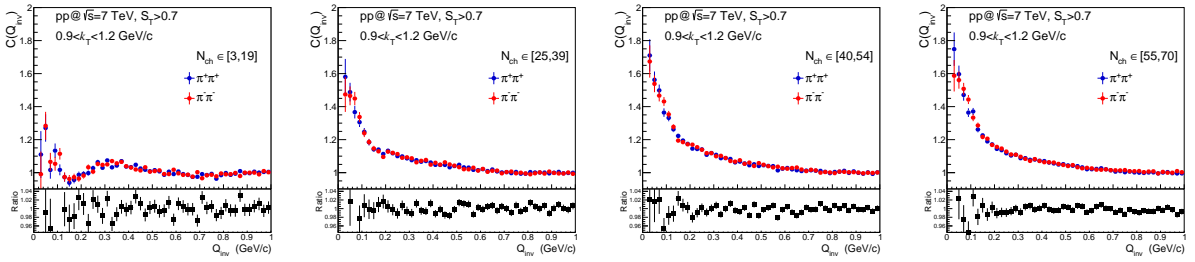
Fig. 11.4 $C(Q_{inv})$ for $\pi^+\pi^+$ and $\pi^-\pi^-$ in spherical analysis for $(0.9 < k_{\mathrm{T}}(\mathrm{GeV}/c) < 1.2)$.
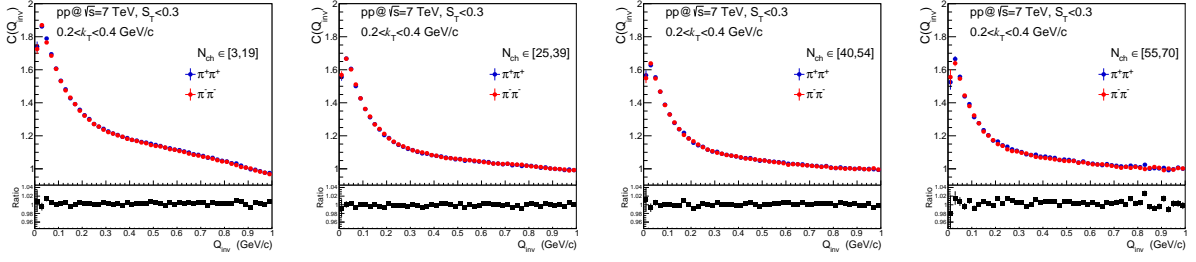
Fig. 11.5 $C(Q_{inv})$ for $\pi^+\pi^+$ and $\pi^-\pi^-$ in jet-like analysis for $(0.2 < k_{\mathrm{T}}(\mathrm{GeV}/c) < 0.4)$.
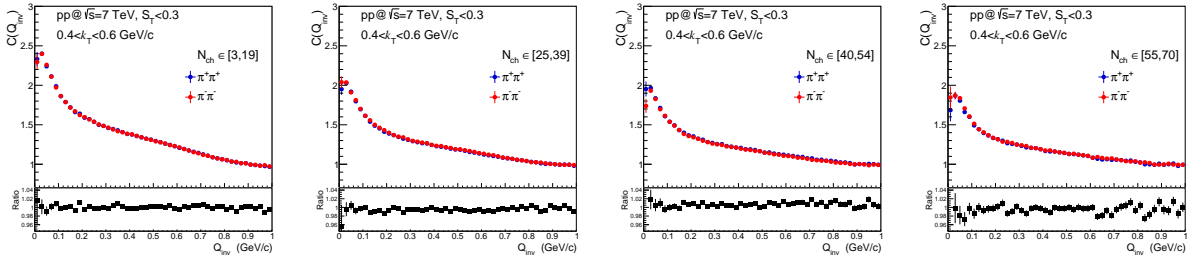
Fig. 11.6 $C(Q_{inv})$ for $\pi^+\pi^+$ and $\pi^-\pi^-$ in jet-like analysis for $(0.4 < k_{\mathrm{T}}(\mathrm{GeV}/c) < 0.6)$.
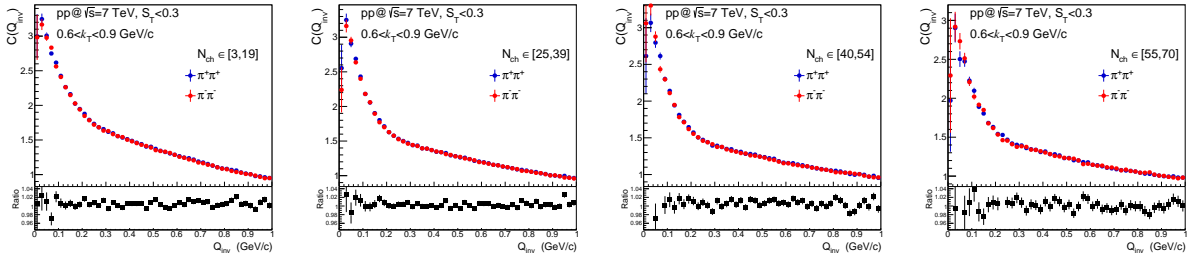
Fig. 11.7 $C(Q_{inv})$ for $\pi^+\pi^+$ and $\pi^-\pi^-$ in jet-like analysis for $(0.6 < k_{\mathrm{T}}(\mathrm{GeV}/c) < 0.9)$.
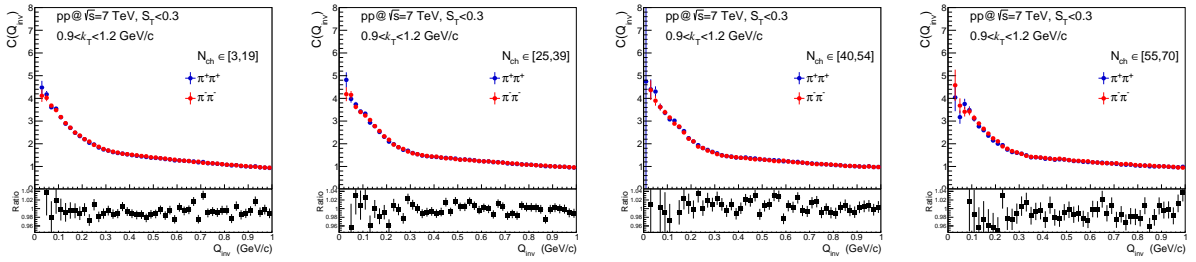
Fig. 11.8 $C(Q_{inv})$ for $\pi^+\pi^+$ and $\pi^-\pi^-$ in jet-like analysis for $(0.9 < k_{\mathrm{T}}(\mathrm{GeV}/c) < 1.2)$.
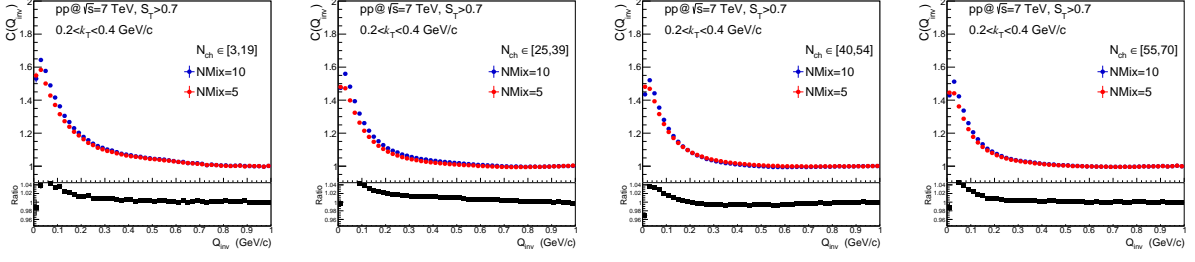
Fig. 11.9 With and without ITS $C(Q_{inv})$ in spherical events for $(0.2 < k_{\mathrm{T}}(\mathrm{GeV}/c) < 0.4)$.
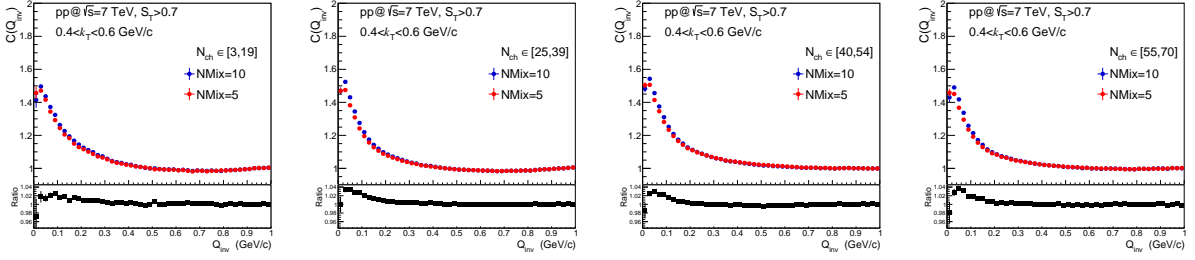
Fig. 11.10 With and without ITS $C(Q_{inv})$ in spherical events for $(0.4 < k_{\mathrm{T}}(\mathrm{GeV}/c) < 0.6)$.
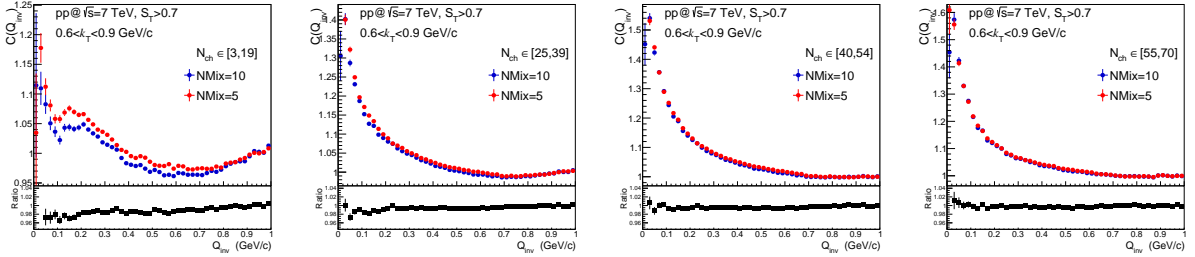
Fig. 11.11 With and without ITS $C(Q_{inv})$ in spherical events for $(0.6 < k_{\mathrm{T}}(\mathrm{GeV}/c) < 0.9)$.
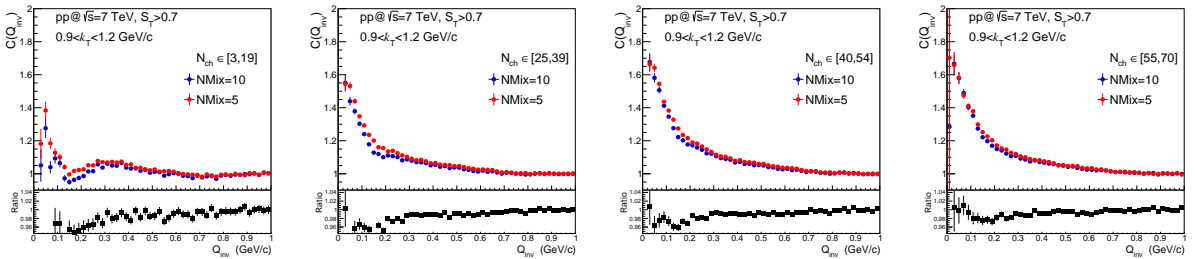
Fig. 11.12 With and without ITS $C(Q_{inv})$ in spherical events for $(0.9 < k_{\mathrm{T}}(\mathrm{GeV}/c) < 1.2)$.
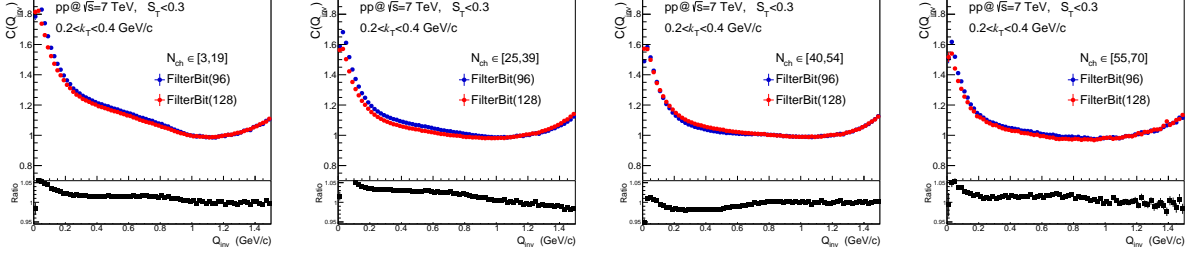
Fig. 11.13 With and without ITS $C(Q_{inv})$ in jet-like events for $(0.2 < k_T(\text{GeV}/c) < 0.4)$.
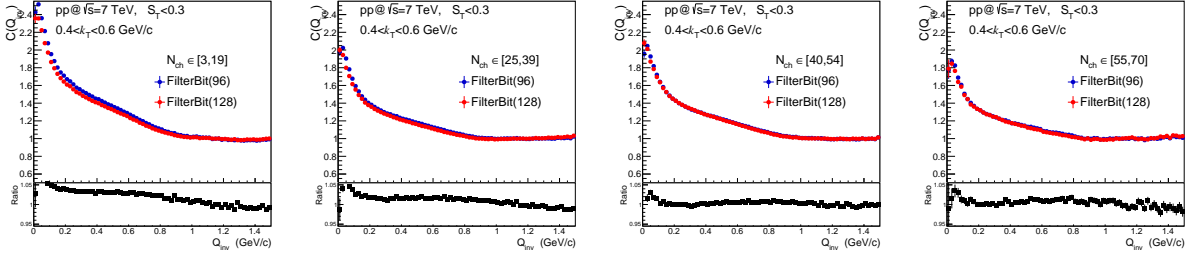
Fig. 11.14 With and without ITS $C(Q_{inv})$ in jet-like events for $(0.4 < k_T(\text{GeV}/c) < 0.6)$.
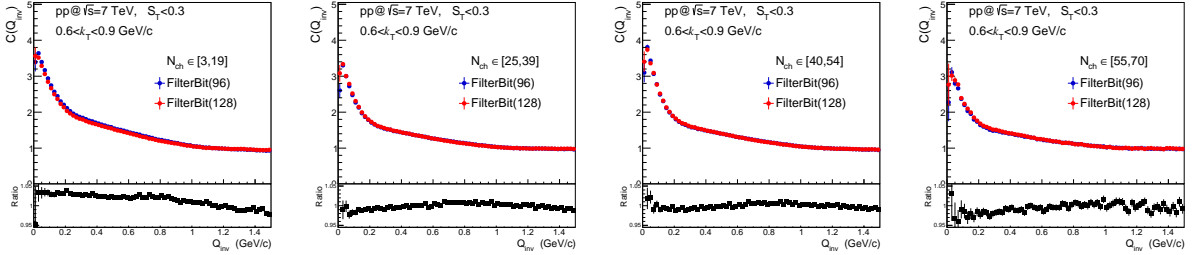
Fig. 11.15 With and without ITS $C(Q_{inv})$ in jet-like events for $(0.6 < k_T(\text{GeV}/c) < 0.9)$.
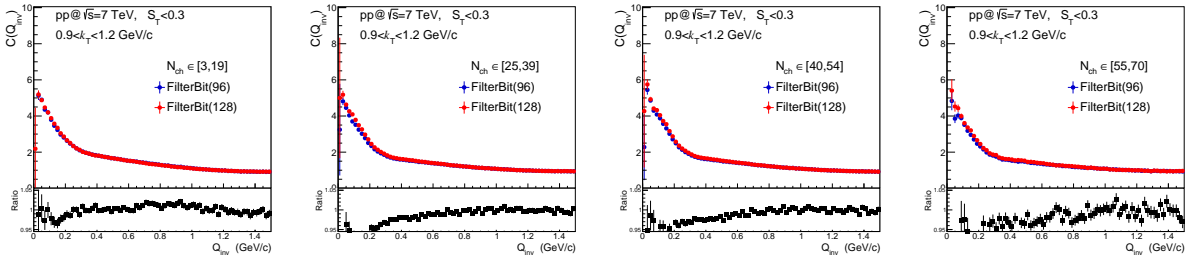
Fig. 11.16 With and without ITS $C(Q_{inv})$ in jet-like events for $(0.9 < k_T(\text{GeV}/c) < 1.2)$.
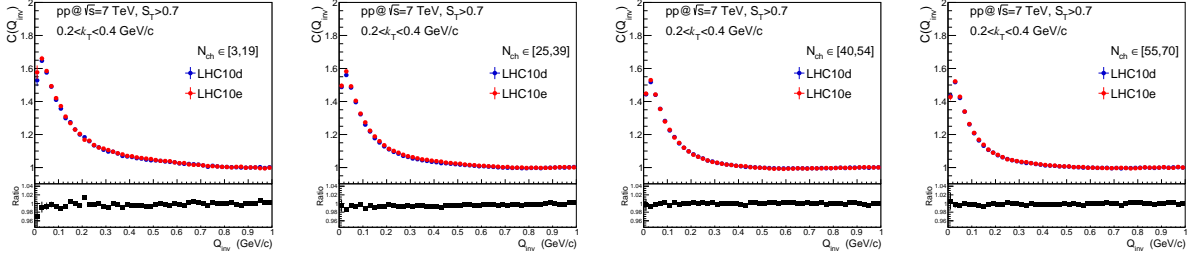
Fig. 11.17 $C(Q_{inv})$ correlation functions for two large ALICE data taking periods in spherical analysis for $(0.2 < k_T(\text{GeV}/c) < 0.4)$.
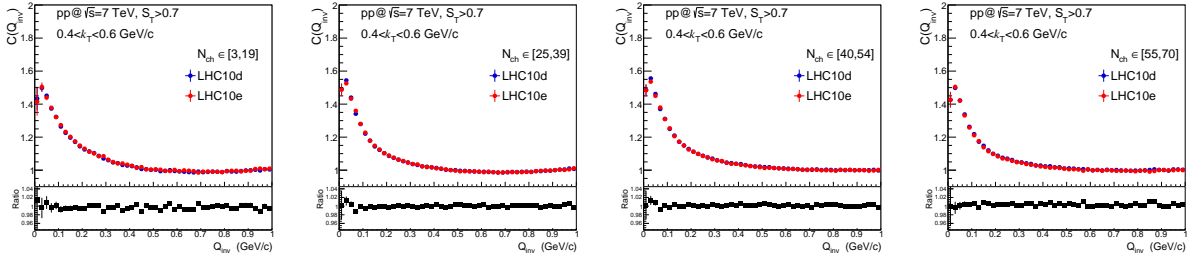
Fig. 11.18 $C(Q_{inv})$ correlation functions for two large ALICE data taking periods in spherical analysis for $(0.4 < k_T(\text{GeV}/c) < 0.6)$.
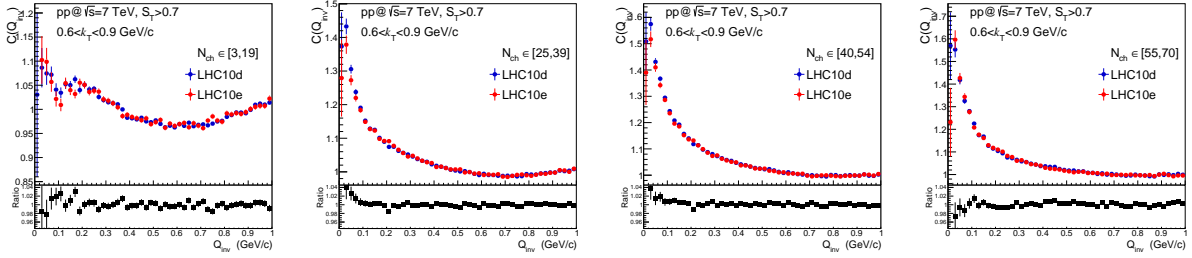
Fig. 11.19 $C(Q_{inv})$ correlation functions for two large ALICE data taking periods in spherical analysis for $(0.6 < k_T(\text{GeV}/c) < 0.9)$.
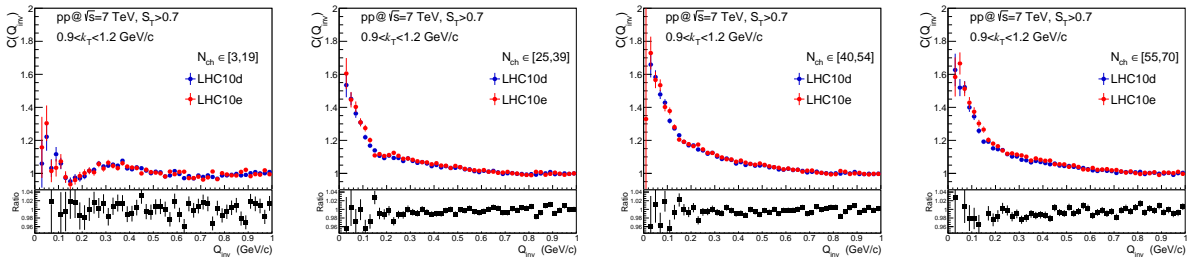
Fig. 11.20 $C(Q_{inv})$ correlation functions for two large ALICE data taking periods in spherical analysis for $(0.9 < k_T(\text{GeV}/c) < 1.2)$.
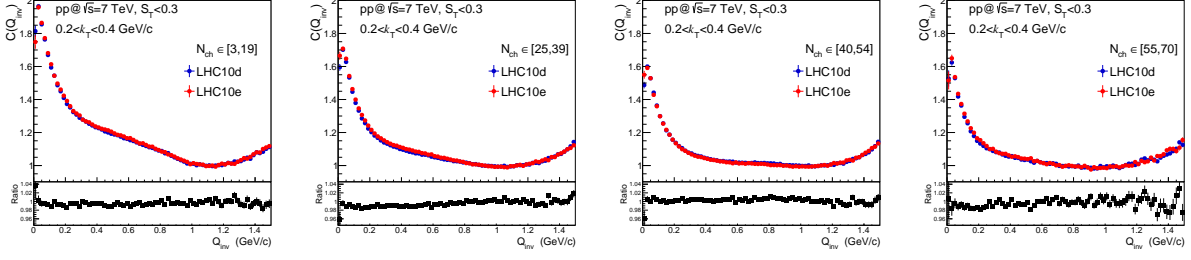
Fig. 11.21 $C(Q_{inv})$ correlation functions for two large ALICE data taking periods in jet-like event analysis for $(0.2 < k_T(\text{GeV}/c) < 0.4)$.
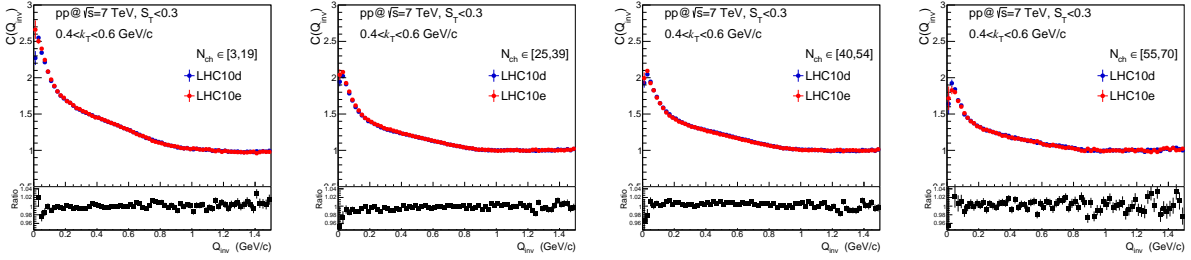
Fig. 11.22 $C(Q_{inv})$ correlation functions for two large ALICE data taking periods in jet-like event analysis for $(0.4 < k_T(\text{GeV}/c) < 0.6)$.
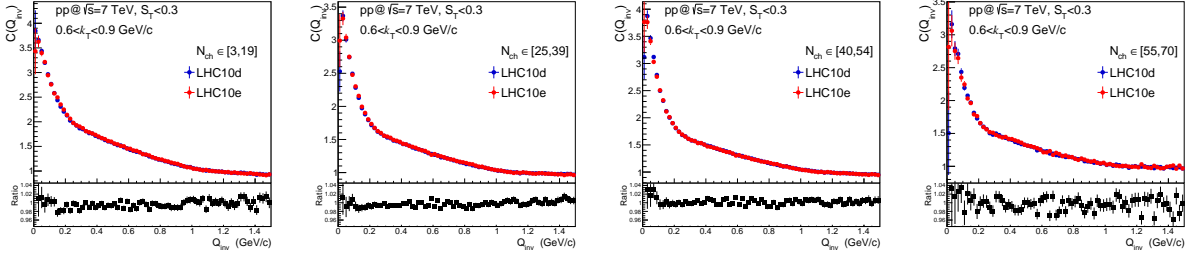
Fig. 11.23 $C(Q_{inv})$ correlation functions for two large ALICE data taking periods in jet-like event analysis for $(0.6 < k_T(\text{GeV}/c) < 0.9)$.
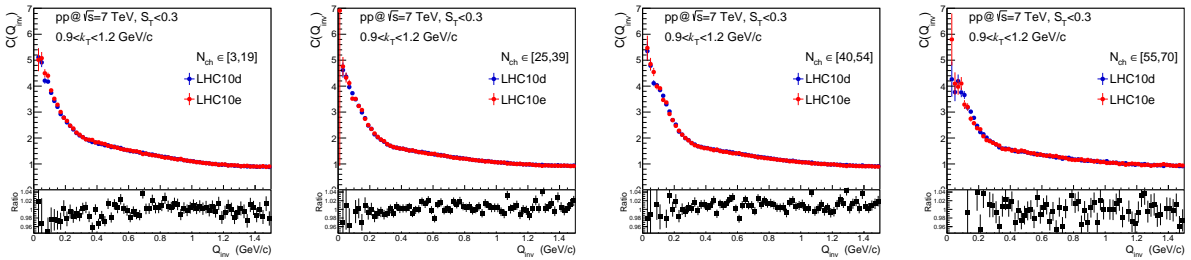
Fig. 11.24 $C(Q_{inv})$ correlation functions for two large ALICE data taking periods in jet-like event analysis for $(0.9 < k_T(\text{GeV}/c) < 1.2)$.
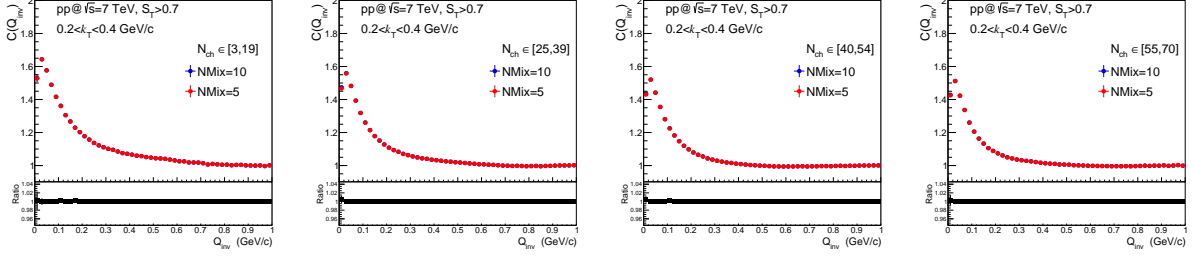
Fig. 11.25 $C(Q_{inv})$ correlation functions with different numbers of mixed events for spherical events analysis for $(0.2 < k_T(\text{GeV}/c) < 0.4)$.
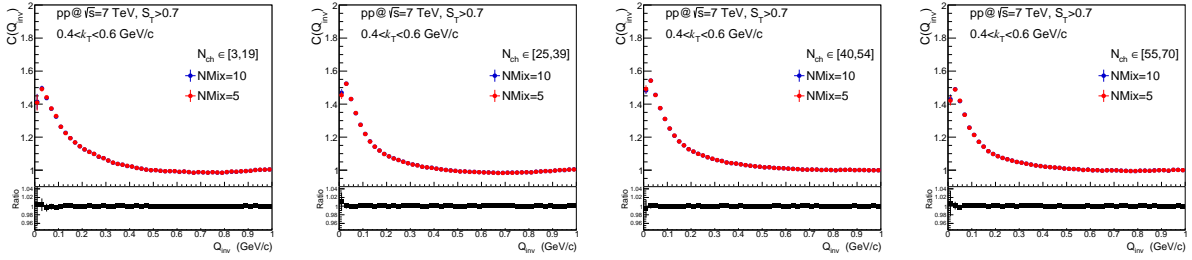
Fig. 11.26 $C(Q_{inv})$ correlation functions with different numbers of mixed events for spherical events analysis for $(0.4 < k_T(\text{GeV}/c) < 0.6)$.
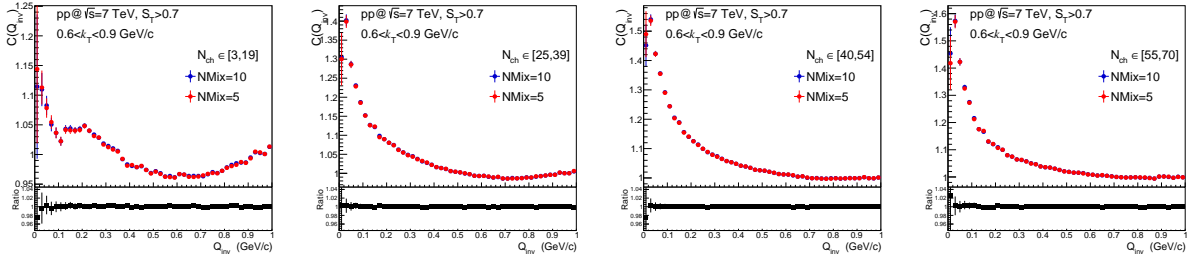
Fig. 11.27 $C(Q_{inv})$ correlation functions with different numbers of mixed events for spherical events analysis for $(0.6 < k_T(\text{GeV}/c) < 0.9)$.
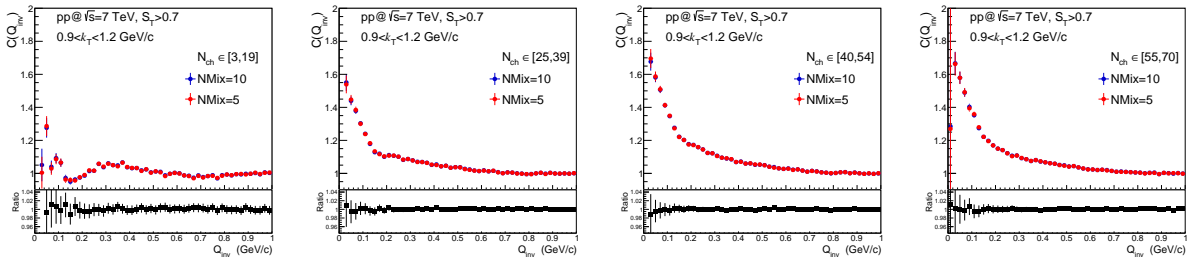
Fig. 11.28 $C(Q_{inv})$ correlation functions with different numbers of mixed events for spherical events analysis for $(0.9 < k_T(\text{GeV}/c) < 1.2)$.
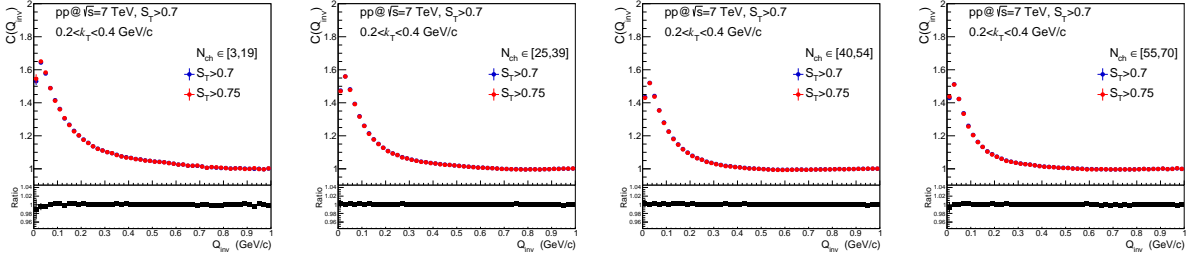
Fig. 11.29 $C(Q_{inv})$ for $S_T > 0.7$ and $S_T > 0.75$ events analysis for $(0.2 < k_T(\mathrm{GeV}/c) < 0.4)$.
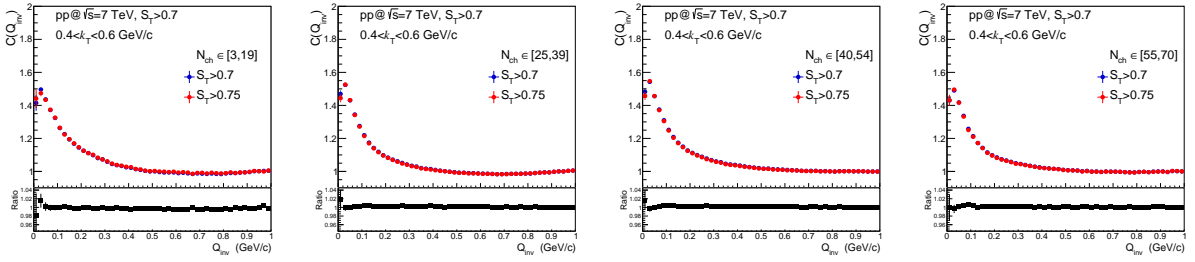
Fig. 11.30 $C(Q_{inv})$ for $S_T > 0.7$ and $S_T > 0.75$ events analysis for $(0.4 < k_T(\mathrm{GeV}/c) < 0.6)$.
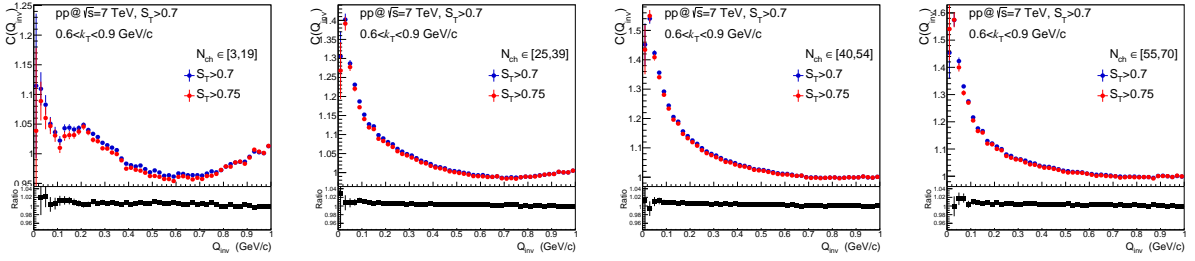
Fig. 11.31 $C(Q_{inv})$ for $S_T > 0.7$ and $S_T > 0.75$ events analysis for $(0.6 < k_T(\mathrm{GeV}/c) < 0.9)$.
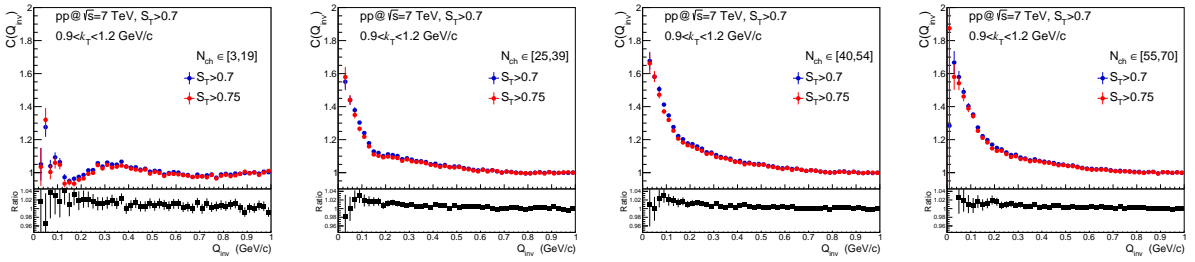
Fig. 11.32 $C(Q_{inv})$ for $S_T > 0.7$ and $S_T > 0.75$ events analysis for $(0.9 < k_T(\mathrm{GeV}/c) < 1.2)$.
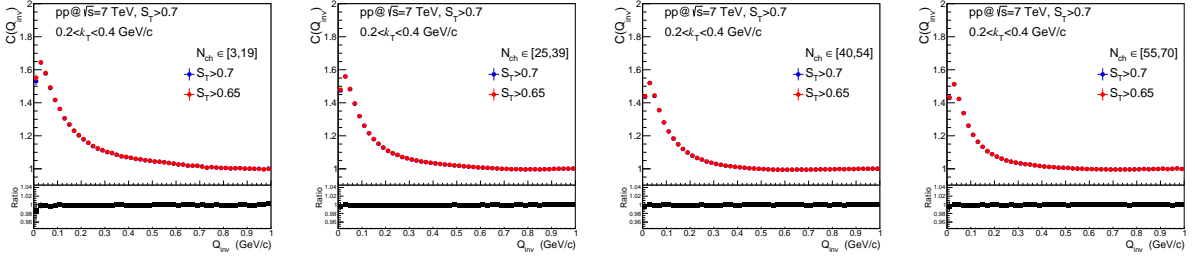
Fig. 11.33 $C(Q_{inv})$ for $S_T > 0.7$ and $S_T > 0.65$ events analysis for $(0.2 < k_T(\text{GeV}/c) < 0.4)$.
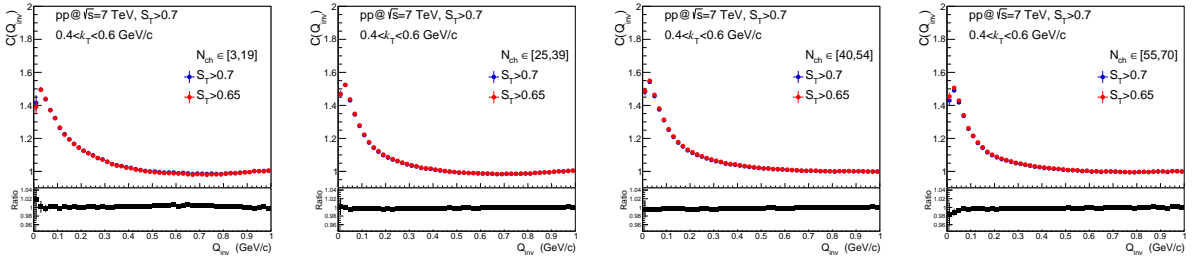
Fig. 11.34 $C(Q_{inv})$ for $S_T > 0.7$ and $S_T > 0.65$ events analysis for $(0.4 < k_T(\text{GeV}/c) < 0.6)$.
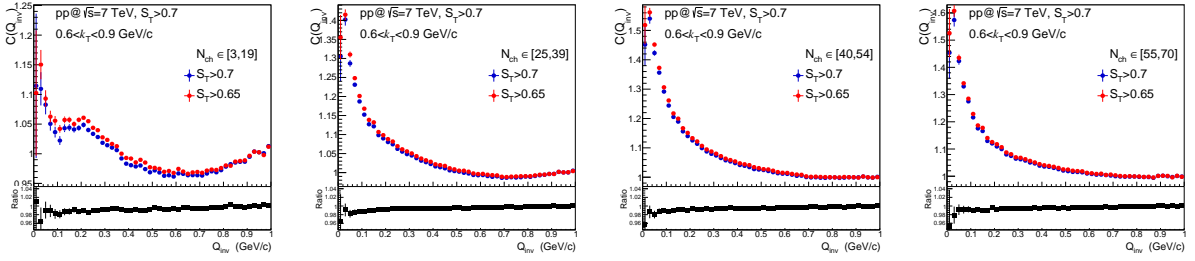
Fig. 11.35 $C(Q_{inv})$ for $S_T > 0.7$ and $S_T > 0.65$ events analysis for $(0.6 < k_T(\text{GeV}/c) < 0.9)$.
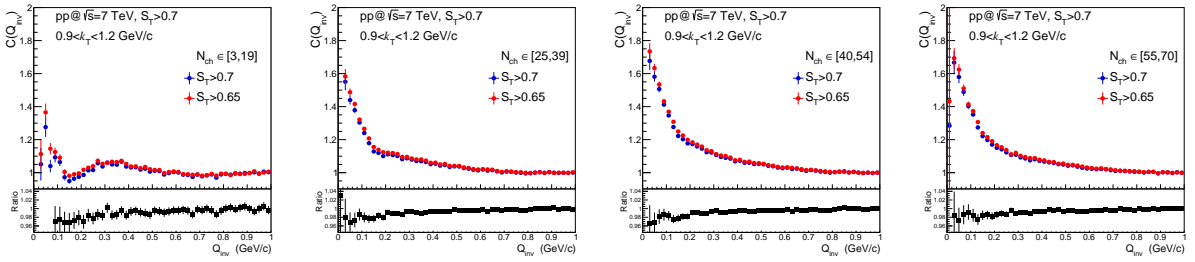
Fig. 11.36 $C(Q_{inv})$ for $S_T > 0.7$ and $S_T > 0.65$ events analysis for $(0.9 < k_T(\text{GeV}/c) < 1.2)$.
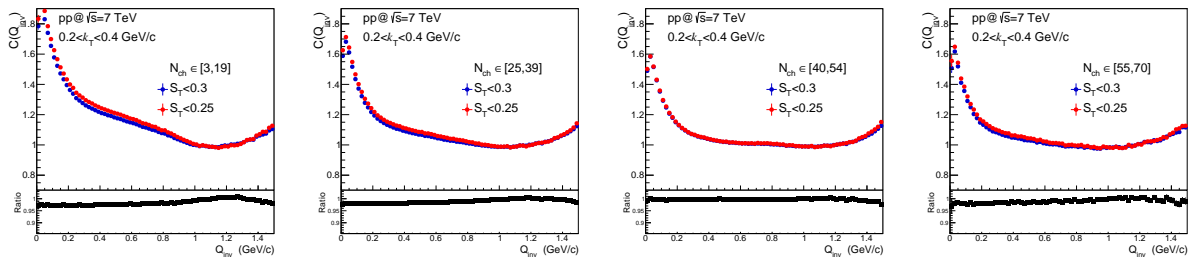
Fig. 11.37 $C(Q_{inv})$ for $S_T < 0.3$ and $S_T < 0.25$ events analysis for $(0.2 < k_T(\text{GeV}/c) < 0.4)$.
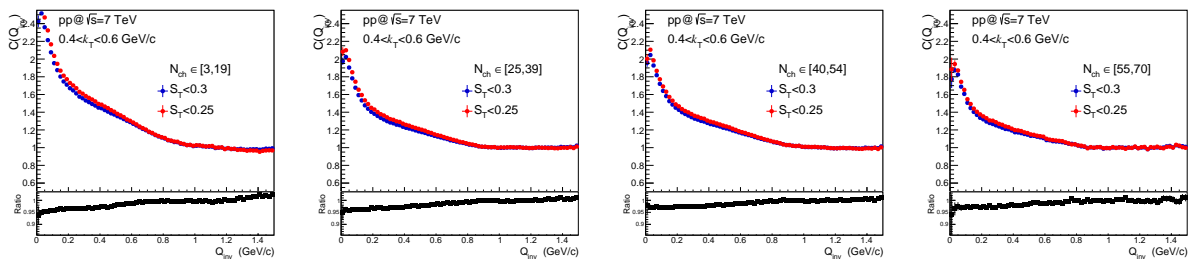
Fig. 11.38 $C(Q_{inv})$ for $S_T < 0.3$ and $S_T < 0.25$ events analysis for $(0.4 < k_T(\text{GeV}/c) < 0.6)$.
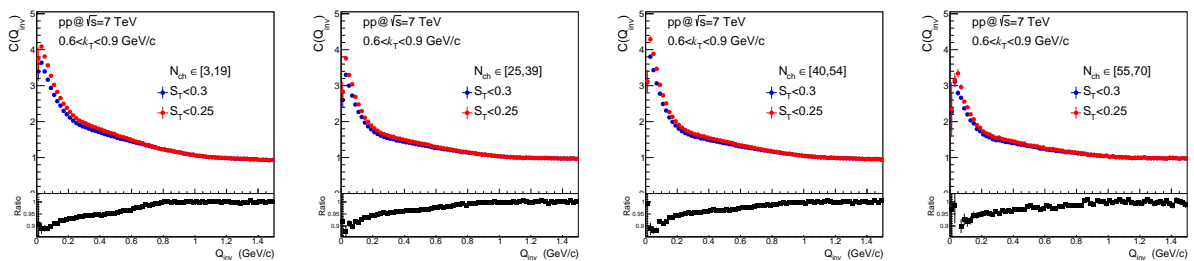
Fig. 11.39 $C(Q_{inv})$ for $S_T < 0.3$ and $S_T < 0.25$ events analysis for $(0.6 < k_T(\text{GeV}/c) < 0.9)$.
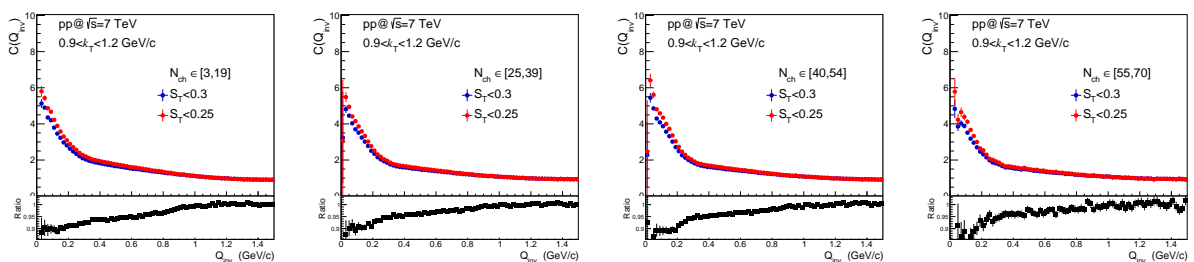
Fig. 11.40 $C(Q_{inv})$ for $S_T < 0.3$ and $S_T < 0.25$ events analysis for $(0.9 < k_T(\text{GeV}/c) < 1.2)$.
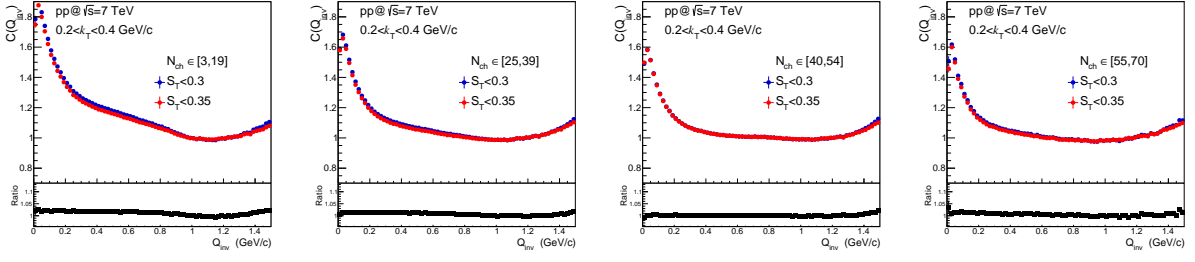
Fig. 11.41 $C(Q_{inv})$ for $S_T < 0.3$ and $S_T < 0.35$ events analysis for $(0.2 < k_T(\text{GeV}/c) < 0.4)$.
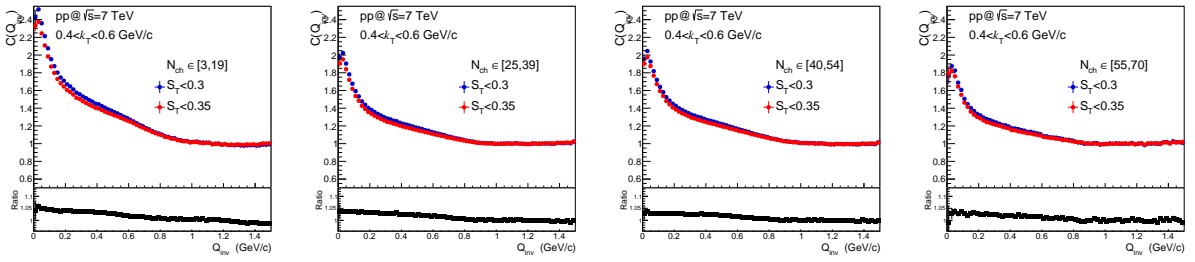
Fig. 11.42 $C(Q_{inv})$ for $S_T < 0.3$ and $S_T < 0.35$ events analysis for $(0.4 < k_T(\text{GeV}/c) < 0.6)$.
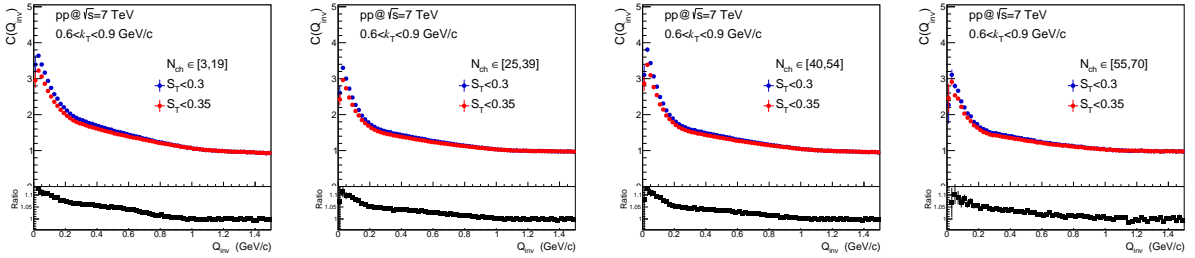
Fig. 11.43 $C(Q_{inv})$ for $S_T < 0.3$ and $S_T < 0.35$ events analysis for $(0.6 < k_T(\text{GeV}/c) < 0.9)$.
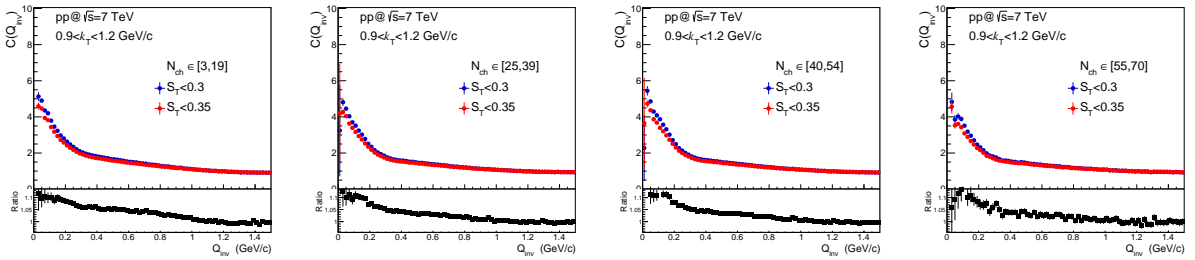
Fig. 11.44 $C(Q_{inv})$ for $S_T < 0.3$ and $S_T < 0.35$ events analysis for $(0.9 < k_T(\text{GeV}/c) < 1.2)$.

11.1.8   Fit range variation

While fitting we measure the maximum of the correlation function and fit in the range in (Q_{in}, starting from 0, where 98% of the full signal is situated. Then we vary this range on both sides for 25% and use these changes to fit results as a symmetric contribution to systematic uncertainty. The change in the fit range where we enlarge the range usually doesn't create a big change, so the reduction in range is the driving the size of the systematic uncertainty. In the variation we always choose the bigger error of the possible two.

ΔR/R ($S_T > 0.7$)	$\langle N_{ch} \rangle$ 32 $\pm$ 5	$\langle N_{ch} \rangle$ 48 $\pm$ 5	$\langle N_{ch} \rangle$ 63 $\pm$ 5
$0.2 < k_{\mathrm{T}}(\mathrm{GeV}/c) < 0.4$	5%	4%	3%
$0.4 < k_{\mathrm{T}}(\mathrm{GeV}/c) < 0.6$	7%	6%	3%
$0.6 < k_{\mathrm{T}}(\mathrm{GeV}/c) < 0.9$	14%	11%	4%

Reported uncertainties lead to error overestimation due to their obvious correlation with available statistics. For the first multiplicity bin in spherical events we do not report errors due to large non-femtoscopic contributions induced by the sphericity event cut. In further analysis this will be controlled in a similar way as is done for jet-like events.

ΔR/R ($S_T < 0.3$)	$\langle N_{ch} \rangle$	$\langle N_{ch} \rangle$ 32 $\pm$ 5	$\langle N_{ch} \rangle$ 48 $\pm$ 5	$\langle N_{ch} \rangle$ 63 $\pm$ 5
$0.2 < k_{\mathrm{T}}(\mathrm{GeV}/c) < 0.4$	3%	6%	4%	3%
$0.4 < k_{\mathrm{T}}(\mathrm{GeV}/c) < 0.6$	11%	12%	10%	12%
$0.6 < k_{\mathrm{T}}(\mathrm{GeV}/c) < 0.9$	12%	6%	9%	10%

11.1.9   Event generator induced systematic effects

In this section we estimate systematics effect due to Monte Carlo event generator induced bias. We assume the PYTHIA corrected correlation function fit results as the baseline and compare to the ones corrected by PHOJET. From the relative difference of these two Monte Carlo event generator results a small contribution of about 1% is expected in most multiplicity and k_{T} bins.

$\Delta R_{PYTHIA}/R_{PHOJET}$	$\langle N_{ch} \rangle$ 9 $\pm$ 5	$\langle N_{ch} \rangle$ 32 $\pm$ 5	$\langle N_{ch} \rangle$ 48 $\pm$ 5
$0.2 < k_{\mathrm{T}}(\mathrm{GeV}/c) < 0.4$	<1%	1%	7%
$0.4 < k_{\mathrm{T}}(\mathrm{GeV}/c) < 0.6$	<1%	1%	2%
$0.6 < k_{\mathrm{T}}(\mathrm{GeV}/c) < 0.9$	1%	1%	1%

11.1.10   Estimate of the total systematic effects

All mentioned contributions to systematics are assumed to be non-correlated and are added in quadrature and a square root of the sum is used as a symmetric systematic uncertainty of the measured homogeneity radii. For the systematic uncertainty of correlation functions in spherical events we see that in all checks the variations are very small and concentrated in the first 5 bins ($Q_{in} < 100\,\mathrm{MeV}/c$). If we prescribe a 1% variation for every of one of 4 checks than a using

the RMS approach a reasonable estimate of systematic uncertainty for correlation functions is about 2%. For jet-like events the variation of 0.05 in transverse sphericity is more influential than in spherical events. Here the jet contribution is even more enhanced and a variation of more than 5% in the higher k_T bins is expected. As an overestimate of the uncertainty we take 3% and 5% for the first two bins in k_T respectively and 10% for the rest.

Total systematic uncertainty for fitted homogeneity radii is calculated in the same fashion. The biggest source of uncertainty is the fit range variation. All other sources are in the 1-2% range of variation so assuming they are uncorrelated the RMS gives:

ΔR_{TOT}/R ($S_T > 0.7$)	$\langle N_{ch} \rangle$ 32 ± 5	$\langle N_{ch} \rangle$ 48 ± 5	$\langle N_{ch} \rangle$ 63 ± 5
$0.2 < k_T(\text{GeV}/c) < 0.4$	6%	5%	3%
$0.4 < k_T(\text{GeV}/c) < 0.6$	8%	7%	3%
$0.6 < k_T(\text{GeV}/c) < 0.9$	14%	11%	5%

From previous results it is expected that the range of systematic uncertainties are $5 - 15\%$ depending on the k_T and multiplicity bin. With the introduction of a S_T cut, the available data set is further reduced which induces even larger final uncertainties.

ΔR_{TOT}/R ($S_T < 0.3$)	$\langle N_{ch} \rangle$ 9 ± 5	$\langle N_{ch} \rangle$ 32 ± 5	$\langle N_{ch} \rangle$ 48 ± 5	$\langle N_{ch} \rangle$ 63 ± 5
$0.2 < k_T(\text{GeV}/c) < 0.4$	4%	6%	8%	8%
$0.4 < k_T(\text{GeV}/c) < 0.6$	11%	12%	10%	12%
$0.6 < k_T(\text{GeV}/c) < 0.9$	12%	6%	9%	10%

Here we show only the biggest deviations so these numbers somewhat overestimate the real uncertainty. For higher k_T bins statistics enhance the uncertainty and no reasonable estimate of systematics can be done.

11.1.11 Systematical uncertainty to correlation functions

All above mentioned systematic effects also contribute to the total bin-by-bin systematic uncertainty to the correlation function. For this reason we fit the shown ratios with a third order polynomial and add the fitted bin-by-bin contributions in quadrature to produce the systematic uncertainty of the correlation functions.

The dominating sources of systematic uncertainty are the filter bit variation and the sphericity bin variation. Here the uncertainty goes in some multiplicity and k_T bins up to 8-10%. For Monte Carlo corrected correlation functions we also include a comparison between PYTHIA and PHOJET event generators to the total uncertainty. The PYTHIA results are used as the benchmark and the difference to PHOJET as the systematics contribution. The MC closure test results, comparison between reconstructed and generator level Monte Carlo results, are not used as contributions to the final systematic uncertainty.

Chapter 12

Preliminary results and consistency checks

In this analysis we fitted $C(Q_{inv})$ correlation functions using an exponential and Gaussian fit function. To accommodate for the observed discrepancy between fitted functions and correlations we chose in later steps to vary the exponent of the Gaussian making it a free parameter.

$$C(Q) = 1 + \lambda \cdot Exp(-(R \cdot Q)^{\alpha}) \tag{12.1}$$

It was consistently shown that the exponential $\alpha \approx 1$ described the data better. This deviation from the Gaussian was also reported by others [53][54]. In the appendix we show the connection between these two fit functions and how their fit results can be reasonably compared. This is especially necessary when one is in need of data from various publications where only Gaussian fits were performed. To describe the residual non-femtoscopic correlations we fit the PYTHIA same sign correlation functions with a Gaussian and use the measured width of the background as input for the final fit function.

$$C(Q_{inv}) = (1-\lambda) + \lambda K_C(Q_{inv}) \big[1 + exp(-R_{inv}Q_{inv}) \big] + B(Q_{inv}) \tag{12.2}$$

The 1D homogeneity radii were extracted using the "exponential Bowler-Sinyukov" formula. An informative overview of various proposed fit functions and their interpretations can be found in [55].

12.0.12   Spherical (isotropic) events

Spherical events are a real subset of all minimum bias events. They are more numerous in high multiplicity events but also at low multiplicity constitute a significant portion of the set of all events[2]. This is why it is to be expected that they exhibit a familiar functional dependence of homogeneity radii on pair k_T. Here the error bars and boxs represent the statistical and the systematics uncertainty respectively.

In comparison to published results [4] spherical events do not show a k_T scaling or an indication that there is a hydrodynamic effect driving the k_T dependence. The results shown in
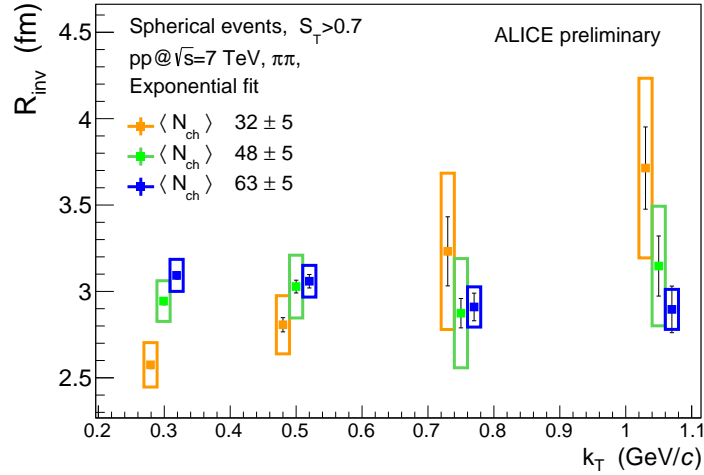
Fig. 12.1 Extracted HBT radii for spherical events in proton-proton collisions at $\sqrt{s}=7$ TeV in dependence of pair k_T .

figure 12.1 indicate that for high multiplicity spherical events homogeneity radii do not change much for a large range of k_T-s which means that both low energy and high energy pion pairs are produced at the same mean radius. The lowest multiplicity bin shows a clear rise with k_T .

12.0.13 Jet-like events

The difference between minimum bias events and spherical events should mostly be contained in the non-femtoscopic contributions which dominate jet-like events. With their removal the corrected correlation functions give novel information pertaining to the in-jet Bose-Einstein effects[56].

For the fitting we use:

$$C_{JET}(Q_{inv}) = (1-\lambda') + \lambda' K_C(Q_{inv}) \left[1 + \lambda' exp(-R_{inv,JET} Q_{inv}) \right] \tag{12.3}$$

where λ' is equivalent to the chaoticity parameter but should have a different interpretation considering the fact that it is measuring the amplitude of the Bose-Einstein symmetrization signal for in-jet identical pion pairs.

As was explained in the beginning of this thesis, high k_T pion pairs belong predominantly to the same jet structure, while low k_T pairs do not. Fitted homogeneity radii show some k_T dependence. A monotonic reduction of homogeneity radii with pair k_T is observed for the first three k_T bins.
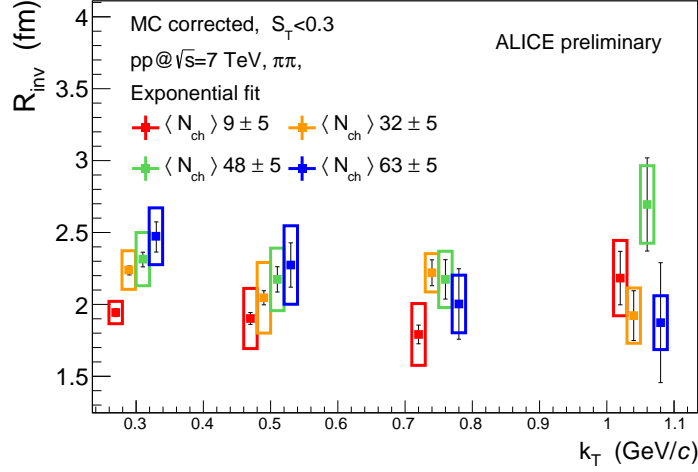
Fig. 12.2 Extracted HBT radii for jet-like events in proton-proton collisions at $\sqrt{s} = 7$ TeV in dependence of pair k_T.

12.0.14 Comparison to published ALICE results

In this section we address the question of comparison between the newly produced event shape dependent correlation functions and already published ALICE results for all sphericities. The fit results are for current k_T and multiplicity binning for a Gaussian fit function with a Gaussian background. Since our multiplicity and k_T bins differ we present only the first two bins for general comparison. We would also like to stress that in this comparison the non-femtoscopic contributions differ between sphericity, multiplicity and k_T bin and that these considerations should be taken into account.
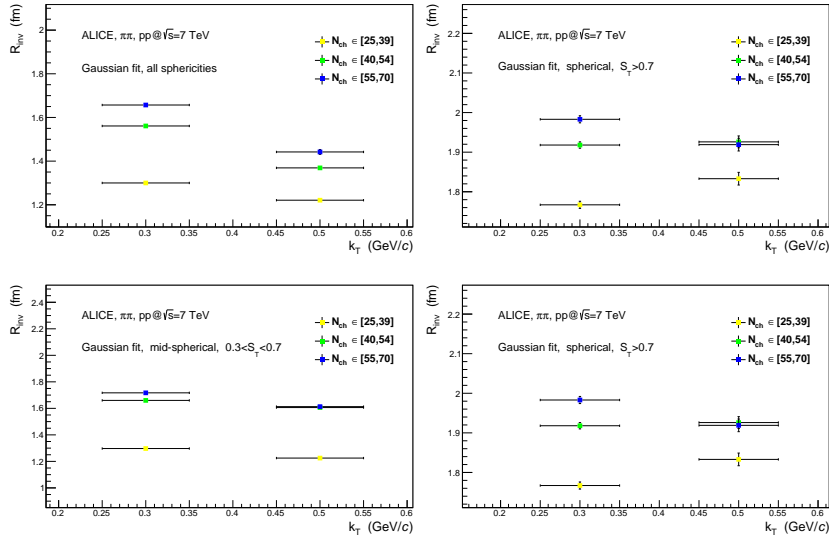
Fig. 12.3 Gaussian fit results for four bins of transverse sphericity. Results produced for THIS THESIS.

12.0.15 Reproduction of published ALICE results using AODs

As a standard test of reproducibility we present fit results of minimum bias event homogeneity radii with k_T and multiplicity bins as in [4]. There are several differences between our analysis and the published results' one which need to be taken into account. Most of them are relatively minor and should create no significant differences between results but some need to be emphasized.

$\langle dN_{ch}/d\eta \rangle$	$N_{ch}^{|\eta|<1.2}$	$N_{ch}^{|\eta|<0.8}$
2.8	1-11	1-8
6.6	12-16	9-12
9.2	17-22	13-17
12.0	23-28	18-21
14.9	29-34	22-26
17-9	35-41	27-31
21.4	32-51	32-27

Our analysis is done using AODs of LHC10c,d,e data sets comprising of 500 million events. We use FilterBit(96) which is, as explained before, a standard ITS and TPC cut with a tight static DCA. The published analysis used ESDs with a 100 million events and a p_T dependent DCA cut. A novelty in our analysis is the use of the GetRefMultiplicityComb08() estimator as opposed to GetRefMultiplicity(). The new estimator has a set η acceptance of ± 0.8 which introduces further differences between the two analysis. The new estimator will be used for final results. Since the published results were done with $|\eta| < 1.2$ the comparison is presented in bins of $\langle dN_{ch}/d\eta \rangle$. We used the same exact fitting procedure as was documented in the published ALICE paper[4].

$$C(q_{inv}) = [(1-\lambda) + \lambda K(inv)(1 + exp(-R_{inv}^2 Q_{inv}^2))]B(q_{inv})$$

where K is the Coulomb function averaged over a spherical source, R_{inv} is the femtoscopic radius, and B is the here to describe non-femtoscopic background contributions. For B there are various functional forms in use, for the published paper a second order polynomial was used of the form $A + B*q + C*q^2$. Free parameters (A,B,C) were determined using the same PYTHIA data as in the rest of this AN. Every k_T and multiplicity bin had its background triad determined separately.

In three multiplicity bins the highest k_T measurement does not conform to published results within 1σ which should be expected considering the number of measurements. All other radii are withing systematic uncertainty which demonstrates a clear agreement and a separate confirmation of published results and current analysis code.
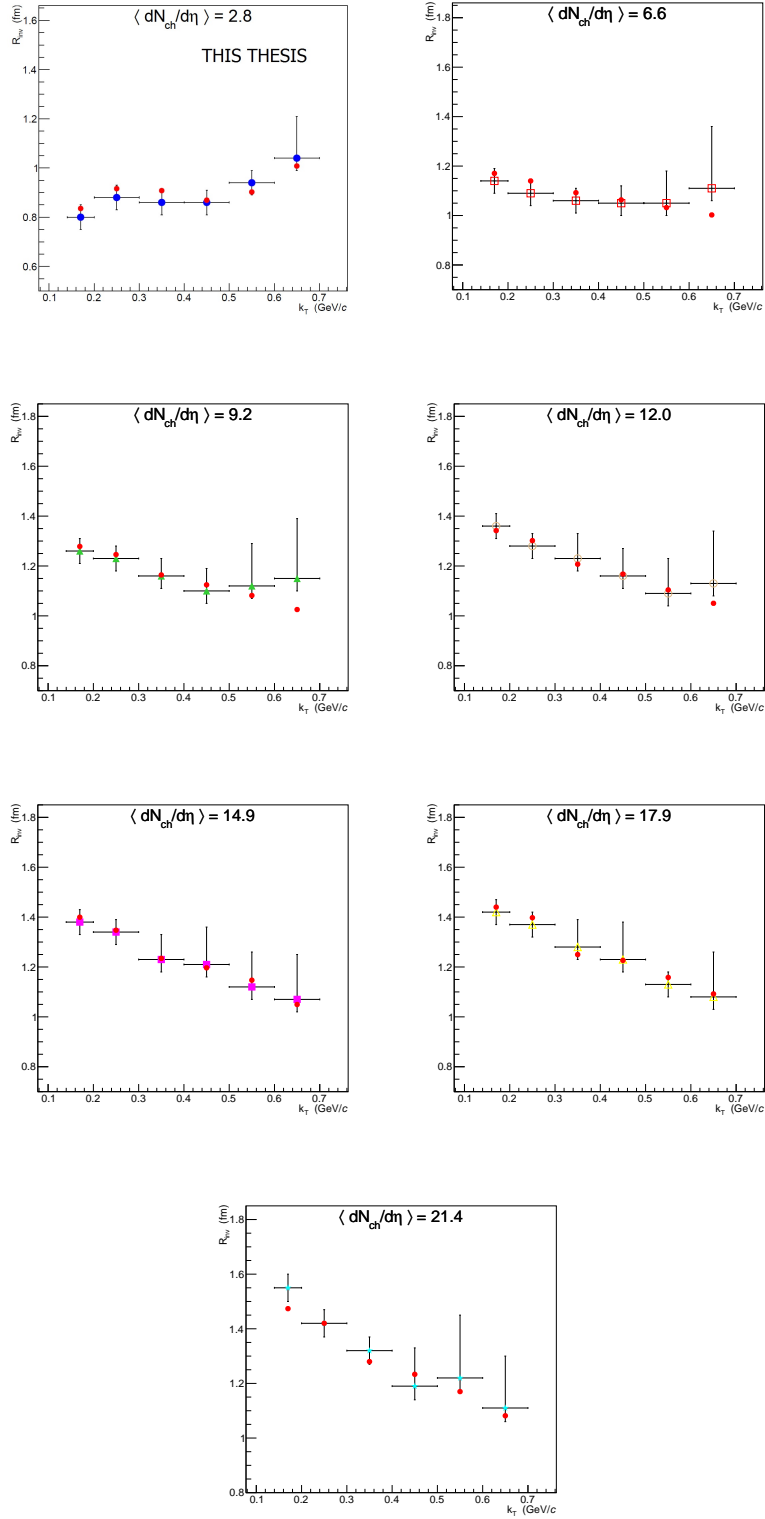
Fig. 12.4 Comparison to published results of R_{inv} in dependence to k_T and multiplicity. Error bars represent systematic uncertainty.

12.0.16 Weighted average R_{inv} approach

In order to confirm that the produced correlation functions and their respective homogeneity radii agree with sphericity integrated results we calculate the weighted average of jet-like ($S_T < 0.3$), mid-spherical ($0.3 < S_T < 0.7$) and spherical ($0.7 < S_T$) events homogeneity radii. For the weights we use the number of events per sphericity bin

$$R_{inv}^{average} = \frac{w_S R_{inv}^S + w_M R_{inv}^M + w_J R_{inv}^J}{w_S + w_M + w_J}$$

where w are the weights and the sub/superscriptions S, M and J represent spherical, midspherical and jet-like events. From 6.1 we know that approximately 54% of the events fall in to the mid-spherical event category which means that they will dominate the weighted average.

Validity of the approach

The weighted average has to be understood as an approximative comparison method with a clear understanding of when it is viable.

From the sphericity calculation event rejection criteria, at least two tracks with $p_T > 0.5$ GeV/c, we know that there will be a relevant rejection rate for the lower multiplicity events which might introduce discrepancies and thus render the weighted average approach inapplicable for the lower multiplicities. Here we see that the rejection rate only plays a role for the lowest
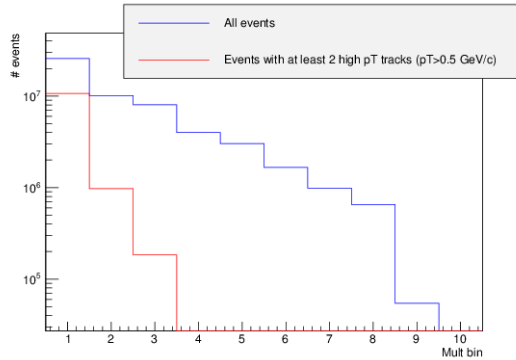
Fig. 12.5 Sphericity calculation event rejection rate dependence to event multiplicity bin.

multiplicities. The other consideration to keep in mind is the correlation function comparison where the definitions point to possible sources of discrepancy.

Correlation function considerations

The standard correlation function is a ration of two distributions.

$$C(Q_{inv}) = \frac{P(p_1 - p_2)}{P(p_1)P(p_2)} = \frac{P(p_1 - p_2)^{event}}{P(p_1 - p_2)^{mixed}}$$

$$C(Q_{inv}) = \frac{P_E}{P_M} = \frac{P_E^S + P_E^M + P_E^J}{P_M^S + P_M^M + P_M^J + P_M^{S,M,J}}$$

If discriminated by sphericity the numerator will contain three distributions, for each sphericity bin, while the denominator will have one for each sphericity bin and an extra mixed one.

$$C^S(Q_{inv}) = \frac{P_E^S}{P_M^S} \quad C^M(Q_{inv}) = \frac{P_E^M}{P_M^S} \quad C^S(Q_{inv}) = \frac{P_E^J}{P_M^J}$$

With the separation of these probabilities into three correlation functions there is no a priori way of connecting the three distinct correlation function into the sphericity integrated one without some addition information. It might be possible if by chance the denominator distributions "resemble" each other. Then a weighted average R_{inv} should give reasonable results hopefully within the systematic uncertainty. Here we see that the rejection rate and other effects make
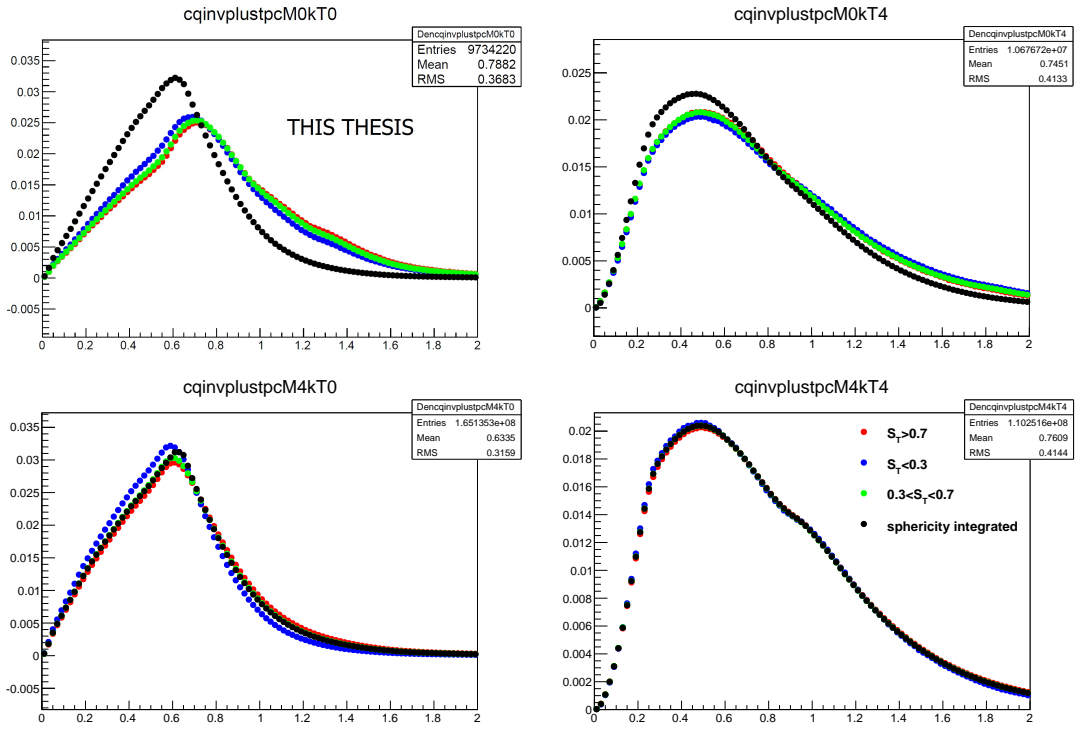
Fig. 12.6 Comparison of correlation function denominators for high and low values of charged particle multiplicity (M4,M0) and pair k_T (kT4,kT0.)

averaging problematic in the lower multiplicity bins. For the higher k_T and multiplicity bins the denominator distributions are sensible and allow for a meaningful weighted average comparison to sphericity integrated results.

Results of comparison

Here we show a comparison of weighted average homogeneity radii to AOD analysis sphericity integrated results and published results. As expected the weighted average produces results
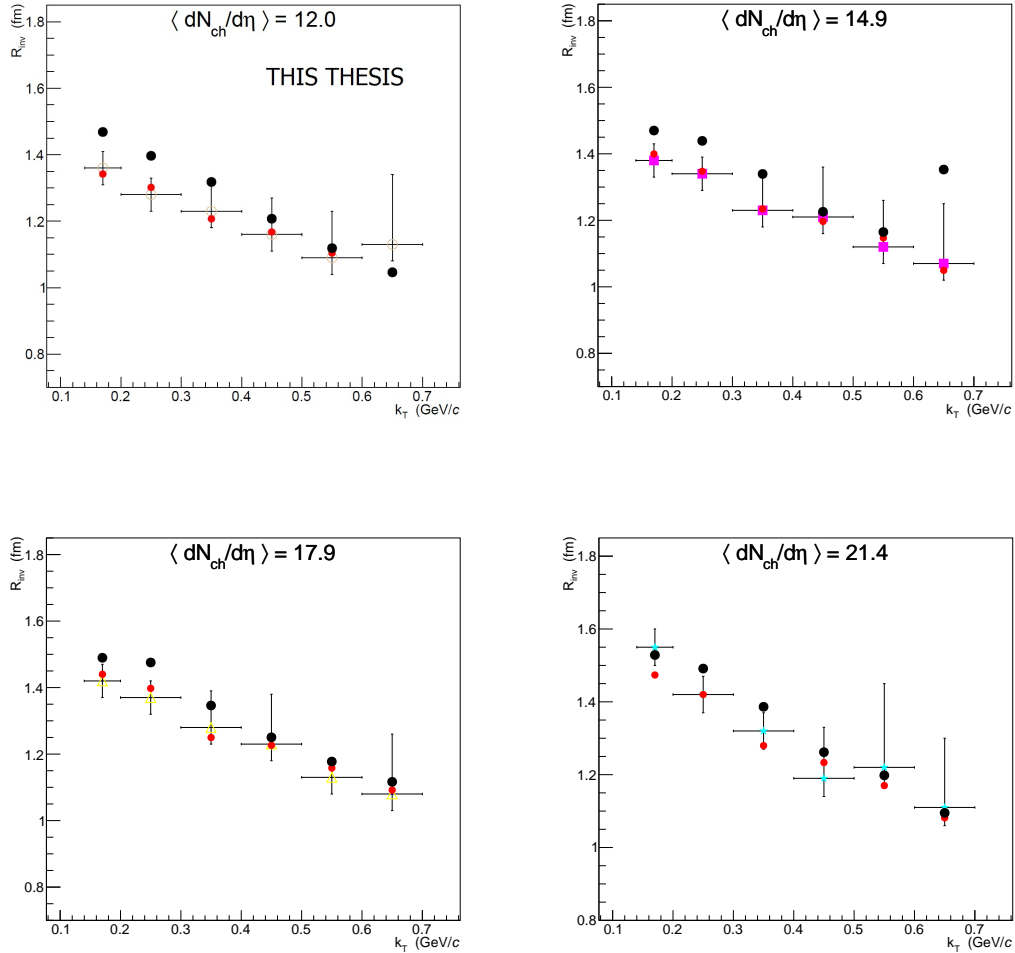
Fig. 12.7 Comparison of weighted average homogeneity radii (black) to AOD analysis sphericity integrated results (red) and published results (points with error bars) for four higher multiplicity bins.

within the systematic uncertainty.

12.0.17 Independent confirmation of results

As a final check of the AliFemtoSphericityEventCut() method introduced into the AliRoot repository and used in this analysis we show a comparison to a different analysis code, expanded with the sphericity cut, which was shown to reproduce published results. For all three sphericity bins the correlations agree well.

Finally, to check if the observed depletion in the low Q_{inv} and high k_T region for spherical events
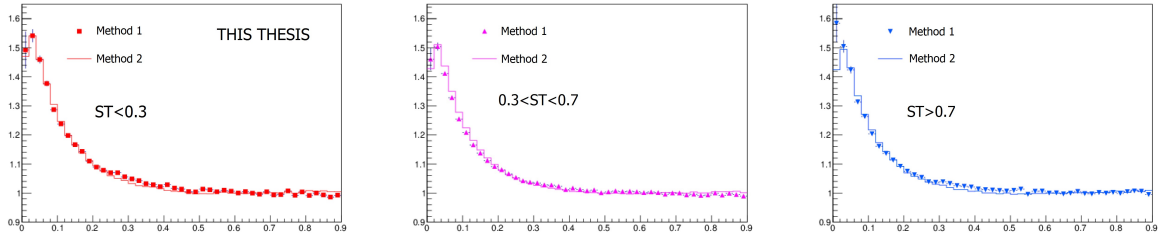
Fig. 12.8 Comparison of correlation function obtained by two independent analysis for three sphericity bins for the multiplicity bin $N_{ch} \in [13 - 17]$.

can be observed we present Figure 12.9. Here it is shown that there is a clear agreement between the two analysis methods and that a evolution of the mentioned depletion is well observed.
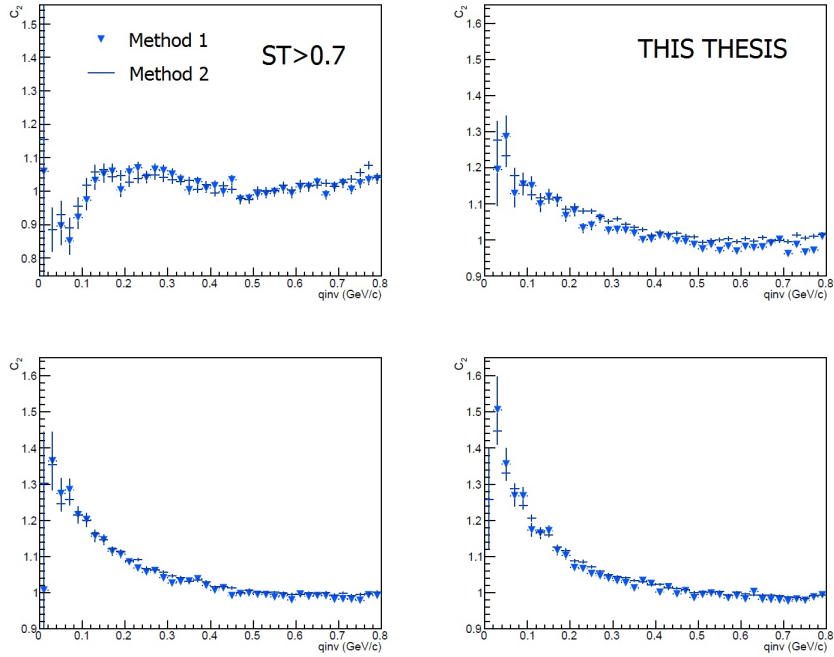
Fig. 12.9 Comparison of spherical event correlation function obtained by two independent analysis for $0.6 < k_T < 0.7$ GeV/c and four consecutive multiplicity bins $[1 - 8]$, $[9 - 13]$, $[14 - 17]$ and $[17 - 23]$.

Chapter 13

λ considerations

In this section we consider the effects of λ variation and free fitting to the extracted homogeneity radii. The λ parameter is the intercept height of the correlation function at $Q_{inv} = 0$ GeV/c. It is directly connected to the chaoticity of the emitter and should in principle be equal to unity for fully chaotic sources. Experimentally, it is known that a coherence induced by clearly methodological circumstances like particle miss-identification or resolution effects might lower the λ parameter.

13.1 Two fitting methods and the stability of λ

To follow the behaviour of λ we consider two approaches. First approach uses the following fitting function:

$$C(Q_{inv}) = [(1 - \lambda) + \lambda K(inv)(1 + \lambda exp(-R_{inv}^{\alpha} Q_{inv}^{\alpha}))]$$

where α is set to 1 thus making the supposed fit shape exponential or Gaussian. This method emphasizes both the role of λ and of the Coulomb effect at low Q. The second approach is an easy way to take into account the dilution by secondaries and Coulomb correct. Here the quantum statistical part of the Bowler-Sinyukov expression is specifically separated and solved for making the final correlation function as simple as possible.

$$C(Q_{inv}) = [(1 - f_c^2) + f_c^2 K(inv) C_2^{QS}(Q_{inv})]$$

Here $f_c^2 = 0.85$ stands for fraction of coherent pions coming from the emitter. Experimental motivation to the set value can be found in [6]. As an internal check of consistency one can use a new variable λ' which when fitted should take a value of unity thus proving that both the dilution and Coulomb correction has been performed correctly.

$$C_2^{QS} = 1 + \lambda' exp(-R_{inv}^{\alpha} Q_{inv}^{\alpha})$$

In both cases, fitting $C(Q_{inv})$ or C_2^{QS}, the initial correlation function is Monte Carlo corrected before fitting and solving for C_2^{QS}. Here we see that in both cases the spherical events show
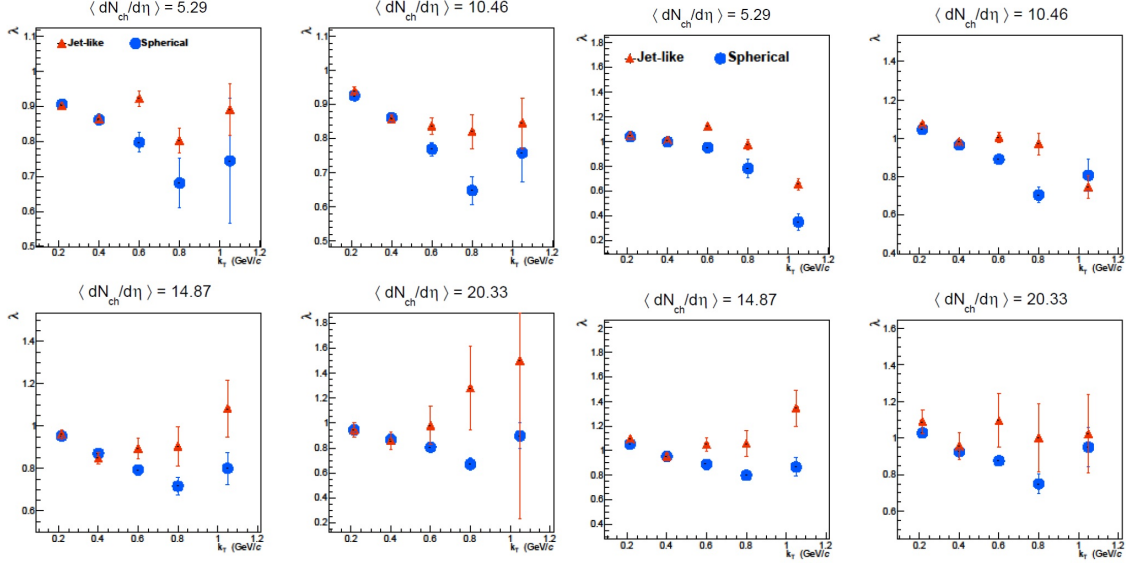
Fig. 13.1 Exponential fit values of λ for spherical and jet-like events. $C(Q_{inv})$ fits are on the left and $C_2^{QS}(Q_{inv})$ on the right.

consistent agreement in λ behaviour while in jet-like events an instability is observed with λ values going to non-physical values. The instability can be attributed to a change in correlation function shape meaning that an interplay of λ and R_{inv} exchange is taking place. No known process predicts such behavior of λ. In the case of a Gaussian fit the outcome is similar but scaled
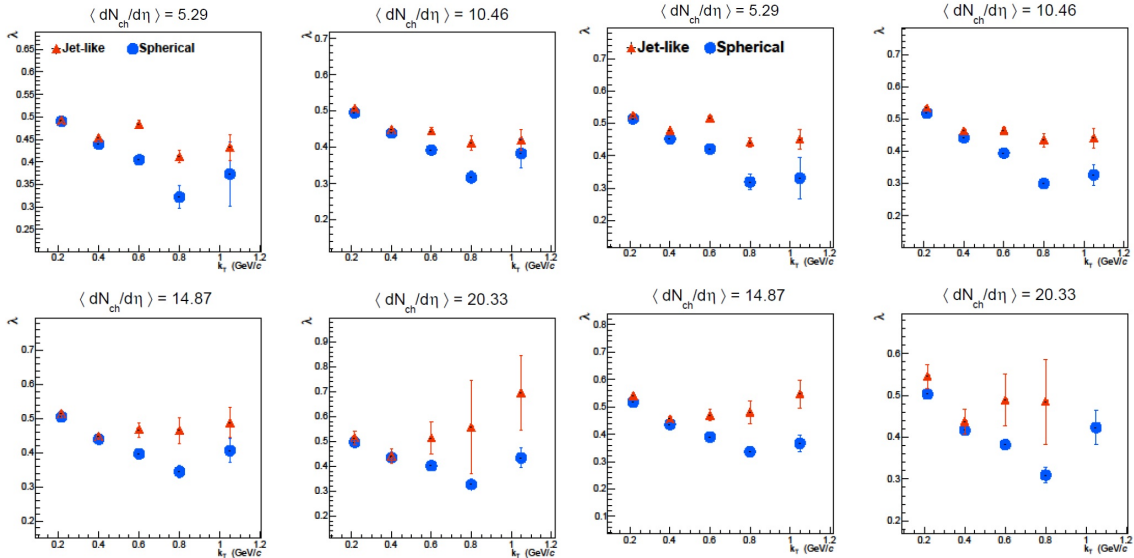
Fig. 13.2 Gaussian fit values of λ for spherical and jet-like events. $C(Q_{inv})$ fits are on the left and $C_2^{QS}(Q_{inv})$ on the right.

down. Again, the spherical event λs are relatively well behaved while the jet-like λs show an

instability of fit. From earlier analysis it is known that the value of λ should be constant of slowly rising with k_T. From this we conclude that a reasonable approach is to prohibit λ instability in influencing the extraction of correct homogeneity radii is to constrain it to a reasonable value physically motivated by the first three stable λ values in Fig 13.1. Model calculations using EPOS agree with this approach.

13.1.1 Fixed λ fit results

From previous fits the mean values are $< \lambda >= 0.851$ for $C(Q_{inv})$ fits and $< \lambda >= 0.996$ for $C_2^{QS}(Q_{inv})$, which confirms that the choice of f_c^2 was justified.
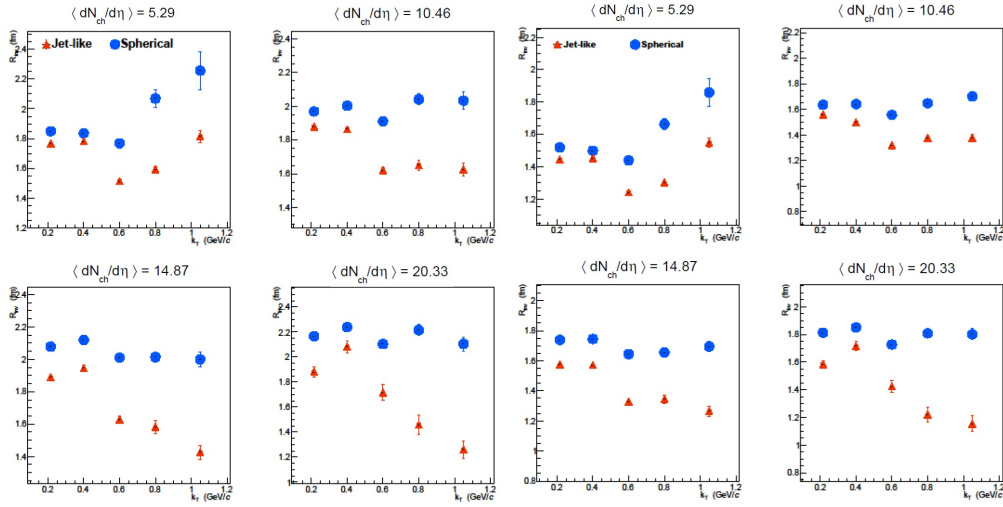
Fig. 13.3 Exponential fit values of R_{inv} for spherical and jet-like events. $C(Q_{inv})$ fits are on the left and $C_2^{QS}(Q_{inv})$ on the right.
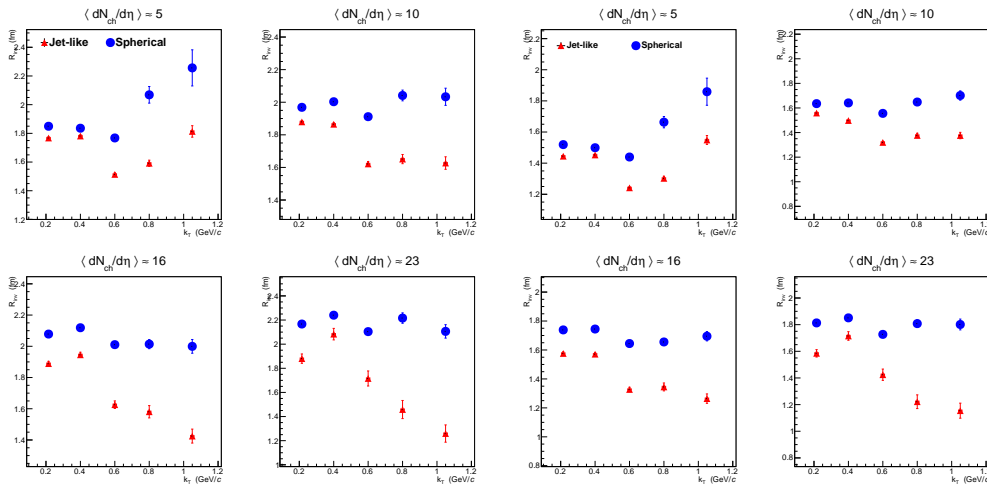
Fig. 13.4 Gaussian fit values of R_{inv} for spherical and jet-like events. $C(Q_{inv})$ fits are on the left and $C_2^{QS}(Q_{inv})$ on the right.

With the fixing of λ the shape change of fitted correlation function is controlled and meaningful homogeneity radii are extracted. In both cases the spherical events show that they keep a diminished dependence to k_T while the jet-like events show a clear multiplicity and k_T dependence. The radii extracted using a Gaussian or an exponential fit function are directly comparable using a known scaling constant. In both cases the general physics message is that spherical events do not show signs of hydrodynamic collectivity. The jet-like events resemble published results in k_T and multiplicity dependence.

13.1.2   Possible explanation of k_T dependence in jet-like events

As a possible explanation of the k_T dependence we offer a sketch. In this plot we propose
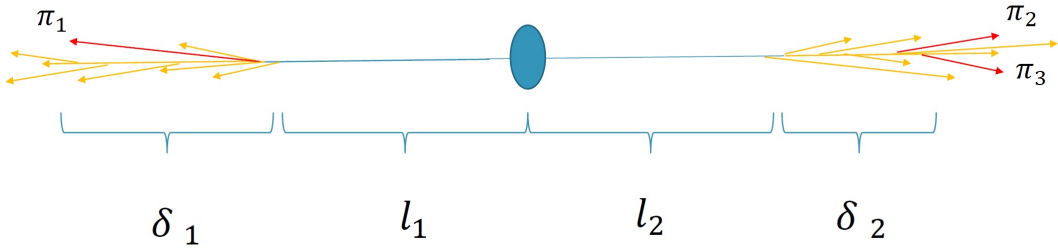
Fig. 13.5 Definition of the range (l) and spread (δ) distances in two jet events.

two distances called range (l) and spread (δ) of pion production points. As was explained earlier in the case of jet-like events a low k_T pion pair is usually formed using opposite jet pions, for example (π_1, π_2). They form a high Q_{inv} pair which consequently does not induce non-femtoscopic background in the low Q_inv range where quantum statistics are abundant. In the case of a high k_T pair, the two pions have a significantly higher chance of originating from the same jet thus creating a low Q_inv contribution to particle correlation. Such pairs like (π_1, π_3) still carry quantum statistical information on the emitter but also create most of the non-femtoscopic background. After the analysis of many jet-like events the extracted "radii" carry different information depending on their pair k_T .

$$R_{inv}(\pi_1, \pi_2) \cong 2 \cdot (l + \delta) \quad , \quad R_{inv}(\pi_1, \pi_3) \cong \delta$$

This means that if higher k_T values were available a simple calculation would allow for determination of the mean values of the range (l) and spread (δ) of pion production points in jet-like events. Consequently, a high k_T homogeneity radius must be lower than a low k_T one since both l and δ are real positive numbers. To do a calculation where the range and spread are reasonably well extracted a measurement of radii for k_T =5 GeV/c or higher should be enough.

13.2 Stability of the fit function exponent

To check if the assumption of a Gaussian or exponential fit function agrees with the general shape of the correlation function we make a Levy fit using the C_2^{QS} method. The fitted function is

$$C(Q_{inv}) = [(1 - f_c^2) + f_c^2 K(inv)(1 + \lambda exp(-R_{inv}^\alpha Q_{inv}^\alpha))]$$

Here we do not assume a range for the value of the exponential but do a free fit for all the parameters.

13.2.1 Free lambda fit
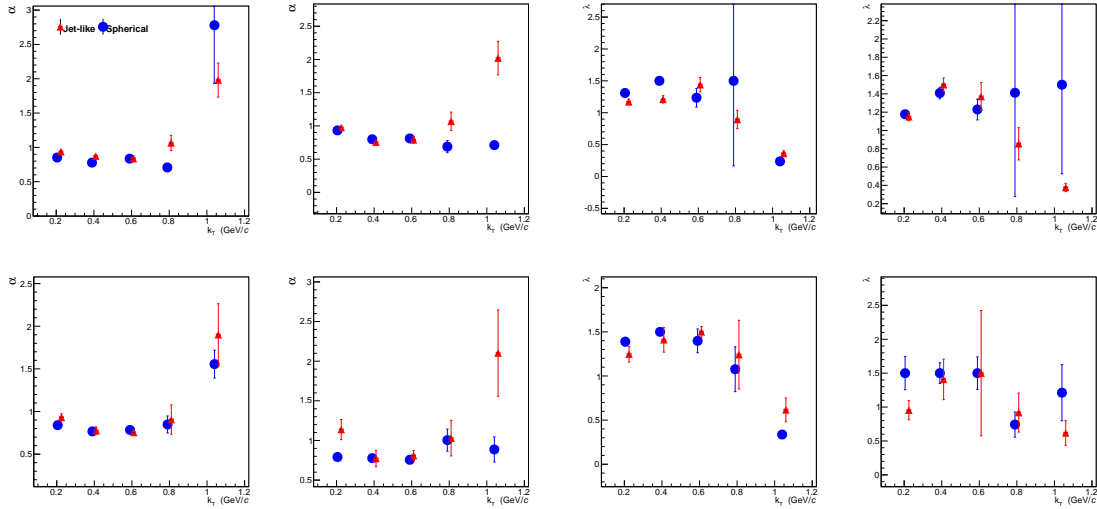
Fig. 13.6 Levy fit of α (left) and λ (right) parameters for spherical and jet-like pp events at $\sqrt{s} = 7$ TeV.

The general instability of fit is in agreement with previous fit results where only λ fits would non-physically oscillate. In a Levy fit one more degree of freedom allows for a more dramatic oscillation indicating general correlation function shape changes with k_T . This observation shows that a general comparison of only one observables dependence to k_T impossible without information on the other degrees of freedom.

13.2.2 Fixed lambda fit

To make a more direct comparison to previous results a fixed λ fit is performed. The value of λ is 0.85 as in the previous fits. The parameter α tends to unity clearly showing that a choice of exponential fit function is better than Gaussian. In addition, the fitted radii, different to previous results, still demonstrate the general characteristic that the decline in fitted radii with k_T and
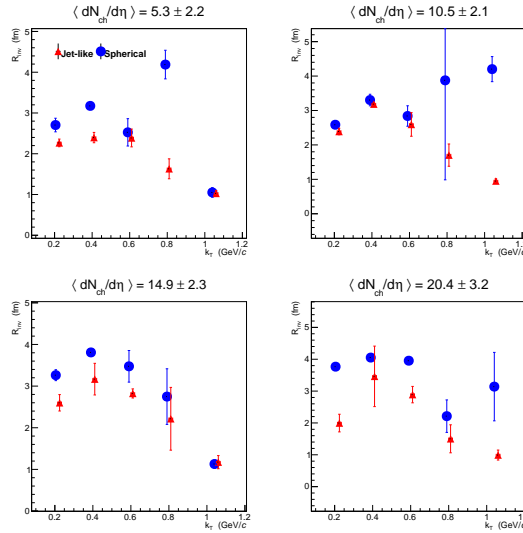
Fig. 13.7 Levy fit of homogeneity radii for spherical and jet-like pp events at $\sqrt{s} = 7$ TeV.
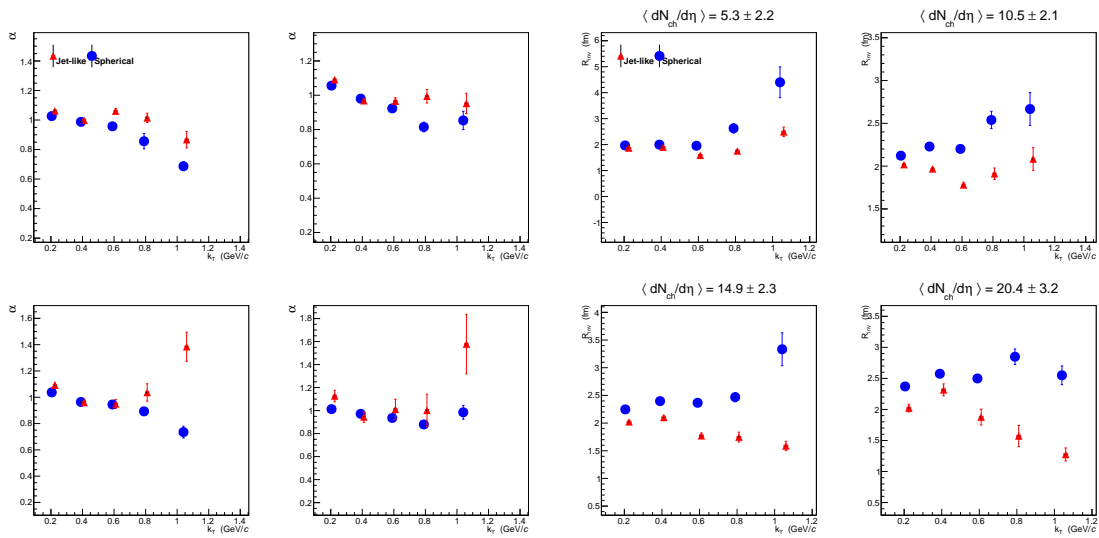
Fig. 13.8 Levy fit of α (left) and homogeneity radii (right) for spherical and jet-like pp events at $\sqrt{s} = 7$ TeV.

multiplicity is characteristic of jet-like events while such behavior is not observed with spherical event radii.

13.3   Physics consistency checks

Here we present all other physics consistency checks that were performed. They consists either from physics message stability tests or an expansion of investigation to other physics systems or observables.

13.3.1 Correlation function error effects

As one additional way of checking the stability of the final physics message we consider the influence of correlation function error per Q_{inv} bin. What is observed is that at lower Q_{inv} the systematics are less abundant and bigger errors are observed. The errors get larger with k_T but are never so large as to make fitting impossible. To check if the larger errors in higher k_T bins influence the physics result we take errors from higher k_T bins and set them onto lower k_T correlation function. With this procedure, all correlation functions have the same Q_{inv} bin errors and are fitted using the same code as before. We fit with a fixed lambda eponential Bowler-Sinykov fit function. Spherical events have much more statistics than jet-like so they
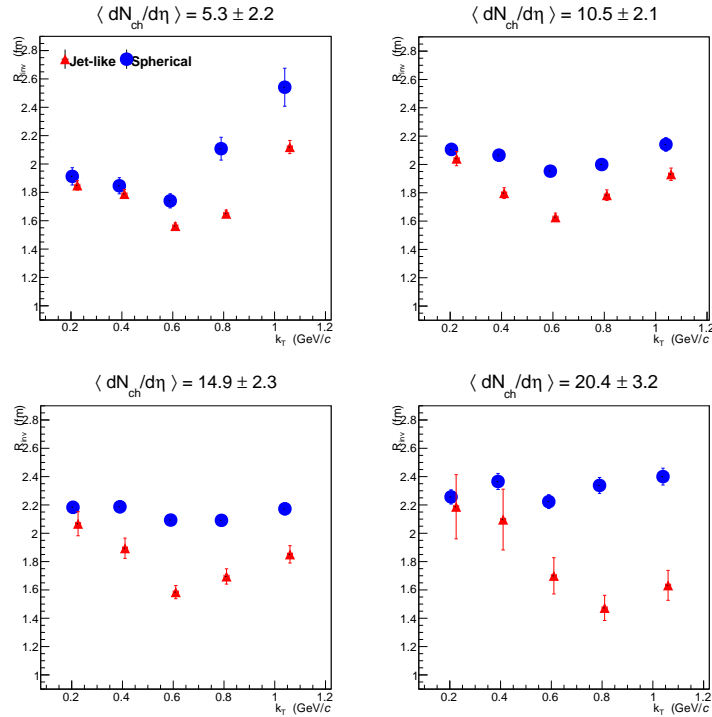
Fig. 13.9 Exponential fit with fixed lambda of correlation functions with large errors for spherical and jet-like *pp* events at $\sqrt{s} = 7$ TeV.

are less influenced by larger errors. For both jet-like and spherical events the physics message is stable, showing that systems with softer production tend to have a lack of k_T dependence in homogeneity radii. Jet-like event femtoscopy confirms that the observed k_T dependence is not due to larger errors at lower Q_{inv}.

13.3.2 Spherical events in p-Pb collisions

Motivated by the observation of a clear lack of k_T dependence in spherical event homogeneity radii for *pp* collisions we checked if a similar behavior can be measured for p-Pb data. Since, larger multiplicities shift the peak of the sphericity distribution towards higher values, we make

a pragmatic choice of $S_T > 0.85$ as our sphericity cut. In Figure 13.10 we see that a clear k_T
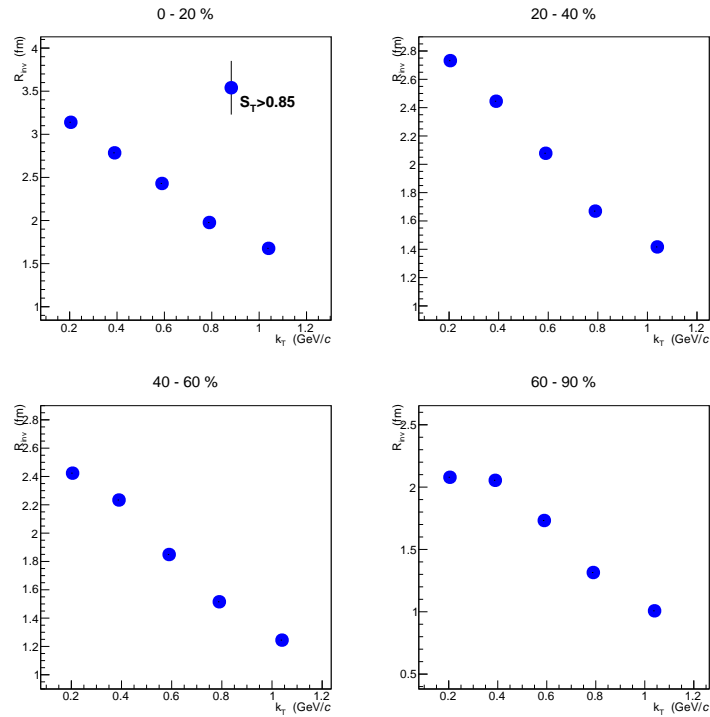
Fig. 13.10 Exponential fit with fixed lambda for spherical p-Pb events at $\sqrt{s} = 5.02$ TeV.

dependence is present in all centrality bins. We take this to be possibly indicative of a change in hydrodynamic behavior or the created system. Investigation using the out-side-long coordinates for various sphericities could possibly shed some light on the subject.

Chapter 14

Final results

Here we show plots with their physics messages. They are a result of taking into account all of the analysis presented in this thesis.
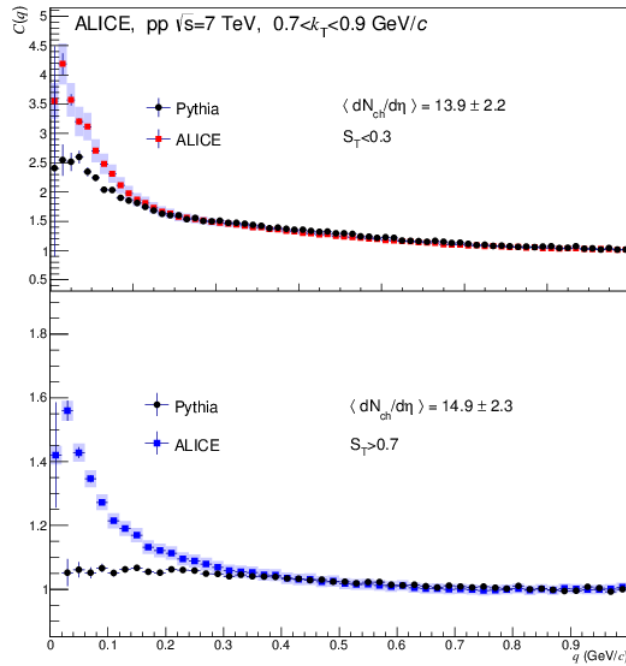
Fig. 14.1 Comparison of measured data to PYTHIA-Perugia0 generated correlation functions of jet-like and spherical *pp* events at $\sqrt{s} = 7$ TeV.

Main physics messages:

1. Non-femtoscopic background is generated by in-jet collimation.

2. A sphericity cut removes background and significantly enlarges the k_T range of the analysis.

3. Generators predict and agree with measured background for a wide Q_{inv} range.

4. Background has structure and can not be described by a simple Gaussian approximation.
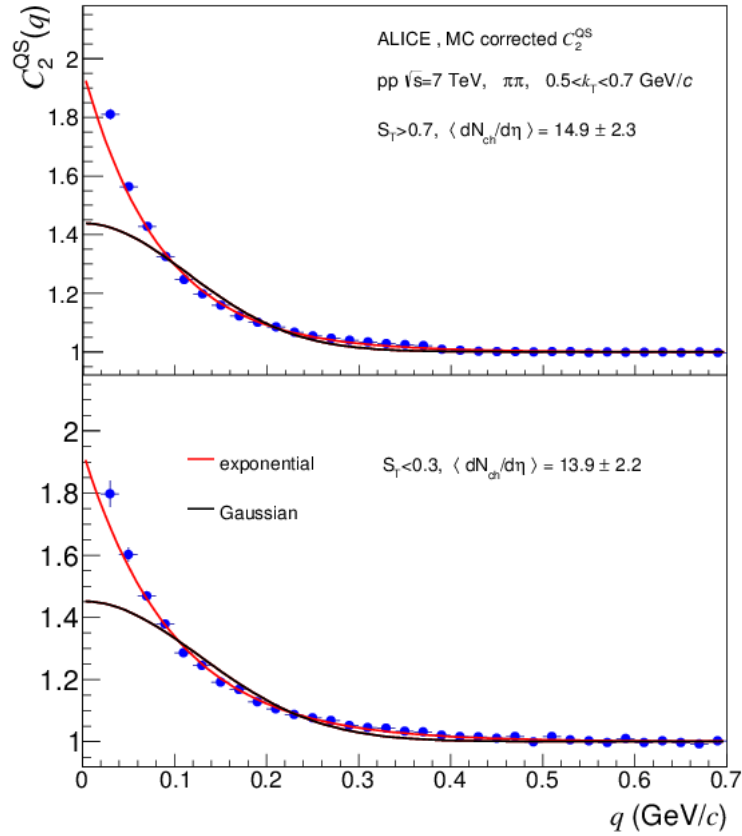
Fig. 14.2 Comparison of measured correlation functions for jet-like and spherical events to Pythia generator results.

Main physics message:

1. Exponential fit function better describes the observed correlations for both sphericity bins.

From internal check we observed a directed change from exponential to a more Gaussian form of correlation functions with the transition from *pp* to *pPb* and *PbPb* collision systems. The change is also dependent to event charged particle multiplicities. No mechanism has been proposed as an explanation for this thus making these and other observations of significant importance in further research.
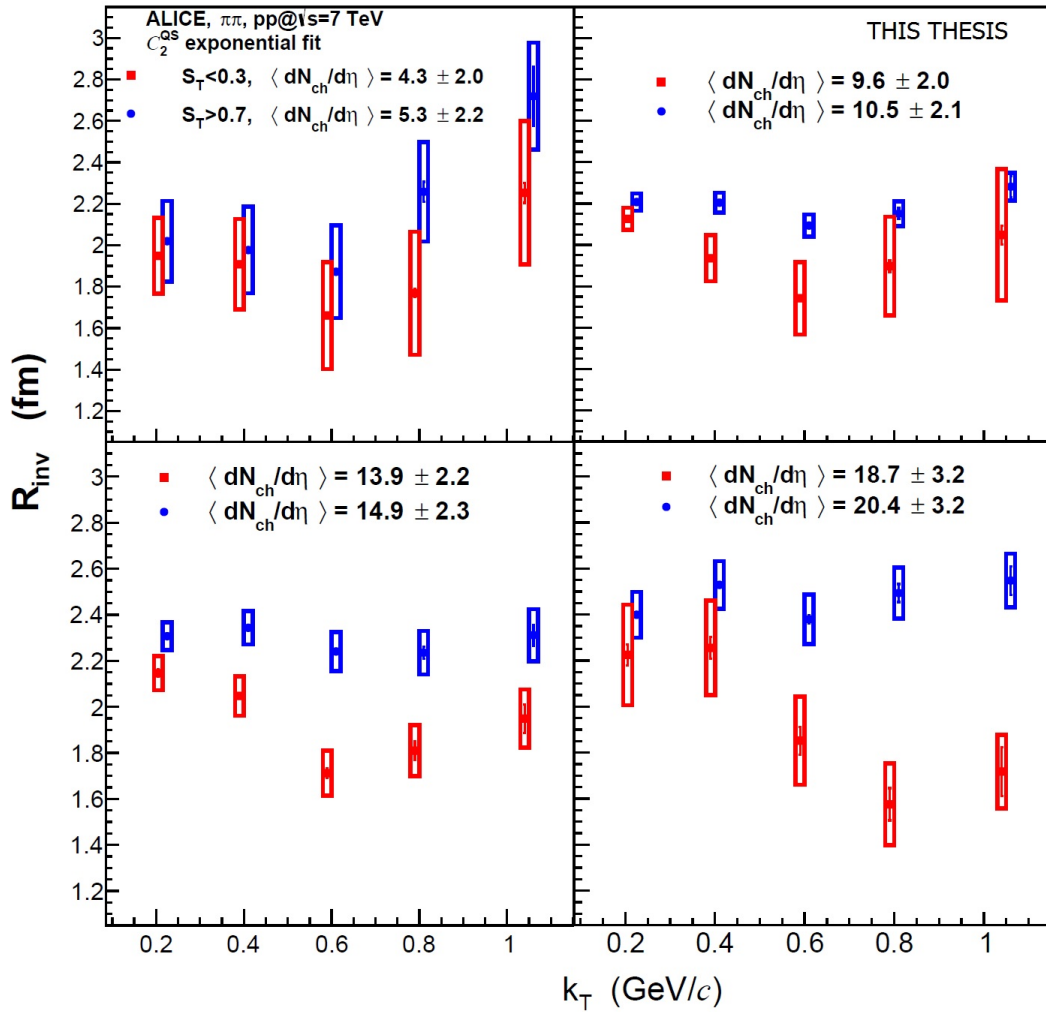
Fig. 14.3 Exponential fit homogeneity radii for jet-like and spherical pp events at $\sqrt{s} = 7$ TeV.

Main physics messages:

1. Spherical events show a diminished dependence to k_T.

2. Jet-like events exhibit a strong multiplicity and k_T dependence in a wide range of k_T.

3. Results for spherical events are against models with radial flow.

This plot is the main result of this analysis. We show that with a spherical event selection a significant portion of background is removed and it is possible to extract HBT radii for a larger range of k_T with respect to traditional analysis methods. The radii show low k_T dependence which is indicative of a lack of radial flow. Since the analysis is performed for only 1D further studies are needed in the 3D so as to ascertain if this trend stays in the out-side-long directions.

14.1 Conclusion

In this analysis we demonstrate one possible method for solving the jet-background problem in the two-particle interferometry analysis. Transverse sphericity has been used for the first time to identify and remove non-femtoscopic correlations and extend the analyzed k_T range extensively.

The fit results for spherical events, using no approximations or ansatz, differ from former published results and demonstrate a diminished k_T dependence of HBT radii. Such observation suggests a lack of radial flow in soft pion production dominated events (spherical). For extraction of jet-like event homogeneity radii we use a method of dividing out know background using Monte Carlo generated data. In this setting, the use of event generators is permitted since they correctly reproduce jet momenta and multiplicities. Jet-like events in a fixed λ fitting show a clear multiplicity and k_T dependence similar to the one observed in published results. A possible interpretation of these radii is that they are connected to the hadronization process within a jet. High k_T -s radii carry information on the hadronization length of the jet and the low k_T -s measure the path length of the jet leading particle before hadronization starts. For both shericity bins the exponential fit function is shown to be better suited for fitting and produces lower fit uncertainties.

This approach of using event shape observables has various possible future application. Within the range of transverse sphericities not used in this analysis $(0.3 < S_T < 0.7)$ there is a wealth of information about in-medium jets and their interactions. For this kind of analysis a better generator should be used. Other event shape observables could also play a significant role in further research. Event shape variables such as sphericity can be used on a segment of all the track making the event cut more differential. Various other analysis that depend on the correct identification of jet background could benefit from the introduction of such observables. In this respect all correlation analysis are candidates for the introduction of event shape selection. Finally, the mentioned change of CF shape with multiplicity could also carry information on a transition in collective behavior. These and many other options for further analysis show that the future of event shape selection in particle correlation research is a fruitful one.

References

[1] B. B. Abelev *et al.* [ALICE Collaboration], *"Femtoscopy of Pb-Pb and pp collisions at the LHC with the ALICE experiment"* J.Phys. G38 (2011) 124008

[2] B. B. Abelev *et al.* [ALICE Collaboration], *"Transverse sphericity of primary charged particles in minimum bias proton-proton collisions at sqrt(s)=0.9, 2.76 and 7 TeV"*, Eur. Phys. J. C, 72:2124, (2012)

[3] A. Banfi, G. P. Salam and G. Zanderighi, *"Resummed event shapes at hadron - hadron colliders"*, JHEP **0408**, 062 (2004) [hep-ph/0407287].

[4] B. B. Abelev *et al.* [ALICE Collaboration], *"Femtoscopy of pp collisions at $\sqrt{s} = 0.9$ and 7 TeV at the LHC with two-pion Bose-Einstein correlations"*, *Phys. Rev. D*, **84**, 11, (2011)

[5] J. Adams *et al.* [ALICE Collaboration], *"Two-pion femtoscopy in p-Pb collisions at $\sqrt{s_{NN}} =$ 5.02 TeV"* Phys.Rev. **C91** (2015) 034906, arXiv:1502.00559 [nucl-ex]

[6] B. B. Abelev *et al.* [ALICE Collaboration], *"Two- and three-pion quantum statistics correlations in Pb-Pb collisions at $\sqrt{sNN}$=2.76 TeV at the CERN Large Hadron Collider"* Phys. Rev. C, **89**, 024911.

[7] Aad, G. *et al.* [ATLAS Collaboration], *"Observation of a new particle in the search for the Standard Model Higgs boson with the ATLAS detector at the LHC"* Phys. Lett. B **716**, 1-29 (2012)

[8] Chatrchyan, S. *et al.* [CMS Collaboration], *"Observation of a new boson at a mass of 125 GeV with the CMS experiment at the LHC"* Phys. Lett B **716**, 30-61 (2012)

[9] Faddeev, L., Popov, V.N. *"Feynman Diagrams for the Yang-Mills Field"* Phys. Lett. **B25** 29 (1967)

[10] A. C. Irving and R. P. Worden, *"Regge Phenomenology"*, Phys. Rept. **34**, 117 (1977).

[11] J. M. Maldacena, *"The Large N limit of superconformal field theories and supergravity"*, Int. J. Theor. Phys. **38**, 1113 (1999) [Adv. Theor. Math. Phys. **2**, 231 (1998)] [hep-th/9711200].

[12] S. S. Gubser, I. R. Klebanov and A. M. Polyakov, *"Gauge theory correlators from noncritical string theory"*, Phys. Lett. B **428**, 105 (1998) [hep-th/9802109].

[13] E. Witten, *"Anti-de Sitter space and holography"*, Adv. Theor. Math. Phys. **2**, 253 (1998) [hep-th/9802150].

[14] Hagedorn, R. *"Statistical thermodynamics of strong interactions at high energies."* Nuovo Cimento Suppl. **3**, 147-186 (1965) alice

[15] Karsch, F., Laermann, E. & Peikert, A. *"Quark mass and flavour dependence of the QCD phase transition."* Nucl. Phys. B **605**, 579-599 (2001)

[16] Aoki, Y., Endrödi, G., Fodor, Z., Katz, S. D., & Szabó, K. K. *"The order of the quantum chromodynamics transition predicted by the standard model of particle physics"* Nature **443**, 675-678 (2006)

[17] Krieg, S. *et al.* [Wuppertal-Budapest Collaboration], *"Equation of state, fluctuations and the other recent results from LQCD"* J. Phys.: Conf. Ser. **535**, 012016 (2014)

[18] B. B. Abelev *et al.* [ALICE Collaboration], *"Measurement of charged jet suppression in Pb-Pb collisions at $\sqrt{s_{NN}} = 2.76$ TeV"* JHEP **1403**, 013 (2014)

[19] B. B. Abelev *et al.* [ALICE Collaboration], *"Centrality, rapidity and transverse momentum dependence of J/Ψ suppression in Pb-Pb collisions at $\sqrt{s_{NN}} = 2.76$ TeV "* Phys. Lett. B **734** 314-327 (2014)

[20] Elia, D. *et al.* [ALICE Collaboration], *"Strangeness production in ALICE "*. J. Phys.:Conf. Ser. 455, 012005 (2013), from International Workshop on Discovery Physics at the LHC (Kruger 2012).

[21] B. B. Abelev *et al.* [ALICE Collaboration], *"Multi-particle azimuthal correlations in p-Pb and Pb-Pb collisions at the CERN Large Hadron Collider"*. Phys. Rev. C **90** 054901 (2014)

[22] *"Heavy Ions: Results from the Large Hadron Collider"* Pramana **79**, 719–735 (2012), arXiv:1201.4264 [nucl-ex]

[23] CERN, *"A new state of matter created at CERN"* <http://press.web.cern.ch/press-releases/2000/02/new-state-matter-created-cern> (2000)

[24] Heinz, U., & Jacob, M. *"Evidence for a new state of matter: an assessment of the results from the CERN lead beam program."* <http://arxiv.org/abs/nucl-th/0002042> (2000)

[25] Adams, J. *et al.* [STAR Collaboration], *"Experimental and Theoretical Challenges in the Search for the Quark Gluon Plasma: The STAR Collaboration's Critical Assessment of the Evidence from RHIC Collisions"* Nucl. Phys. A **757**, 102-183 (2005)

[26] Adcox, K. *et al.* [PHENIX Collaboration], *"Formation of dense partonic matter in relativistic nucleus-nucleus collisions at RHIC: Experimental evaluation by the PHENIX collaboration"* Nucl. Phys. A **757**, 184-283 (2008)

[27] Arsene, I. *et al.* [BRAHMS Collaboration], *"Quark-gluon plasma and color glass condensate at RHIC? The perspective from the BRAHMS experiment"* Nucl. Phys. A **757**, 1-27 (2008)

[28] Back, B. *et al.* [PHOBOS Collaboration], *"The PHOBOS perspective on discoveries at RHIC"* Nucl. Phys. A **757**, 28-101 (2008)

[29] Heinz, U. *"The strongly coupled quark-gluon plasma created at RHIC"* J. Phys. A **42** 214003 (2009)

[30] O. S. Bruning, P. Collier, P. Lebrun, S. Myers, R. Ostojic, J. Poole and P. Proudlock, *LHC Design Report Vol.1: The LHC Main Ring*, CERN-2004-003-V1, CERN-2004-003.

[31] G. Aad *et al.* [ATLAS Collaboration], *The ATLAS Experiment at the CERN Large Hadron Collider*, JINST **3**, S08003 (2008).

[32] ALICE Collaboration, *The ALICE experiment at the CERN LHC* , Journal of Instrumentation 3, S08002 (2008), doi:10.1088/1748-0221/3/08/S08002

[33] S. Chatrchyan *et al.* [CMS Collaboration], *The CMS experiment at the CERN LHC*, JINST **3**, S08004 (2008).

[34] A. A. Alves, Jr. *et al.* [LHCb Collaboration], *The LHCb Detector at the LHC*, JINST**3**, S08005 (2008).

[35] Englert, F., Brout, R. *"Broken Symmetry and the Mass of Gauge Vector Mesons"* Phys. Rev. Lett. **13** (9): 321 (1964)

[36] Higgs, P. *"Broken Symmetries and the Masses of Gauge Bosons"* Phys. Rev. Lett. **13** (16): 508 (1964)

[37] Guralnik, G., Hagen, C., Kibble, T. *"Global Conservation Laws and Massless Particles"* Phys. Rev. Lett. **13** (20): 585 (1964)

[38] ALICE Collaboration. *"ALICE: Technical proposal for A Large Ion Collider Experiment at the CERN LHC"*. Technical Report CERN-LHCC-95-71, LHCC-P-3, CERN, (1995)

[39] K. Aamodt *et al.* [ALICE Collaboration], *"Alignment of the ALICE Inner Tracking System with cosmic-ray tracks"*.
JINST **5** (2010) P03003 [arXiv:1001.0502 [physics.ins-det]].

[40] J. Alme, Y. Andres, H. Appelshauser, S. Bablok, N. Bialas, R. Bolgen, U. Bonnes and R. Bramm *et al.*, *"The ALICE TPC, a large 3-dimensional tracking device with fast readout for ultra-high multiplicity events,"* Nucl. Instrum. Meth. A **622** (2010) 316 [arXiv:1001.1950 [physics.ins-det]].

[41] P. Cortese *et al.* [ALICE Collaboration], *"ALICE: Addendum to the technical design report of the time of flight system (TOF)"*.
CERN-LHCC-2002-016.

[42] H.H.Dalsgaard, *"Pseudorapidity densities in p+p and Pb+Pb collisions at LHC measured with the ALICE experiment"*, CERN-THESIS-2011-241.

[43] K. Aamodt *et al.* [ALICE Collaboration], *"Femtoscopy of pp collisions at $\sqrt{s} = 0.9$ and 7 TeV at the LHC with two-pion Bose-Einstein correlations"*, Phys. Rev. D **84**, 112004 (2011) [arXiv:1101.3665 [hep-ex]].

[44] J. Adam *et al.* [ALICE Collaboration], *"Two-pion femtoscopy in p-Pb collisions at $\sqrt{s_{NN}} =$ 5.02 TeV"*, Phys. Rev. C **91**, 034906 (2015) [arXiv:1502.00559 [nucl-ex]].

[45] R. Hanbury Brown and R. Twiss, textit"A New type of interferometer for use in radio astronomy", Phil.Mag., vol.**45**, pp. 663–682, 1954.

[46] R. Hanbury Brown and R. Twiss, textit"A Test of a new type of stellar interferometer on Sirius", Nature, vol.**178**, pp. 1046–1048, 1956.

[47] R. Lednicky and V. L. Lyuboshits, *Final State Interaction Effect on Pairing Correlations Between Particles with Small Relative Momenta*, Sov. J. Nucl. Phys. **35**, 770 (1982) [Yad. Fiz. **35**, 1316 (1981)].

[48] M. G. Bowler, *"Coulomb corrections to Bose-Einstein correlations have been greatly exaggerated"*, Phys. Lett. B **270**, 69 (1991).

[49] Y. Sinyukov, R. Lednicky, S. V. Akkelin, J. Pluta and B. Erazmus, *"Coulomb corrections for interferometry analysis of expanding hadron systems"*, Phys. Lett. B **432**, 248 (1998).

[50] Aamodt, K. *et al.* [ALICE Collaboration], *"The ALICE experiment at the CERN LHC"*.
JINST 3(08), S08002 (2008)

[51] Alme, J*et al.* [ALICE Collaboration], *"The ALICE TPC, a large 3-dimensional tracking device with fast readout for ultra-high multiplicity events"*. arXiv:1001.1950v1 [physics.ins-det] (2010).

[52] ALICE, *"The ALICE Time of Flight Detector"*
http://aliceinfo.cern.ch/Public/en/Chapter2/Chap2_TOF.html

[53] B. B. Abelev *et al.* [ALICE Collaboration], *"Freeze-out radii extracted from three-pion cumulants in pp, p-Pb and Pb-Pb collisions at the LHC"* Phys.Lett. **B79** (2014), arXiv:1404.1194 [nucl-ex].

[54] CMS Collaboration, *"Measurement of Bose-Einstein Correlations in pp Collisions at $\sqrt{s} = 0.9$ and 7 TeV"* JHEP, **5**, 29, (2011)

[55] Kozlov, G. A., Utyuzh,O. V., Wilk, G., Wlodarczyk, Z. *"Some forgotten features of the Bose-Einstein correlations"*, Physics of Atomic Nuclei, Vol. 71, No. 9, (2008)

[56] Paic, G. & Skowronski, P. K. *"Effect of hard processes on momentum correlations in pp and p anti-p collisions"*, J. Phys. G **31**, 1045 (2005) [hep-ph/0504051].

[57] MissMJ - licensed under the Creative Commons Attribution 3.0 Unported license *en.wikipedia.org/wiki/File:Standard_Model_of_Elementary_Particles.svg* (2006)

Appendix A

Gauss to Exp translation

In this section we show how the exponential and Gaussian fit functions overlap and what is the connection between their fit parameters. The main question to be answered is how does one compare Gaussian and exponential fit results in the case when there is no good indication which is the more appropriate fit function.

First one declares the correlation functions to be a probability density functions (PDFs). Using the standard shape of the PDFs without Coulomb correction:

$$\textbf{PDF(Exp)} = \lambda \cdot Exp(-R \cdot Q) \quad \textbf{PDF(Gauss)} = \lambda \cdot Exp\left(-(R \cdot Q)^2\right)$$

there is no a priori connection to physical observables. Every PDF has to be normalized and the expectation value is defined as:

$$E(x) = \int_0^\infty x \cdot PDF(x)dx.$$

A.1 Exponential PDF

The normalization condition gives the result for the λ parameter.

$$\int_0^\infty N\,\lambda \cdot Exp(-R \cdot Q)dQ = \frac{N\,\lambda}{R} = 1 \quad \rightarrow \quad N = \frac{R}{\lambda}$$

This is admissible since we are not describing an observed correlation but a probability distribution where λ is not the chaoticity parameter, but a normalization requirement. In any case, the HBT radii fits do not suffer from this approach since they are invariant to the correlation/PDF amplitude. Calculating the expectation value:

$$E(Q) = \int_0^\infty R \cdot Q \cdot Exp(-R \cdot Q)dQ = \frac{1}{R} = \langle Q \rangle_{\text{Exp}},$$

result which one would expect.

A.1.1 Gaussian PDF

The normalization condition again gives the result for the λ parameter.

$$\int_0^\infty N\,\lambda \cdot Exp\Big(-(R\cdot Q)^2\Big)dQ = N\,\frac{\sqrt{\pi}\cdot\lambda}{2R} = 1 \quad\rightarrow\quad N = \frac{2R}{\lambda\sqrt{\pi}}.$$

And the expectation value is:

$$E(Q) = \int_0^\infty \frac{2R}{\sqrt{\pi}}\cdot Q\cdot Exp(-R^2\cdot Q^2)dQ = \frac{1}{\sqrt{\pi}\cdot R} = \langle Q\rangle_{\text{Gauss}},$$

which means that within this first moment comparison scheme what the exponential and Gaussian PDF's call "the radius R" is not the same object, but they are shifted relatively by the now famous factor of $\sqrt{\pi}\approx 1.77$. If we change the Gauss PDF definition to

$$\textbf{PDF(Gauss)} = \lambda \cdot Exp\big(-\tfrac{R^2\cdot Q^2}{\sqrt{\pi}}\big)$$

the standard result $\langle Q\rangle_{\text{Gauss}} = 1/R$ is regained.

A.1.2 Switch of R and Q

If one redoes the calculations changing the roles of variable and parameter for R and Q the same result is obtained

$$\langle R\rangle_{\text{Exp}} = \frac{1}{Q} \qquad \langle R\rangle_{\text{Gauss}} = \frac{1}{\sqrt{\pi}\cdot Q}$$

since the mentioned roles of R and Q are completely symmetric.

A.2 The least square method

If one supposes that one of these distributions is the correct one and the other is wrongly used, then by trying to fit the wrong fit function one is really attempting to lower the differences of the fit function and the measured points. If we substitute measured point with one of the functions then we are effectively looking for the lowest value of:

$$I = \int_0^\infty \left[e^{-R'\cdot Q} - e^{-(R\cdot Q)^2}\right]^2 dQ.$$

The integral I is a function of the "correct" and the fitted radius $I(R,R')$. We minimise it with the standard approach.

$$\frac{dI(R,R')}{dR'} = 0.$$

The result is an elaborate expression which is not easily calculated. Using the Mathematica9 package:

$$\frac{R'}{R} \approx 1.89 \quad \text{which is close to} \quad \frac{\langle R' \rangle}{\langle R \rangle} \approx 1.77,$$

where R and R' are the "actual" and the best fit radius respectfully. These calculations explain why the Gaussian and the exponential fit functions differ by $\approx 80\%$. We wish to conclude that by using these calculations one is able to translate from a Gaussian to an exponential fit but is not, and should not, be able to answer the question as to which is the correct one or if indeed either is the correct one. In the end one is left with his senses and the χ^2 test to determine the best fit function.

Chapter 15

Uvod

Mjerenje dvočestičnih korelacija u visoko energetskim sudarima je potvrđena metoda visoke preciznosti određivanja vremensko-prostornih skala stvorenog sustava. Mjerenjem radijalne evolucije sudarom stvorenog emitera, moguće je odrediti važne informacije o stanju proizvedene QCD materije. Detaljno razumijevanje femtoskopskih karakteristika protonskih sudara je dodatno nužno kao prirodna ekstrapolacija ka istraživanju sudara teških iona. Sa početkom rada LHC sudarivača na 7 TeV-a u centru mase, multipliciteti protonskih sudara počinju biti usporedivi s onim izmjerenim u perifernim AA sudarima na RHIC i LHC sudarivačima[1], time povećavajući važnost detaljnog razumijevanja nukleon-nukleon sudara.

proton Nabijeni pioni čine većinu proizvedenih mezona ($\approx 60\%$) te dopuštaju statistički bogatu analizu sa mogučnošću da se detaljno promatraju razne kategorije sudara.

Cilj ovog istraživanja je promatrati korelacije identičnih čestica, posebice nabijenih piona, birajući sudare specifičnih oblika koji su od posebne važnosti. Karakteriziranjem sudara po njihovoj topologiji, koristeći transverzalnu sferičnost [2] kao glavnu globalnu varijablu oblika sudara, moguće je razlikovati sudare koje sadrže čestične mlazove od onih sferičnog oblika sa idejom da se navedene dvije kategorije sudara razlikuju u jačini sudara, te kao takve, nose sebi karakteristične informacije o perturbativnim, odnosno, neperturbativnim svojstvima stvorene QCD materije.

Iz prošlih studija je poznato da nefomtoskopski doprinosi dvočestičnim (HBT) korelacijama, uzrokovani mlazovima ili sličnim strukturama, uzrokuju značajan udio pozadinskog signala u području visokog valnog vektora k_T para [4]. Zbog niskog omjera signala i pozadine, navedene korelacije efektivno zaustavljaju pokušaje analize za visoke vrijednosti k_T para ($k_\mathrm{T} > 0.7$ GeV/c). Još uvijek je otvoreno pitanje na koji način najbolje uzeti u obzir sve nefemtoskopske doprinose te odrediti točne radijuse homogenosti sa pravilnom interpretacijom. U ovom radu mi pred-lažemo novu metodu zasnovanu na činjenici da je sa pravilnim odabirom reza u sferičnosti sudara moguće ukloniti večinu pozadinskog signala te tako značajno proširiti doseg moguće analize

u k_T. Na taj način bi izmjereni radijusi homogenosti bili dobiveni bez unošenja pretpostavki te bi bili neovisni o odabiru Monte Carlo generatora sudara. Ujedno, rezanjem po raznim varijablama oblika sudara moguće je istražiti spektar QCD sistema različitih jakosti sudara te opaziti interakciju mlaza i pratečeg sudara. Na taj način bi se mogao promatrati gubitak energije čestice uzrokovan transportom kroz QCD medij.

U ovom radu, pri analizi sudara sa proizvedenim mlazovima, pokušano je identificirati sve nefemtoskopske doprinose korelacijama putem usporedbe sa Monte Carlo simulacijama. Usporedbom mjerenih podataka ALICE detektora sa PYTHIA i PHOJET generiranim rezultatima za pionske parove istog i suprotnog naboja, moguće je stvoriti ispravljenu korelacijsku funkciju te po prvi put odrediti Bose-Einsteinove korelacije u mlazovima čestica te ponuditi interpretaciju istih.

Nekoliko opcija efektivnog uklanjanja nefemtoskopskih korelacija je sugerirano te uspoređeno unutar ovog rada. Istražena je mogučnost ne-Gausijanskih korelacijskih funkcija. Konačno, pregled razultata sa smjernicama budučih istraživanja je sugeriran sa jasnim ciljom fizikalne interpretacije i generalizacije rezultata.

Predloženo je nekoliko metoda uklanjanja nefemtoskopskih pozadinskih signala te je napravljena usporedba istih. Istražena je mogučnost prilagodbe putem negausijanskih funkcija te su ponuđeni rezultati prilagodbe za nekoliko realističnih opcija.

U ovoj su analizi detaljno istaženi efekti selekcije po obliku događaja na femtoskopsku analizu piona u proton-proton sudarima pri energiji od 7 TeV-a u centru mase. Slijedeća dva poglavlja daju pregled kvatne teorije polja te istraživanja kvark-gluonske plazme. U osamnestom poglavlju je opisan eksperimentalni postav detektora i akceleratora. Poglavlje nakon toga sadrži opis femtoskopije, njezine povezanosti sa HBT efektom te moguće primjene metode. Nadalje, pokazani su rezultati analize mjerenih podataka ALICE detektorom te Monte Carlo generiranih simulacija. Usporedba je napravljena između mjerenih i simuliranih podataka za pionske parove istog te suprotnog naboja. U predzadnjem poglavlju su prikazani svi odobreni ALICE rezultati sa unutarnjih provjerama sistematske neodređenosti. Konačno, razmatrane su λ i α varijable u procesu prilagodbe te njihov utjecaj na konačni rezultat. Disertacija završava sa pregledom rezultata sugeriraući buduće smjernice istraživanja sa jasnim ciljem fizikalne interpretacije te generalizacije rezultata. U dodatku je ponuđen izvod metode usporedbe rezultata dobivenih gausijanskim i eksponencijalnim funkcijama prilagodbe.

Chapter 16

Kvarkovsko-gluonska plazma

Među ovim redovima se nalazi povjesni pregled proučavanja kvarkovsko-gluonske plazme. Dan je opis raznih eksperimenata te njihovi glavni rezultati.

16.1 Kratki pregled

Uz otkriće asimptotske slobode, opaženo je da se QCD materija mora, na dovoljno visokoj temperaturi i tlaku, "otopiti" te iz bezbojnih hadrona stvoriti novu vrstu materije nazvanu kvar gluonskom plazmom. Smatra se da je Svemir prošao kroz takvu fazu, 10^{-12}s nakon Velikog Praska, u trajanju od 10 mikrosekundi. Kako se Svemir širio, kvarkovsko-gluonska plazma se hadronizirala, te se partonska materija ograničila na stvoranje mezoni i hadroni. Povijesno se smatralo da je tranzicija sa stanja slobodnih kvarkova i gluona na hadronsku materiju zapravo fazni prijelaz prve vrste. Prvi proračuni su procijenjivali kritičnu temperaturu malo iznad vrijednosti mase najlakšeg π-mezona [14, 15]. Sa razvojem računalne tehnologije numerički su QCD proračuni na prostorno-vremenskoj rešetci (LQCD) postali dovoljno osjetljivi te pokažu da se rapravo radi o glatkom prijelazu faze [16, 17]. Sljedeći opće prihvaćanje QGP-a napravljena je lista eksperimentalnih potpisa takvog stanja. U slijedećem poglavlju se nalazi kratak popis takve vrste i glavni eksperimentalni rezultati.

16.2 Potpisi kvarkovsko-gluonske plazme

Ako je stanje razvezanih kvarkova i gluona postignuo u eksperimentu, onda, promjena raznih observabli mora pratiti. Usprkos velikom broju takvih observabli, ovdje se nalaze neke od prvih opaženih te najupečatljivijih rezultata.

16.2.1 Potisnuće mlazova

Potisnuće mlazova je fenomen u kojem se jednom od dva suprotno orijentirana mlazova znatno smanji energija i p_T, uzrokovano iterakcijom s vrućom QCD materijom. Energija je raspršena sa

vodećeg partona putem interakcije sa QCD medijem, što je oblik QCD zakočnog zračenja (njem. *bremsstrahlung*). Poput drugih eksperimenata, ALICE kolaboracija je opazila efekt potisnuća
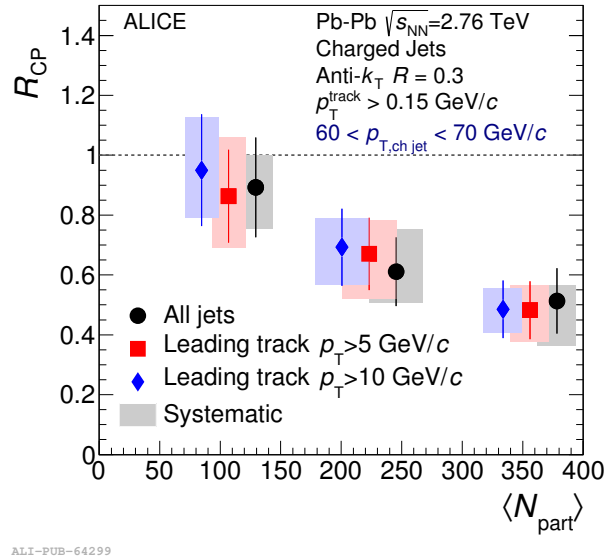
Fig. 16.1 Nuklearni modifikacijski faktor R_{CP} u funkciji srednjeg broja sudionika sudara za pristrane i nepristrane mlazove, R=0.3. Izvor [18]

mlazova. Ovdje je pokazan nuklearni modifikacijski faktor R_{CP}, omjer centralnih i perifernih sudara, kao funkcija multipliciteta. Jasno se vidi da potisnuće raste sa povećanjem multipliciteta što je u potpunom slogu sa pretpostavkom o nastanku kvarkovsko-gluonske plazme.

16.2.2 Potisnuće kvarkoniuma

Kvarkonium je mezon sa kvark-antkvark parom istog okusa. Ovdje razlikujemo $c\bar{c}$ te $b\bar{b}$, koje zovemo J/Ψ i Υ mezonima. Pri visokim temperaturama i gustoćama, partoni su u QCD mediju pod velikim utjecajem raznih polja što dopušta mogučnost zasjenjenja polja partnera u mezonu. Ovaj efekt je nalik zasjenjenja u elektromagnetizmu kod ionizirane plazme. Kao posljedica ovog zasjenjenja, mezoni koji moraju dugo putovati kroz vruću QCD materiju imaju znatno povećanje vjerojatnosti disocijacije te efektivnog raspada mezonske veze. Ovdje je prikazana ovisnost nuklearnog modifikacijskog faktora R_{AA} o centralitetu za inkluzivnu J/Ψ proizvodnju pri PbPb sudarima. Jasno se vidi potisnuće očekivano u slučaju proizvodnje kvarkovsko-gluonske plazme.

16.2.3 Povećanje stranosti

Povećanje u proizvodnji stranih mezona je jedna od pretpostavljenih posljedica kvarkovsko-gluonske plazme. Zbog visoke temperature proizvodnja stranih kvarkova je povečana što se mora vidjeti usporedbom sa rezultatima proizvodnje u proton-proton sudarima.

 ALICE eksperiment vidi jasno pojačanje proizvodnje svih stranih četica. Vrijedno je napomenuti da je povećanje veće u slučaju većih multipliciteta te većeg broja stranih kvarkova u mezonu.
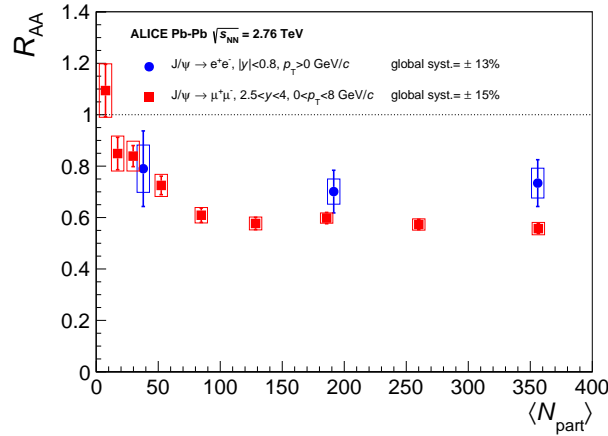
Fig. 16.2 Ovisnost nuklearnog modifikacijskog faktora R_{AA} o centralitetu za inkluzivnu J/Ψ proizvodnju pri PbPb sudarima na $\sqrt{s_{NN}} = 2.76$ GeV, mjereno ALICE detektorom na srednjem i prednjem rapiditetu. Izvor [19]
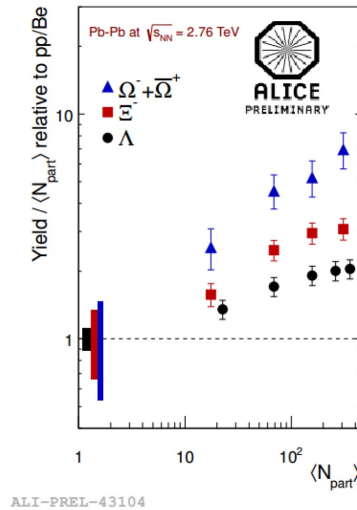
Fig. 16.3 Proizvodnja stranih mezona za PbPb sudare u usporedbi sa proton-proton sudarima, izmjereno na ALICE detektoru [20].

16.2.4 Tok čestica

Potpis hidrodinamičkog toka čestica je u skladu sa postojanjem kvarkovsko-gluonske plazme ali se nebi smio smatrati dokazom iste. Korisna observabla u ovom pogledu je anizotropni tok. On mjeri anizotropiju u mjerenoj distribuciji količine gibanja u ovisnosti o azimutalnom kutu. Pri necentralnim sudarima teških iona, preklop između sudarenih iona je oblika badema, što uzrokuje gradijent tlaka, između vrućeg centra i hladnog ruba sistema, što ujedno ovisi o azimutalnom kutu Φ. Ovako stvorena anizotropija stvara mjerljive efekte u distribuciji količine gibanja emitiranih čestica te je prezntirana putem v_n koeficijenata toka

$$v_n = <cos[n(\Phi - \Psi_n)]>$$

gdje je Φ azimutalni kut, n je red harmonika, te je Ψ_n n-ti red ravnine reakcije.
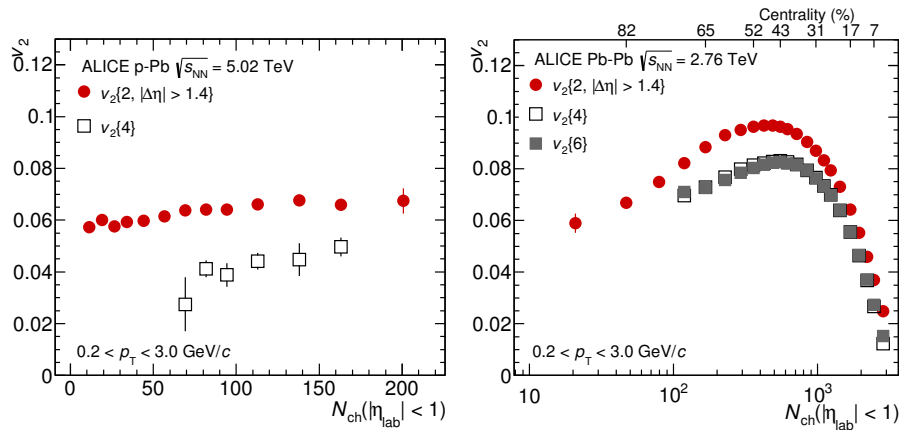
Fig. 16.4 Mjerenje $v_2\{2\}$, $v_2\{4\}$, i $v_2 6$ u p-Pb (lijevo) te Pb-Pb (desno) sudarima. Mjerenje $v_2\{2\}$ je dobiveno sa $|\Delta\eta| > 1.4$ razmakom. [21]

16.3 Sudari teških iona

Od početka 1908-tih godina, sudari teških iona dopuštaju znanstvenicima eksperimentalno promatranje materije na visokim temperaturama i gustoćama. Teorijski i eksperimentalni alati su se trebali razviti kako bi dopustili razumnu kvalitetu znantvenog istraživanja. Observable poput tlaka i temperature su bile jasan izbor, ali pošto one pripadaju u područje termodinamike prvo su trebali biti ispunjeni uvijeti ekvilibracije sistema poput velikog broja interagirajućih čestica te dugo vrijeme života sustava. U tu svrhu sudari elektrona ili protona ne proizvode dovoljno velike multiplicitete. Ipak, poznato je da sudari nukleona na dovoljno visokim energijama stvaraju dovoljno veliku gustoću i temperaturu koja je potrebna za otapanje hadrona i stvaranje kvarkovsko-gluonske plazme. U usporedbi sa Velikim Praskom, koji je trajao oko 10^{-5}s, sustavi stvoreni u sudarima teških iona imaju znatno kraće vrijeme života. Kroz 10^{-21}s sva hadronizacija je gotova i više nema potpisa kvarkovsko-gluonske plazme.

Zadnjih 30 godina provodi se istraživanje sudara atomskih jezgara. Program je započeo
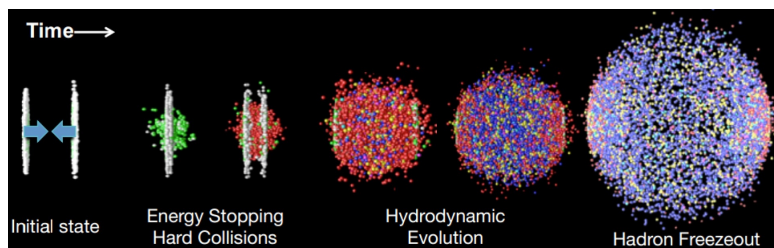
Fig. 16.5 Shema sudara teških iona. Preuzeto iz [22].

sa Super Proton Synchrotron (SPS) akceleratorom na CERN-u, te sa Alternating Gradient

Synchrotron u Brookhaven National Laboratory (BNL) u Upton, New York. Oba sustava su započela eksperimente sa laganim nukleonima, te su prešli na teže jezgre tek krajem 1990-tih. Energijski režim rada na CERN-ovom je akceleratoru dopustio potvrdu stvaranja novog stanja materije [23, 24]. Uskoro je nova generacija akceleratora i eksperimenata preuzela vodstvo u istraživanju. Na BNL-u je započeo rad Relativistic Heavy Ion Collider (RHIC) sudarivača, zajedno sa njegova četiri eksperimenta; BRAHMS, PHENIX, PHOBOS i STAR. RHIC-ov je energijski režim garantirao znatan napredak postižući $\sqrt{s_{NN}} = 200$ GeV-a odnosno 40 TeV u centru mase. Kao što je bilo očekivano, sva četiri eksperimenta su potvrdila opažanje stvaranja nove vrste materije [25–28]. Rezultati su ujedno pokazali da se vruća QCD materija ne ponaša kao slabo interagirajući plin nego pokazuje jasne potpise kolektivnog toka nalik na gotovo savršenu relativističku tekućinu niske viskoznosti [36].

Danas, oba akceleratora, RHIC i LHC, znatno doprinose istraživanju kvarkovsko-gluonske plazme te sudara teških iona.

Chapter 17

Oblici sudara te transverzalna sferičnost

Mogućnost korištenja topologije sudara pri efektivnoj karakterizaciji jačine sudara oslanja se na činjenicu da se dominantni mehanizam QCD produkcije čestica mijenja ovisno o ukupnoj invarijantnoj masi $Q^2 = \sum_i (p^\mu p_\mu)_i$ početnog partonskog sudara. Procesi mekanih sudara karakterizirani su neperturbativnom QCD produkcijom laganih mezona, bez preferiranog smjera pa tako i bez čestične kolimacije. Mlazovi, produkti jakih raspršenja, se nalaze u režimu perturbativne QCD teorije te kolimiraju većinu proizvedenih čestica. Osnovno razlikovanje putem topologije sudara dopušta računalno jednostavan način razlikovanja jakih i slabih procesa.

Pri događajima visokog multipliciteta, mora se dogoditi proces visoke konverzije energije u masu. To se može dogoditi kao jedno jako raspršenje koje stvara mlazove ili kao više-čestična interakcija gdje mnoštvo nisko-energijskih procesa stvara velik broj laganih mezona. Ovi procesi stvaraju drugačiji rasap čestica u $\eta - \phi$ ravnini na što bi observable osjetljive na oblik događaja morale biti osjetljive.

U ovoj je analizu bila odabrana transverzalna sferičnost (S_T) kao glavna observabla opažanja te su istražene razne posljedice njezine primjene u femtoskopskoj analizi piona.

17.1 Transverzalna sferičnost

U ovoj smo analizi koristili transverzalnu sferičnost kao observablu oblika događaja. Ona je skalar koji karakterizira rasap čestica u $\eta - \phi$ ravnini. Trasverzalna sferičnost razmatra sve primarne nabijene čestice sudara te se zato zove "izravnom" globalnom varijablom oblika događaja. Njezina je funkcija razlikovati topologije sferičnog oblika te oblika mlaza, razdvajajući ih na suprotnim stranama spektra sferičnosti.

Događaji koji pokazuju nakupljanje čestica su prepoznati da sadrže korelacije nalik mlazova dok su sudari sa jednolikom raspodjelom čestica u $\phi - \eta$ ravnini prepoznati kao sferični događaji.

Da bi se izbjegao utjecaj doprinosa u smjeru gibanja čestica računanje trasverzalne sferičnosti je ograničen samo na transverzalne količine gibanja čestica te je sferičnost prikazana putem

svojstvenih vrijednost matrice transverzalne količine gibanja:

$$S_{XY} = \frac{1}{\sum_i p_T^i} \sum_i \frac{1}{p_T^i} \begin{pmatrix} (p_x^i)^2 & p_x^i \cdot p_y^i \\ p_x^i \cdot p_y^i & (p_y^i)^2 \end{pmatrix}, \tag{17.1}$$

gdje su svijstvene vrijednosti λ_1 i λ_2. Transverzalna sferičnost je tako definirana sa

$$S_T = \frac{2 \cdot \min(\lambda_1, \lambda_2)}{\lambda_1 + \lambda_2}. \tag{17.2}$$
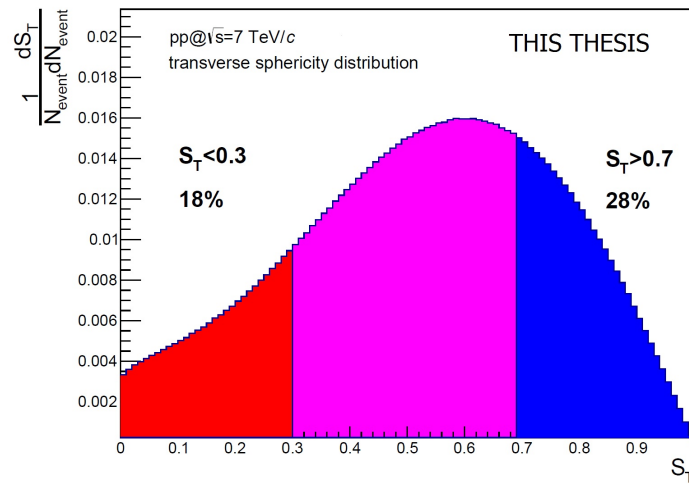
Fig. 17.1 Distribucija transferzalne sferičnosti za proton-proton sudate pri $\sqrt{s} = 7$ TeV.

Putem ove konstrukcije $S_T \in [0,1]$, gdje je $S_T \approx 0$ sudar visoke nesferičnosti odnosno topologije koja sadrži čestične strukture nalik mlaza te $S_T \approx 1$ sasvim izotropan te sferičan događaj.
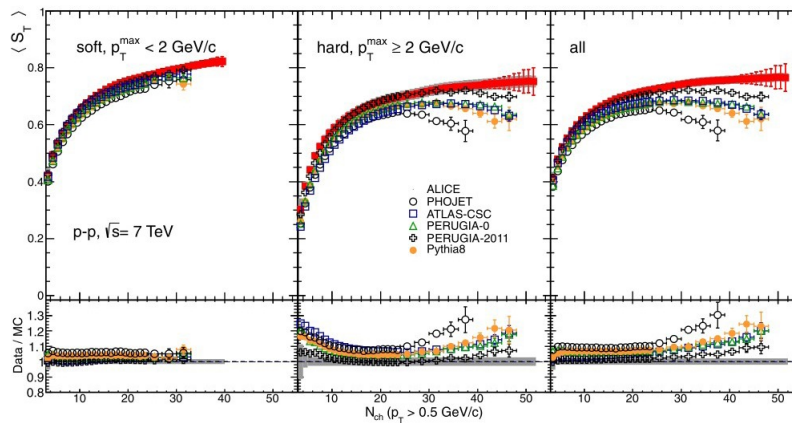
Fig. 17.2 Srednja transverzalna sferičnost u ovisnosti o multiplicitetu nabijenih čestica. Mjerenja ALICE kolaboracije su uspoređena sa generatorima: PHOJET, PYTHIA6 (prilagodba vrste: ATLAS-CSC, PERUGIA-0 te PERUGIA-2011) i PYTHIA8. [2]

Ovakva karakterizacija nudi mogućnost pažljivog biranja sferičnosti te razmatranja raznih topologija događaja. Događajima takve topologije da su karakterizirani kao "srednje sferični" $(0.3 < S_T < 0.7)$ je najčešće teško prepoznati mlazove jer ih zapravo nemaju, unatoč ograničenoj kolimaciji četica, ili ih imaju ali prikrivene u pozadinskom rasapu čestica. Postoji i mogućnost da događaj bez mlazova ima strukturu nalik mlaza. Takvi događaji će isto biti prepoznati kao srednje sferišni. U ovoj je analizi sferičnost računana na isti naćin kao u 17.1 koristeći sve tragove čestica sa $|\eta| < 0.8$ te $p_T > 0.5$.

Nove prilagodbe Pythia generatora sadrže opažene distribucije transverzalne sferičnosti te pokazuju znatno bolje slaganje sa mjerenjima.

17.1.1 Sferični događaji $(S_T > 0.7)$

Sferični događaji su podskup svih mjerenih događaja koji pokazuju manjak bilo kakve strukture mlaza ili čestične kolimacije. Takvi događaji ne sadrže dominaciju produkcije putem jakih sudara ili potisnitih mlazova. U ovakvim izotropnim događajima većina je energije potrošena u nalik
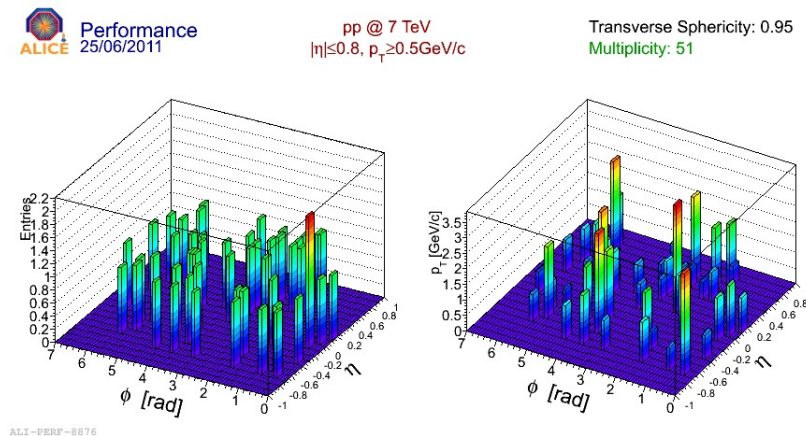
Fig. 17.3 Događaj visoke sferičnosti sa svojim karakterističnim oblikom.

termalnoj produkciji laganih mezona tako da je p_T spektar pomaknut prema nižim vrijednostima u odnosu na onaj osnovnog skupa sudara. Isto tako, u $\phi - \eta$ ravnini se ne vide lokalizirane strukture čestica ili visoki p_T tornjevi jer p_T spektar ne sadrži rep polinomnog oblika pri visokim vrijednostima količine gibanja.

Sferični događaji visokog multipliciteta se moraju razumjeti kao događaji gdje je glavnica čestične produkcije sadržana u nisko energetskoj QCD hadronizaciji te ne u jakim raspršenjima gdje je pristup putem Feynmanovih dijagrama više primjenjiv.

Definicija transverzalne sferičnosti sadrži jasnu ovisnost o multiplicitetu. Ta činjenica znaći da događaji visokog multipliciteta najčešće imaju višu sferičnost $S_T \approx 1$ dok događaji niske sferičnosti imaju više oblik mlaza sa $S_T \approx 0$. Ova karakteristika je jasno opažena u mjerenjima.

Mora se naglasiti da se to ne smije uzeti kao direktna funkcionalna ovisnost, ili mapiranje, između sferičnosti i multipliciteta, ili da sveki događaj visokog multipliciteta mora biti sferičan, kao što će biti pokazano u ovoj analizi.

17.1.2 Događaji niske sferičnosti ($S_T < 0.3$)

Događaji niske sferičnosti pokazuju eksplicitne znakove čestične kolimacije zbog mlazova, mini-mlazova ili potisnutih mlazova. Oni su u strukturi nalik olovke te sadrže produkciju čestica karakterističnu jakim raspršenjima.
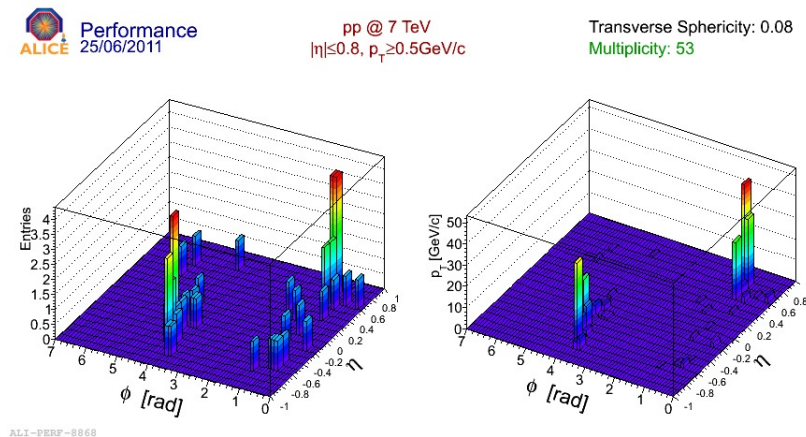
Fig. 17.4 Događaj niske sferičnosti i visokog multipliciteta.

Kolimacija čestica donosi i više-čestične korelacije u prostoru količine gibanja. Konstituenti svakog mlaza imaju sličan smjer te količinu gibanja što nije produkt kvantno-statističkih uvjeta nego QCD hadronizacije. Ovaj višak čestične korelacije doprinosi mjerenoj dvočestičnoj korelaciji pri tradicionalnim femtoskopskim analizama te se smatra pozadinom koja se mora parametrizirati i/ili ukloniti. U ovoj analizi će biti pokazano da je rez u S_T varijabli razumna metoda uklanjanja pozadinskog signala.

Slika 17.4 demonstrira da su p_T tornjevi $\eta - \phi$ ravnini za sferične događaje znatno niži od onih u događajima sa mlozovima te da su događaji sa strukturom mlaza te visokog multipliciteta točno prepoznati kao nisko-sferični događaji.

Usporedba p_T spektra za događaje visoke i niske sferičnosti

Razlika između p_T spektara događaja visoke i niske sferičnosti pokazuje točno razumijevanje termalne slike sferičnih događaja. Biranjem sferičnih događaja uspješno je uklonjen polinomski rep koji se nalazi u sudarima sa mlazovima.
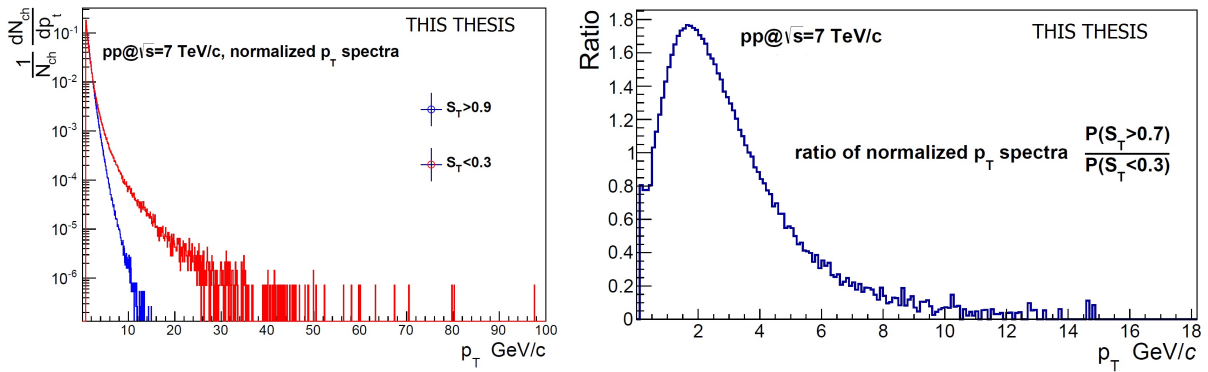
Fig. 17.5 Usporedba p_T spektra za događaje visoke i niske sferičnosti.

Pošto u slici 17.5 omjer spektara nikad ne ide u 1, spektri pokazuju ne slaganje za sve vrijednosti p_T te tako pokazuju jasnu razliku u fizičkim uvjetima ovih dviju klasa sudara. QCD sistemi okarakterizirani ovakvim p_T distribucijama se moraju razlikovati u mehanizmima produkcije čestica što se mora i očitovati u više-čestičnim korelacijama.

Analize dvo-čestičnih korelacija su posebno osjetljive na doprinose mlazova zbog nemogućnosti potiskivanja takvih signala putem kombinatorike ili jednostavnih rezova u mjerenim tragovima čestica bez da znatno ograniče dostupnu statistiku ili efektivni doseg analize. Zato je tro-čestična analiza prirodna alternativa femtoskopskoj analizi sa potisnutim pozadinskim doprinosom[53].

Chapter 18

Q_{inv} korelacijske funkcije - ALICE podatci

Izvedena je 1D femtoskopska analiza na nekoliko vrijednosti multipliciteta te k_T za događaje sa ekstremalnim vrijednostima sferičnosti S_T. Stvorene korelacijske funkcije su normalizirane tako da je najniža točka, izvan femtoskopski relevantnog dijela, te male statistične neodređenosti skalirana na vrijednost 1. Tu je pretpostavljeno da ne postoje nepoznati antikorelacijski efekti visoke amplitude koji bi mogli postaviti minimum korelacijske funkcije niže od 1, što je teorijski postavljen minimum za korelacije identičnih bozona. Slika 18.1 jasno pokazuje ideju ove analize.
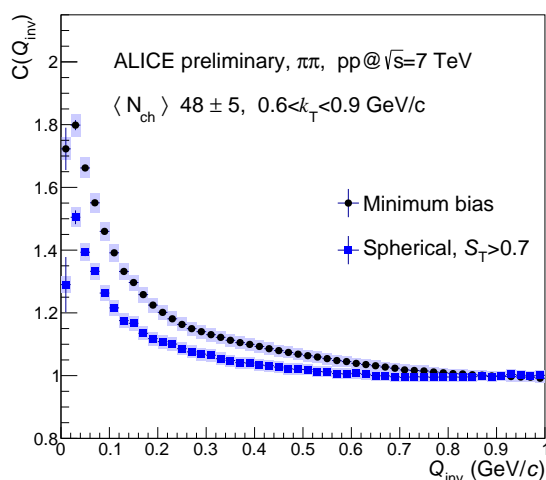
Fig. 18.1 Usporedba $C(Q_{inv})$ između sferičnih događaja te punog skupa događaja.

Sferični događaji sadrže daleko manje nefemtoskopskih doprinosa te su puno boljeg oblika za visoke vrijednosti k_T . Jasno je da Monte Carlo simulacije sadrže dovoljno podataka da bi opisali večinu pozadinskog signala. Koristeći visoki rez u sferičnosti moguće je posegnuti visoke vrijednosti k_T bez unošenja neželjenih pretpostavki simuliranih podataka. Za događaje sa mlazovima prepostavke modela ne bi trebale stvarati probleme jer generatori jasno pokazuju

dobro slaganje sa mjerenjima p_T, J_T i N_{ch} spektara tako da je i glavnica nefemtoskopskih doprinosa sadržana u njima.

18.1 Analiza bez reza u sferičnosti

ALICE kolaboracija je objavila rezulate femtoskopske analize piona za proton-proton te olovo-olovo sudare [1]. Ovdje su prikazane mjerene Q_{inv} korelacijske funkcije za događaje bez reza u sferičnosti. Pri niskim vrijednostima k_T, mjerene korelaije gotovo da ne sadrže nefemtoskopske doprinose uzrokovane mlazovima. Jedini nefemtoskopski doprinosi su uzrokovani odbijanjem zbog Coulombove sile te se nalaze na najnižim vrijednostima Q_{inv}. Sa porastom u k_T doprinosi mlazova postaju sve znatniji dominirajući korelacijom za najvišu vrijednost k_T. Takvi doprinosi urokuju rast korelacijske funkcije iznad teorijskog maksimuma te jasno pokazuju ograničenost tradicionalne analize bez reza u sferičnosti. Očekivano je smanjenje amplitude
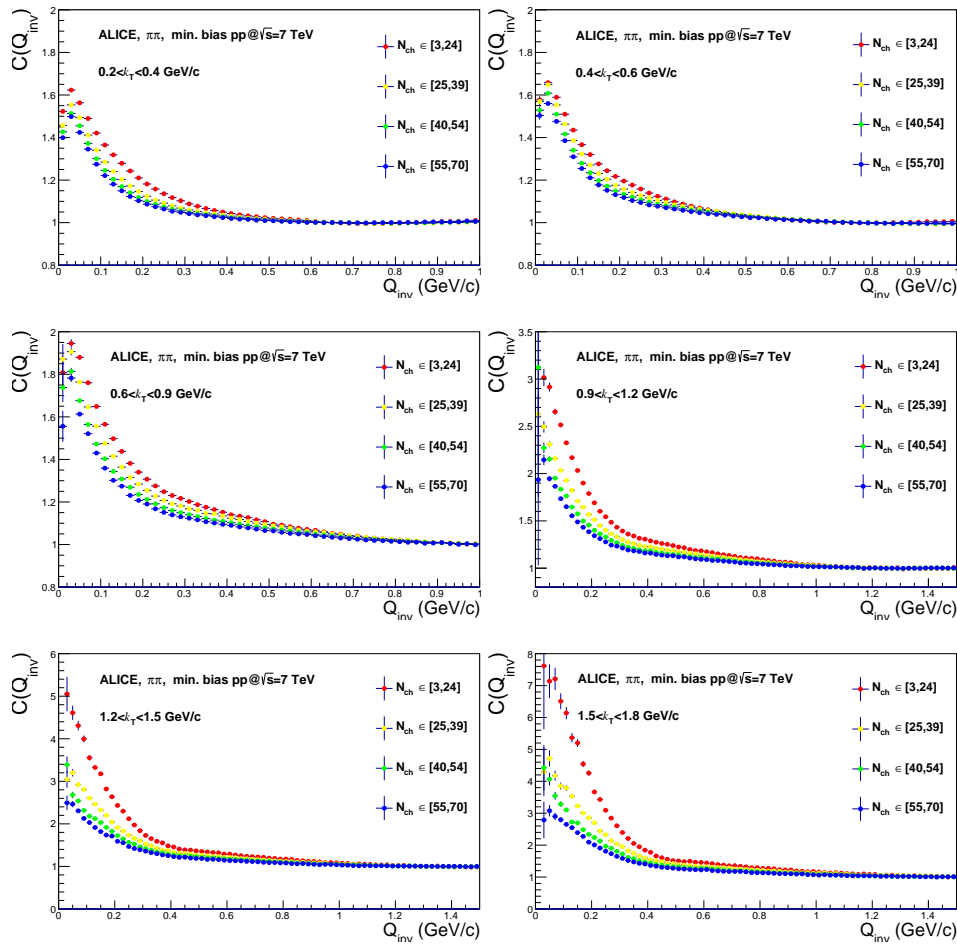
Fig. 18.2 $C(Q_{inv})$ identičnih piona za šest vrijednosti k_T izmjerene ALICE detektorom pri proton-proton sudarima sa $\sqrt{s} = 7$ TeV-a.

te rast širine korelacijskih funkcija sa rastom multipliciteta. Pošto postoji inverzna ovisnost

širine korelacijske funkcije i radijusa homogenosti jasno ja događaji većeg multipliciteta imaju veći radijus. Srednja vrijednost $0.6 < k_\mathrm{T} < 0.9$ GeV/c observable je ujedno i efektivni doseg tradicionalne femtoskopske analize. Pri najnižim multiplicitetima korelacijska funkcija raste do teorijskog maksimuma dok za veće vrijednosti sve korelacijske funkcije prelaze teorijski maksimum. Ovo je znam da se radijusi homogenosti mogu odrediti jedino uz kvalitetno razumjevanje pozadinskog signala što stvara prostor za znatan doprinos simulacija pri analizi.

18.2 Sferični događaji ($S_\mathbf{T} > 0.7$)

Za ovu je analizu izabran rez u sferičnosti $S_\mathrm{T} > 0.7$. Biti će pokazano da je navedeni rez dovoljno dobar u uklanjanju većine pozadine uzrokovane mlazovima bez znatnog ograničavanja dostupne statistike. Otprilike 30% svih sudara ispunjava uvijete ovog reza. Na niskom k_T korelacijske funkcije pokazuju malu promjenu u odnosu na rezultate bez reza. Pri visokom k_T korelacije su sličnog oblika i amplitude, ali znatno veće statističke neodređenosti zbog ograničenja u broju izmjerenih sudara. Opaženo je novo ponašanje korelacija pri najnižim vrijednostima multipliciteta. Ono je posljedica reza u sferičnosti. Jednostavno objašnjenje bi bilo da pri niskom multiplicitetu te visokom sfericitetu, čestice zauzimaju jednolik rasap u ϕ što znači da one ujedno i imaju relativno konstantan razmak u $\Delta\phi$ između sebe. Pri takvoj konfiguraciji, vrlo je mala vjerojatnost par čestica niskog Q_{inv} jer bi morali imati malenu separaciju u ϕ. Pri miješanju događaja ova situacija je izbjegnuta jer se mješanje vrši sa 10 događaja što znači da je proizvoljna $\Delta\phi$ separacija jednako moguća. Ovakvo potisnuće korelacija pri niskom Q_{inv} za visoke vrijednosti sfericiteta bi trebalo biti prisutno u simuliranim podatcima. Kasnije će ova tvrdnja biti i dokazana.

18.3 Događaji niske sferičnosti ($S_\mathbf{T} < 0.3$)

Usporedba sa prošlim rezultatima pokazuje da događaji niske sferičnosti sadrže znatan doprinos nefemtoskopskih korelacija, čak i za niske vrijednosti k_T. Korelacijske funcije su općenito veće amplitude te širine. U daljnjim razmatranjima uzimamo u obzir oblike, doseg i amplitudu nefemtoskopskih doprinosa pri razvoju mogućih metoda uklanjanja pozadinskih signala za događaje niske sferičnosti.

Kao što je i očekivano, nefemtoskopski doprinosi rastu sa k_T te počinju dominirati korelacijama. Ovo se razumije kao posljedica biranja pionskih parova koji pripadaju istom mlazu. Pri visokom k_T čestice uglavnom imaju sličan smjer i količinu gibanja pa tako i mali Q_{inv}. Ovaj trend rasta amplitude sa k_T se nastavlja kroz sve vrijednosti k_T te daje korelacijama najvišeg k_T amplitudu pet puta veću od teorijskog maksimuma. To je jasan znak da korelacijske funkcije događaja niske sferičnosti sadrže znatan doprinos nefemtoskopskih korelacija.
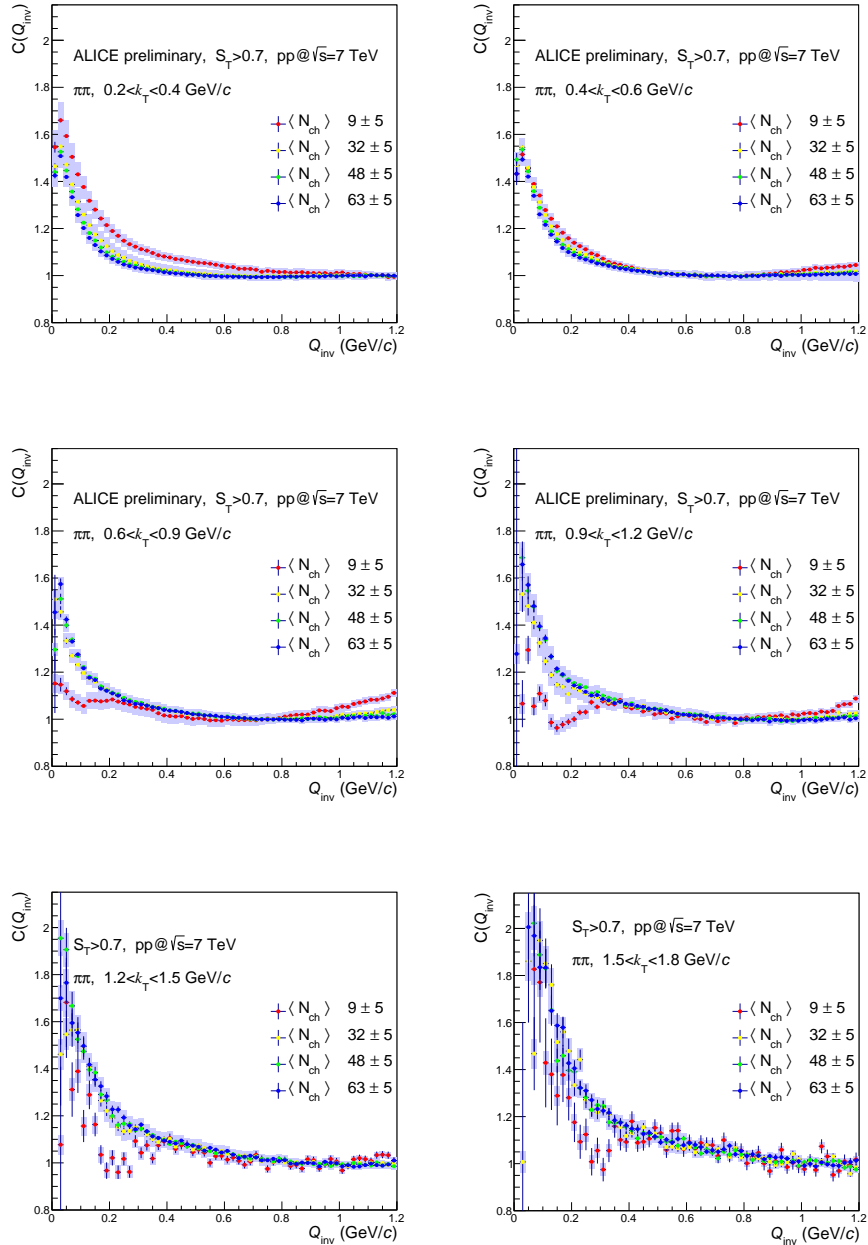
Fig. 18.3 Pionske $C(Q_{\text{inv}})$ funkcije sferičnih događaja za šest vrijednosti k_{T} mjerene ALICE detektorom pri proton-proton sudarima na $\sqrt{s} = 7$ TeV-a.

Zbog velikog doprinosa nefemtoskopskih korelacija te njihovog drugačijeg oblika, uklanjanje pozadinskog signala bi trebalo biti moguće. Iz prikazanih korelacija je moguće vidjeti da oko $Q_{inv} \approx 0.4$ GeV/c Bose-Einsteinove korelacije izmjene dominaciju sa nefemtoskopskim doprinosima. Jasno je da dobiveni radijusi homogenosti iz ovakvih korelacijskih funkcija moraju biti znatno manji od onih kod sferičnih događaja.

Pozadinski signal se pokazao pravilnog oblika te bez oscilacija što znatno olakšava proces uklanjanja putem dobro izabranog simulatora podataka. U sljedećem poglavlju je pokazana us-
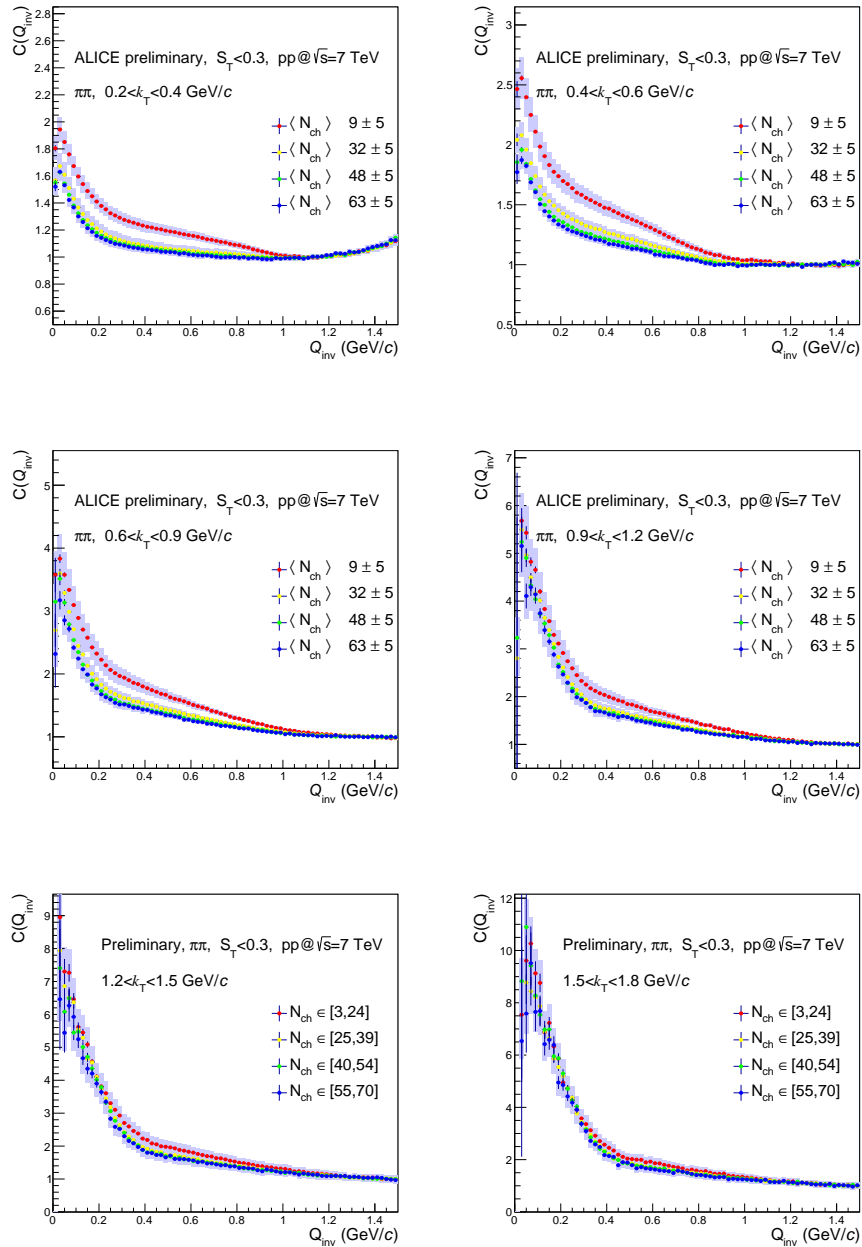
Fig. 18.4 Pionske $C(Q_{inv})$ funkcije događaja niske sferičnosti za šest vrijednosti k_T mjerene ALICE detektorom pri proton-proton sudarima na $\sqrt{s} = 7$ TeV-a.

poredba Monte Carlo simulacija te je razmotrena metoda uklanjanja nefemtoskopskih doprinosa na prirodan način.

Chapter 19

Konačni rezultati

Ovdje su prikazani konačni rezultati ove analize te njihova interpretacija.
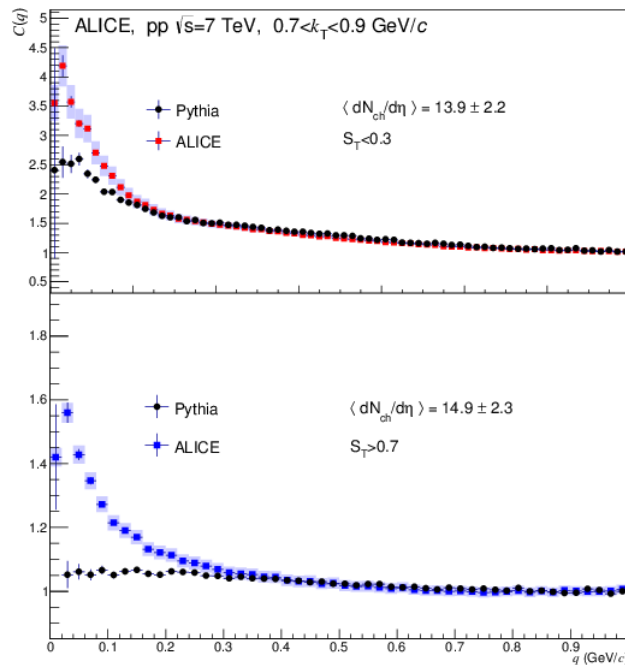
Fig. 19.1 Usporedba korelacijskih funkcija za mjerene i PYTHIA-Perugia0 generirane podatke protonskih sudara na energiji od 7 TeV-a u centru mase u dvije kategorije sferičnosti.

Glavni zaključci:

1. Nefemtoskopski pozadinski signali su uzrokovani čestičnom kolimacijom u mlazovima.

2. Rez u sferičnosti uspješno uklanja pozadinske korelacije te znatno proširuje k_T doseg.

3. Pozadinski signal generiranih podataka se slaže sa mjerenjima u širokom Q_{inv} rasponu.

4. Pozadinski signal ima strukturu koja se ne može opisati jednostavnim gausijanskim oblikom.
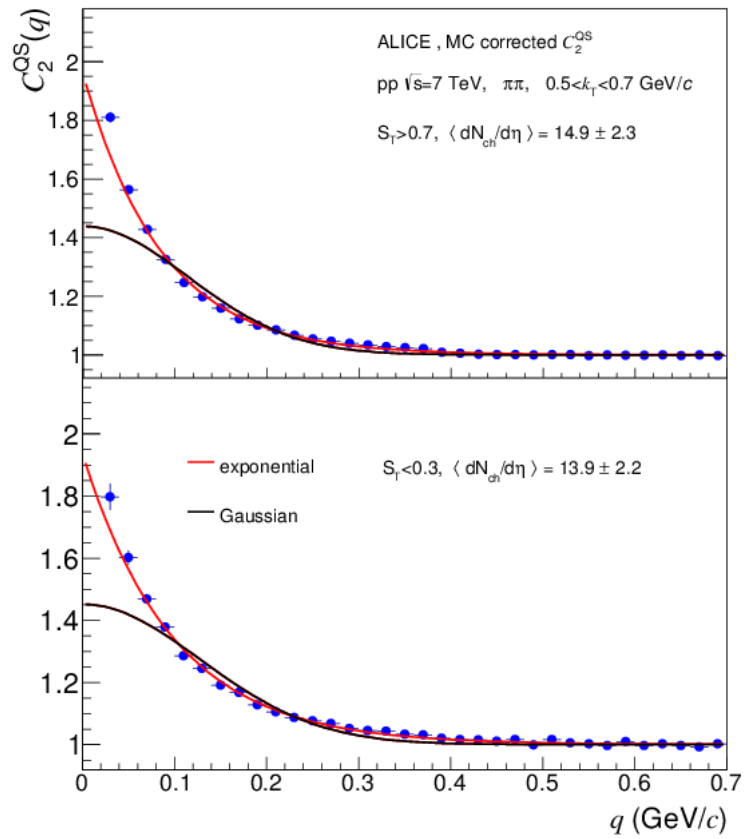
Fig. 19.2 Usporedba eksponencijalne i gausijanske prilagodbe na mjerene podatke protonskih sudara za dvije vrijednosti sferičnosti.

Glavni zaključci:

1. Eksponencijalni oblik funkcije prilagodbe bolje opisuje mjerene podatke za obje vrijednosti sfericiteta.

Opažena je promjena oblika iz eksponencijalnog u gausijanski sa povečanjem broja nabijenih čestica u sudaru. Do sada nije preložen niti jedan mehanizam koji bi objasnio ovo ponašanje.
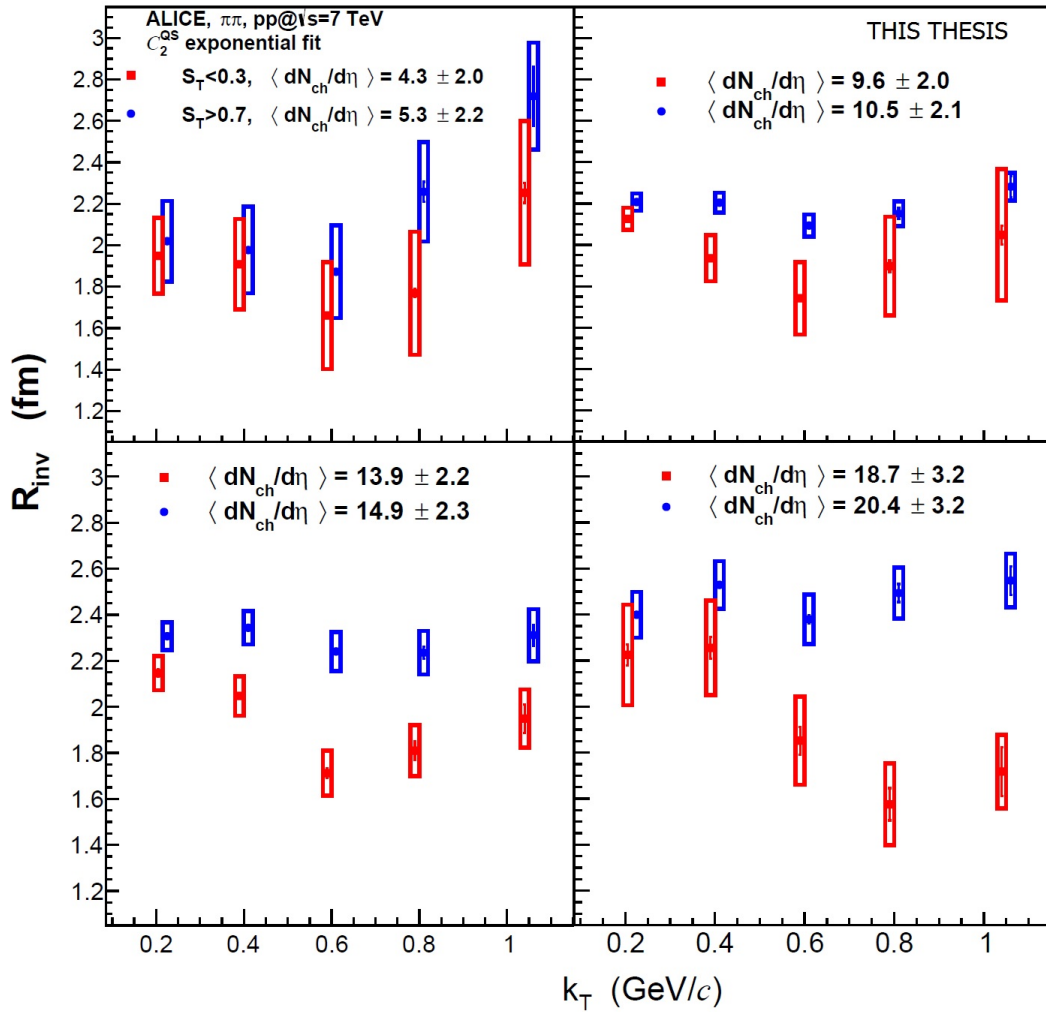
Fig. 19.3 Radijusi homogenosti eksponencijalne prilagodbe u ovisnosti o k_T para ya protonske sudare na 7 TeV-a energije u centru mase za dvije vrijednosti sferičnosti.

Glavni zaključci:

1. Sferični događaji pokazuju smanjenu ovisnost o k_T para.

2. Sudari sa mlazovima pokazuju jaku ovisnost o multiplicitetu i k_T para.

3. Rezultati prilagodbe za sferične sudare ukazuju na manjak hidrodinamičke kolektivnosti čestica.

Ovo je glavni rezultat one analize. Pokazano je da se značajan udio pozadinskih korelacija može ukloniti putem reza u sferičnosti što omogučava određivanje radijusa homogenosti pri visokim vrijednostima k_T para. Opažen je manjak ovisnosti radijusa o k_T para što se može interpretirati kao nedostatak hidrodinamičke kolektivnosti proizvedenih čestica.

19.1 Zaključak

U ovom smo radu razvili metodu uklanjanja pozadinskih korelacija u dvočestičnim interfer-ometrijskim analizama. Transverzalna sferičnost je po prvi put korištena u identifikaciji te uklanjanju nefemtoskopskih signala.

Radijusi homogenosti za sferične sudare pokazuju jasno odstupanje od ranije publiciranih rezultata te ne sadrže ovisnost o k_T para. Ovo opažanje je sukladno manjku hidridinamičke kolektivnosti pri onim sudarima u kojima dominira niskoenergetska proizvodnja piona, sferičnim sudarima. Pri određivanju radijusa homogenosti za sudare sa mlazovima korištene su dvočestične korelacije iz simuliranih podataka. Ovakva uporaba je dopuštena s obzirom na njihovo uspješno opisivanje osnovnih distribucija mlazova poput multipliciteta i transverzalnog impulsa. Radijusi homogenosti za sudare sa mlazovima pokazuju jasnu ovisnost o multiplicitetu sudara te k_T para. Ovo ponašanje je slično publiciranim rezultatima za sudare bez selekcije po sferičnosti. Ovako određeni radijusi potencijalno nose informaciju o hadronizacijskim duljinama u mlazovima. Za obje ekstremalne vrijednosti sferičnosti korelacijske funkcije su bolje opisane eksponencijalnom funkcijom.

Pristup selekcije događaja po obliku sudara ima jasnu budučnost u primjeni. Sudari srednjih vrijednosti sferičnosti ($0.3 < S_T < 0.7$) sadrže još nepromatrane informacije o interakciji mlaza sa QCD medijem. Pri ovakvoj analizi treba koristiti dodatnu selekciju po nekoj drugoj karakteristici sudara. Selekcija po obliku sudara se može koristiti na segmentu svih opaženih čestica što može razotkriti dodatne detalje o samom procesu proizvodnje čestica u sudaru. Razne druge analize koje ovise o točnom prepoznavanju doprinosa mlazova bi mogle primijeniti selekciju po sferičnosti kao jednu od metoda uklanjanja pozadinskog signala. Konačno, ranije spomenuta ovisnost oblika korelacije o multiplicitetu sudara bi se mogla iskoristiti za identifikaciju potpisa prijelaza u kolektivnosti proizvedenih čestica. Ovi i mnogi drugi primjeri potencijalne primjene reza u sferičnosti pokazuju na mogučnost da selekcija po obliku događaja postane standardna metoda istraživanja u eksperimentalnoj fizici na visokim energijama.

Životopis

- 12. veljače 1986. rođen u Zagrebu, Hrvatska

- lipanj 2000. Osnovna škola Augusta Šenoe, Zagreb, Hrvatska

- svibanj 2004. X. Gimnazija, Zagreb, Hrvatska

- lipanj 2010. Diplomirao na Prirodoslovno-matematičkom fakuletu u Zagrebu, Hrvatska

- srpanj 2011. Asistent/znanstveni novak na fizičkom odsjeku PMF-a u Zagrebu, Hrvatska

- rujan 2011. član ALICE kolaboracije na CERN-u, Švicarska

Popis radova:

1. **"Multi-strange baryon production in pp collisions at $\sqrt{s} = 7$ TeV with ALICE"**
   B. Abelev *et al.* [ALICE Collaboration].
   arXiv:1204.0282 [nucl-ex]
   10.1016/j.physletb.2012.05.011
   Phys. Lett. B **712**, 309 (2012)

2. **"Transverse sphericity of primary charged particles in minimum bias proton-proton collisions at $\sqrt{s} = 0.9$, 2.76 and 7 TeV"**
   B. Abelev *et al.* [ALICE Collaboration].
   arXiv:1205.3963 [hep-ex]
   10.1140/epjc/s10052-012-2124-9
   Eur. Phys. J. C **72**, 2124 (2012)

3. **"Measurement of charm production at central rapidity in proton-proton collisions at $\sqrt{s} = 2.76$ TeV"**
   B. Abelev *et al.* [ALICE Collaboration].
   arXiv:1205.4007 [hep-ex]
   10.1007/JHEP07(2012)191
   JHEP **1207**, 191 (2012)

4. **"Measurement of electrons from semileptonic heavy-flavour hadron decays in pp collisions at $\sqrt{s} = 7$ TeV"**
   B. Abelev *et al.* [ALICE Collaboration].
   arXiv:1205.5423 [hep-ex]

10.1103/PhysRevD.86.112007

Phys. Rev. D **86**, 112007 (2012)

5. **"Anisotropic flow of charged hadrons, pions and (anti-)protons measured at high transverse momentum in Pb-Pb collisions at $\sqrt{s_{NN}}$=2.76 TeV"**
B. Abelev *et al.* [ALICE Collaboration].
arXiv:1205.5761 [nucl-ex]
10.1016/j.physletb.2012.12.066
Phys. Lett. B **719**, 18 (2013)

6. **"Measurement of prompt J/ψ and beauty hadron production cross sections at mid-rapidity in pp collisions at $\sqrt{s} = 7$ TeV"**
B. Abelev *et al.* [ALICE Collaboration].
arXiv:1205.5880 [hep-ex]
10.1007/JHEP11(2012)065
JHEP **1211**, 065 (2012)

7. **"Production of muons from heavy flavour decays at forward rapidity in pp and Pb-Pb collisions at $\sqrt{s_{NN}}$ = 2.76 TeV"**
B. Abelev *et al.* [ALICE Collaboration].
arXiv:1205.6443 [hep-ex]
10.1103/PhysRevLett.109.112301
Phys. Rev. Lett. **109**, 112301 (2012)

8. **"$K_s^0 - K_s^0$ correlations in pp collisions at $\sqrt{s} = 7$ TeV from the LHC ALICE experiment"**
B. Abelev *et al.* [ALICE Collaboration].
arXiv:1206.2056 [hep-ex]
10.1016/j.physletb.2012.09.013
Phys. Lett. B **717**, 151 (2012)

9. **"Charge separation relative to the reaction plane in Pb-Pb collisions at $\sqrt{s_{NN}} = 2.76$ TeV"**
B. Abelev *et al.* [ALICE Collaboration].
arXiv:1207.0900 [nucl-ex]
10.1103/PhysRevLett.110.012301
Phys. Rev. Lett. **110**, no. 1, 012301 (2013)

10. **"Net-Charge Fluctuations in Pb-Pb collisions at $\sqrt{s_{NN}} = 2.76$ TeV"**
B. Abelev *et al.* [ALICE Collaboration].
arXiv:1207.6068 [nucl-ex]

10.1103/PhysRevLett.110.152301

Phys. Rev. Lett. **110**, no. 15, 152301 (2013)

11. **"Measurement of electrons from beauty hadron decays in pp collisions at $\sqrt{s} = 7$ TeV"**
B. Abelev *et al.* [ALICE Collaboration].
arXiv:1208.1902 [hep-ex]
10.1016/j.physletb.2013.01.069
Phys. Lett. B **721**, 13 (2013)

12. **"D_s^+ meson production at central rapidity in proton–proton collisions at $\sqrt{s} = 7$ TeV"**
B. Abelev *et al.* [ALICE Collaboration].
arXiv:1208.1948 [hep-ex]
10.1016/j.physletb.2012.10.049
Phys. Lett. B **718**, 279 (2012)

13. **"Pion, Kaon, and Proton Production in Central Pb–Pb Collisions at $\sqrt{s_{NN}} = 2.76$ TeV"**
B. Abelev *et al.* [ALICE Collaboration].
arXiv:1208.1974 [hep-ex]
10.1103/PhysRevLett.109.252301
Phys. Rev. Lett. **109**, 252301 (2012)

14. **"Centrality Dependence of Charged Particle Production at Large Transverse Momentum in Pb–Pb Collisions at $\sqrt{s_{\mathrm{NN}}} = 2.76$ TeV"**
B. Abelev *et al.* [ALICE Collaboration].
arXiv:1208.2711 [hep-ex]
10.1016/j.physletb.2013.01.051
Phys. Lett. B **720**, 52 (2013)

15. **"Measurement of inelastic, single- and double-diffraction cross sections in proton–proton collisions at the LHC with ALICE"**
B. Abelev *et al.* [ALICE Collaboration].
arXiv:1208.4968 [hep-ex]
10.1140/epjc/s10052-013-2456-0
Eur. Phys. J. C **73**, no. 6, 2456 (2013)

16. **"Production of $K^*(892)^0$ and $\phi(1020)$ in pp collisions at $\sqrt{s} = 7$ TeV"**
B. Abelev *et al.* [ALICE Collaboration].
arXiv:1208.5717 [hep-ex]

10.1140/epjc/s10052-012-2183-y

Eur. Phys. J. C **72**, 2183 (2012)

17. **"Coherent J/ψ photoproduction in ultra-peripheral Pb-Pb collisions at $\sqrt{s_{NN}} = 2.76$ TeV"**

    B. Abelev *et al.* [ALICE Collaboration].

    arXiv:1209.3715 [nucl-ex]

    10.1016/j.physletb.2012.11.059

    Phys. Lett. B **718**, 1273 (2013)

18. **"Pseudorapidity density of charged particles in p + Pb collisions at $\sqrt{s_{NN}} = 5.02$ TeV"**

    B. Abelev *et al.* [ALICE Collaboration].

    arXiv:1210.3615 [nucl-ex]

    10.1103/PhysRevLett.110.032301

    Phys. Rev. Lett. **110**, no. 3, 032301 (2013)

19. **"Transverse momentum distribution and nuclear modification factor of charged particles in p-Pb collisions at $\sqrt{s_{NN}} = 5.02$ TeV"**

    B. Abelev *et al.* [ALICE Collaboration].

    arXiv:1210.4520 [nucl-ex]

    10.1103/PhysRevLett.110.082302

    Phys. Rev. Lett. **110**, no. 8, 082302 (2013)

20. **"Long-range angular correlations on the near and away side in p-Pb collisions at $\sqrt{s_{NN}} = 5.02$ TeV"**

    B. Abelev *et al.* [ALICE Collaboration].

    arXiv:1212.2001 [nucl-ex]

    10.1016/j.physletb.2013.01.012

    Phys. Lett. B **719**, 29 (2013)

21. **"Charged kaon femtoscopic correlations in pp collisions at $\sqrt{s} = 7$ TeV"**

    B. Abelev *et al.* [ALICE Collaboration].

    arXiv:1212.5958 [hep-ex]

    10.1103/PhysRevD.87.052016

    Phys. Rev. D **87**, no. 5, 052016 (2013)

22. **"Measurement of the inclusive differential jet cross section in pp collisions at $\sqrt{s} = 2.76$ TeV"**

    B. Abelev *et al.* [ALICE Collaboration].

    arXiv:1301.3475 [nucl-ex]

10.1016/j.physletb.2013.04.026

Phys. Lett. B **722**, 262 (2013)

23. **"Charge correlations using the balance function in Pb-Pb collisions at $\sqrt{s_{NN}}$ = 2.76 TeV"**
B. Abelev *et al.* [ALICE Collaboration].
arXiv:1301.3756 [nucl-ex]
10.1016/j.physletb.2013.05.039
Phys. Lett. B **723**, 267 (2013)

24. **"Centrality determination of Pb-Pb collisions at $\sqrt{s_{NN}}$ = 2.76 TeV with ALICE"**
B. Abelev *et al.* [ALICE Collaboration].
arXiv:1301.4361 [nucl-ex]
10.1103/PhysRevC.88.044909
Phys. Rev. C **88**, no. 4, 044909 (2013)

25. **"Centrality dependence of π, K, p production in Pb-Pb collisions at $\sqrt{s_{NN}}$ = 2.76 TeV"**
B. Abelev *et al.* [ALICE Collaboration].
arXiv:1303.0737 [hep-ex]
10.1103/PhysRevC.88.044910
Phys. Rev. C **88**, 044910 (2013)

26. **"J/Psi Elliptic Flow in Pb-Pb Collisions at $\sqrt{s_{NN}}$ = 2.76 TeV"**
E. Abbas *et al.* [ALICE Collaboration].
arXiv:1303.5880 [nucl-ex]
10.1103/PhysRevLett.111.162301
Phys. Rev. Lett. **111**, 162301 (2013)

27. **"Centrality dependence of the pseudorapidity density distribution for charged particles in Pb-Pb collisions at $\sqrt{s_{NN}}$ = 2.76 TeV"**
E. Abbas *et al.* [ALICE Collaboration].
arXiv:1304.0347 [nucl-ex]
10.1016/j.physletb.2013.09.022
Phys. Lett. B **726**, 610 (2013)

28. **"Cross Sections and Transverse Single-Spin Asymmetries in Forward Jet Production from Proton Collisions at $\sqrt{s}$ = 500 GeV"**
L. C. Bland *et al.* [AnDY Collaboration].
arXiv:1304.1454 [hep-ex]

29. **"Charmonium and e^+e^- pair photoproduction at mid-rapidity in ultra-peripheral Pb-Pb collisions at $\sqrt{s_{NN}}$=2.76 TeV"**

E. Abbas *et al.* [ALICE Collaboration].

arXiv:1305.1467 [nucl-ex]

10.1140/epjc/s10052-013-2617-1

Eur. Phys. J. C **73**, no. 11, 2617 (2013)

30. **"Mid-rapidity anti-baryon to baryon ratios in pp collisions at $\sqrt{s}$ = 0.9, 2.76 and 7 TeV measured by ALICE"**

    E. Abbas *et al.* [ALICE Collaboration].

    arXiv:1305.1562 [nucl-ex]

    10.1140/epjc/s10052-013-2496-5

    Eur. Phys. J. C **73**, 2496 (2013)

31. **"D meson elliptic flow in non-central Pb-Pb collisions at $\sqrt{s_{NN}}$ = 2.76TeV"**

    B. Abelev *et al.* [ALICE Collaboration].

    arXiv:1305.2707 [nucl-ex]

    10.1103/PhysRevLett.111.102301

    Phys. Rev. Lett. **111**, 102301 (2013)

32. **"Performance of the ALICE VZERO system"**

    E. Abbas *et al.* [ALICE Collaboration].

    arXiv:1306.3130 [nucl-ex]

    10.1088/1748-0221/8/10/P10016

    JINST **8**, P10016 (2013)

33. **"Directed Flow of Charged Particles at Midrapidity Relative to the Spectator Plane in Pb-Pb Collisions at $\sqrt{s_{NN}}$=2.76 TeV"**

    B. Abelev *et al.* [ALICE Collaboration].

    arXiv:1306.4145 [nucl-ex]

    10.1103/PhysRevLett.111.232302

    Phys. Rev. Lett. **111**, no. 23, 232302 (2013)

34. **"Energy Dependence of the Transverse Momentum Distributions of Charged Particles in pp Collisions Measured by ALICE"**

    B. B. Abelev *et al.* [ALICE Collaboration].

    arXiv:1307.1093 [nucl-ex]

    10.1140/epjc/s10052-013-2662-9

    Eur. Phys. J. C **73**, no. 12, 2662 (2013)

35. **"Multiplicity dependence of the average transverse momentum in pp, p-Pb, and Pb-Pb collisions at the LHC"**

    B. B. Abelev *et al.* [ALICE Collaboration].

    arXiv:1307.1094 [nucl-ex]

10.1016/j.physletb.2013.10.054

Phys. Lett. B **727**, 371 (2013)

36. **"Multiplicity dependence of two-particle azimuthal correlations in pp collisions at the LHC"**

    B. Abelev *et al.* [ALICE Collaboration].

    arXiv:1307.1249 [nucl-ex]

    10.1007/JHEP09(2013)049

    JHEP **1309**, 049 (2013)

37. **"Long-range angular correlations of π, K and p in p-Pb collisions at $\sqrt{s_{\mathrm{NN}}}$ = 5.02 TeV"**

    B. B. Abelev *et al.* [ALICE Collaboration].

    arXiv:1307.3237 [nucl-ex]

    10.1016/j.physletb.2013.08.024

    Phys. Lett. B **726**, 164 (2013)

38. **"K^0_S and Λ production in Pb-Pb collisions at $\sqrt{s_{NN}}$ = 2.76 TeV"**

    B. B. Abelev *et al.* [ALICE Collaboration].

    arXiv:1307.5530 [nucl-ex]

    10.1103/PhysRevLett.111.222301

    Phys. Rev. Lett. **111**, 222301 (2013)

39. **"Multi-strange baryon production at mid-rapidity in Pb-Pb collisions at $\sqrt{s_{NN}}$ = 2.76 TeV"**

    B. B. Abelev *et al.* [ALICE Collaboration].

    arXiv:1307.5543 [nucl-ex]

    10.1016/j.physletb.2014.05.052, 10.1016/j.physletb.2013.11.048

    Phys. Lett. B **728**, 216 (2014), [Erratum-ibid. B **734**, 409 (2014)]

40. **"Multiplicity Dependence of Pion, Kaon, Proton and Lambda Production in p-Pb Collisions at $\sqrt{s_{NN}}$ = 5.02 TeV"**

    B. B. Abelev *et al.* [ALICE Collaboration].

    arXiv:1307.6796 [nucl-ex]

    10.1016/j.physletb.2013.11.020

    Phys. Lett. B **728**, 25 (2014)

41. **"J/ψ production and nuclear effects in p-Pb collisions at $\sqrt{S_{NN}}$ = 5.02 TeV"**

    B. B. Abelev *et al.* [ALICE Collaboration].

    arXiv:1308.6726 [nucl-ex]

    10.1007/JHEP02(2014)073

    JHEP **1402**, 073 (2014)

42. **"Two- and three-pion quantum statistics correlations in Pb-Pb collisions at $\sqrt{s_{NN}} =$ 2.76 TeV at the CERN Large Hadron Collider"**
    B. B. Abelev *et al.* [ALICE Collaboration].
    arXiv:1310.7808 [nucl-ex]
    10.1103/PhysRevC.89.024911
    Phys. Rev. C **89**, no. 2, 024911 (2014)

43. **"Centrality, rapidity and transverse momentum dependence of J/ψ suppression in Pb-Pb collisions at $\sqrt{s_{\mathrm{NN}}}$=2.76 TeV"**
    B. B. Abelev *et al.* [ALICE Collaboration].
    arXiv:1311.0214 [nucl-ex]
    10.1016/j.physletb.2014.05.064
    Phys. Lett. B **734**, 314 (2014)

44. **"Measurement of charged jet suppression in Pb-Pb collisions at $\sqrt{s_{NN}}$ = 2.76 TeV"**
    B. Abelev *et al.* [ALICE Collaboration].
    arXiv:1311.0633 [nucl-ex]
    10.1007/JHEP03(2014)013
    JHEP **1403**, 013 (2014)

45. **"Production of charged pions, kaons and protons at large transverse momenta in pp and Pb–Pb collisions at $\sqrt{s_{\mathrm{NN}}}$ =2.76 TeV"**
    B. B. Abelev *et al.* [ALICE Collaboration].
    arXiv:1401.1250 [nucl-ex]
    10.1016/j.physletb.2014.07.011
    Phys. Lett. B **736**, 196 (2014)

46. **"Performance of the ALICE Experiment at the CERN LHC"**
    B. B. Abelev *et al.* [ALICE Collaboration].
    arXiv:1402.4476 [nucl-ex]
    10.1142/S0217751X14300440
    Int. J. Mod. Phys. A **29**, 1430044 (2014)

47. **"Measurement of quarkonium production at forward rapidity in pp collisions at $\sqrt{s} = 7$ TeV"**
    B. B. Abelev *et al.* [ALICE Collaboration].
    arXiv:1403.3648 [nucl-ex]
    10.1140/epjc/s10052-014-2974-4
    Eur. Phys. J. C **74**, no. 8, 2974 (2014)

48. **"$K^*(892)^0$ and $\Phi(1020)$ production in Pb-Pb collisions at $\sqrt{s_{NN}}$=2.76 TeV"**
    B. B. Abelev *et al.* [ALICE Collaboration].

arXiv:1404.0495 [nucl-ex]

10.1103/PhysRevC.91.024609

Phys. Rev. C **91**, no. 2, 024609 (2015)

49. **"Freeze-out radii extracted from three-pion cumulants in pp, p–Pb and Pb–Pb collisions at the LHC"**
B. B. Abelev *et al.* [ALICE Collaboration].
arXiv:1404.1194 [nucl-ex]
10.1016/j.physletb.2014.10.034
Phys. Lett. B **739**, 139 (2014)

50. **"Measurement of visible cross sections in proton-lead collisions at $\sqrt{s_{\mathrm{NN}}}$ = 5.02 TeV in van der Meer scans with the ALICE detector"**
B. B. Abelev *et al.* [ALICE Collaboration].
arXiv:1405.1849 [nucl-ex]
10.1088/1748-0221/9/11/P11003
JINST **9**, no. 11, P11003 (2014)

51. **"Azimuthal anisotropy of D meson production in Pb-Pb collisions at $\sqrt{s_{\mathrm{NN}}} = 2.76$ TeV"**
B. B. Abelev *et al.* [ALICE Collaboration].
arXiv:1405.2001 [nucl-ex]
10.1103/PhysRevC.90.034904
Phys. Rev. C **90**, no. 3, 034904 (2014)

52. **"Transverse momentum dependence of inclusive primary charged-particle production in p-Pb collisions at $\sqrt{s_{\mathrm{NN}}} = 5.02$ TeV"**
B. B. Abelev *et al.* [ALICE Collaboration].
arXiv:1405.2737 [nucl-ex]
10.1140/epjc/s10052-014-3054-5
Eur. Phys. J. C **74**, no. 9, 3054 (2014)

53. **"Measurement of prompt D-meson production in $p - Pb$ collisions at $\sqrt{s_{NN}}$ = 5.02 TeV"**
B. B. Abelev *et al.* [ALICE Collaboration].
arXiv:1405.3452 [nucl-ex]
10.1103/PhysRevLett.113.232301
Phys. Rev. Lett. **113**, no. 23, 232301 (2014)

54. **"Neutral pion production at midrapidity in pp and Pb-Pb collisions at $\sqrt{s_{\mathrm{NN}}} = 2.76\,\mathrm{TeV}$"**
B. B. Abelev *et al.* [ALICE Collaboration].

arXiv:1405.3794 [nucl-ex]

10.1140/epjc/s10052-014-3108-8

Eur. Phys. J. C **74**, no. 10, 3108 (2014)

55. **"Suppression of $\psi(2S)$ production in p-Pb collisions at $\sqrt{s_{NN}}$ = 5.02 TeV"**
    B. B. Abelev *et al.* [ALICE Collaboration].
    arXiv:1405.3796 [nucl-ex]
    10.1007/JHEP12(2014)073
    JHEP **1412**, 073 (2014)

56. **Measurement of electrons from semileptonic heavy-flavor hadron decays in pp collisions at $\sqrt{s} = 2.76$ TeV"**
    B. B. Abelev *et al.* [ALICE Collaboration].
    arXiv:1405.4117 [nucl-ex]
    10.1103/PhysRevD.91.012001
    Phys. Rev. D **91**, no. 1, 012001 (2015)

57. **"Beauty production in pp collisions at $\sqrt{s}$ = 2.76 TeV measured via semi-electronic decays"**
    B. B. Abelev *et al.* [ALICE Collaboration].
    arXiv:1405.4144 [nucl-ex]
    10.1016/j.physletb.2014.09.026
    Phys. Lett. B **738**, 97 (2014)

58. **"Suppression of $\Upsilon(1S)$ at forward rapidity in Pb-Pb collisions at $\sqrt{s_{NN}} = 2.76$ TeV"**
    B. B. Abelev *et al.* [ALICE Collaboration].
    arXiv:1405.4493 [nucl-ex]
    10.1016/j.physletb.2014.10.001
    Phys. Lett. B **738**, 361 (2014)

59. **"Elliptic flow of identified hadrons in Pb-Pb collisions at $\sqrt{s_{NN}}$ = 2.76 TeV"**
    B. B. Abelev *et al.* [ALICE Collaboration].
    arXiv:1405.4632 [nucl-ex]

60. **"Multiparticle azimuthal correlations in p -Pb and Pb-Pb collisions at the CERN Large Hadron Collider"**
    B. B. Abelev *et al.* [ALICE Collaboration].
    arXiv:1406.2474 [nucl-ex]
    10.1103/PhysRevC.90.054901
    Phys. Rev. C **90**, no. 5, 054901 (2014)

61. **"Production of $\Sigma(1385)^{\pm}$ and $\Xi(1530)^{0}$ in proton-proton collisions at $\sqrt{s} = 7$ TeV"**
    B. B. Abelev *et al.* [ALICE Collaboration].

arXiv:1406.3206 [nucl-ex]

10.1140/epjc/s10052-014-3191-x

Eur. Phys. J. C **75**, no. 1, 1 (2015)

62. **"Multiplicity dependence of jet-like two-particle correlations in p-Pb collisions at $\sqrt{s_{NN}}$ = 5.02 TeV"**
B. B. Abelev *et al.* [ALICE Collaboration].
arXiv:1406.5463 [nucl-ex]
10.1016/j.physletb.2014.11.028
Phys. Lett. B **741**, 38 (2015)

63. **"Exclusive J/ψ photoproduction off protons in ultra-peripheral p-Pb collisions at $\sqrt{s_{NN}}$ = 5.02 TeV"**
B. B. Abelev *et al.* [ALICE Collaboration].
arXiv:1406.7819 [nucl-ex]
10.1103/PhysRevLett.113.232504
Phys. Rev. Lett. **113**, no. 23, 232504 (2014)

64. **"Upgrade of the ALICE Experiment: Letter Of Intent"**
B. Abelev *et al.* [ALICE Collaboration].
10.1088/0954-3899/41/8/087001
J. Phys. G **41**, 087001 (2014).

65. **"Technical Design Report for the Upgrade of the ALICE Inner Tracking System"**
B. Abelev *et al.* [ALICE Collaboration].
10.1088/0954-3899/41/8/087002
J. Phys. G **41**, 087002 (2014).

66. **"Event-by-event mean p_T fluctuations in pp and Pb-Pb collisions at the LHC"**
B. B. Abelev *et al.* [ALICE Collaboration].
arXiv:1407.5530 [nucl-ex]
10.1140/epjc/s10052-014-3077-y
Eur. Phys. J. C **74**, no. 10, 3077 (2014)

67. **"Production of inclusive Υ(1S) and Υ(2S) in p-Pb collisions at $\sqrt{s_{NN}}$ = 5.02 TeV"**
B. B. Abelev *et al.* [ALICE Collaboration].
arXiv:1410.2234 [nucl-ex]
10.1016/j.physletb.2014.11.041
Phys. Lett. B **740**, 105 (2015)

68. **"Charged jet cross sections and properties in proton-proton collisions at $\sqrt{s}$ = 7 TeV"**

B. B. Abelev *et al.* [ALICE Collaboration].
arXiv:1411.4969 [nucl-ex]

69. **"Inclusive photon production at forward rapidities in proton-proton collisions at $\sqrt{s}$ = 0.9, 2.76 and 7 TeV"**
B. B. Abelev *et al.* [ALICE Collaboration].
arXiv:1411.4981 [nucl-ex]

70. **"Centrality dependence of particle production in p-Pb collisions at $\sqrt{s_{NN}}$= 5.02 TeV"**
J. Adam *et al.* [ALICE Collaboration].
arXiv:1412.6828 [nucl-ex]

71. **"Forward-backward multiplicity correlations in pp collisions at $\sqrt{s}$=0.9, 2.76 and 7 TeV"**
J. Adam *et al.* [ALICE Collaboration].
arXiv:1502.00230 [nucl-ex]

72. **"Two-pion femtoscopy in p-Pb collisions at $\sqrt{s_{NN}} = 5.02$ TeV"**
J. Adam *et al.* [ALICE Collaboration].
arXiv:1502.00559 [nucl-ex]

73. **"Measurement of jet suppression in central Pb-Pb collisions at $\sqrt{s_{NN}} = 2.76$ TeV"**
J. Adam *et al.* [ALICE Collaboration].
arXiv:1502.01689 [nucl-ex]

74. **"Measurement of charged jet production cross sections and nuclear modification in p-Pb collisions at $\sqrt{s_{NN}} = 5.02$ TeV"**
J. Adam *et al.* [ALICE Collaboration].
arXiv:1503.00681 [nucl-ex]

75. **"Measurement of dijet k_{T} in p-Pb collisions at $\sqrt{s_{NN}} = 5.02$ TeV"**
J. Adam *et al.* [ALICE Collaboration].
arXiv:1503.03050 [nucl-ex]